

DEVELOPMENT AND APPLICATIONS OF CHEMICAL SENSORS FOR THE DETECTION OF
ATMOSPHERIC CARBON DIOXIDE AND METHANE

By

WESLEY T. HONEYCUTT

Bachelor of Science in Chemistry
University of Oklahoma
Norman, OK
2011

Submitted to the Faculty of the
Graduate College of the
Oklahoma State University
in partial fulfillment of
the requirements for
the Degree of
DOCTOR OF PHILOSOPHY
May 2017

DEVELOPMENT AND APPLICATIONS OF CHEMICAL SENSORS FOR THE DETECTION OF
ATMOSPHERIC CARBON DIOXIDE AND METHANE

Dissertation Approved:

Dr. Nicholas F. Materer

Dissertation Adviser

Dr. Allen Aplett

Dr. Christopher J. Fennell

Dr. Jeffrey L. White

Dr. M. Tyler Ley

ACKNOWLEDGEMENTS

The author would like to acknowledge a few people who have been instrumental to this work. Notably, my advisor, Dr. Materer, has been essential to getting this project to move forward and be successful. I would also like to acknowledge my committee members. The author would also like to thank support members of various groups which have participated on this project including: Dr. Peter Clark-project PI, Leonard Garcia-site liason for field work in Farnsworth, TX, Dr. Jamey Jacob-site liason for field work at UAV airfield and co-PI, Jake LeFlore-research specialist for Civil Engineering, Taehwan Kim-postdoc on this project with Dr. Ley, Pouya Amrollahi-research assistant on this project with Dr. Ley, Xiaodan 'Sonia' Li-postdoc with Dr. Ley who provided data analysis, Taylor Mitchell-Aerospace engineer working on this project, David Porter-lab manager for Civil Engineering, Larry Vaughn, and all members of the Physical Sciences instrument shop. The author is thankful for support from various individuals outside of this project who have contributed to it in some way including Dr. Claire M. Curry, Janet Honeycutt, Shoaib Shaikh, lab-mates past and present, fellow Chemistry Department graduate students, and Leon.

Acknowledgements reflect the views of the author and are not endorsed by committee members or Oklahoma State University.

Name: WESLEY T. HONEYCUTT

Date of Degree: MAY 2017

Title of Study: DEVELOPMENT AND APPLICATIONS OF CHEMICAL SENSORS FOR THE
DETECTION OF ATMOSPHERIC CARBON DIOXIDE AND METHANE

Major Field: CHEMISTRY

Abstract:

This is a description of the design of a low-power, low-cost networked array of sensors for the remote monitoring of carbon dioxide and methane. The goal was to create a scalable self-powered two-dimensional array for the detection of these gases in a large area. The sensor selection, electronic design, and data communication was studied and optimized to allow for multiple units to form a self-assembling network for acre-scale coverage with minimal human intervention. The final electronic design of the solar-powered units is flexible, providing a foundation for future field deployable remote monitoring devices. Sensors were selected for this application from commercially available models based on low-power, low-cost, market availability, detection range, and accuracy around the global baseline criteria. For environmental monitoring, carbon dioxide sensors are characterized near 400 ppm and methane from 2 to 200 ppm. For both gases, exertions up to several 1000 pm were examined to mimic large releases. An Xbee mesh network of radios was utilized to coordinate the individual units in the array, and the data was transferred in real-time over the cellular network to a dedicated server. The system was tested at a site north of the Oklahoma State campus, an unmanned airfield east of Stillwater, OK, and an injection well near Farnsworth, TX. Data collected from the Stillwater test sites show that the system is reliable for baseline gas levels. The gas injection well site was monitored as a potential source of carbon dioxide and methane leaks due to the carbon dioxide injection process undertaken there for carbon sequestration and enhanced oil recovery efforts. The sensors are shown to be effective at detecting gas concentration at the sites and few possible leak events are detected.

TABLE OF CONTENTS

Acknowledgements	iii
Abstract	iv
Table of Contents	v
List of Figures	viii
List of Tables	xiii
1 Introduction	1
1.1 Subterranean Carbon Sequestration	1
1.2 Monitoring Strategies	5
2 Comparison of Commercially Available CO ₂ and CH ₄ sensors	10
2.1 Introduction	10
2.2 Objectives	11
2.3 Methods	12
2.3.1 Precision and Baseline Noise Tests	16
2.3.2 Limit of Detection	17
2.4 Results and Discussion	20
2.4.1 Precision and Baseline Noise Tests	21
2.4.2 Response Time	22
2.4.3 Limit of Detection	24
2.5 Conclusion	25
3 Determining the Battery Shutoff Circuit Behavior of a Commercially Available Solar Charging Circuit	31
3.1 Introduction	31
3.2 Discharge Behavior and Cutoff Point	32
3.3 A Direct Comparison of Batteries and Damage Due to Repeated Discharge	32
3.4 Conclusions	34
4 Networking with from an Xbee Modem Mesh to a Cellular Modem	38
4.1 Network Topologies for Remote Sensing	38
4.2 Modems and Radios	40
4.3 Data Storage and Transmission	46
5 Development of a Networked Gas Sensor Array for the Detection of CO ₂ and CH ₄ Concentrations	50
5.1 Introduction	50
5.2 Device Design	51

5.2.1	Gas Sensors	52
5.2.2	Power Management	53
5.3	Circuit Description	55
5.3.1	Power Supply	57
5.3.2	Processor and Memory	59
5.3.3	XBee Wireless Communication	60
5.3.4	Cellular Communication	63
5.3.5	Sensor Breakout Board	63
5.3.6	Gascard Implementation	69
5.3.7	Ground Protection	74
5.4	Air Sampling	75
5.4.1	Passive Sampling	75
5.4.2	3D Printed Parts	76
5.4.3	Active Sampling	79
5.5	Prototyping	85
5.6	Mass Production	88
5.7	Conclusions	91
6	Results of Prototyping Tests and Long-term Tests of a Networked Sensor Array at a Proving Ground on the OSU Campus	93
6.1	Introduction	93
6.2	Preliminary Deployment and Unscheduled Mechanical Stress Testing	93
6.2.1	Detected Events	93
6.2.2	Storm Damage	95
6.3	Comparing Collected Data from Long-Term Array against Accepted Weather Report Data	101
6.4	Conclusions	107
7	Results of Data Collected Tests from a Networked Sensor Array at the OSU Unmanned Airfield	108
7.1	Introduction	108
7.2	Sensor Network	109
7.3	Data Analysis	109
7.3.1	Carbon Dioxide	111
7.3.2	Methane	112
7.3.3	Peak Events	114
7.4	Conclusions	116
8	Results of Data Collected from a a Networked Sensor Array near a Gas Injection Well Field Site near Farnsworth, TX	118
8.1	Introduction	118
8.2	Sensor Network	119
8.3	Data Analysis	121

8.3.1	Carbon Dioxide	122
8.3.2	Methane	124
8.3.3	Peak Events	126
8.4	Conclusions	127
9	Conclusion	129
9.1	Introduction	129
9.2	Summary of Work and Findings	129
9.3	Beyond the Project Goals	131
	Bibliography	132
10	Bibliography	133
A	Sensor Board - Primary Circuit	147
B	Sensor Board - Sensors Breakout Circuit	161
C	Sensor Board - Cellular Modem Breakout Circuit	166
D	OpenSCAD Code Used for 3D Printed Part	167
E	Assembly Instructions For Sensor Nodes	172
VITA	183

List of Figures

1.1	A summary of carbon dioxide injection wells	3
1.2	The steps in subterranean plume migration	5
2.1	Gas Mixing Apparatus Diagram	15
2.2	Carbon dioxide baselines	17
2.3	Methane baselines	18
2.4	Carbon dioxide Gaussian distribution	19
2.5	Methane Gaussian distriution	27
2.6	Gas Mixing Apparatus	28
2.7	Trendline comparision of sensor responses	29
2.8	MQ-4 concentration step plot showing overshoot	30
3.1	Battery shutoff behavior by protection circuit	33
3.2	Shutoff behavior of battery circuit with a $141\ \Omega$ load	34
3.3	Shutoff behavior of battery circuit with a $188\ \Omega$ load	35
3.4	Shutoff behavior of battery circuit with a $235\ \Omega$ load	35
3.5	Battery discharge time vs. current	36
3.6	Battery degredation upon repeated tests	37
4.1	Point-to-point Network Topology	39
4.2	Line Network Topology	39
4.3	Bus Network Topology	40
4.4	Star Network Topology	41
4.5	Mesh Network Topology	42
4.6	Hybrid Network Topology	43
4.7	Xbee modem	44

4.8	Xbee Mesh Sample	45
4.9	Sensor and Communication Nodes Functional Diagram	46
4.10	Data Collection Scheme - Sensor Node	47
4.11	Data Collection Scheme - Communication Node	48
4.12	Data Collection Scheme - Server Storage	49
5.1	Equipment outline	53
5.2	Tycon Power Systems enclosures	54
5.3	Control board	56
5.4	Control board - Sensor node parts	57
5.5	Control board - Communicaiton node parts	57
5.6	Circuit - Fuse protected 12 V terminal circuit	58
5.7	Circuit - 3.3 V DC/DC converter circuit	58
5.8	Circuit - 5 V Dc/DC converter circuit	60
5.9	Circuit - External crystal oscillator	60
5.10	Circuit - Example of switch and associated LED	61
5.11	Circuit - ICSP header pinout	61
5.12	Circuit - DS3231 real time clock circuit	61
5.13	Circuit - EEprom memory IC and connections	62
5.14	Circuit - microSD memory slot with switch circuitry	62
5.15	Cellular modem breakout board	63
5.16	Cellular modem part	64
5.17	Circuit - Schematic of XBee device	64
5.18	Circuit - Cellular communication breakout board schematic	65
5.19	Sensor breakout board	66
5.20	K-30 Carbon dioxide part	66
5.21	Circuit - Carbon dioxide sensor with level translator	67
5.22	Circuit - Mainboard carbon dioxide level translator	67
5.23	Mq-4 methane sensor part	68
5.24	Mq-4 methane sensor part with sensing element exposed	68
5.25	Circuit - methane sensor socket with amplifier	69
5.26	Circuit - SPI and level translator for methane sensor	69

5.27	Sensirion SHT75 temperature sensor part	70
5.28	Freescape MPXS6115 pressure sensor part	70
5.29	Circuit - SHT75 schematic on sensor board	71
5.30	Circuit - MOSFET switches used with the SHT75 clock line	71
5.31	Circuit - SHT75 data level translator on mainboard	71
5.32	Circuit - MPXA6115A pressure sensor and amplifier	72
5.33	Circuit - Gascard 4 V power supply	72
5.34	Circuit - Pump power and adjustment	73
5.35	Circuit - Serial to asynchronous communication translator	74
5.36	Labeled cartoon of 3D printed part	77
5.37	Early 3D printed part production	78
5.38	Closeup of Makerbot 2 detail	79
5.39	Closeup of Makerbot 2 detail, curved	80
5.40	Closeup of EOSINT detail	81
5.41	Closeup of EOSINT detail, curved	82
5.42	Early prototype of plastic parts	82
5.43	3D printed part attached to the board	83
5.44	3D printed part with silicone	83
5.45	3D printed part joins	84
5.46	Lexan box housing	84
5.47	Arduino Mega development board	86
5.48	Internals of sensor node	87
5.49	A delivery of control boards from the assemblers	89
6.1	Long term field testing site	94
6.2	Carbon dioxide detection by a prototype units	95
6.3	Methane detection by two prototype units	96
6.4	Storm damage to prototype sensors	97
6.5	Storm damage to UNIT 0003 - 1	98
6.6	Storm damage to UNIT 0003 - 2	99
6.7	Storm damage to UNIT 0004	100
6.8	Temperature data collected vs. weather data	102

6.9	Humidity data collected vs. weather data	103
6.10	Pressure data collected vs. weather data	104
6.11	Carbon Dioxide Concentration at Proving Ground	105
6.12	Methane Concentration at Proving Ground	106
7.1	UAV Sensors	109
7.2	Map of Airport Sensors	110
7.3	Distribution of Sensor Responses in a Daily Cycle	111
7.4	Aligned Data from UAS CO ₂ Sensors	112
7.5	Averaged Response from all UAS CO ₂ Sensors	113
7.6	Distribution of Responses from UAS CO ₂ Sensors	113
7.7	Aligned Data from UAS CH ₄ Sensors	114
7.8	Averaged Response from all UAS CH ₄ Sensors	115
7.9	Distribution of Responses from UAS CH ₄ Sensors	115
7.10	UAS Detected Events	116
8.1	Proposed grid of sensors at Farnsworth, TX site	119
8.2	Final sensor placement at Farnsworth, TX site	120
8.3	Mounting of Sensors on Power Poles	121
8.4	Distribution of Sensor Responses in a Daily Cycle	123
8.5	Aligned Data from Farnsworth, TX CO ₂ Sensors	123
8.6	Averaged Response from all Farnsworth, TX CO ₂ Sensors	124
8.7	Distribution of Responses from Farnsworth, TX CO ₂ Sensors	125
8.8	Aligned Data from Farnsworth, TX CH ₄ Sensors	125
8.9	Averaged Response from all Farnsworth, TX CH ₄ Sensors	126
8.10	Distribution of Responses from Farnsworth, TX CH ₄ Sensors	127
8.11	Farnsworth, TX Detected Events	128
E.1	Instructions for sensor node assembly, slides 1-6.	173
E.2	Instructions for sensor node assembly, slides 7-12.	174
E.3	Instructions for sensor node assembly, slides 13-18.	175
E.4	Instructions for sensor node assembly, slides 19-24.	176
E.5	Instructions for sensor node assembly, slides 25-30.	177

E.6	Instructions for sensor node assembly, slides 31-36.	178
E.7	Instructions for sensor node assembly, slides 37-42.	179
E.8	Instructions for sensor node assembly, slides 43-48.	180
E.9	Instructions for sensor node assembly, slides 49-54.	181
E.10	Instructions for sensor node assembly, slides 55-60.	182

List of Tables

2.1	Manufacturer listed properties of evaluated carbon dioxide sensors	13
2.2	Manufacturer listed properties of evaluated methane sensors	13
2.3	Ratios of calibrated gases used in mixed gas experiments.	14
2.4	Precision and Accuracy of Carbon Dioxide Sensors	23
2.5	Precision and Accuracy of Methane Sensors	23
2.6	Detection Limits of Carbon Dioxide Sensors	25
2.7	Detection Limits of Methane Sensors	25
5.1	Device hierarchy	52
5.2	Power use of sensors	55

CHAPTER 1

Introduction

Great strides are made in science which provide Man with more capabilities to measure the environment. To make best use of these advances, a determined approach must be made to the design of systems applying these tools. The design of a proper system using advanced sensing techniques is essential to ensuring that the core science is able to benefit the users. The work reported in this dissertation is a summary of projects related to the application of existing gas sensors to the detection of microseepage of carbon dioxide and methane from subterranean storage sites. This work will discuss comparison of several individual gas sensors, the design of a networked array which utilizes these sensors, construction of the individual node units of this network, deployment of the networks at several sites, and the data resulting from experiments at these sites.

1.1 Subterranean Carbon Sequestration

The effect of carbon dioxide in the atmosphere on terrestrial temperature has been known to science since the late 19th century as quantified by Arrhenius [1]. As carbon dioxide output from anthropogenic sources increases [2], it becomes increasingly important to find solutions to prevent excessive buildup. One such proposed solution is injection of excess carbon dioxide underground. There, the injected gas can be stored in naturally occurring subterranean voids or those left by mining and hydrocarbon extraction processes. Alternately, the carbon dioxide can be used as an extraction fluid to pull valuable hydrocarbons such as methane still remaining in these wells in a process termed Enhanced Oil Recovery (EOR).

Sites of particular interest are bituminous sands, unreachable coal beds, deep saline aquifers, and salt caverns [3, 4].

In sequestration efforts, carbon dioxide is collected from significant waste streams such as those produced by coal-fired power plants, and injected into underground voids [4]. The procedure involves pressurization of carbon dioxide into a supercritical fluid and injection into a drilled hole. As the fluid is pumped into the well, it expands to fill porous regions as the pressure reaches a penetration threshold. It is theorized that the majority of the injected gas will be converted from fluid carbon dioxide to carbonate salts with time after the injection. By this process, the waste streams from large industrial producers of carbon dioxide is converted from an emitted greenhouse gas pollutant to a more manageable solid form. As it is accepted that the injected carbon dioxide will remain underground for many years, it is considered to be a viable solution to excess emissions. Studies comparing the collection and injection methods of the gas into different storage locations at small scale suggest that carbon sequestration by the injection of flue gas into underground voids is a net benefit in terms of greenhouse gas mediation efforts [5]. A summary of this process is depicted in Figure 1.1. In a secondary process, as the carbon dioxide seeps from the storage depth, it undergoes biogenic reduction to methane, an even more potent greenhouse gas [6]. Most of this gas is expected to remain in the storage site as well, but reliable sensing method for detecting problems due to changes in flux of both these gases is essential to the safe deployment of this method in the interest of environmental health and safety.

The pressurized carbon dioxide gas can be used to liberate hydrocarbons from the ground by treating the gas as an extraction solvent rather than a permanent injectable. This is the premise of the use of carbon dioxide injection as a method of enhanced oil recovery (EOR). Pressurized carbon dioxide is pumped into new or existing wells and the fluid fills in spaces in the surrounding earth, replacing an existing material which is easily dissolved into the carbon dioxide [7] and potentially liberating valuable gases trapped in these underground areas such as methane [8]. Additionally, a variant of this process can be used to extract crude oil which has not been liberated by traditional drilling. Most EOR projects occur at existing oil and gas developments or at “depleted” sites [9]. A report from the National Energy Technology Laboratory of the United States Department of Energy claims that the sequestration of 20 billion metric tons of carbon dioxide has been employed as part of EOR

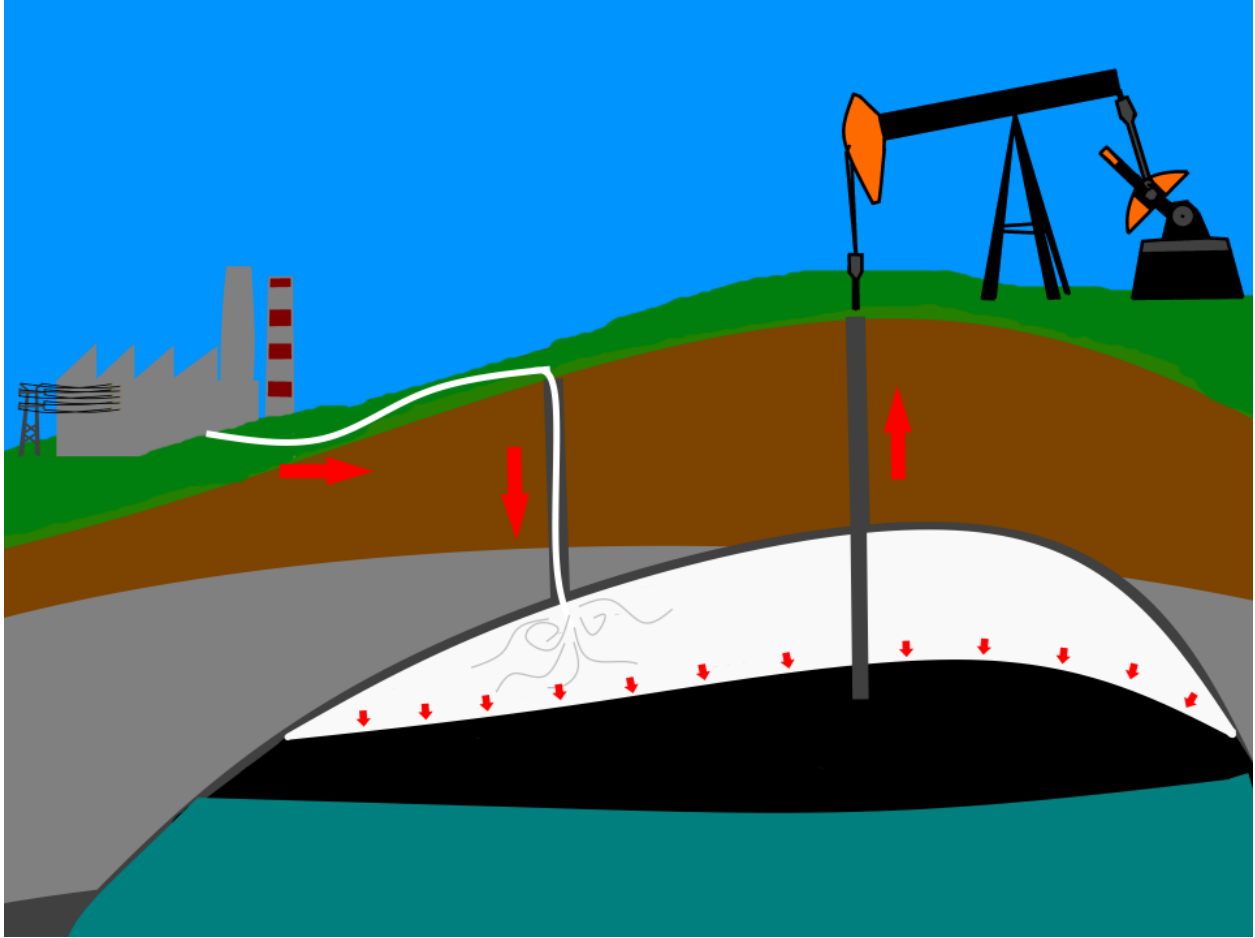


Figure 1.1: This diagram shows a simplified explanation of the carbon dioxide injection process. The cartoon depicts carbon dioxide being collect from a large industrial source, e.g. a power plant, and pumped into a deep saline aquifer well. The gas is injected as a supercritical fluid near the top of a void surrounded by a sturdy rock formation. The pressure from the expanding fluid pressurizes the well. Remaining oil in the well sitting in a layer above the aquifer is easily pumped out by existing infrastructure.

programs since their discovery [10, 11]. As of 2014, 53% of all commercial-scale EOR projects in the United States utilize gas injection techniques, and the number of projects using this method is expected to increase as there is more push for carbon dioxide sequestration in conjunction with rising energy prices [12]. Unlike environmental remediation sequestration efforts, the majority of the carbon dioxide gas for EOR projects is pumped from geologic sources. Only a third of the gas used in small-scale EOR research wells was procured from flue gas [9].

There are some concerns regarding the potential outcomes of such storage regimes [13]. A large leak of the sequestered carbon dioxide which has not undergone conversion to carbonate

salts has the potential for catastrophic and expensive consequences. A plume of carbon dioxide has the potential of suffocating all animal life in an area, as evidenced by the events at Lake Nyos [14] and Lake Monoun [15] in Cameroon which caused massive loss of human life. It is essential that this outcome be avoided, therefore it is equally essential to monitor the gas flux from the storage sites over time. Small leaks over time, while less catastrophic in nature, would undermine the assumption that carbon sequestration as a fail-proof storage mechanism for excess carbon dioxide waste gas as the presumed net gain in environmental health would be lost over longer periods. There have been no studies of carbon dioxide leakage from carbon sequestration sites over long time scales. This is due, in part, to the recent development of the technique. However, there are currently inadequate monitoring technologies for this kind of study. Often, atmospheric ramifications of sequestration and EOR is ignored entirely. Only half of small-scale EOR testing projects conducted atmospheric monitoring, instead most rely on subsurface monitoring and geochemical modeling techniques [9].

If the fluidized carbon dioxide in the rocky subsurface environment can be thought of as a mobile phase in a large solid substrate, it is reasonable to suspect that voids in the solid material would physically separate as layers. It is proposed by some researchers that the injected carbon dioxide will migrate towards the surface, eventually seeping out in small quantities, in a process known as microseepage [16, 17, 18]. This is the vertical migration of an underground “plume” which moves toward the surface. This plumed gas eventually will leak from the subterranean storage site from small fissures in the ground. A simplified cartoon of plume migration is depicted in Figure 1.2.

The migration of carbon dioxide is recognized as an important factor for determining the economic feasibility of an injection well, and as a prospective legislative issue [19]. It is difficult and costly to monitor these gas plumes experimentally. Instead, researchers rely heavily on computer modeling, which has been shown to be effective for predicting the lateral diffusion of the plume underground [20, 21]. The scope of many theoretical studies of carbon dioxide injection primarily focuses on lateral plume migration through individual layers, assuming that there is minimal vertical migration [22]. While this is predominantly the case, moderately porous materials with interconnected channels induce gas mobility to a similar degree as inter-particulate spaces in laboratory testing [23]. Certain models for the prediction of plume migration after injection are simplified by assumptions which may not accurately

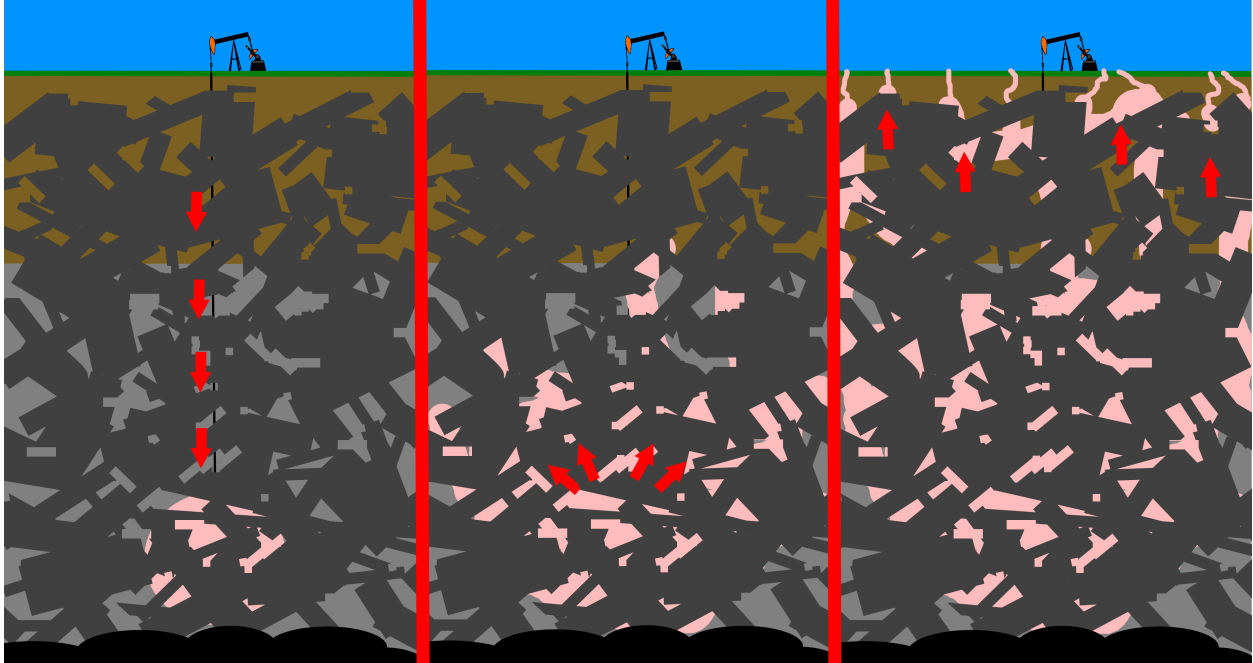


Figure 1.2: This cartoon depicts a simplified illustration of the plume which forms during CO₂ injection. In the leftmost image, a quantity of CO₂ is pumped in from the surface (represented somewhat inaccurately by the oil derrick). As more CO₂ is left in the well, the supercritical fluid expands through crevices in the rock and sediment layers predominantly toward the surface. Eventually, this stored gas will reach the surface and begin to gradually seep out through a process known as microseepage.

model the physical world, including the assumption that the surface layer is impermeable to the fluidized gas [24]. Fluidized carbon dioxide does not increase porosity of solid material, however the focus on lateral plume migration in theoretical models does not adequately address the potential for microseepage from subterranean storage environments.

1.2 Monitoring Strategies

Monitoring of gas flux transitioning from subsurface storage areas to the atmosphere can take place using a variety of techniques at various locations around a wellhead and plume site. Atmospheric monitoring methods include optical sensors such as non-dispersive infrared (NDIR), light detection and ranging (LIDAR), sorbent sampling of tracer molecules, and eddy covariance (EC) flux monitoring; near-surface monitoring methods include soil sampling, flux accumulation, hyperspectral imaging, and many more [25]. While this list is limited in scope, it touches upon some of the most commonly deployed strategies. Yet, there are many shortcomings with the available technology. There is currently no option which allows

for sensitive detection of analyte gases at a short time-scale with remote monitoring for long measuring periods. The current implementation of these strategies ranges from being ineffective to outright hazardous.

The relative inaccessibility of many injection well sites poses a problem. Soil sampling has long been used for determining the effects of wells on the local soil environment. Operators go to field sites and take either core samples or headspace samples from multiple sites in the area. While monitoring agencies and injection well operators can send employees to the field sites to collect data, this is difficult and inefficient. There is a recent push to introduce more remote monitoring technologies to reduce these shortcomings. Spectroscopy remains an ever attractive options for remote sensing of local gas concentrations. Hyperspectral imaging, LIDAR, and other similar technologies working in combination have been shown to be powerful in detecting leak anomalies [26, 27]. Yet these technologies often require a trained operator to function. The recent availability of unmanned aerial systems has been of particular interest for remote monitoring [28]. Yet these systems only allow for temporary scanning of a single set of sites. Planes must be refueled, batteries recharged, and sensors redeployed for each one of these scans. The attractiveness of unmanned aerial systems is limited by the power constraints of these units. Continual monitoring of a site requires active maintenance. Satellites in geosynchronous orbit allow for constant hovering above large areas. A recent study by NASA of a methane leak has shown that the modern LIDAR equipment was even able to measure an above-ground gas plume from a large leak [29]. The gas leak depicted in the article by Thompson et al. was exceptionally large. Most leak events and microseepage occurrences are likely very minor deviations from the local baseline. Current space based spectrometers cannot detect near-baseline deviations of small leakage sites. Additionally, the deploying a satellite is still prohibitively expensive. This means that continual monitoring of every potential leakage site is bottlenecked by the available satellites. Custom built terrestrial remote monitoring stations in development for the In Salah injection well have been shown to have strong detection capabilities in simulated leaks [30, 31]. Yet these proposed sensors are only capable of single site monitoring as of this publication. As potential leakage from subterranean storage site may occur over a large area and from surrounding abandoned wells [32, 33], single site detection is not practical for monitoring of the large area potentially affected by an injected carbon dioxide plume. Eddy Covariance is praised for the large area

that can be monitored, however the devices are maintenance intensive, requiring adequate infrastructure in the sequestration area and computational power due to data complexity [34]. Current remote monitoring techniques may serve to reduce the man-hours required compared to traditional soil sampling regimes, yet they fall short of the desired goals of true remote detection of small local environmental changes.

Possibly the most selective method for detecting flux of injected chemicals to the atmosphere is the use of tracer chemicals. Addition of a trace quantity of a chemical which is inert to the system is made during the injection process. Sites can be monitored by selective testing for these chemicals. The low signal-to-noise ratio of optical detection for tracer chemicals in flux gas is an attractive option, but has the potential for environmental damage by way the persistent pollutant nature of the perfluorocarbons used as tracers [35, 36]. For crude oil well-to-well analysis, it has long been established that the addition of an anthropogenic radioisotope can be detected from pumped material based on characteristic radiation from the sample. Only certain chemicals meet the needs of carbon dioxide injection wells [37]. Notable among this subset is the use of halogenated organic compounds, sulfur hexafluoride, and hydrogen sulfide. Many of these chemicals have been identified as environmentally hazardous compounds. Many of the halogenated organic compounds recommended for use, often freon variants, are persistent chemicals with high greenhouse gas potentials. Sulfur hexafluoride, while attractive due to its inert qualities, is extremely persistent with high radiative forcing such that it is considered to be more than 26,000 times more greenhouse warming potential over the 100 years than carbon dioxide [38]. Some tracers, such as hydrogen sulfide, have been shown to enter aquifers, causing them to be non-potable sources for future use [39]. These tracer chemicals may not even be effective in supercritical fluids. It is proposed by Vanderweijer et al. that higher solubility of carbon dioxide in water than tracer chemicals may lead to inaccurate concentration measurements in offshore injection environments and wells known to contain significant water deposits [19]. An optimal solution to the monitoring of injection wells would quantify the migrating gas without requiring an environmentally persistent tracer.

There are no monitoring devices which can collect data from multiple sites simultaneously at fast time-scales over a continuous period. This is evidenced by the lack of available data on the diel cycle of gas concentrations. Isolated studies have been conducted which have

established the day-night cycling of gases such as carbon dioxide and methane, yet these often only measure a few points of data per 24-hour cycle. Determining the diel cycle for these gases is valuable to climate scientists, biologists, and agricultural engineers, and data of the diel cycle of concentration over various terrestrial and aquatic local environments is available in the literature for carbon dioxide [40, 41, 42, 43, 44, 45] and methane [46, 47, 48, 49, 50, 51]. While only a sampling of the available literature is mentioned in the previous citations, a critical analysis of all of these sources shows that current technologies are not utilized to detect concentration often, for a long time, and over a large area. These studies usually involve a single sampling instrument operated continuously for a short period, samples taken with large gaps between points, or distributed detection of multiple sites not performed concurrently. Recent developments of devices under the “internet of things” notion suggest that construction of devices for this purpose should be simple. Yet no one has done it. The specialized knowledge required to construct these devices, the programming experience required to operate them, and the time required to perfect such devices to a field-deployable state appears to have deterred many scientists from attempting to create units of this class. The construction and characterization of instruments designed for distributed detection in the scientific literature would provide a framework for other scientists-reducing the barrier to these technologies for applications described in this monograph as well as further applications.

A technological niche exists for a relatively inexpensive device which can monitor a large number of sites easily with little human interaction. A solution to this problem exists in the application of available technology to develop a distributed sensing unit that wirelessly transmits information to a gathering center. This idea in itself is not completely without precedent. Wireless sensor arrays have been used before in agricultural applications to monitor conditions [52] and aerial cloud analysis [53]. In these cases they have demonstrated the capacity to perform required monitoring functions over a large area with low cost and human interaction. An adaptation of this technology to fit with the needs of gas monitoring at wellheads provides our solution.

To apply the wireless sensor array technology to environmental monitoring of gas flux, we must consider the sensors to connect to the network. The sensors developed for this project will directly measure the concentration of gas at the surface using a combination of infrared sensors and atmospheric condition sensors. While the idea of deploying a large

number of NDIR sensors is not completely new either [54], the technology suggested for these deployments (short closed-path NDIR) requires constant pumping to operate, making it energetically expensive and impractical for a remote monitoring network. This project will utilize a unique combination of the pumped closed path NDIR sensors and passive gas sensors to reduce energy cost.

In this work, various sensors with purported detection capabilities near the global baseline for carbon dioxide and methane will be investigated and directly compared in Chapter 2. Sensors from this analysis will be used in the construction of the gas sensor array. The low-power constraints of this array will be considered by testing batteries from a commercially available solar-powered enclosure for shutoff thresholds and repeated discharge damage in Chapter 3. The devices will be programmed for low-power operation based on available battery charge from these data. The networking strategy for the proposed array will be discussed and implemented in Chapter 4. A detailed description of the individual circuitry of the devices will be presented in Chapter 5. This discussion of the device will also include considerations made for sampling regimes and layout. The constructed devices in the networked array of gas sensors will be deployed to three sites, a prototyping field north of the OSU campus in Chapter 6, an unmanned aerial systems test field in Chapter 7, and a carbon dioxide injection well near Farnsworth, TX in Chapter 8. At these sites, the data produced by the sensors will be compared to known data from weather stations to confirm that the arrays are producing results consistent with accepted data. The data produced by sensors at the airfield and injection well sites will be characterized by statistical analysis and event threshold determination.

In the appendices, information is made available to facilitate future replication of the work described here. Complete schematics for the printed circuit boards used in these devices are included in Appendix A, B, and C. A script used to generate a 3D printed part for atmospheric interface is given in Appendix D. Detailed assembly instructions for the devices used in this work are given in Appendix E.

CHAPTER 2

Comparison of Commercially Available CO₂ and CH₄ sensors

2.1 Introduction

Environmental monitoring of local gas concentration is becoming increasingly important to ensure worker safety and for early identification of potential leaks. Real time monitoring of carbon dioxide and methane gas concentrations are of interest since these gases impact animal health and crop growth. Since gases are considered greenhouse gases, monitoring industrial sites are important in understand their impact on the environment. In designing monitoring devices, the sensor for gas concentration analysis must be matched to the specific operational requirements, such as precision, reliability, and power consumption. Example sensor elements include those used in HVAC air handlers [55, 56], chemical processing units[57], oil well monitoring devices [58, 59], and environmental monitoring [60, 61, 62, 63, 64]. Given the myriad of other applications, the uses cited represent only a small sample of the various applications and varieties of sensor elements. Despite the large number of sensors which are commercially available, there is limited literature that directly compares sensors. This lack of information limits ones ability to select the optimal sensor for a given application. To address this issue, this paper compares an array of commercially available, low-cost sensors for carbon dioxide (chemical formula CO₂) and methane (chemical formula CH₄) at concentration typical to those required for environmental monitoring around carbon dioxide sequestering operations and oil fields.

Potential sensors range from small, inexpensive chemiresistive sensors to complex

and costly optical systems. The low-cost chemiresistive based methane sensors are typically used in gas warning systems [65]. On the other end, Light Imaging Detection and Ranging (LIDAR) is an accurate and effective method for remote monitoring of industrial sites, for example oil wells [66]. However, these devices are limited by cost and operational complexity, and are not suitable for portable self-powered monitoring devices. The sensors need good sensitivity and precision around the baseline atmospheric concentration for each analyte, which is around 400 ppm for carbon dioxide [67, 68] For methane, the baseline atmospheric concentration is under 2 ppm [69, 70, 71]. Thus, for methane, sensors were selected and tested near their baseline. In addition to concentration, power consumption, reliability, and ease of integration are also important factors. Sensors will be selected based on their sensitivity at atmospheric levels, ease of use, power consumption, price, and market availability.

2.2 Objectives

The objective of this study is to determine the suitability of commercially available low-cost sensors for integration into portable self-powered monitoring equipment. The low-cost sensors currently available can be generally divided by detection method, either optical absorption or electrical changes due to a chemical reaction with the analyte (chemiresistive). Previous researchers have cited concerns with electrochemical sensors for these gases, as they have a short lifetime and lack robustness [72]. The selection process is restricted to sensors that are commercially available in large volumes (at least 1000 units) at low-cost (defined here as less than \$100 per unit in bulk).

Optical sensors typically have excellent sensitivity, selectivity, and fast response to concentration changes. Optical methods of detecting carbon dioxide and methane are based on the measuring the absorption of light at 2352 cm^{-1} and 3015 cm^{-1} , respectively [73, 74]. Sensors utilizing these specific wavelengths are termed dispersive infrared instruments and are typically bulky, costly and fragile. Low-cost sensors utilize nondispersive infrared (NDIR) sensing, which utilizes a source which emits at a broad spectrum coupled with a narrow band pass filter across the absorbance maximum. As a result, lower cost parts can be used and the design can be both more compact and robust. These optical methods utilize the Beer-Lambert Law to relate absorptions to concentrations, and thus are only dependent on the geometry of the sensor and physical properties of the gas. [75] In general, NDIR detection is utilized

for carbon dioxide do due its relatively large molar adsorption coefficient results in a short path length. Methane is limited in practical applications due to its low absorbance coefficient and overlap interfered symmetric C-H stretches, making methane difficult to distinguish from ethane or propane, for example. [76]. Small chemiresistive sensors for carbon dioxide and methane are primarily based on reactions between the analyte and a semiconductor film, typically tin oxide. [72] Although, chemiresistive sensors have significant drawbacks, including selectivity, these sensors are easy to produce and have very low cost, leading to widespread use. Commercially, there are several available chemiresistive for detection of methane. These sensors work by measuring changes in electron transport through the metal oxide semi-conductive film, in the presence of oxygen and reactive gases [77]. When the film is exposed to methane, the molecule adsorbs and reacts with surface oxygen species. This liberates free electrons in the bulk and reduces the electrical resistance [78, 79].

To drive the chemical reactions at a reasonable rate, the film must be heated to at least 350 °C to work effectively [80]. drastically increases power consumption. Additionally, the measured transduction depends on the surface of the film, the presence of oxygen containing species, and the reaction rate. As such, the output depends on the relative humidity, temperature, and preparation of the film. Unlike optical sensors which depend only on physical properties of the analyte, the output of these sensors have a complex relationship to the gas concentration which varies from sensor to sensor. For carbon dioxide, the authors located a chemiresistive sensor which operates slightly different. This variant detects resistance changes that occur when carbon dioxide adsorbs and reacts to form a carbonate on the surface of the film [81].

2.3 Methods

To test the sensors under controlled conditions, an experimental setup (Figure 2.1) was constructed. This setup allows a known concentration to be prepared from a calibrated gas cylinder. A high-quality bench-top analyzer (California Analytical Instruments, Inc. ZRE Non-Dispersive Infrared Analyzer) sensitive to both carbon dioxide and methane. The analyzer can be periodically calibrated using the calibrated gas mixture to ensure accuracy. The calibrated gas tank contained a mixture of gases in one of the ratios listed in Table 2.3 depending on the specific experiment being performed. The gas mixtures were provided by

Table 2.1: Manufacturer listed properties of evaluated carbon dioxide sensors

Sensor	Supplier	Type	Sampling Method	Cal. Range	Op. Range
K-30 SE-0018	CO ₂ Meter	NDIR	flow or diffusion	0-5000 ppm	0-10000 ppm
COZIR AMB GC-020	CO ₂ Meter	NDIR	flow or diffusion	0-5000 ppm	0-10000 ppm
Gascard CO ₂	GHG Analytical	NDIR	flow	0-50000 ppm	0-50000 ppm
MSH-P/CO ₂ /NC/5/V/P/F	Dynament	NDIR	diffusion	0-2491 ppm	0-5000 ppm
MSH-DP/HC/CO ₂ /NC/P/F	Dynament	NDIR	diffusion	100-2500 ppm	0-5000 ppm
Telaire T6615	General Electric	NDIR	flow or diffusion	0-2000 ppm	0-2000 ppm

Sensor	Warm Up	T	Humidity	Auto-cal	V Input	Avg. I	Peak I
K-30 SE-0018	<1 min	0-50°C	0-95%	Yes	4.5-14 VDC	40 mA	<150 mA
COZIR AMB GC-020	<3 s	0-50°C	0-95%	Yes	3.25-5.5 VDC	1.5 mA	33 mA
Gascard CO ₂	30 s	0-45°C	0-95%	Yes	7-30 VDC		
MSH-P/CO ₂ /NC/5/V/P/F	45 s	-20-50°C	0-95%	No	3.0-5.0 VDC	75-85 mA	
MSH-DP/HC/CO ₂ /NC/P/F	45 s	-20-50°C	0-95%	No	3.0-5.0 VDC	75-85 mA	
Telaire T6615	10 min	0-50°C	0-95%	Yes	0-5 VDC	33 mA	180 mA

Table 2.2: Manufacturer listed properties of evaluated methane sensors

Sensor	Supplier	Type	Sampling Method	Cal. Range	Op. Range
MQ-4	Futurelec	Chemoresistive	diffusion		200-10000 ppm
Gascard CH ₄	GHG Analytical	NDIR	flow	0-50000 ppm	0-50000 ppm
MSH-P/HC/NC/5/V/P/F	Dynament	NDIR	diffusion	0-5000 ppm	0-10000 ppm
MSH-DP/HC/CO ₂ /NC/P/F	Dynament	NDIR	diffusion	5000-11000 ppm	0-10000 ppm
TGS-2600	Figaro Engineering	Chemoresistive	diffusion		1-30 ppm
TGS-2610	Figaro Engineering	Chemoresistive	diffusion		1000-25000 ppm
TGS-2611	Figaro Engineering	Chemoresistive	diffusion		500-10000 ppm

Sensor	Warm Up	T	Humidity	Auto-cal	V Input	Avg. I	Peak I
MQ-4				No			
Gascard CH ₄	30 s	0-45°C	0-95%	Yes	7-30 VDC		
MSH-P/HC/NC/5/V/P/F	30 s	-20-50°C	0-95%	No	3.0-5.0 VDC	75-85 mA	
MSH-DP/HC/CO ₂ /NC/P/F	30 s	-20-50°C	0-95%	No	3.0-5.0 VDC	75-85 mA	
TGS-2600				No	5.0±0.2 VDC	4.2±4 mA	
TGS-2610				No	5.0±0.2 VDC	5.6±5 mA	
TGS-2611				No	5.0±0.2 VDC	5.6±5 mA	

Sensors with no listed warm up time, but required 7 day burn in time

and certified by Airgas Inc. The calibrated gas mixture diluted using either air or nitrogen gas by a set of flow controls to produce specific partial pressures of analyte gases. In the case of sensors configured for gas flow, the sensor being tested was connected directly to the apparatus by flexible hose connection. For sensors that are diffusion based, the sensor was placed in an exposure chamber connected by flexible hose. Using the exposure chamber, the relative rise time of the various sensors was measured and compared. The mixing time or the time required for the chamber to reach and maintain gas concentration, even when the concentration of the incoming gas was changing was determined to be negligible with

respect to the response times of the sensors. All experiments were referenced to the California Analytical Instruments ZRE Analyzer.

Table 2.3: Ratios of calibrated gases used in mixed gas experiments.

Carbon Dioxide	Methane	Bulk Gas
3000 ppm	3000 ppm	nitrogen
100 ppm	100 ppm	nitrogen
0 ppm	20 ppm	nitrogen

Commercially available carbon dioxide and methane sensors were selected and evaluated based on the needs for a potable self-powered sensor. Table 2.1 lists the selected carbon dioxide sensors with important properties obtained from the manufacturer. Table 2.2 lists the methane sensors and respective properties. Certain sensors were chosen with specific provided specifications. The K-30, COZIR, Dynamant, and Telaire sensors are all NDIR sensors. These were chosen as low-cost, lightweight sensors with satisfactory detection parameters of carbon dioxide. Dynamant also provides a dual gas NDIR sensor designed to measure both carbon dioxide and methane concentrations. The carbon dioxide and methane Gascard sensors sold by GHG Analytical were an order of magnitude more expensive than the other NDIR sensors, having a cost between that of the low-cost sensors and that of the bench-top analyzers. Their specifications and the included internal pressure and temperatures compensation make them attractive enough to make up for the expense. In addition to the Gascard sensor, the Dynamant hydrocarbon sensors were chosen as the inexpensive candidates for methane detection. Chemoresistive sensors include the MQ-4 and TGS-26xx series sensors. The TGS sensors manufactured by Figaro Engineering Inc. are used in commercial methane detectors and have been previously evaluated by other groups [82]. There are several different MQ versions optimized for hydrocarbon sensing. The MQ-4 from Hanwei Electronics was chosen as this variant was specifically tuned for methane. The chemiresistive sensors required various minimum conditioning periods before use by their respective manufacturers. This “burn-in” time was met or exceeded for all chemiresistive sensors.

Due to the unique interface requirements of each sensor unit, development kits were purchased when possible. For those without development kits available, an Arduino microcontroller with a prototyping board was used. The chemiresistive sensors were energized using the recommend voltage for the heater element and the response was measured as

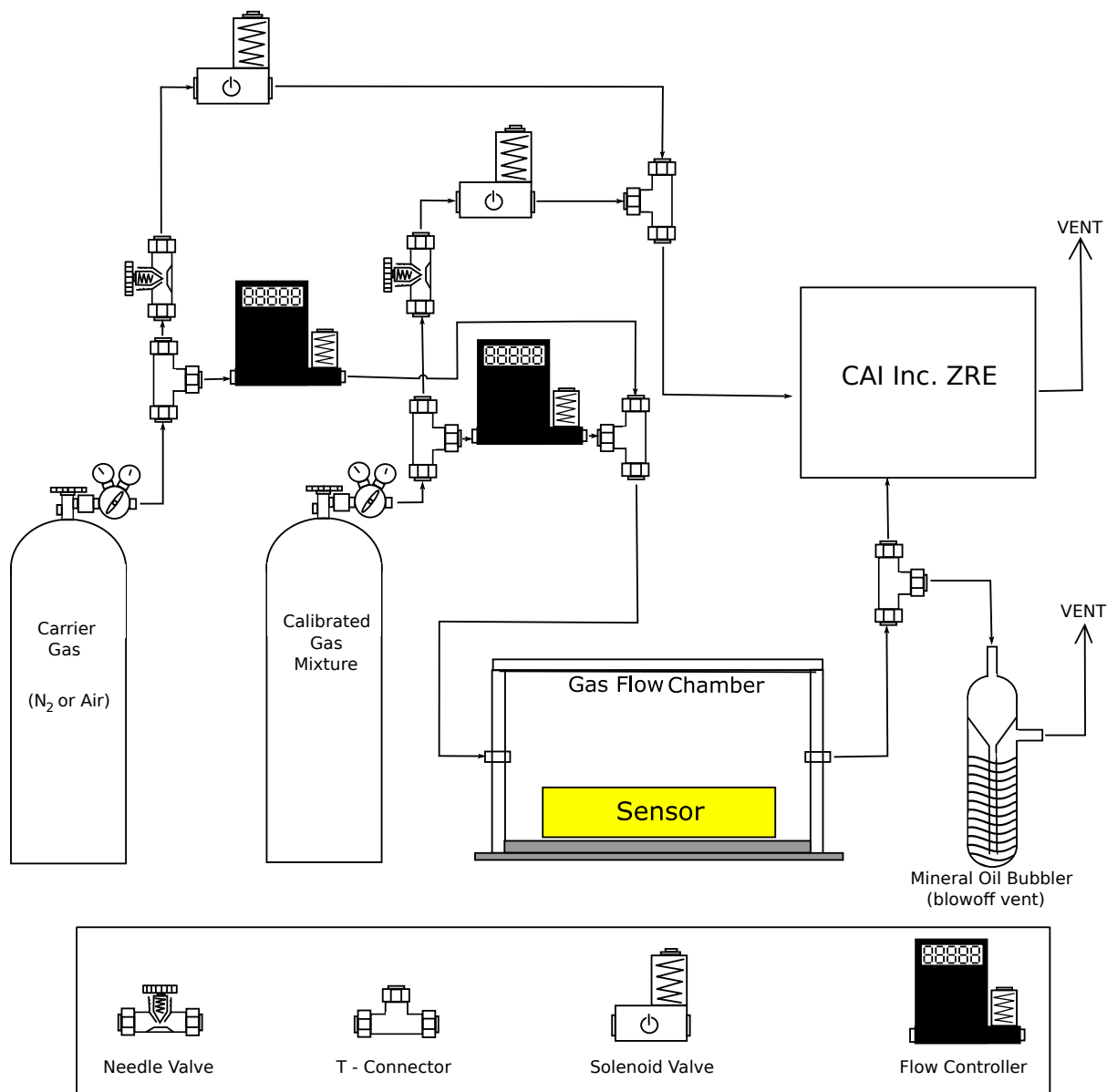


Figure 2.1: Component diagram of controlled gas exposure apparatus with chamber for diffusion-type sensors. The gas from the cylinders is mixed by controlling the ratio of flow by the flow controllers. Multiple solenoid valves are able to completely shut flow off from the tanks. The mixed gas is fed to the flow chamber. The gas flowing through the chamber exits and goes to the California Analytical Instruments Inc. ZRE unit for analysis. A mineral oil bubbler is present to prevent overpressure of the exiting gas.

voltage, after buffering and filtering, across a $10\text{ k}\Omega$ resistor. Data were logged as a function of time using software provided by the manufacturer as part of development kits when provided, or using an Arduino microcontroller with microSD card.

2.3.1 Precision and Baseline Noise Tests

The measurement precision of each sensor was performed using the exposure apparatus discussed above. The baseline carbon dioxide tests were performed with a measured concentration of approximately 400 ppm in nitrogen gas, while the baseline methane tests were performed under medical grade air. The 0 ppm methane concentration was chosen as the expected atmospheric or environmental level will be close to 0 ppm. All of the chemiresistive sensors required atmospheric concentrations of oxygen to measure the methane. The concentration of gas used to fill the chamber was verified with the bench-top analyzer (California Analytical Instruments, Inc. ZRE Non-Dispersive Infrared Analyzer). The precision of the sensors was determined by a 20 to 30 hour data collection time at a known concentration and uniform flow. First, a Fourier analysis was performed on the data collected from each sensor. These analyses showed no significant periodic variations in the output during the respective tests. Next, the data streams were processed to provide the individual difference from the mean reported value, and a histogram of these differences was plotted. The digitized sensor outputs have a finite number of possible output values, so no further bins were created while producing the analysis. A Gaussian fit was applied to the histograms to determine the degree of fit. The histograms with Gaussian peak fitting can be seen in Figures 2.4 and 2.5 for the carbon dioxide and methane sensors, respectively. These plots have been scaled to show detail. The narrow FWHM of the K-30 and Gascard sensors plot in Figure 2.4 shows that both devices can be shown to give high quality data near the global mean concentration of carbon dioxide. Similarly, the Gascard in Figure 2.5 shows good data quality near the global baseline for methane. The digitization level of the Dynamant sensors causes errors near this methane concentration. No curve could be reasonably obtained from one of these sensors due to it only oscillating between two values. The MQ-4 sensor is notably out of scale from the other methane sensors. The adjusted scale in Figure 2.5-B allows this peak to be visible. This clearly shows that the MQ-4 should not be used for quantitative work. Finally, the concentration drift was measured using the difference between the highest and lowest points in an extended run.

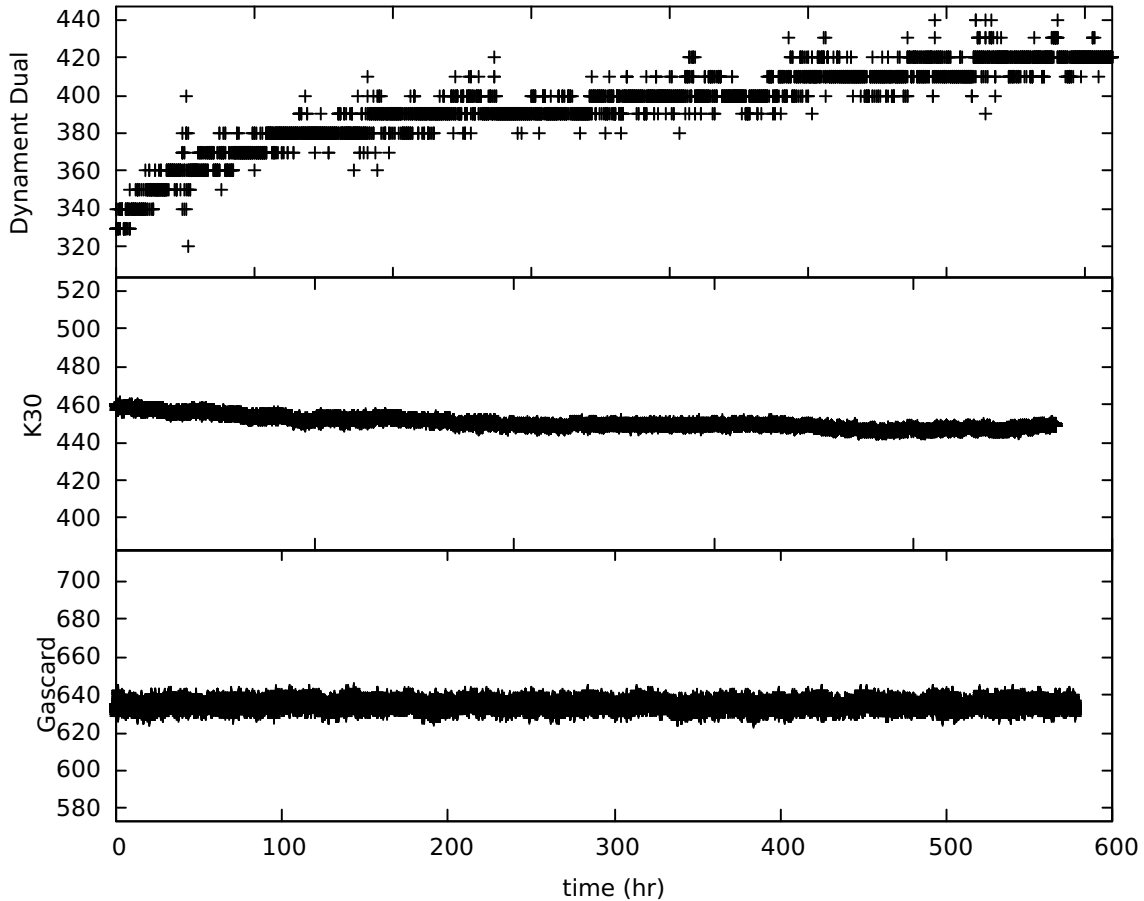


Figure 2.2: Long term baseline data were collected at the atmospheric baseline conditions (using a bottle of compressed medical grade breathing air, approximately 400 ppm carbon dioxide) in the gas mixing chamber. The baseline drift and noise can be observed in these plots.

2.3.2 Limit of Detection

Utilizing the gas mixing apparatus described in Section 2.3, a series of tests were conducted to determine the limit of detection and calibration curve of the selected sensors. For these tests, multiple sensors were in operation concurrently as shown in Figure 2.6. The sensors are organized by flow capable sensors such as the Gascard units and environmental exposure-based sensors housed within the gas enclosures. Sensor modules in the small gas flow enclosures included the K30 carbon dioxide sensor and socket for chemiresistive methane sensors (MQ-4 and the TGS series). The larger chamber contained the COZIR, Telaire, Dynament, and K30 sensors.

A calibration curve of each sensor was developed using varied concentrations of gas

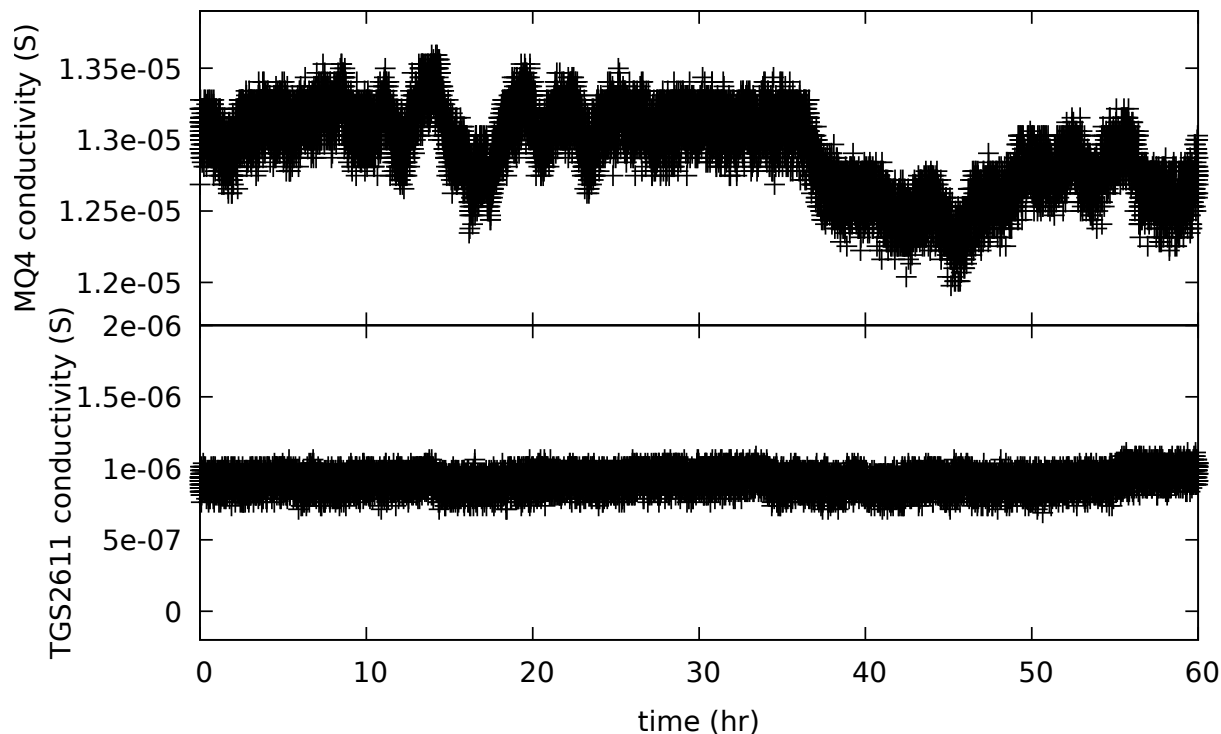


Figure 2.3: Long term baseline data were collected at the atmospheric baseline conditions (using a bottle of compressed medical grade breathing air, approximately 0 ppm methane) in the gas mixing chamber. The baseline drift and noise can be observed in these plots.

through system and, when appropriate, subtracting the baseline reading to the average concentration after stabilization. In these experiments, the carrier gas was first introduced. After a stable baseline was obtained, the calibrated concentration was introduced, after 24 hours, the calibrated gas was introduced, and after 24 hours, it was turned off. The carrier gas was reintroduced and the system was allowed to stabilize for the next measurement. During this procedure, contraction data from each sensor was continually collected. With this method, the average baseline and response to each concentration can be extracted. This process allows the ramp-up when the calibration gas is introduced and ramp-down when the calibration gas was vented, along with any initial overshoot as observed for the chemostresistive sensor to be edited from the data stream. The California Analytical Instruments Inc. ZRE Non-Dispersive Infrared Analyzer was used design calibration curves for each sensor. The mean (μ) and standard deviation (σ) were calculated from each individual baseline and average at each calibration point. The Limit of Detection (L_D) was calculated for each sensor run using the standard approach [83, 84]:

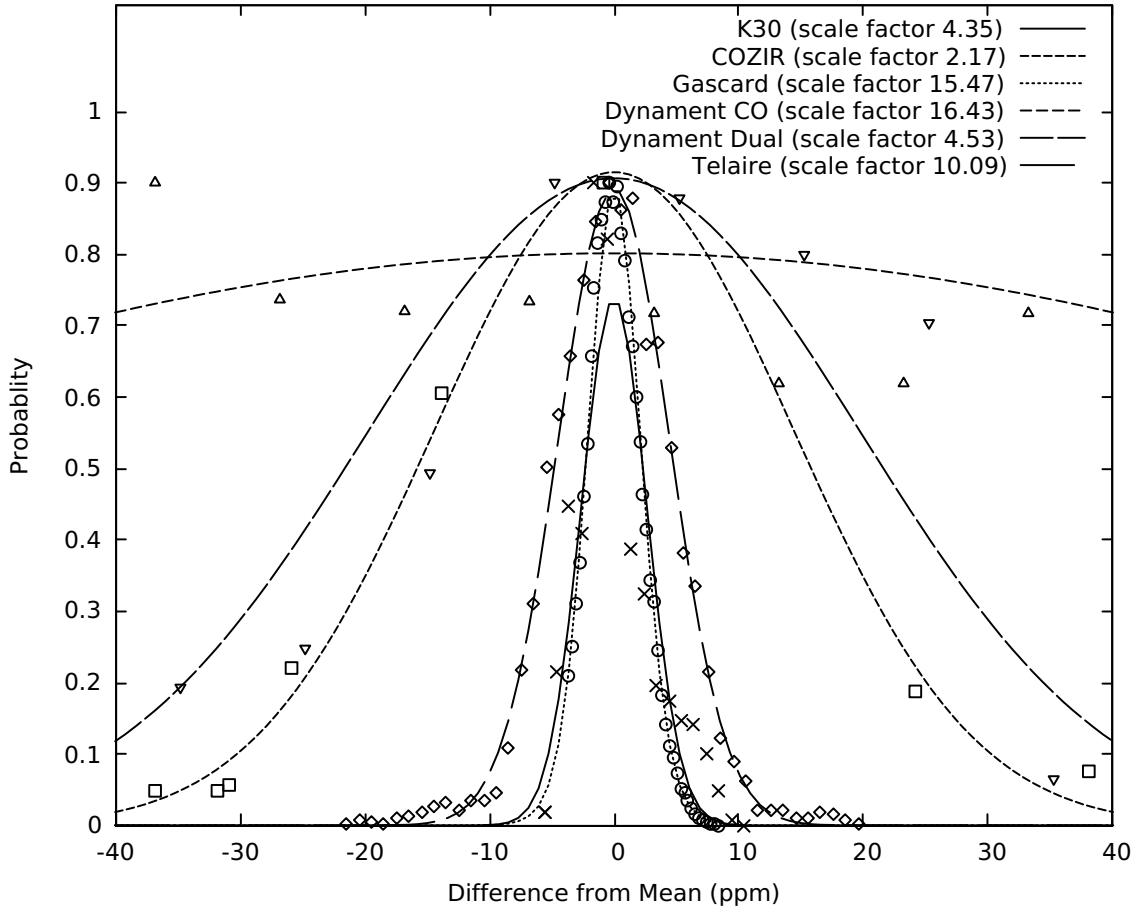


Figure 2.4: This is a plot of the probability density function by Gaussian non-linear fitting on frequency distribution of responses by the carbon dioxide sensors. Responses for each sensor were counted in bins based on distance from the mean in concentration units. The Gaussian peaks have been scaled in the y range to show detail. Plots have been scaled such that the most probable point is set at 90% probability. The scale factor for each curve is listed on the legend.

$$L_D = 3 \cdot \sigma$$

Plots were made of the sensor response at different carbon dioxide spikes. These figures were produced such that:

$$x = \mu_{ZRE,peak} - \mu_{ZRE,baseline}$$

$$y = \mu_{sensor,peak} - \mu_{sensor,baseline}$$

An example plot is shown below in Figure 2.7.

The Beer-Lambert law results in all sensors with optical detection schemes showing a linear response. The chemiresistive sensors produce non-linear calibration curves. As these sensors are dependent on the analyte gases adsorbing to the surface of a substrate to generate an electrical signal, the response curve is can be modeled using a Langmuir-like or Langmuirian form. This form is consistent with that provided by the manufacture. The calibration curve was determined by fitting the experimental data using the Levenberg-Marquardt algorithm in *gnuplot* [85] taking the form:

$$f(x) = \frac{Q \cdot b \cdot x}{1 + b \cdot x}$$

A trendline is shown in both parts of Figure 2.7. The slope (m) and intercept (b) are used in calculations from the results of linear regression modeling for optical sensors, and the coefficients of the Langmuir isotherm Q and b are used in calculations from the results of fitting the isotherm model. The mean limit of detection (μ_{L_D}) was adjusted for each sensor. Since detection limits are not comparable across arbitrary and unrelated units, these values were correlated to the ZRE Non-Dispersive Infrared Analyzer response by the calibration curve produced in the trendline. For optical sensors with a linear calibration curve:

$$L_{D(corr)} = m \cdot L_D + b$$

For sensors fit to a Langmuirian curve:

$$L_{D(corr)} = \frac{Q \cdot b \cdot L_D}{1 + b \cdot L_D}$$

2.4 Results and Discussion

The tests showed that the Edinburgh Gascard sensors reliably generated accurate information on the gas concentration. The GE Telaire and K-30 sensor both gave reasonable results for sensors in their price range. The Dynament sensors and CO₂Meter COZIR sensor were found to be less reliable than other sensors in their cohort. Finally, the MQ-4 sensor proved to be rather inaccurate for gauging gas concentration, rather it is more suitable to giving a rough idea of the presence of methane.

2.4.1 Precision and Baseline Noise Tests

The summary of results from this analysis can be found in Tables 2.4 and 2.5. Statistical analysis data for these curves are given in terms of standard deviation and the full width at half max (FWHM). Of the carbon dioxide sensors shown in Table 2.4, the Gascard and K-30 sensors both showed relatively narrow distributions of response. The Gascard shows a strong degree of fit with the Gaussian plot, giving a FWHM of 5.01 ppm. The K-30 tends toward higher concentration values and appears to show two overlapping peaks. These peaks have similar FWHM values, suggesting a shift in the mean measured value. The ppm values, being the ratio volume of the analyte to a unit volume, are dependent on temperature and pressure. Possible periodic temperature and pressure variations, which are corrected for by the Gascard sensor, are responsible. It is suggested that implementation using the K-30 sensor for high-accuracy measurements should incorporate pressure and temperature sensing units to correct these deviations in post-processing. The breadth of the strongest Gaussian peak in the histogram of responses from the K-30 sensor suggests a similarly narrow distribution around the mean as the Gascard. For both of these sensors, the drift was ± 20 ppm. The distribution of responses around the mean by the GE Telaire sensor produces a diffuse broad distribution compared to the relatively narrow ones from the K-30 and Gascard sensors. The breadth of the GE Telaire peak (FWHM 10.4) is interesting when compared to the K-30 sensor, as the sensing mechanism and path lengths are very similar. Looking closer, it was discovered that the Telaire sensor is sensitive to ambient light levels. The data reported this sensor shifting noticeably with ambient light levels. The change in response from the K-30 sensor under similar conditions is negligible.

Comparing the response for both the Telaire and K-30 sensors was monitored with and without ambient light. The data showed that the Telaire sensor is significantly more sensitive to outside light sources than the K-30. The change in response from the K-30 sensor during this test was negligible, while the data reported by the Telaire was observed to shift noticeably. The COZIR AMB GC-020 sensor compared with the K-30 sensor (both produced by the same manufacturer) was significantly noisier and less precise. Of all carbon dioxide sensors tested, the sensors produced by Dynament showed poor performance at typical atmospheric concentrations. While the single-gas carbon dioxide sensor gave a level of precision on par with the COZIR sensor, the dual-gas sensor reported carbon dioxide concentrations over a

wide span of values. The Dynament sensors can perform acceptably when utilized for hazard monitoring, but they are less suitable for gas monitoring.

Of the methane sensors shown in Table 2.5 the Edinburgh Gascard again proved the most precise. The normal distribution of responses around the reported mean from the Gascard is a very narrow peak. The Gascard did report some relatively large fluctuations, several peak widths higher than the mean response. Although these fluctuations could be explained by the exposed nature of the sensor during these tests, it suggests that some digital filtering may be required for portable devices. The single gas Dynament methane sensor produced a narrow distribution of responses, but the results from the dual-gas Dynament sensor were inconclusive. The dual-gas Dynament sensor only reported two values for methane, rather than a normal distribution of several values. Possibly, the internal digitization in the sensor provides limited resolution around the baseline value of 0 ppm. Assuming that an approximate FWHM could be approximated by the difference between these two points around a mean, the dual-gas sensor would have a FWHM equivalent to that produced by the single-gas sensor. Finally, the MQ-4 sensor produced a wide range of values. The distribution around the mean is so broad, that the tails are off the scale in Figure 2.5. While the FWHM of these responses from the MQ-4 show that the peak only deviates 1.19 ppm around the mean, it is comparatively much less precise than the other sensors in the experiment.

With the exception of the carbon dioxide and methane Gascard sensors, there was poor accuracy. In the case of some sensors including the K-30, Telaire, COZIR, and Dynament carbon dioxide sensors, this issue could be rectified by recalibration of the sensors. All of these sensors must be calibrated before use and cannot be used directly from the supplier if the user hopes to obtain an accurate concentration value. For some of the tested devices such as the MQ-4 methane sensor, good accuracy may be outside of the reasonable expectation of sensor ability.

2.4.2 Response Time

Most of the sensors tested registered change in concentration on a timescale which could not be measured accurately with the current experimental design. For the optical sensors, the sampling time was controlled by internal electronics, which sample several times a minute. For environmental monitoring, the response from all sensors were effectively

Table 2.4: Precision and Accuracy of Carbon Dioxide Sensors

Sensor	\bar{C}^*	σ	FWHM
K-30 SE-0018	451	1.91	4.51
COZIR AMB GC-020	362	14.1	33.3
Gascard CO ₂	635	2.12	5.01
MSH-P/HC/CO ₂ /	395	86.4	204
MSH-DP/CO ₂ /	2316	17.6	41.4
Telaire T6615	454	4.42	10.4

Table 2.5: Precision and Accuracy of Methane Sensors

Sensor	\bar{C}	σ	FWHM
MQ-4 [†]	97.6	0.507	1.19
Gascard CH ₄	15.9	0.580	1.37
MSH-P/HC/CO ₂ /	48.2	3.54	8.33
MSH-DP/HC/	15.4	no data	no data

* While \bar{C} denotes the average concentration as determined by the sensor during the test, it should be noted that these data were collected by uncalibrated sensors. The values of σ and FWHM are based on \bar{C} .

[†] Data for the MQ-4 are listed in terms of electrical response rather than parts-per notation.

[‡] All other data in Tables 2.4 and 2.5 are in units of ppm

immediate. However, chemoresistive sensors responded on a notably different timescale was the MQ-4 sensor. In these experiments, the MQ-4 methane sensor was selected as a worst-case model sensor. A smaller sensor enclosure (internal volume 1 in³) was constructed to maximize gas exchange within the chamber and minimize the time required to obtain a stable new concentration. A test was conducted to determine the response time of this sensor by introduction of gas to the system until a stable value was produced, then vented with purified air until the previous baseline was regained. The ratio of gas introduced to the system was changed between each acquisition period to determine if there was a relationship between the concentration of introduced gas and the time to produce a stable response. Figure 2.8 depicts a plot of the responses from one of these experiments. The sensor produces a sharp overshoot, with some instances displaying a percentage overshoot exceeding 100% of the final

concentration determined by the system. This large overshoot is likely due to the heating coil inside the sensor, which artificially inflates the apparent concentration as voltage is flowed through the resistive wire. Minor signal ringing follows this spike, until the response is made stable. A smaller overshoot can be observed when the mix gas is shut off, and replaced by pure air. The MQ-4 works by a thermometric response, and as such, it is reasonable that the mixed gas introduced to the system changed the temperature near the sensor, and this contributed to the degree of overshoot observed. This would not explain the overshoot when the gas was switched to pure air, as it was the same temperature as the mixed gas.

The rise time of a system, defined as the time for the response to change from 10% of the mean response to 90% of the mean response, is less useful for this system due to the extreme overshoot observed. Settling time, the time for a system to change from the baseline to a window around the mean during the ringing portion, is more useful for this application. The settling time for the MQ-4 sensor did not appear to be concentration dependent. A stable value was produced within 2.5% of the mean after 78 ± 10 s, averaged over all response time experiments.

2.4.3 Limit of Detection

The correlated limits of detection are listed in Table 2.6. Of the tested carbon dioxide sensors, the Edinburgh Gascard shows the greatest sensitivity. This is consistent with expectations based on the path length of the sensor. The Dynamant single analyte sensor shows a lower limit of detection than the dual analyte sensor produced by the same manufacturer. The K-30 and Telaire sensors show comparable detection limits. The COZIR sensor exhibits the poorest limit of detection.

Of the tested methane sensors, the Edinburgh Gascard again shows the greatest sensitivity. The MQ-4 and TGS2611 sensors, have very low limits of detection. It was observed that these thin film sensors were very sensitive to changes in temperature and humidity. It should be noted that these tests were carried out in a controlled environment which sought to eliminate those sources of error. An application without these sorts of controls may be subject to much more error. Furthermore, individual MQ-4 sensors varied a great deal in response compared to other sensors of the same type. The Dynamant sensors have appear to have a limit of detection under 10 ppm. These numbers are artificially deflated.

Table 2.6: Detection Limits of Carbon Dioxide Sensors

	$L_{D(corr)}$
K-30 SE-0018	31.1
COZIR AMB GC-020	65.7
Gascard CO ₂	0.00862
MSH-P/HC/CO ₂ /	57.6
MSH-DP/CO ₂ /	6.60
Telaire T6615	22.9

Table 2.7: Detection Limits of Methane Sensors

	$L_{D(corr)}$
MQ-4	1.24 [†]
Gascard CH ₄	0.569
MSH-P/HC/CO ₂ /	7.44 [‡]
MSH-DP/HC/	2.42 [‡]
TGS-2600	33.3 [†]
TGS-2610	29.0 [†]
TGS-2611	3.95 [†]

[†] Calculated from Langmuirian fitting.

[‡] Failed to produce consistent response within tested range.

The Dynament sensors could not reliably detect any concentration of gas below 100 ppm, and these null results have skewed the trendline of detection limits. Values we observed cannot be guaranteed below this threshold. The TGS-2600 and TGS-2610 sensors are generalist hydrocarbon and contaminant sensors, these sensors were less sensitive to changes in methane than the TGS-2611, which is specific to methane.

2.5 Conclusion

Based on the comparison of these commercially available low-cost sensors, selection of a sensor for practical applications can be simplified. The obvious choice for low concentration applications is the Gascard series of sensors. However, this sensor is comparatively more

expensive than the other sensors in this paper on a scale of 10-100 times. For applications with modest budgets, the K-30 and Telaire sensors are viable for carbon dioxide detection, and the TGS-2611 sensor is similarly viable for methane. The K-30 sensor costs roughly a tenth of the cost of the similarly-able Telaire sensor. Therefore, we also recommend it over the Telaire offering. The MQ-4 is an incredibly inexpensive alternative to the TGS series, available for only a few dollars. For very low cost devices, the MQ-4 sensor is an option if the user only needs a rough estimate of concentration, rather than the precision found in other, more expensive, offerings. During our study, the TGS sensors proved difficult to purchase, most suppliers not stocking this device and only at a high price when available. Use of the Dynament sensors is not advisable due to inaccuracies and inconsistencies of the devices considering their cost (roughly 100 times that of the MQ-4 sensor).

Sensor choice for the detection of ppm level concentration of carbon dioxide and methane is a matter of compromises. There appears to be no single sensor which simultaneously fulfills traits of sensitivity at atmospheric levels, low power consumption, low price, and market availability. It is the opinion of the authors that the devices which best fill these needs from the available options are the K-30 and MQ-4 sensor. The K-30 sensor provided acceptable sensitivity for a low cost in terms of money and power. The MQ-4 sensor appears to be surprisingly sensitive to small changes in concentration (based on the adjusted limit of detection discussed in Table 2.7), but data it produces should not be taken as accurate (see the discussion of the broad peak in Figure 2.5-B). However, the MQ-4 does appear to be able to detect larger changes in concentration which would represent localized leak. We must consider the application the sensor array. If the cost of an accurate sensor such as the methane Gascard is 1000 times greater than an inaccurate sensor such as the MQ-4, it is more valuable to the goals of the network to have a much larger number of units than it is to have just a few powerful sensors. If the goal of the device array is to detect a leak, the MQ-4 is sufficient for most units. We believe that the TGS2611 would be more suited to this task, but the difficulty in acquisition prevents it from being a viable option at scale at this time.

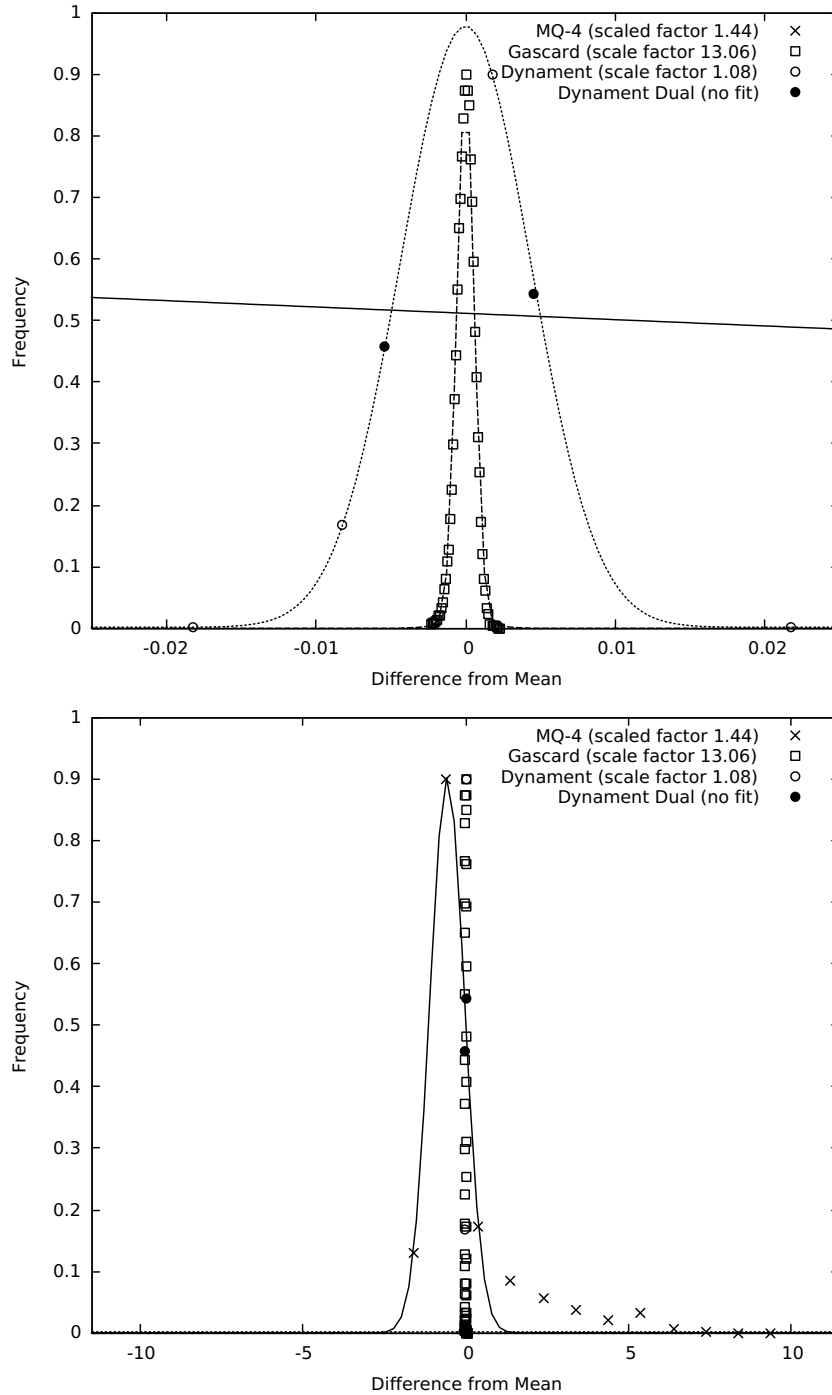


Figure 2.5: Figure 2.5-A is a plot of the probability density function by Gaussian non-linear fitting on frequency distribution of responses by the methane sensors. Responses for each sensor were counted in bins based on distance from the mean in concentration units. The Gaussian peaks have been scaled in the y range to show detail. Plots have been scaled such that the most probable point is set at 90% probability. The scale factor for each curve is listed on the legend. The digitized output from the Dynamant Dual sensor produced only two possible values. A Gaussian fit could not be calculated from the available points. The MQ-4 extent curve is not visible in the domain of Figure 2.5-A. By increasing the scale of the domain to that in Figure 2.5-B, the curve is visible.

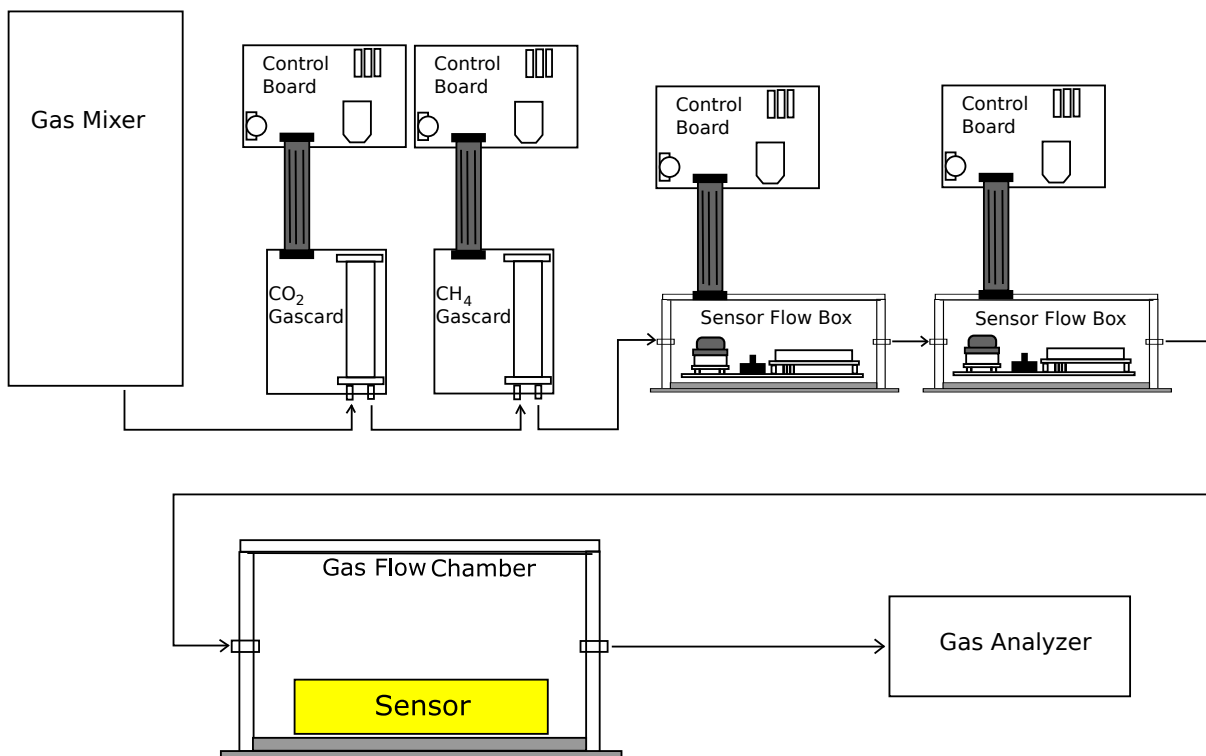


Figure 2.6: The gas mixing apparatus discussed in Section 2.3 was used with additional sensor housings. The diagram shows the flow of gas from the mixing apparatus to Gascard sensors, small enclosures containing sensors, the large gas flow chamber, and finally to the ZRE gas analyzer.

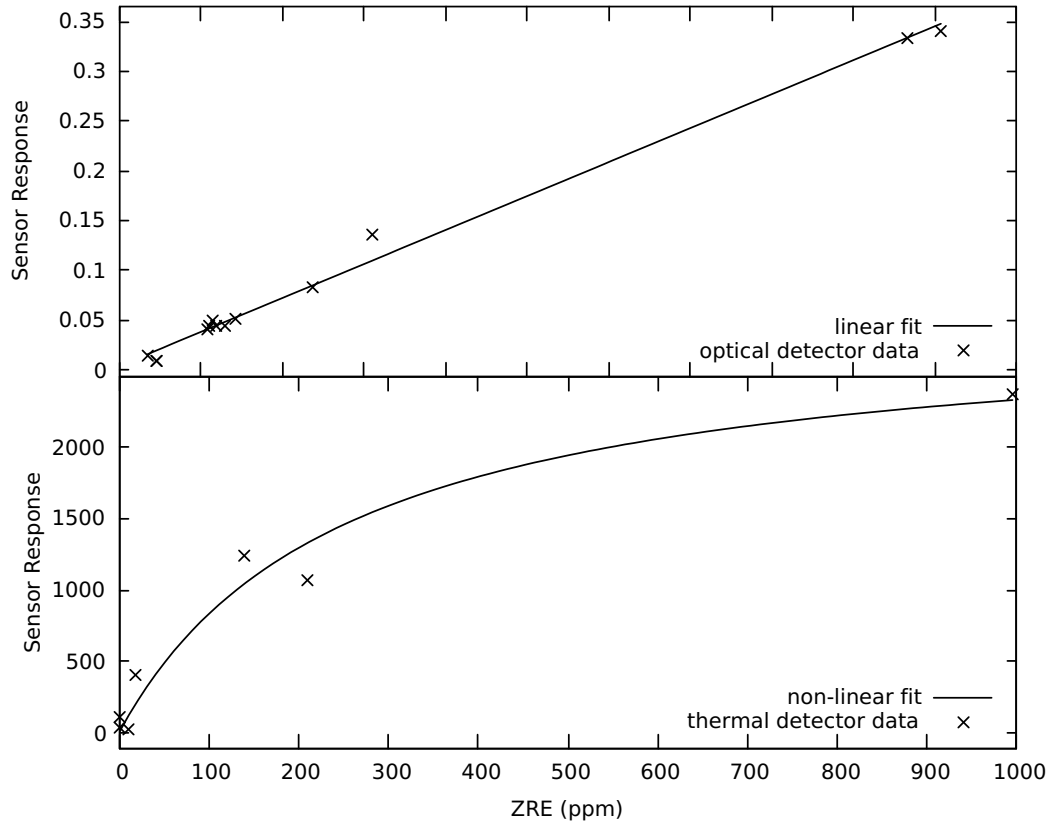


Figure 2.7: A sample plot of the calibration of sensor signals to ZRE Non-Dispersive Infrared Analyzer reported concentration during carbon dioxide and methane spikes. The top part of the figure shows the response of an optical carbon dioxide sensor with the expected linear behavior. The bottom part of the figure shows the response of a chemiresistive methane sensor with a fit of the non-linear response.

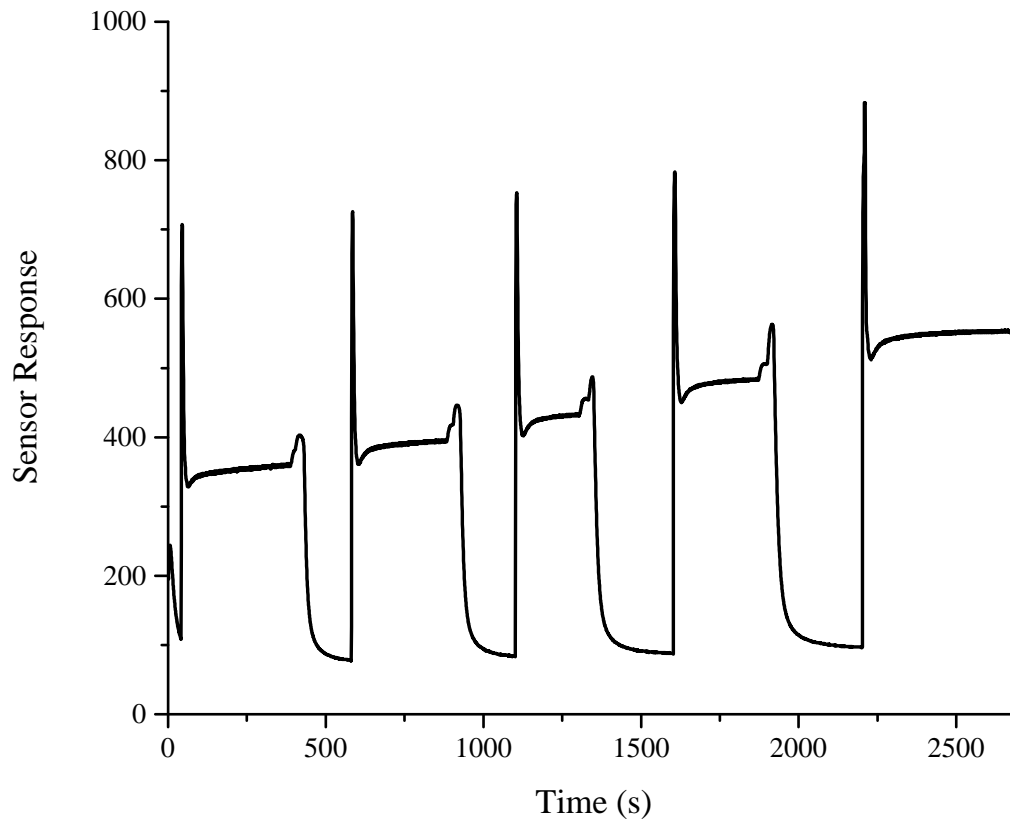


Figure 2.8: The MQ-4 sensor showed noticeable delay between introduction of gas and production of a stable response. In this plot, the large overshoot during sensor cycling, likely caused by the heating coil in the device, is apparent.

CHAPTER 3

Determining the Battery Shutoff Circuit Behavior of a Commercially Available Solar Charging Circuit

3.1 Introduction

The nature of the sensor array designed to cover a relatively large area of land imposes limitations upon the power supply of the system. Since the area to be covered may include elevation changes, anthropogenic developments, and other uncontrollable factors, it would not be convenient to constrain the array by wired connection as the array will be adapted to individual site conditions. Therefore, each unit must be designed with internal and self-sustaining power supplies.

Two different types of commercially available solar power generation and storage units with weatherproof enclosures were selected from Tycon Power Systems. The majority of the sensors would be housed in the Remote Pro 2.5 W Continuous Remote Power System die cast enclosure and a few sensor units with features requiring more power were housed in the Remote Pro 15 W Continuous Remote Power System steel enclosure . The 2.5 W enclosure includes a 12 V battery rated for 9 A h of use, a charging and distribution circuit, and a 10 W solar panel. The 15 W enclosure includes a 12 V battery rated for 98 A h, a charging and distribution circuit, and a 60 W solar panel [86].

Before equipment construction, the power shutoff features of the Tycon systems required evaluation. Tests were undertaken to determine battery behavior drain while connected to the proprietary circuit provided with the Tycon units.

3.2 Discharge Behavior and Cutoff Point

The 9 Ah battery specification was tested for veracity by monitoring a discharge of power through a resistor connected to the supply terminals on the distribution circuit included with the enclosure. The voltage through the circuit was monitored by a PicoScope 4224 oscilloscope to determine the time and value when the circuit was opened to prevent battery damage. The tests put minimal strain on the battery, in regard to the specified maximum number of charging cycles. Multiple batteries were tested, allowing charging while a test took place, and the shut down time was averaged across batteries.

The circuit ceased to discharge after the voltage through the circuit dipped below a 10.7 V threshold value. This number is close to the expected threshold value, which is labeled on the circuit. The behavior of the circuit near low voltage levels in one test is shown in Figure 3.1 in terms of lifetime with respect to the voltage detected. While the battery begins naturally losing stored energy at an increased rate near the end, the protection circuit cuts in at about 10.7 V and breaks the circuit.

3.3 A Direct Comparison of Batteries and Damage Due to Repeated Discharge

The value of the resistor in the simple circuit varied over the course of the experiment. Individual shutoff behavior at certain power draw rates is shown in Figures 3.2, 3.3, and 3.4. While these figures are summarized in Figure 3.5, the individual endpoints show the types of deviations. Notably, the shape of the curve near the cutoff point is different for the two batteries. One ends in a simple pseudo-parabolic curve, while the second battery seems to resist the threshold more, taking on a pseudo-Gaussian shape. This interesting effect does not seem to have apparent correlation to the capacity of either battery, it is interesting to see two different curve shapes for batteries which should be similar in behavior.

Tests showed that for these batteries and this circuit, the time which battery took to discharge was inversely related to the current allowed to flow through the circuit (see Figure 3.5). This is behavior which is expected for a normal battery capacity. Since more than one battery was used in this test, the capacity of the two batteries can be compared.

Furthermore, the battery capacity of the battery changed as the experiment was repeated multiple times. In Figure 3.6 the calculated capacity of each battery after each test

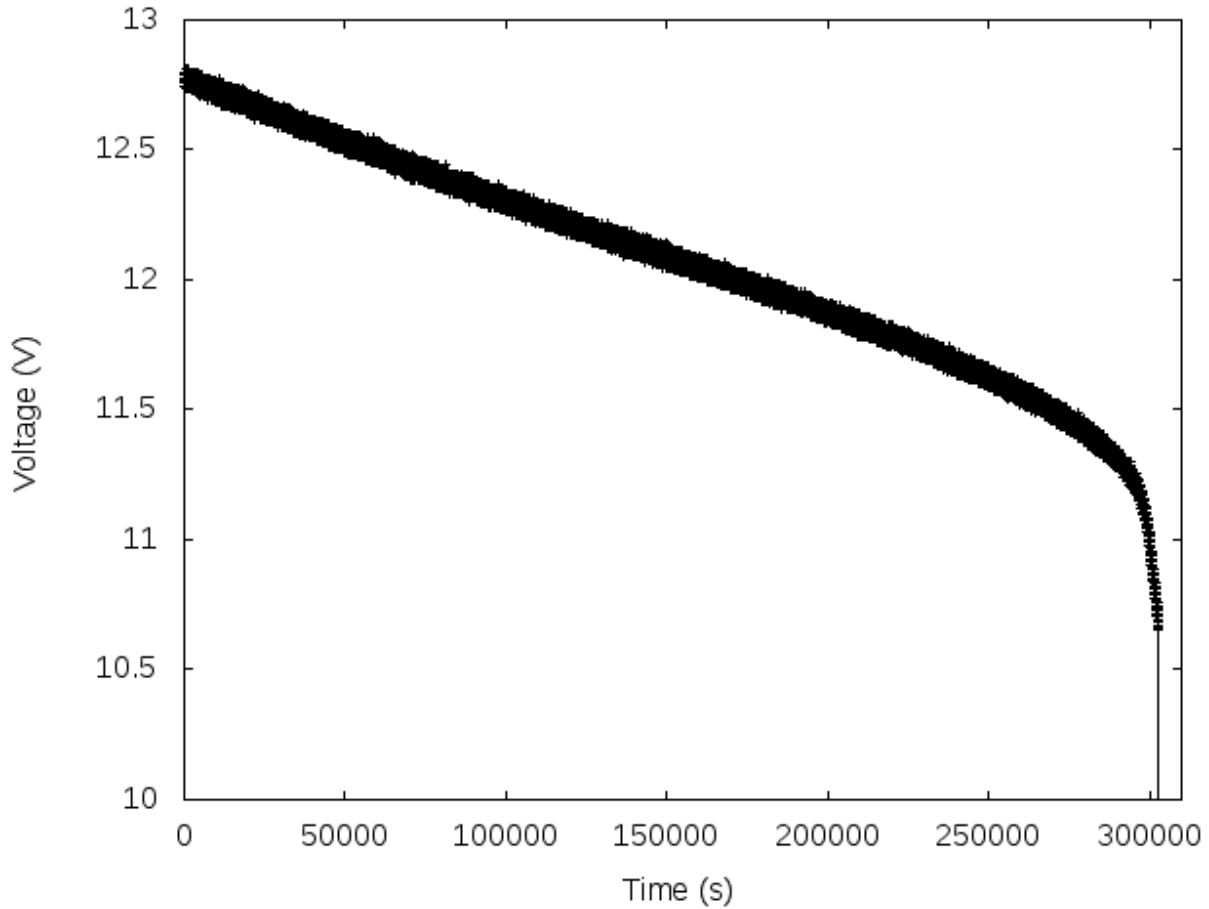


Figure 3.1: Battery shutoff behavior by protection circuit.

is shown. These data suggest that the battery must be decaying with each cycle, despite the intervention of the shutoff circuitry. Based on these data, the capacity of the analyzed 12V battery at the beginning of the tests was determined to be 5.5 A h and 5.1 A h for the first and second batteries, respectively. This is well below the specified capacity of 9 A h by the distributor. One possible explanation for this behavior is that the power distribution circuit provided by the enclosure supplier does not adequately protect against memory effects. It was noted during production that batteries plugged into the power distribution circuit, without being connected to recharging circuits or loads, would discharge over time to an unusable state. This required many batteries to be replaced, as the full discharge left them below the power threshold required to charge on a simple trickle charger.

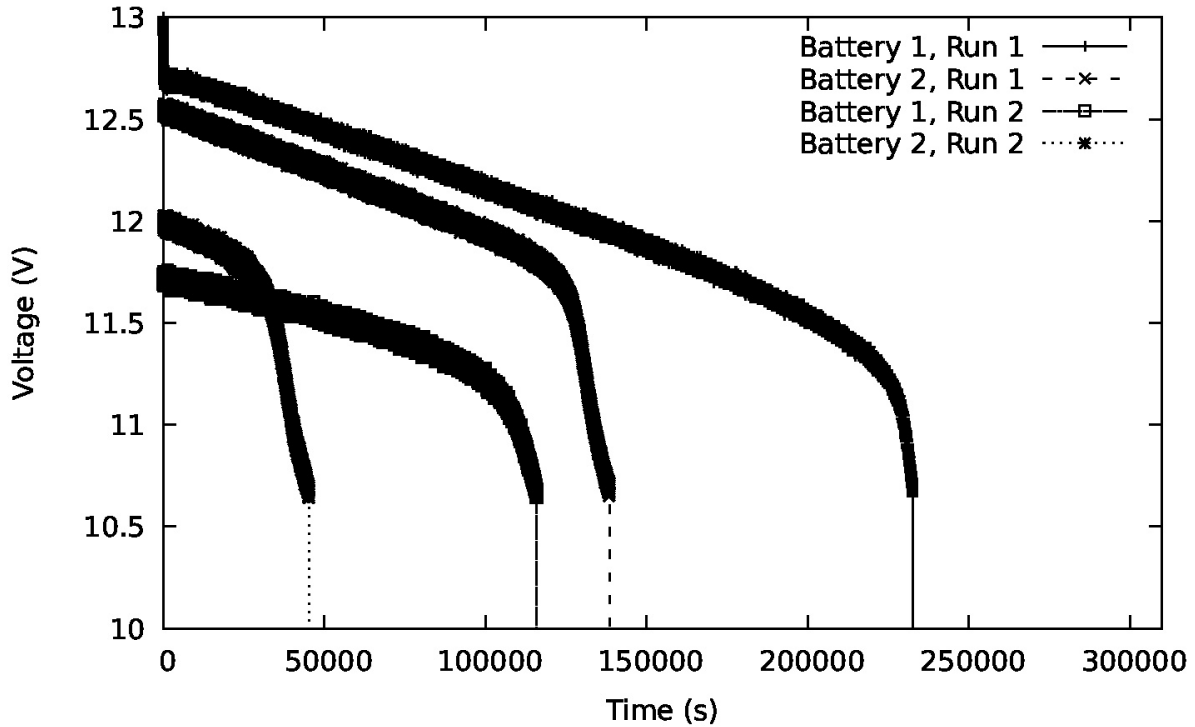


Figure 3.2: Shutoff behavior of battery circuit with a $141\ \Omega$ load.

3.4 Conclusions

Based on the tests conducted on the batteries connected to the shutoff circuit during prototyping, we can determine a few things. First, while the nominal capacity of the batteries is listed by the manufacturer as $9\ \text{A h}$, the true capacity is closer to $5.35\ \text{A h}$. This reduces the available uptime for future systems based on this equipment. Second, the protection circuit included with the Tycon equipment does not prevent cycling damage to the battery. Although the protection circuit can operate as designed to prevent the battery from dropping below a threshold where significant damage to the capacity may occur, it should not be recommended to get to that point. Systems connected to this device should be designed to enter a low-power mode before this threshold. Finally, batteries should be kept disconnected while not in service. Although lead-acid batteries are designed to be rechargeable, the trickle charge circuit of the Tycon system cannot be relied on to recharge a battery which has been allowed to completely discharge.

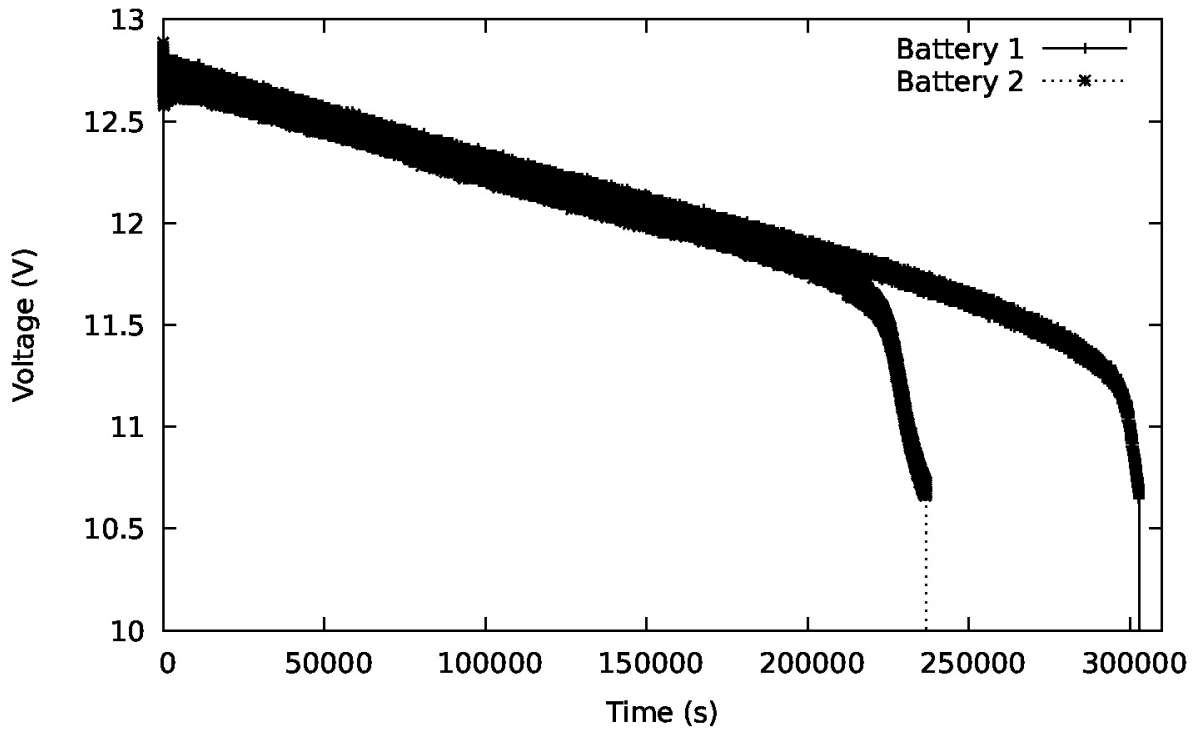


Figure 3.3: Shutoff behavior of battery circuit with a 188 Ω load.

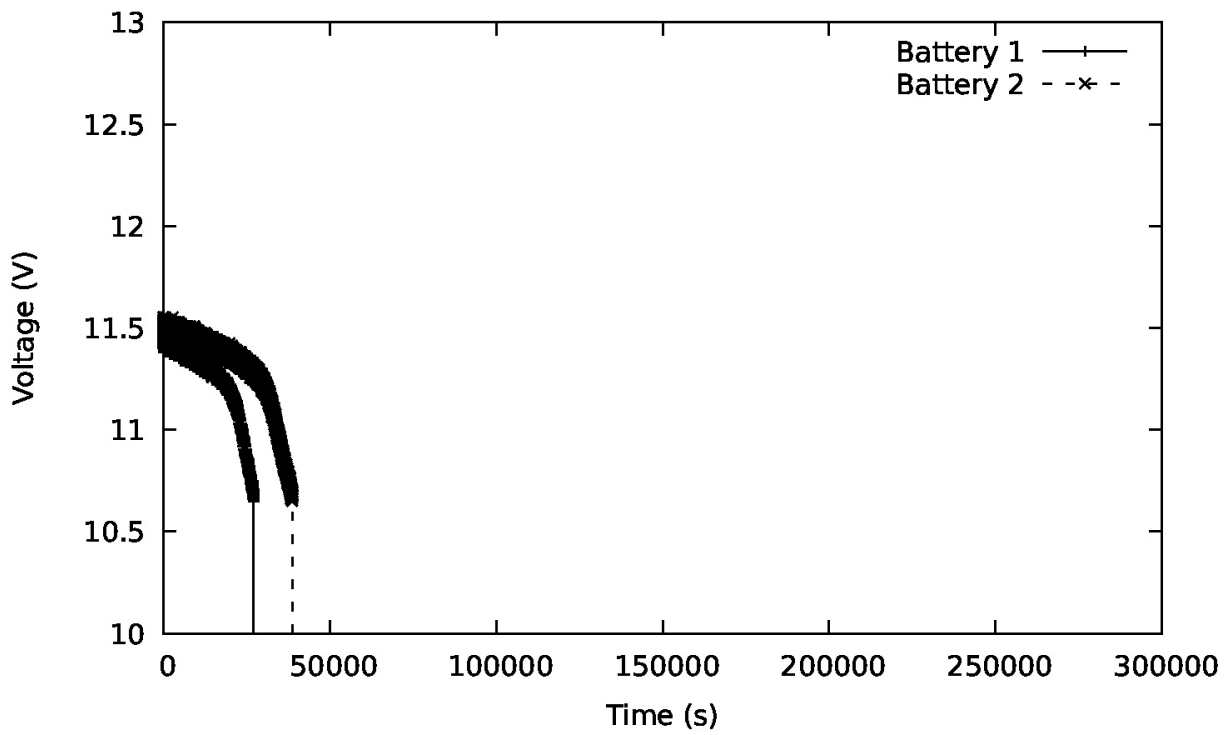


Figure 3.4: Shutoff behavior of battery circuit with a 235 Ω load.

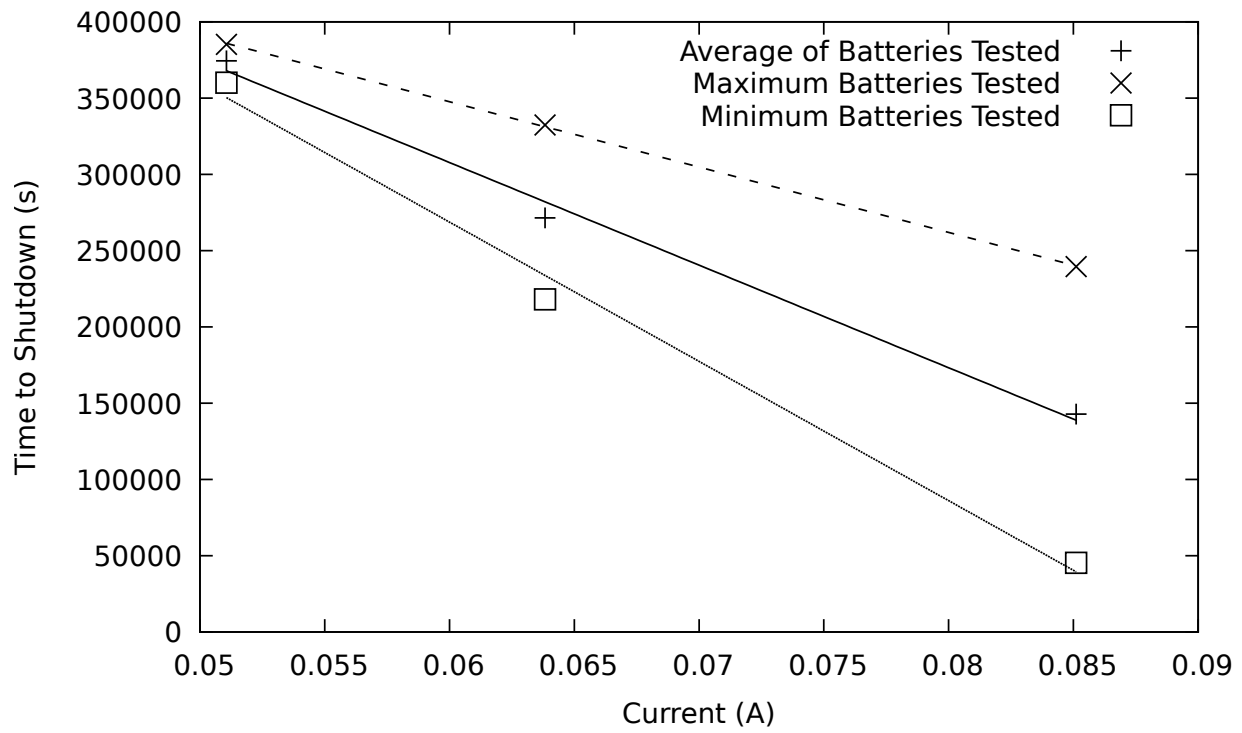


Figure 3.5: The time for a battery to reach the discharge cutoff point was determined by varying the resistor loads. We can see from this plot that this is a linear relationship.

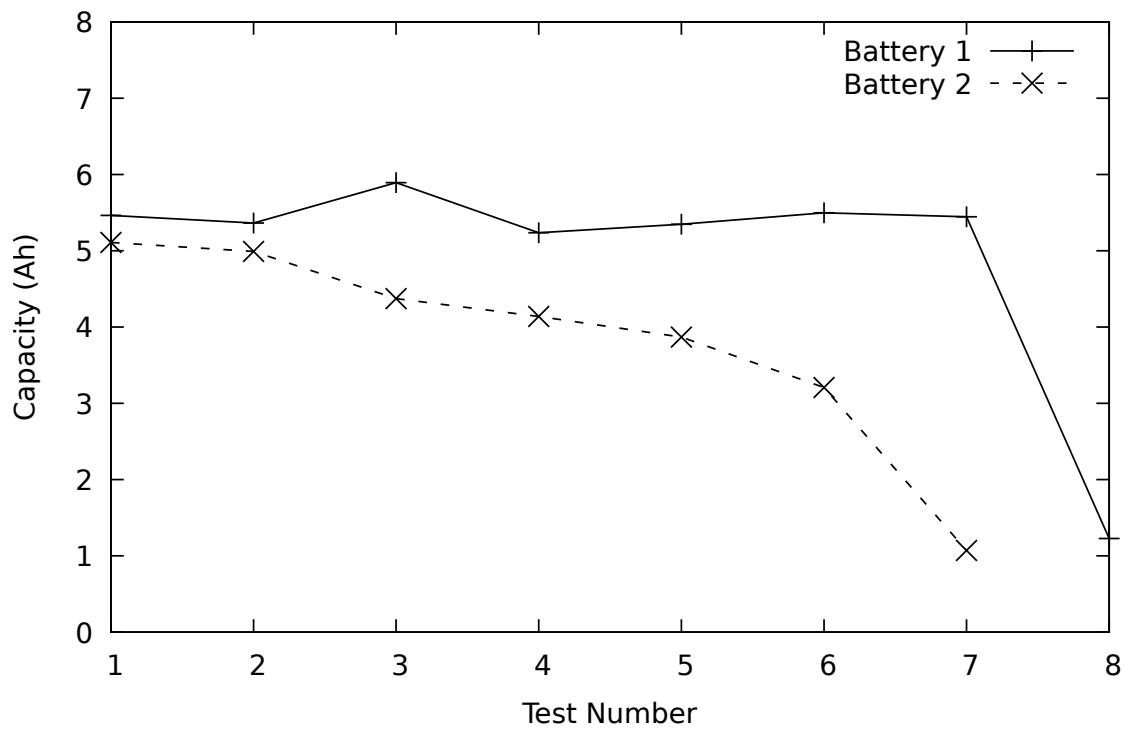


Figure 3.6: Changes in the battery capacity over time suggest that the batteries quickly decay over a few cycles. The capacity of two batteries are plotted here with respect to repeated use. The tested batteries were shut down at 10.7 V like all other battery tests. This plot shows that the capacity of the batteries still depleted with repeated discharges to this point.

CHAPTER 4

Networking with from an Xbee Modem Mesh to a Cellular Modem

4.1 Network Topologies for Remote Sensing

The design of a network is a much-studied endeavor, and many of the nuances of network topologies have been described in literature [87, 88]. It is useful to examine each of these topologies to determine which is best suited for the task at hand. In the case of device designed for remote monitoring must be able to provide the data to researchers at a distant location. Additionally, as this is a network of multiple sensing units, there must be some way to communicate data between sensors. There are several methods to do this. The most straightforward method of designing a network, is to establish point-to-point communications. To field this method, each node in the network would utilize a long range modem to connect to the ‘home’ server, as depicted in Figure 4.1. Outfitting each node with a powerful modem would be costly in parts, network plan maintenance, and energy. The infrastructure of the units would require large power sources to keep up a high duty cycle. Thus, it is practical to limit network connections directly to the server by the large modems to as few units as possible. In this manner, two classes of nodes are established: communication nodes and sensor nodes. The sensor nodes could use a lower power communication method.

The most cost effective option for sensor connection is a wire to transmit signals between units, yet this is inadequate for this project. Wired connection is not used due to the scope and shape of the network. Simple wired connections often follow some basic network topologies. The most rudimentary wired connection would connect each unit to

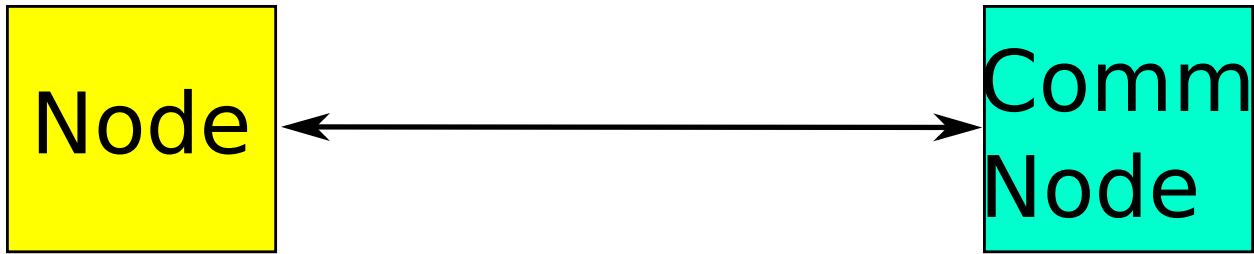


Figure 4.1: This cartoon depicts the nodal arrangement of a point-to-point network. Each unit connects directly with the ‘home’ server.

the nearest neighbor. This line network topology, as depicted in Figure 4.2, requires each unit to pass information to the nearest neighbors before reaching a terminal node, which would be equipped with a large modem to send data to the ‘home’ server. A variation of this design, is the bus network topology, shown in Figure 4.3. The bus allows for a slightly more broad area to be managed by a network, with addressing functionality to send data to correct locations. Both of these networks do not match the needs of this project. A wired connection produces a physical failure point which is difficult to maintain for prolonged periods in outdoor conditions. The scope and breadth of the project demands that a large area be covered by sensor, rather than a long line. To wire a line or bus network over an area, would require the snaking of data cabling around and possibly over difficult terrain. A wireless network is much better suited to this task.

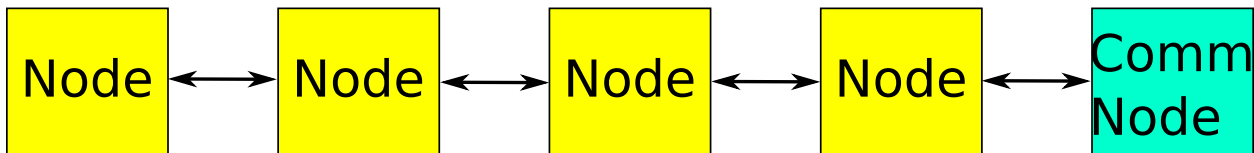


Figure 4.2: This cartoon depicts the nodal arrangement of a line or linear network. Data are passed between nearest neighbor units in a line until they reach the ‘home’ server.

A wireless network can offer a large number of network topologies without a tangle of wires. A simple network design which can cover a large area as intended by the project is a star topology, depicted in Figure 4.4. This network directs all data to a central unit. We can design this central unit to have a longer range modem to connect to the ‘home’ server. Yet this design is also limiting. By requiring all sensor nodes to communicate directly to a communication node, the network reaches a size limit based on the signal range of the antenna. For low power wireless modems, this range limit may be too small. To address

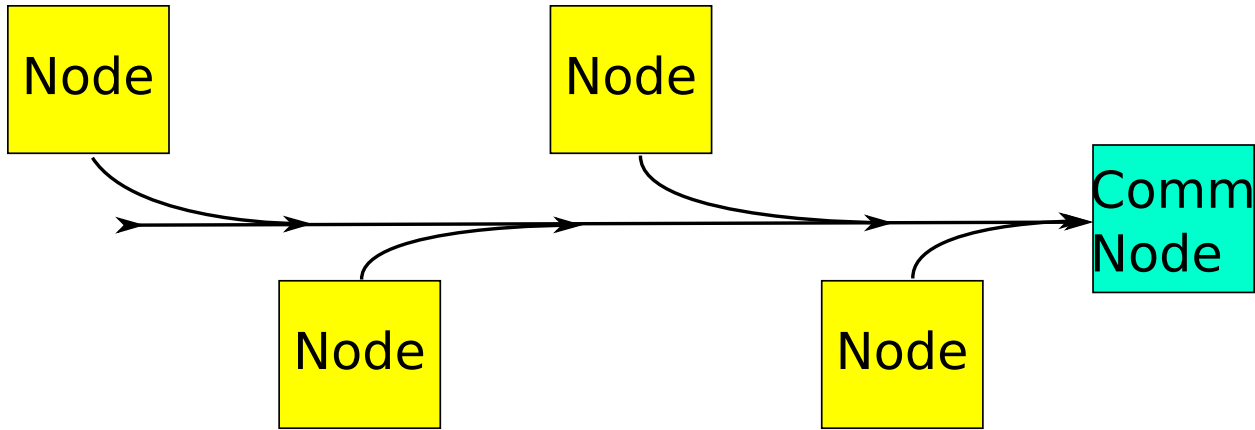


Figure 4.3: This cartoon depicts the nodal arrangement of a bus network. Data are passed in a bus cable to the ‘home’ server. Units are assigned addresses. If data packets match the address the data are accepted and stored.

this shortcoming, it becomes beneficial for all units in the network to communicate data to the others. The theoretical example of this is the mesh network, depicted in Figure 4.5. In this archetypal example, each node in the network connects with every other node. In this way, a single unit can be designated as a communication node. When the sensor nodes are designed to pass data between them until the data reach the communication node. The constraints of the mesh network are great, requiring each unit to be within range of the other units. Instead, a hybrid network is desirable, see Figure 4.6. This network design allows as many of the nodes to mesh as possible, while keeping the ability to adapt forms of the star, bus, and linear topologies. This network design provides the most adaptability for an area network to conform to the needs of the layout of units and the environmental conditions.

4.2 Modems and Radios

To construct a hybrid network for our sensor array, we need two types of wireless radios. The mesh portion of the network is performed using the Xbee mesh protocol. The Digi International XBee-PRO 900HP module XBP9B-DMUT-002 was used for this application (Figure 4.7). This unit is a spread spectrum transmitter licensed to operate between 902.4 MHz and 927.6 MHz at an output of 0.298 W [89]. The device communicates with a controller via UART interface and can transmit to other units via the DigiMesh, repeater, point-to-point, point-to-multipoint, and peer-to-peer protocols. The unit selected transmits data at a rate of

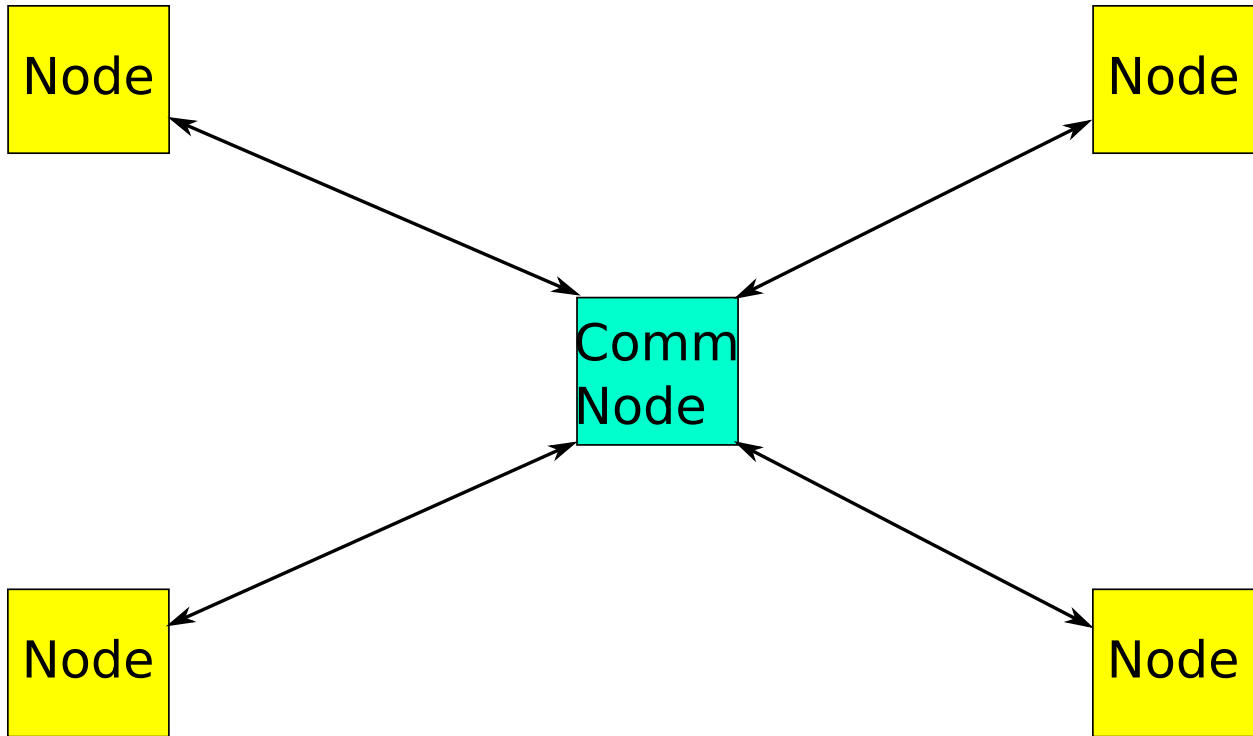


Figure 4.4: This cartoon depicts the nodal arrangement of a star network. Data are passed from low level units to a higher level unit at the center.

200 Kbps with a claimed maximum range of 9 miles with the proper antenna. For this setup, we will be using small omni-directional one-eighth wavelength dipole antenna connected by U.FL cable to the modem. The modems in the network will communicate using the Digimesh protocol. Digimesh is a proprietary implementation of the Zigbee protocol which homogenizes the network, and Zigbee is an enhancement of the IEEE 802.15.4 protocol [90] which adds mesh topology to the existing physical address and mac address protocols. The Zigbee protocol adds routing, ad hoc networking, and self-healing mesh capabilities to the established protocol [91, 92]. This addition allows the units to automatically self-assemble a mesh of units, designating each as a coordinator, router, and end device.

Each part of the Zigbee mesh has a particular job, the coordinator is a central unit that assigns addresses, the routers move data to the coordinator, and the end devices just supply data. This topology allows the end devices to persist in sleep mode for most of the time, waking up only to sample data and send it along. However, it requires the router and coordinator nodes to remain more active. This shortcoming is amended with the use of the Digimesh topology. This protocol allows for the formation of a true mesh which does not

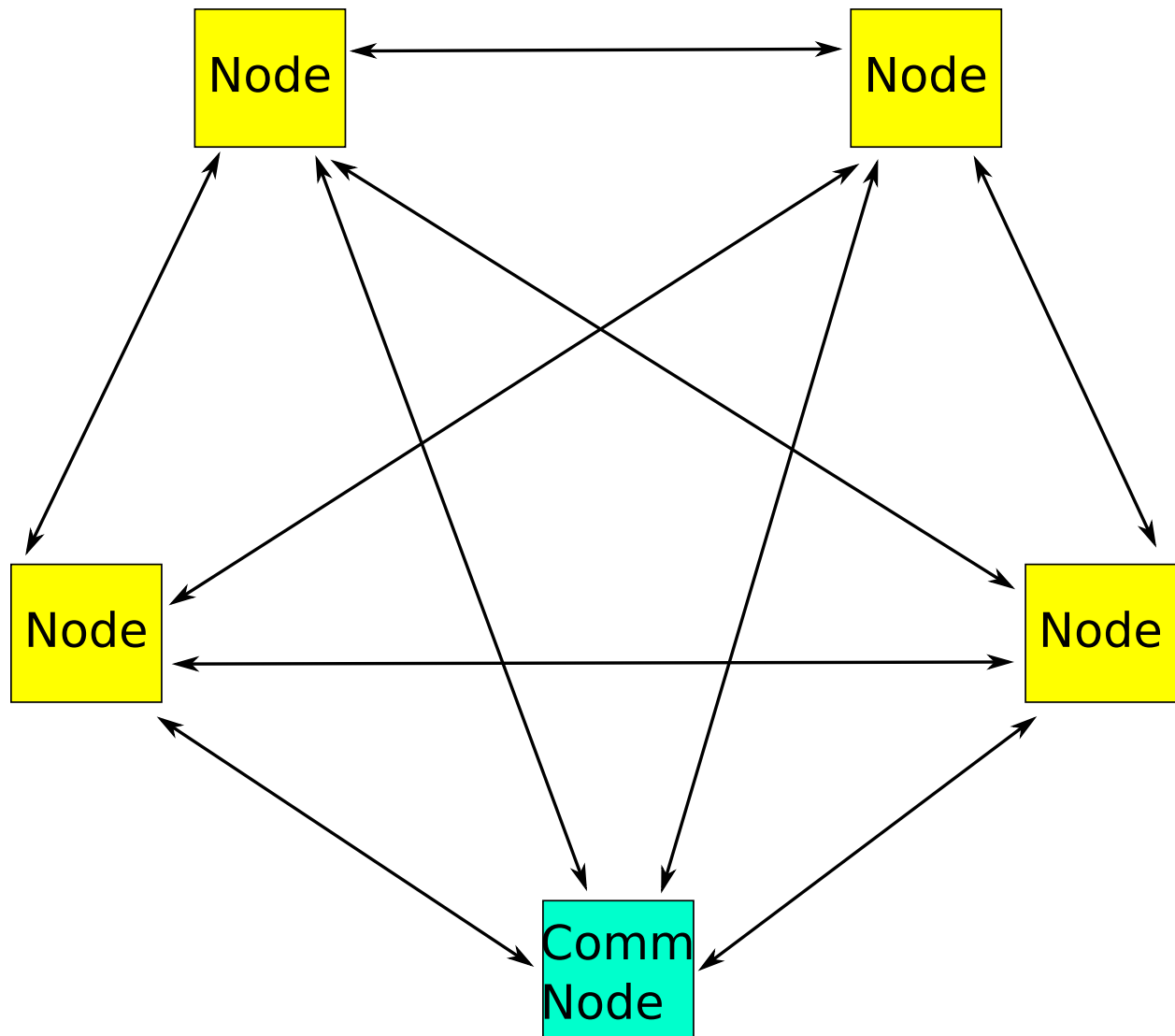


Figure 4.5: This cartoon depicts the nodal arrangement of a mesh network. Data are shared between units equally, and all units are connected equally. Any node can be replaced with a communication node to transmit data back to the ‘home’ server.

have assigned tasks to individual units. By combining a wake-on-lan type feature with the Zigbee protocol, all units can simultaneously act as coordinators, routers, and end devices. A low-power mode can be maintained by these sensors between sampling, responding to a wake command to route information along or to sample the environment. This design is advantageous for our application. Where the coordinator mesh nodes may be well suited to the larger communication nodes in our network, the sensor nodes in our network are not particularly well suited to the always-on requirement for the Zigbee end device type. While

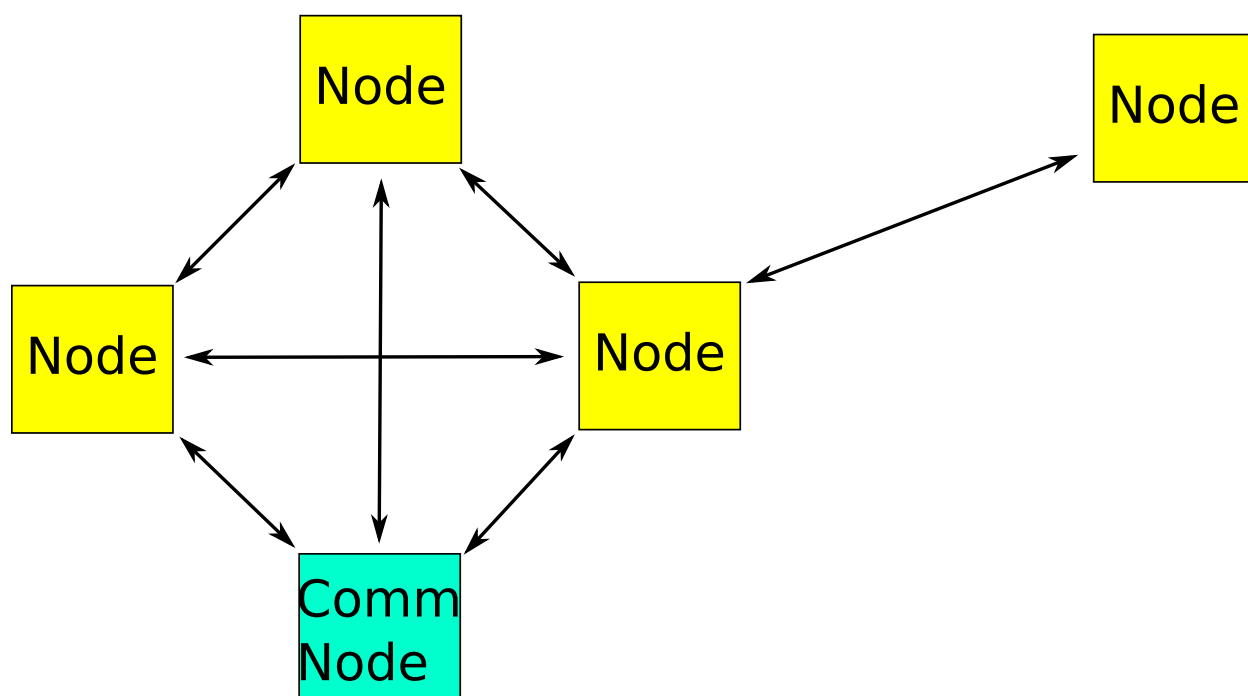


Figure 4.6: This cartoon depicts the nodal arrangement of a hybrid network. Data are shared among units when possible, but portions of the network may share similarities with line, bus, and star networks.

it would be possible to maintain a router state for some time, multiple days of inclement weather would negatively impact the power collected by the solar cells, and holes might appear in the network. Therefore, using the Zigbee protocol exclusively limits the network topology to one which eliminates the use of router nodes, commonly referred to as a “star” network. This topology would limit the physical area covered by the network array. The homogenization of the nodes using the Digimesh protocol eliminates these issues. One example of the automatically generated mesh network can be seen in Figure 4.8. In this case, the mesh generating algorithm decided it would be best to coordinate most of the sensors as end

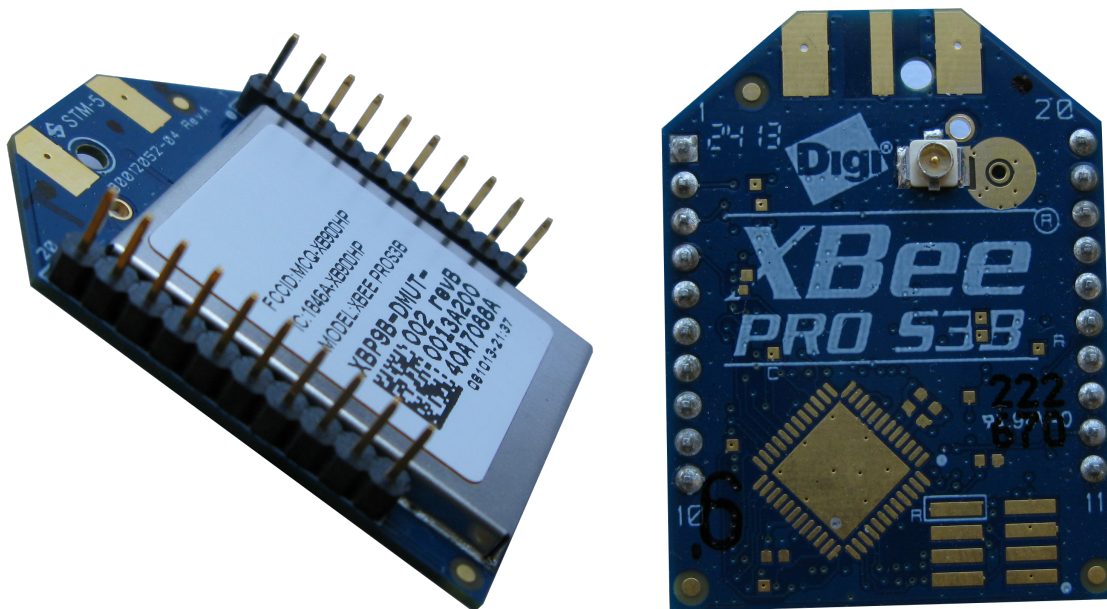


Figure 4.7: An image of one of the Xbee wireless modems used in this project.

nodes connected to the unit labeled with ‘934A’ as the last four numbers in the identification code. However, not all sensors coordinated with this like a star network. The unit with the identifying number ending in ‘7051’ acts as a router for the unit ‘9377.’

To send data directly back to the ‘home’ server, a node in each subnet was equipped with a long range cellular modem. The communication nodes included an extra breakout board as described in Section 5.3.4. This breakout board utilizes the NimbeLink Skywire EVDO cellular modem to establish communication with the home server over a cellular data network. The Skywire device communicates using the Evolution-Data Optimied (EVDO) TIA-856 Rev. A protocol. This telecommunications standard provides for wireless transmission of data as an evolution of the code division multiple access (CDMA) standard [93]. CDMA is the technique by which all cellular communications are based. Data from different users are multiplexed to asynchronously access a channel and spread information across spectrum subchannels. This technology is more suitable for sending large volumes of data, such as a collection of data acquired by an array of sensors, than a direct single-channel communication pathway. Additionally, by employing the EVDO standard in the sensor array, the communication nodes

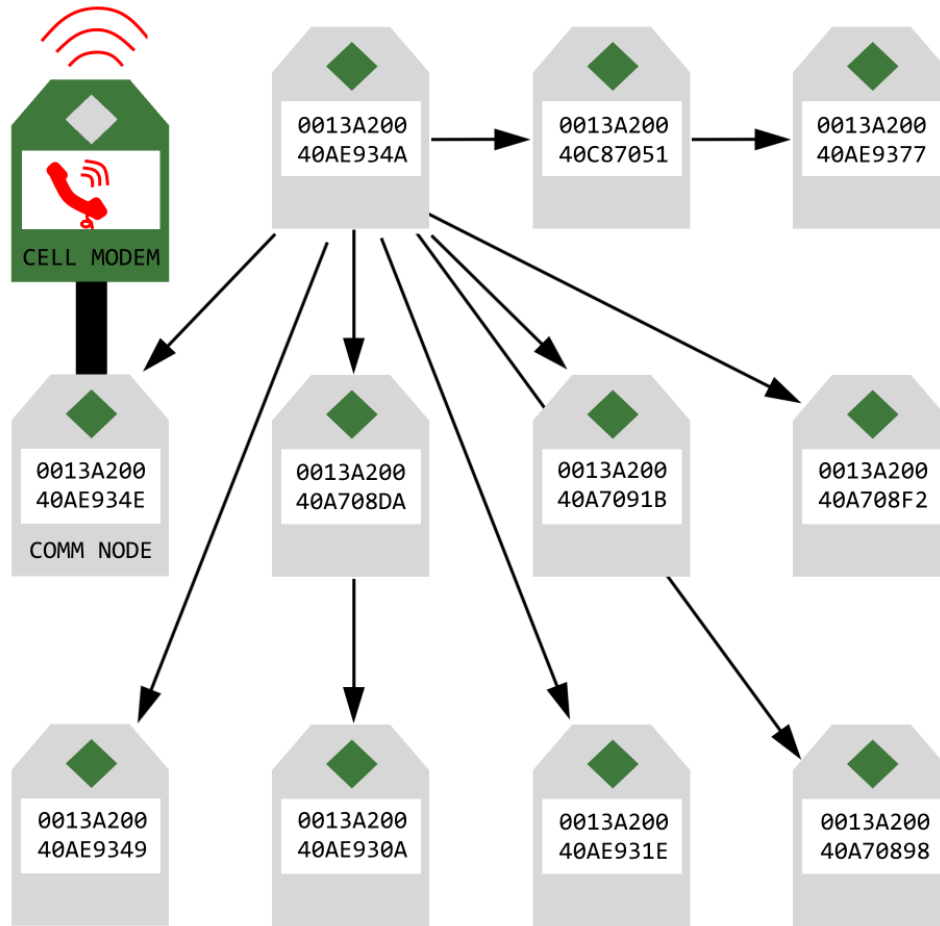
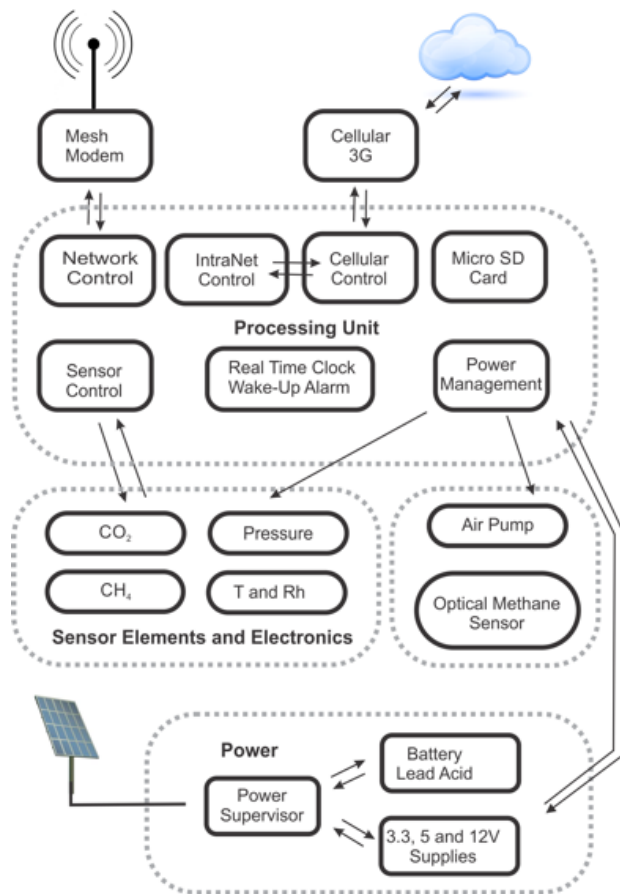


Figure 4.8: This is a map of one of the networks used in the testing field. This is an example of a hybrid network. The various sensor nodes all connect to a single sensor node, like in a star network. This node connects with the communication node which, in turn, connects via cellular data to the home server.

can make use of preexisting data infrastructure to transfer the data over long distances.

With these different levels of wireless modems, a two-tiered approach can be applied to the network. By keeping many of the components the same across tiers, the communication nodes serve much the same function as the sensor nodes, but with increased capabilities. A functional diagram of the communication and sensor nodes can be seen in Figure 4.9.

Communcation Node



Sensor Node

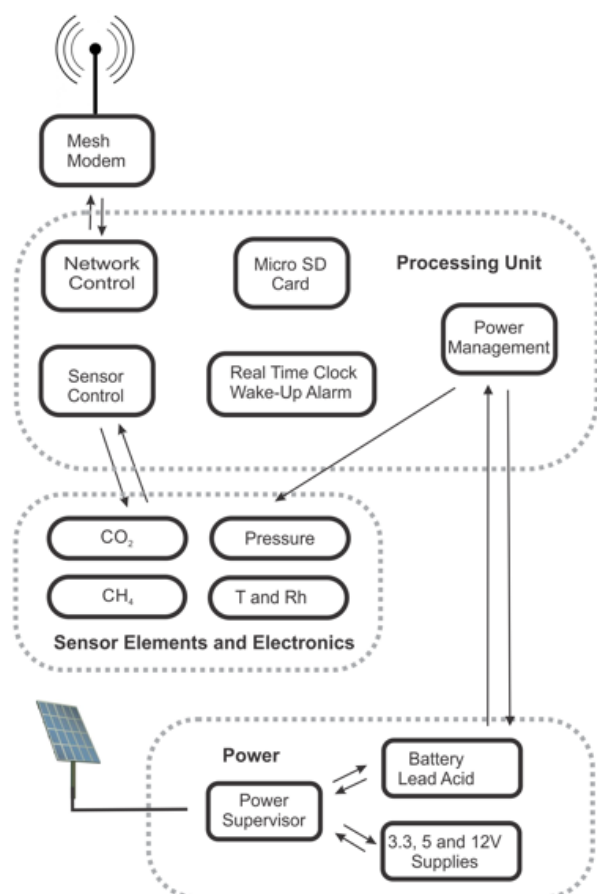


Figure 4.9: Functional diagrams for both the sensor and communication nodes in the network. Note how the communication node has all of the same parts as the sensor node with some additions.

4.3 Data Storage and Transmission

Each tier of the sensor network is programmed to treat data differently. While all units are designed to collect data from their own sensors, they are also designed to collect and store the data transmitted from other nodes in the network. This creates a data redundancies which minimizes risks to the network. If a single unit goes down, all is not lost. Even if one of the large communication nodes is knocked off-line, the data collection is not compromised. Each of the other units will collect and store the data on a physically retrievable SD card. This resiliency was designed to prevent issues outside of the control of the group, such as weather, cellular network outages, and unforeseeable damage.

The unprocessed sensor data and diagnostic information is collected every 15 minutes and stored in the ring buffer (see Figure 4.10). The ring buffer also contains markers to allow the system to continue where it left off after being reset or after a complete power failure. About one month of data can be stored before the data must be written to the SD card. Depending on the battery charge, the new data is written to the SD card from the ring buffer once an hour. At this time, data is also sent to the communication nodes. If the system charge is low, the system will wait until until the battery is significantly recharged before to turning on the SD card for writing and transmitting the data. The SD card writing and data transmission are performed independently with separate pointers into the ring buffer. The power-managed SD card provides a local backup. File rotation is performed every week to insure that the data file is kept within a reasonable size. The network routing is optimized every hour. In the mesh setup, data packets can transfer from one node to another node as they travel to the communication node. This increases both the range and reliability of the system.

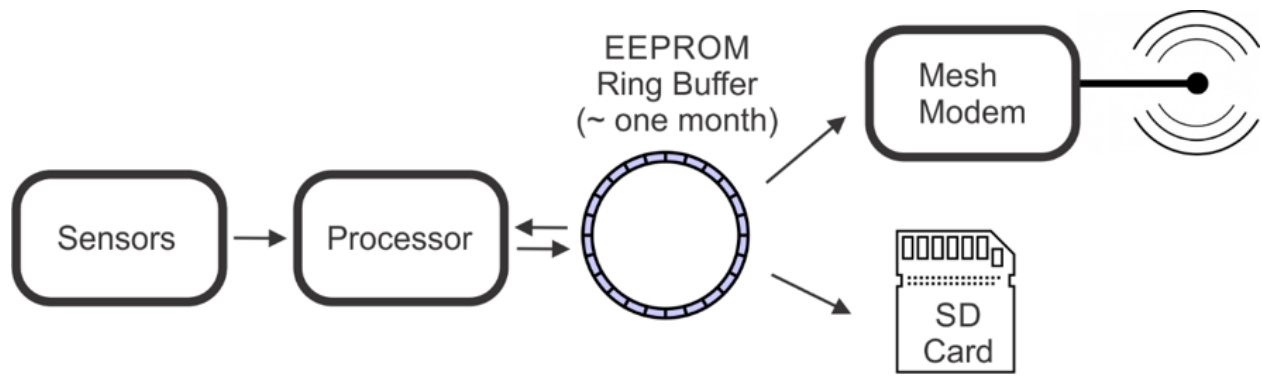


Figure 4.10: Data collection scheme for the sensor nodes. The data collected by the sensors are routed by the processor into a ring buffer. These data from the buffer are periodically dumped to both the SD card on the node as well as synced with other nodes in the network.

The communication nodes direct the self-assembly of the ad-hoc hybrid network and collect transmitted data (see Figure 4.11). Data are received at specific times from each sensor node and are identified by the modems 64-bit identification number. The processor writes the data to the ring buffer and periodically transfers the data to the SD card. Again, file rotation is performed. The SD card is written every hour or when the buffer reaches 75% capacity. The high capacity scenario is only possible if a sensor node has delayed sending data due to routing or power issues. Power management for the communication nodes is

critically important, but is mediated to some extent due to the large capacity of the solar panel and batteries. The communication nodes have been tested with a network containing 20 sensor nodes. Currently, the number of sensors in each network can scale to 55 nodes.

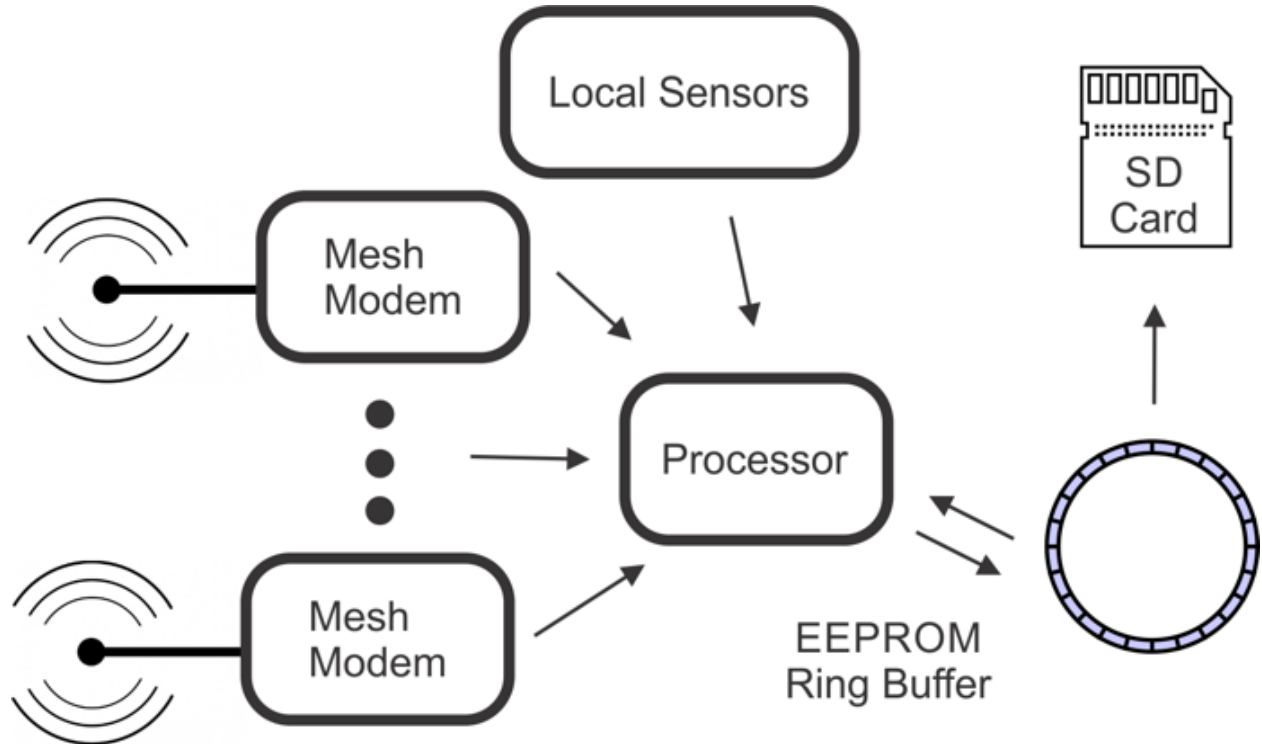


Figure 4.11: Data collection scheme for a sensor communication node. The data collected by the sensors are routed by the processor into a ring buffer. Data communicated by the mesh network is also routed into the ring buffer. These data are stored in the SD card of the communication node until a pull request from the home server is received.

Once an hour, the communication nodes connect to a ‘home’ server on the OSU main campus. The scheme used to transfer the data is shown in Figure 4.12. Each sensor node transmits the directory of the SD card to the server. At this time, it is possible for the server to request specific files from any sensor node on the mesh network, or change performance parameters contained on each sensor node. In a typical operation, the server looks at the file sizes on the SD card and requests any new data as indicated by an increase in the file size. The final line count is recorded by the server along with the new file size to ensure that the next data transfer continues where the last one left off. The raw data are stored in a SQL database. Each communication node has a unique database table assigned to it for raw data. Periodically, the raw data are processed to obtain the measured values from

the sensors and other monitoring points. The processed data are saved in a unique table in a SQL database. This second processing step allows all checksums to be validated, and a variety of post-processing algorithms to be applied to the data without modifying any of the raw data.

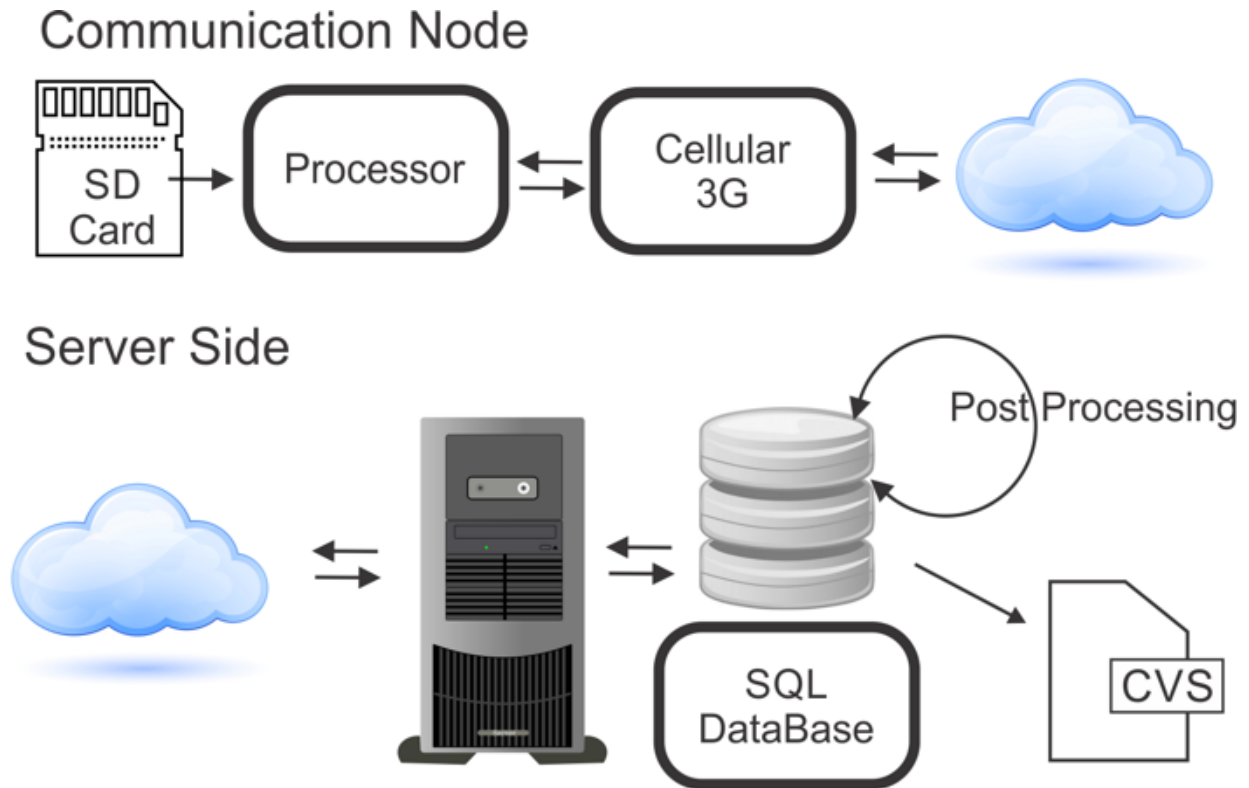


Figure 4.12: Scheme utilized by the communication node and server to transmit data back to OSU from the field sites. Upon a pull request from the server, the processor on the communication node takes the data from the SD card and sends the requested data lines through the cellular network. The server stores these data in an SQL database, and post processing operations are executed on the stored data. Upon user interface with the server, the data can be pulled from the database into an easy to read CSV file.

Sensor network data and node parameters are stored in SQL database which is queried during data upload. Basic information on the sensor history is also stored in this database and can be accessed at a website associated with the ‘home’ server. The collected data are accessible through the SQL server. The data stored on the server can be pulled from to any computer with the server address and login credentials. A Python script is available to select the data the user wants to pull and store in a text file of comma separated values.

CHAPTER 5

Development of a Networked Gas Sensor Array for the Detection of CO₂ and CH₄ Concentrations

5.1 Introduction

When faced with the problem of modeling gas emissions from underground storage facilities, a single sensor may not be adequate. This task requires monitoring of a large area of land over long time scales. Single sensors cannot monitor such a broad area, and it is expensive to employ a technician to monitor many sensors over time. To satisfy the needs of this problem, A wireless sensor array was designed based on a mesh network design to both sample the environment and coordinate remote data collection. The sensor array was designed with sensors optimal to the conditions of the environment based on the results discussed in Chapter 2. A set of sensors were added to a unit, a single node in the array. Each unit was solar powered and designed to withstand the environmental conditions of a normal field site. The each unit, or node, in the array was given the ability to communicate with other nodes in the network. Data passed from these nodes was sent to a central server at regular intervals to store the observations. In this manner, a remotely monitored array was constructed to determine gas properties over a larger area than one sensor could monitor alone.

In this chapter, the design and construction of the individual nodes in the sensor is described. First, a simplified schematic of the network is offered and explained. Next, the circuits employed by the sensors are described, including information about relevant breakout

boards. This chapter discusses the individual circuit design for power supply, processing and memory, xbee wireless communication, cellular communication, environmental sensors, small gas concentration sensors, larger pumped gas concentration sensors, and ground protection. The difference between the passive and active gas sampling regimes is discussed. A specially designed 3D printed part was produced specifically for passive sampling, and this part is explained in detail. Finally, this chapter relates the development of the prototype boards and movement into production of 110 units for deployment in the field.

5.2 Device Design

To best facilitate the collection and analysis of the data from remote sites, a tiered device hierarchy was created. Most of the nodes were computationally simple, acting as end points of the network by collecting the data. These sensor nodes require the gas sensors, light power supply hardware, and radio for simple wireless communication to other nodes. The middle tier of the network collects data from the sensor nodes and communicates it to the next level. These communication nodes are computationally simple much like the sensor nodes, but they spend more time and energy processing than the smaller sensor nodes. Thus the communication nodes require similar gas sensors and radio, but with a more robust power supply. The coordinated data is transmitted to the upper level via cellular phone protocols, necessitating a cell modem. With the extra power made available to the communication nodes, better quality sensors could be added to them, allowing verification of incoming data. They employ a set of actively pumped sensors in addition to the passive sensors included in the smaller nodes. The highest tier of the network would be a computational workstation housed at the base of operations. This computer, connected to the municipal power supply, is stationary and can afford to have any number of configurations. It acts as a receiver of the field data. Data are sent to a web server being run by this workstation. An organized list of requirements for the device hierarchy can be see in table 5.1.

The nodes can be generalized as a set of functional units, such as depicted in Figure 5.1. The functional units are grouped as “power”, “Arduino based processing”, and “glue electronics.” Although the power supply capacity of each node on the tier differs, the power supervisor and supplies required for each unit are essentially the same. The “Arduino based processing” parts are shared between tiers as well. By producing similar board infrastructure

Tier and Name	Device Requirements
Tier 0 Web Server	Large Storage Space
Tier 1 Communication Node	Simple gas sensors Advanced gas sensors Moderate power supply Wireless communication Cellular modem
Tier 2 Sensor Node	Simple gas sensors Low power supply Wireless communication

Table 5.1: Hierarchy and respective requirements of devices in the network array designed for this project

on tiers 1 and 2, parts unique to a certain tier such as the cellular modem are added on as additional breakout parts to the central board. The “glue electronics” may be expected to change for the more powerful sensors included with the communication nodes, but sensor redundancy in these nodes can work with the more powerful sensors used in addition to the simple ones. The redundancies provide the advantage of comparison of response between the sensor types, providing calibration during the post-process.

5.2.1 Gas Sensors

Several commercially available carbon dioxide and methane sensors were selected and evaluated for applicability to the sensor array. A full description of sensor choice can be found in Chapter 2. Certain sensor units were chosen for specific promised abilities. Notably, the K-30 model from CO₂Meter was chosen and cheap, lightweight sensors which promised satisfactory detection of carbon dioxide. The Gascard sensors sold by GHG Analytical were an order of magnitude more costly than the other sensors, but the advertised capability made them attractive enough to make up for the expense. The MQ-4 methane sensor was chosen as the inexpensive methane detector; though it lacks the high sensitivity to concentration changes which the other sensors possess, it will serve to detect large shifts in the methane present. Due to the unique interface requirements of each sensor unit, development kits were purchased when possible for prototyping.

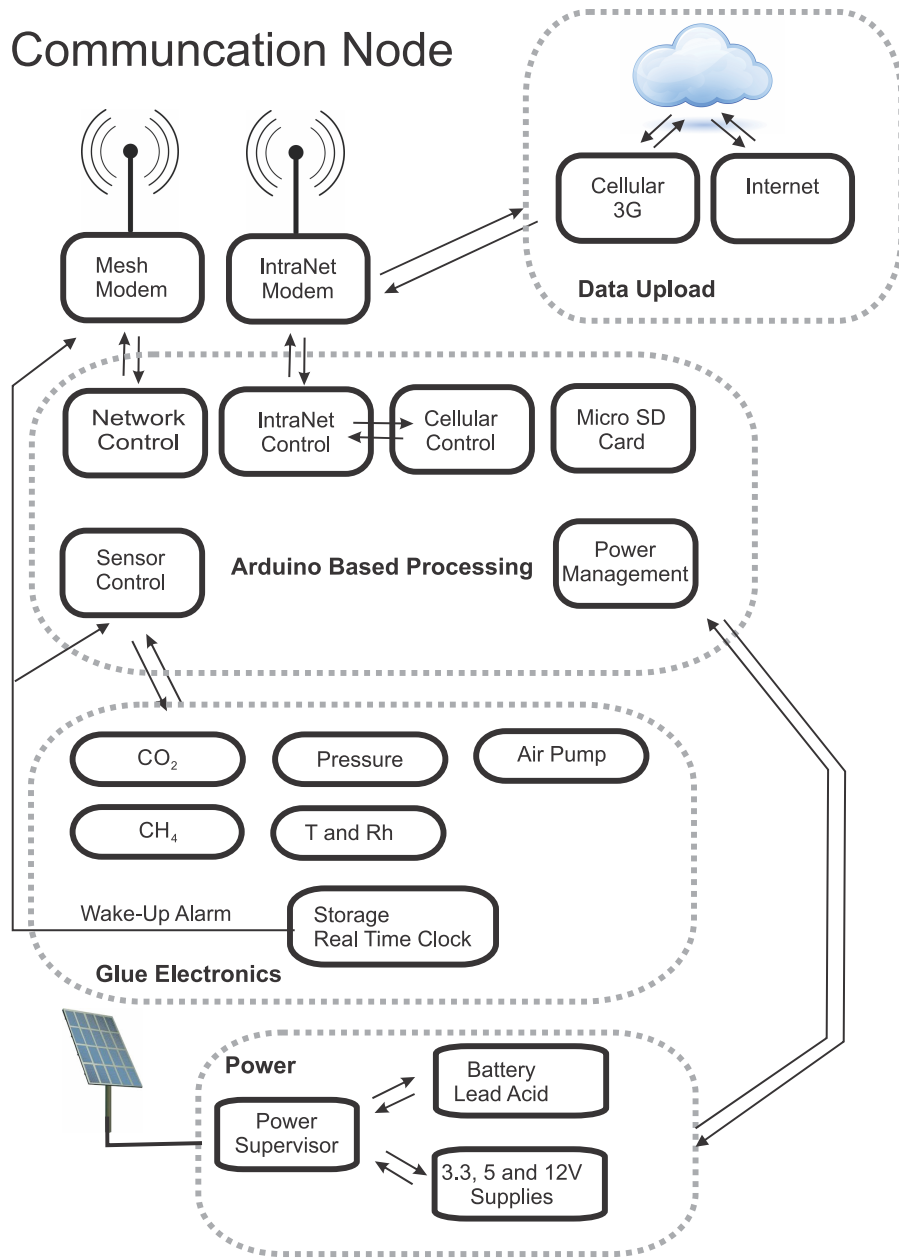


Figure 5.1: A generalized representation of the equipment to be included in each node.

5.2.2 Power Management

The nature of the sensor array designed to cover a relatively large area of land imposes limitations upon the power supply of the system. Since the area to be covered may include elevation changes, anthropogenic developments, and other uncontrollable factors, it would not be convenient to constrain the array by wired connection as the array will be adapted

to individual site conditions. Therefore, each unit must be designed with internal and self-sustaining power supplies. Two different types of commercially available solar power generation and storage units with weatherproof enclosures were selected from Tycon Power Systems. The majority of the sensors would be housed in the Remote Pro 2.5 W Continuous Remote Power System die cast enclosure (Figure 5.2 A) and a few sensor units with features requiring more power were housed in the Remote Pro 15 W Continuous Remote Power System steel enclosure (Figure 5.2 B). The 2.5 W enclosure includes a 12 V battery rated for 9 Ah of use, a charging and distribution circuit, and a 10 W solar panel. The 15 W enclosure includes a 12 V battery rated for 98 Ah, a charging and distribution circuit, and a 60 W solar panel [86].



Figure 5.2: The (A) Remote Pro 2.5 W Continuous Remote Power System and (B) Remote Pro 15 W Continuous Remote Power System—image from Tycon Power Systems’ website shows typical units.

During prototyping of the the devices using readily available Arduino development boards, the power consumption of the unit was found to quickly outstrip the combined charging and storage of power within the unit. The individual sensors were tested with a Fluke 179 True RMS Multimeter to ascertain the current and voltage across the power leads to verify the values provided in the specifications for each part. The calculated power from each of these measurements is summarized in the first part of Table 5.2. The Arduino prototype was found to use 2.7 W of power, over the continuous use rating of 2.5 W for the small enclosure power system. By subtracting the sensor power from the total consumption of the Arduino prototype, it was determined that the Arduino circuitry was too power intensive for this application. Thus it became clear that a dedicated power supply circuit would need to be designed for the deployed units.

Table 5.2: Power use of sensors examined, information based on manufacturer data sheets.

Device Type	Part	Power Use (mW)	Used in Deployed Model?
CO ₂ Sensor	K-30 SE-0018		Yes
	Gascard CO ₂		Yes
CH ₄ Sensor	MQ-4		Yes
	Gascard CH ₄		Yes
DC/DC Converter	A		Yes
	B		No
	C		No
	D		Yes

5.3 Circuit Description

Figure 5.3 shows several views of the control board. In Figure 5.4, the sensor node control board is shown. This unit utilizes the same PCB as the control board used in the communication node, but less of the parts are filled in. The figure is labeled to show the location of parts on the board relating to some of the important circuits. In Figure 5.5, the communication node control board is shown. This PCB is completely filled with components. The labels on this figure relate to the communication board-specific circuits, and the circuits mentioned previously in Figure 5.4 are present as well.

The sensor command module was designed in such a way as to minimize wasted power. A selection of parts considered for use in the board were measured for current and voltage to

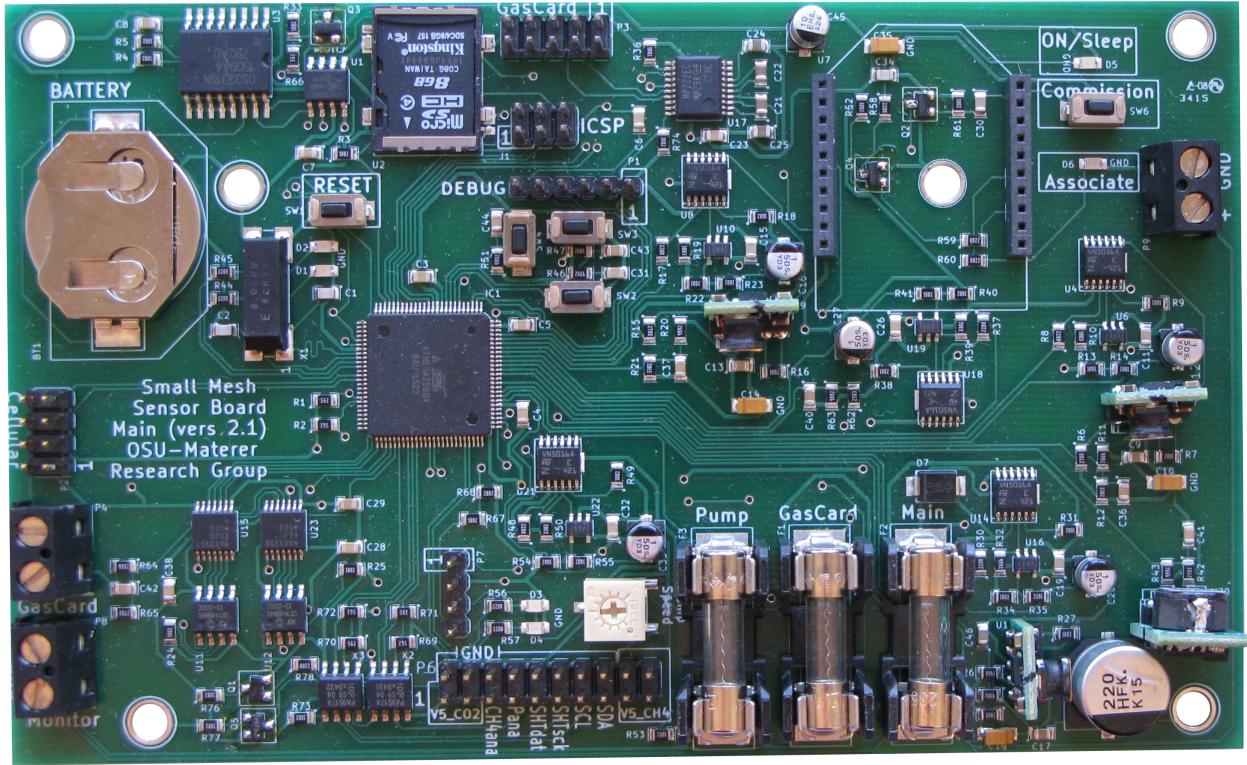


Figure 5.3: The fully built communication node command board designed for this study.

determine their power use, and these results are summarized in the second part of Table 5.2. The control board designed for this project uses 1.7 W during full use. To prepare for times when the solar panel cannot provide continuous charging, a problem which can last for long periods in the deployment area, 32% of the year is at least half-cloudy and 8% of the year is heavily overcast [94]. A lower power use mode was programmed. The control board can select a medium mode which reduces the frequency of sampling by some of the more energy expensive sensors. This is automatically triggered by the control program if the battery charge is determined to be at 70% charge. A hibernation mode was also programmed. This mode disables the sensors, communication circuitry, and microprocessor, leaving only power supply and real-time clock connected to the circuit. Below a certain battery voltage threshold, the unit can hibernate to prevent complete power drain, and it will restart again once the battery registers above the threshold voltage. Using only 0.1 mW during hibernation, this mode prevents the units from requiring manned intervention during inclement conditions.

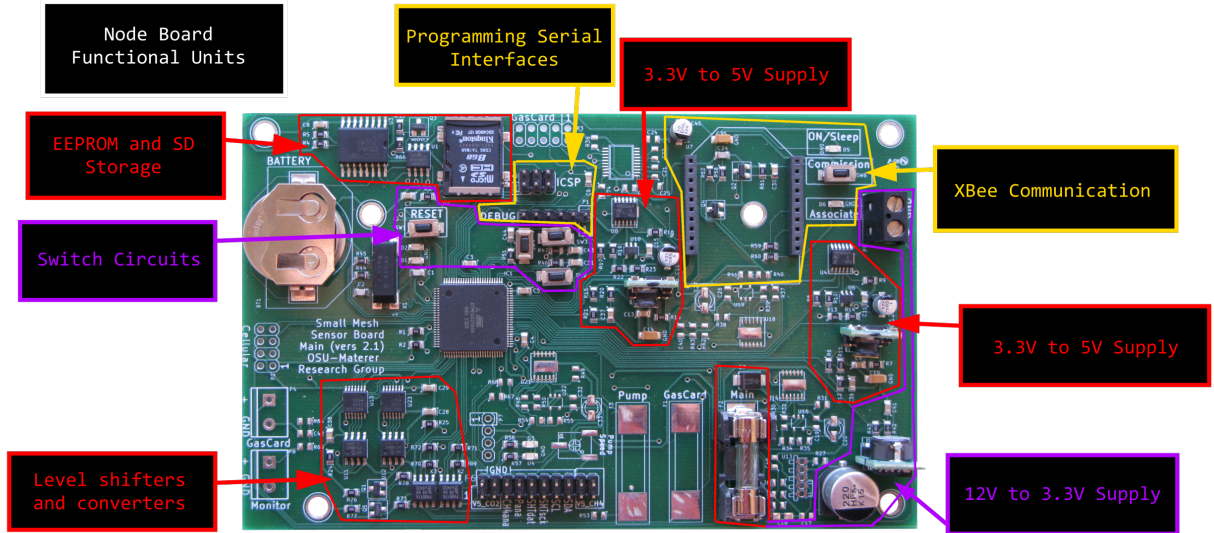


Figure 5.4: This diagram outlines some of the most important circuits placed on the control board used for the sensor nodes.

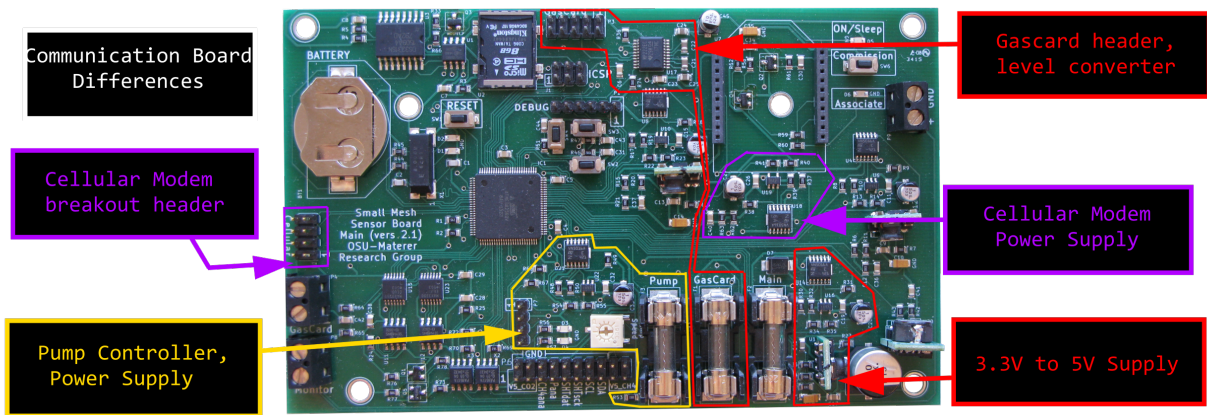


Figure 5.5: This diagram outlines important circuits on the control board used for the communication nodes which differ from those included on the sensor nodes.

5.3.1 Power Supply

The unit is powered from the case supply circuit through 22 AWG wire connected via terminal block. This 12 V line goes through a 1 A cartridge fuse and powers several circuits (Figure 5.6). The 12V line sends power to a 3.3 V DC/DC converter circuit, two separate 5 V DC/DC converter circuits, and the power supply for the Gascard (for the larger nodes only). The 12 V goes directly into a Murata Power Solutions OKI-78SR-33/1.5-W36-C fixed output 1.5 A DC/DC converter which steps down the DC current from 12 V to 3.3 V (Figure 5.7).

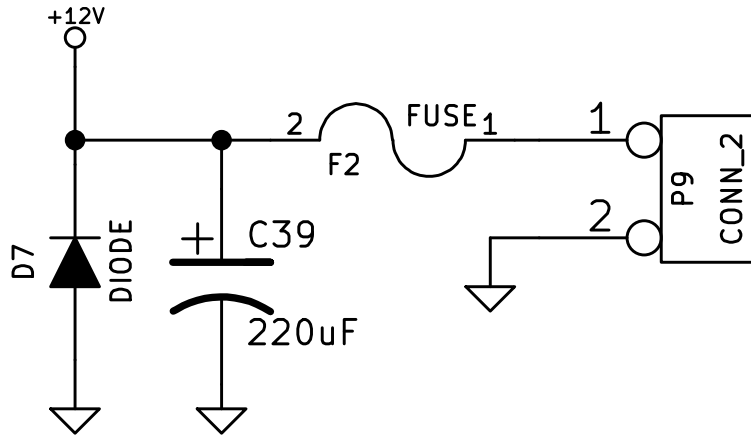


Figure 5.6: Fuse protected 12 V terminal circuit.

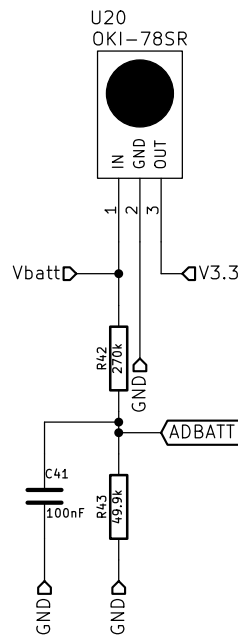


Figure 5.7: 3.3 V DC/DC converter circuit.

Each of the 5 V DC/DC converter circuits begins by running the 12 V line through a STMicroelectronics VN5016AJ-E single channel high side driver which delivers current of a clamped voltage to components further downstream (Figure 5.8). The VN5016AJ-E is switched by a current sense input. When this current sense is low, the current delivered by the chip is proportional to the load current based on a known ratio. This switch is controlled by the microcontroller based on current sense readings. The current of the voltage clamp is passed through a Texas Instruments TLV2471IDBVR 600 μ A 2.8 MHz rail-to-rail input/output high

drive operational amplifier which is operating as a closed loop non-inverting amplifier. The high side driver delivers the power to the input of a Murata Power Solutions OKR-T/1.5-W12-C adjustable output 1.5 A DC/DC converter. This device efficiently converts power between 0.591 V and 6 V based on trim, and it may be turned off when a separate pin is pulled low. The power delivered to the unit by the high side driver is used to pull the on/off pin high with a 10K resistor. The calculated resistance required for the trim pin to achieve 5.00 V is 268 Ω . A 270 Ω resistor was determined to produce voltage within bounds of the requirements for the components powered by this converter without requiring an expensive non-standard resistor value. The 5 V line produced by the converter is monitored by the ATmega 2560 chip on an A/D pin protected by resistors. An optional terminal block header was installed to monitor the voltage being produced by the solar panel. This simple circuit is protected by resistors and connects to one of the A/D pins on the ATmega 2560.

5.3.2 Processor and Memory

The board commands are coordinated by an Atmel ATmega 2560 lower power 8-bit microcontroller with 64 kB flash operating on a RISC architecture (referred to as ATmega 2560 in this manuscript). The ATmega 2560 is connected to a MA-506 8MHz ± 30 ppm crystal oscillator with equivalent length traces (Figure 5.9). Several push-button switches with associated LEDs are connected directly to the controller to act as human interface for simple commands such as reset, on/off, and dump log (Figure 5.10). Interface with the RISC architecture can occur through either a TTL/RS-232 header or an in-circuit serial programming header for programming firmware or debugging (Figure 5.11). These headers connect directly to the ATmega 2560 and do not pass through any RS-232 type translators.

Logging is managed by the controller using timestamps from a DS3231 real-time clock (Figure 5.12). The real time clock uses a CR-2016 coin cell battery to maintain correct count of the date. Data can be logged using two memory storage methods. The first is 24LC1026 1024 kb serial EEPROM (Figure 5.13). The second is a micro Secure Digital stable storage, an Alps SCHD3A0100 micro SD card holder which is activated by a Vishay Si2377EDS p-type MOSFET connected to the ATmega 2560 chip (Figure 5.14).

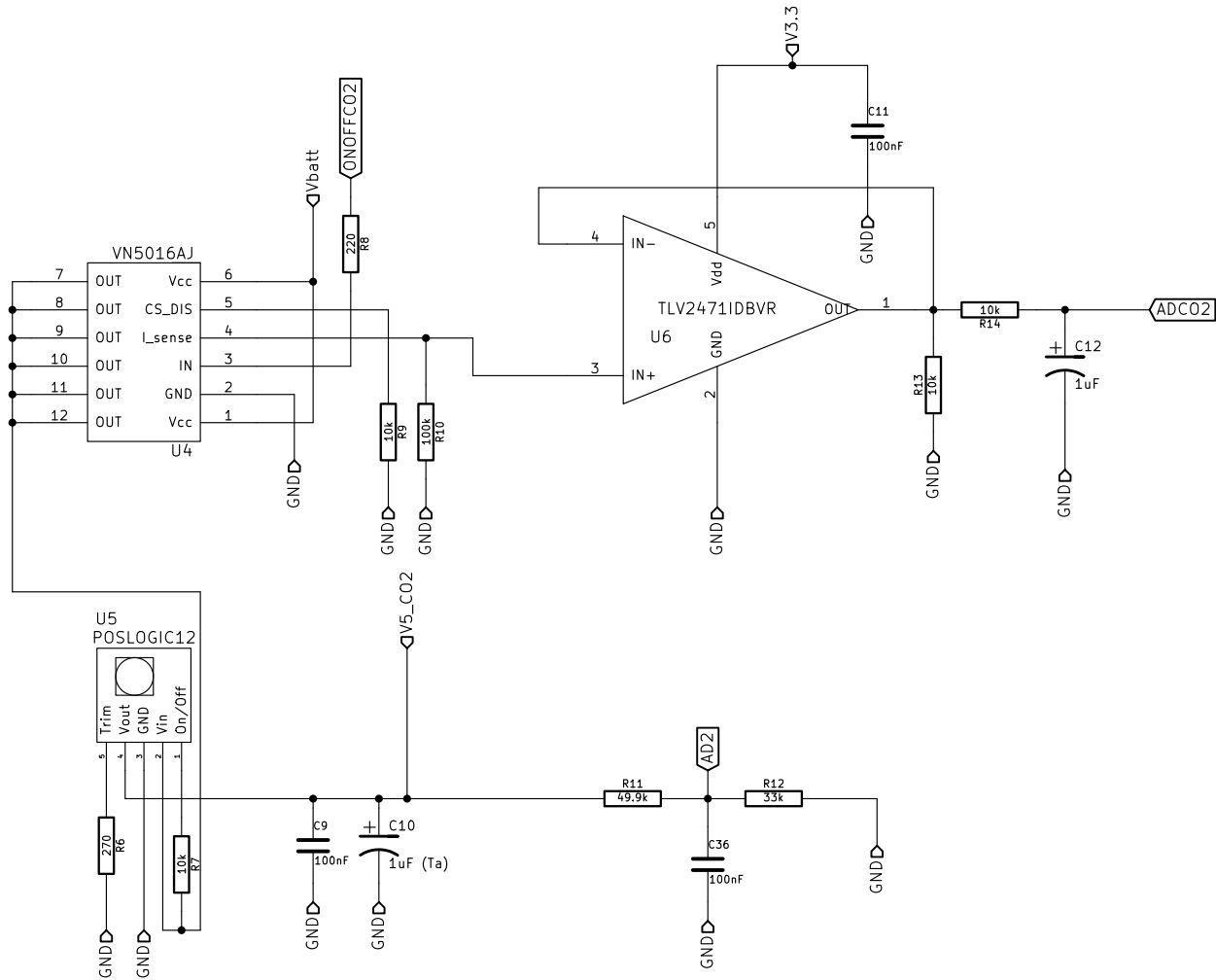


Figure 5.8: 5 V Dc/DC converter circuit

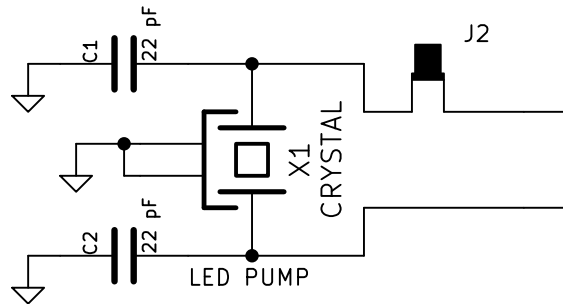


Figure 5.9: External crystal oscillator.

5.3.3 XBee Wireless Communication

Communication of the nodes with the rest of the mesh will occur by way of an XBee wireless device. For this application, the XBee-Pro 900HP model was chosen (Figure 5.17).

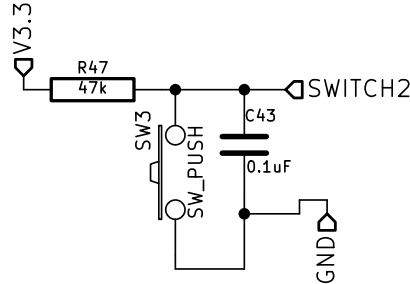
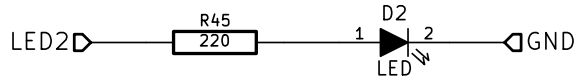


Figure 5.10: Example of switch and associated LED.

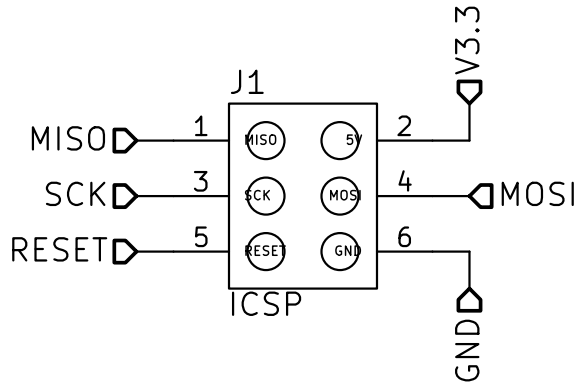


Figure 5.11: ICSP header pinout.

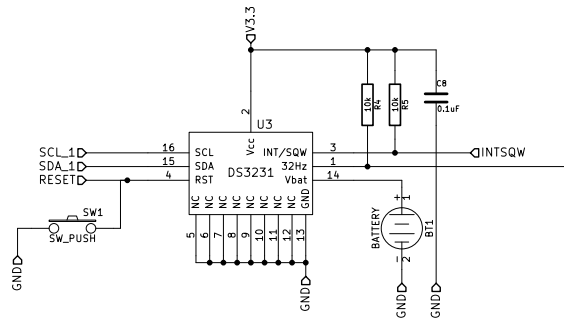


Figure 5.12: DS3231 real time clock circuit.

This 900 MHz radio module is capable of data transfer rates of up to 200 kbps with impressive range, depending on the antenna gain. The XBee communicates directly with the ATmega 2650 chip via TX/RX serial communication. Traces also directly connect with the board to send signals telling the radio to reset and sleep. The circuit has some human interface

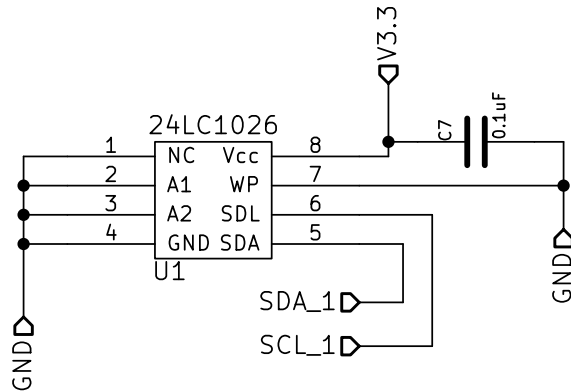


Figure 5.13: EEprom memory IC and connections.

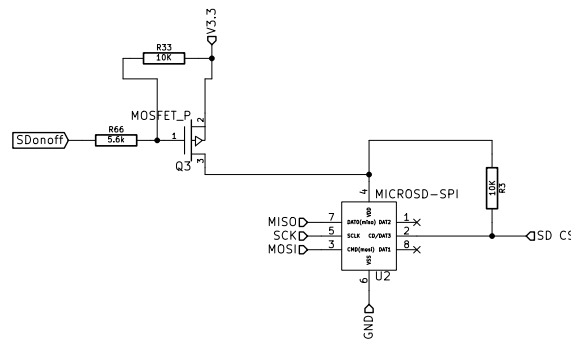


Figure 5.14: microSD memory slot with switch circuitry.

components. One LED provides “on” status, a pushbutton switch is set to the “commission” function of the XBee firmware, and another LED is tied to the “associate” function. The commission button allows the user to wake a device, send node identifying codes, broadcast a request to join a network, and restores default values depending on the number of times the button is pressed. The associate LED provides information about the status of the network and diagnostics which can be interpreted by the rate and number of blinks by the diode. The device is powered by the 3.3 V power line, and the sleeping of the modem is controlled by this same power line. When power begins flowing through the 3.3 V line from an OFF state, an On Semiconductor 2N7002E n-type MOSFET sends a signal to the XBee to activate it. A signal can be sent from the XBee to reset to ATmega 2560 as well. The signal is delayed slightly by a capacitor before another n-type MOSFET sends a signal to the control board with the reset signal.

5.3.4 Cellular Communication

Communication by the control nodes to the data collection site takes place over cellular phone lines. A breakout board is connected to the control board by a ribbon patch cable. The breakout board houses a NimbeLink Skywire EVDO cellular modem. The cellular modem requires a stable 4 V power supply, so a dedicated power circuit was designed (Figure 5.18). Much in the same way the other power supply circuits were constructed, this line draws the 12 V from the battery to a VN5016AJ-E high side driver with switched current sensing using a TLV2471IDBVR op-amp to monitor the current at this point similar to the 5 V power supply circuits. The power is converted using a similar Murata OKR-T/1.5-W12-C DC/DC converter with a 348 Ω resistor dialing in the output voltage required for the modem. Monitoring of the power supply and switch is processed by the ATmega 2560. The cellular modem is powered by the 4 V power line, but a reference voltage to the input/output lines is also required. Since the controller uses 3.3 V, this reference voltage needs to reflect that. The modem communicates with the ATmega 2560 by TX/RX serial port. Two input output lines from the control board connect to n-type MOSFETs. These act as switches to send signals to the modem for on/off and sleep operations.

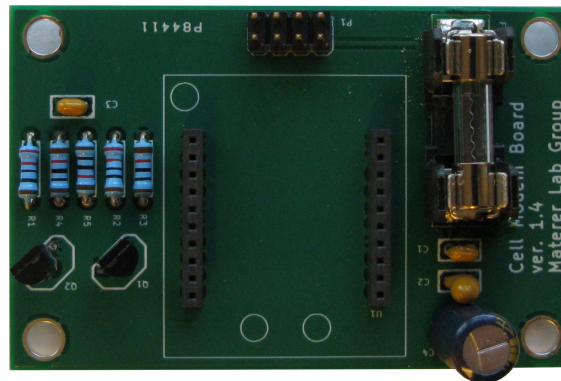


Figure 5.15: This breakout board for which was attached inside the communication nodes was designed to accommodate a NimbeLink Skywaire EVDO cellular modem.

5.3.5 Sensor Breakout Board

While the communication nodes have some more powerful sensors than the end nodes, all types share a set of the inexpensive sensors. These parts are collected on a breakout board referred to in schematics as the “sensor board” (Figure 5.19. Data are transferred to and



Figure 5.16: This is an example of the cellular modem utilized in the communication nodes. The two U.FL connectors allow attachment of antennas for both cellular communication as well as GPS synchronization.

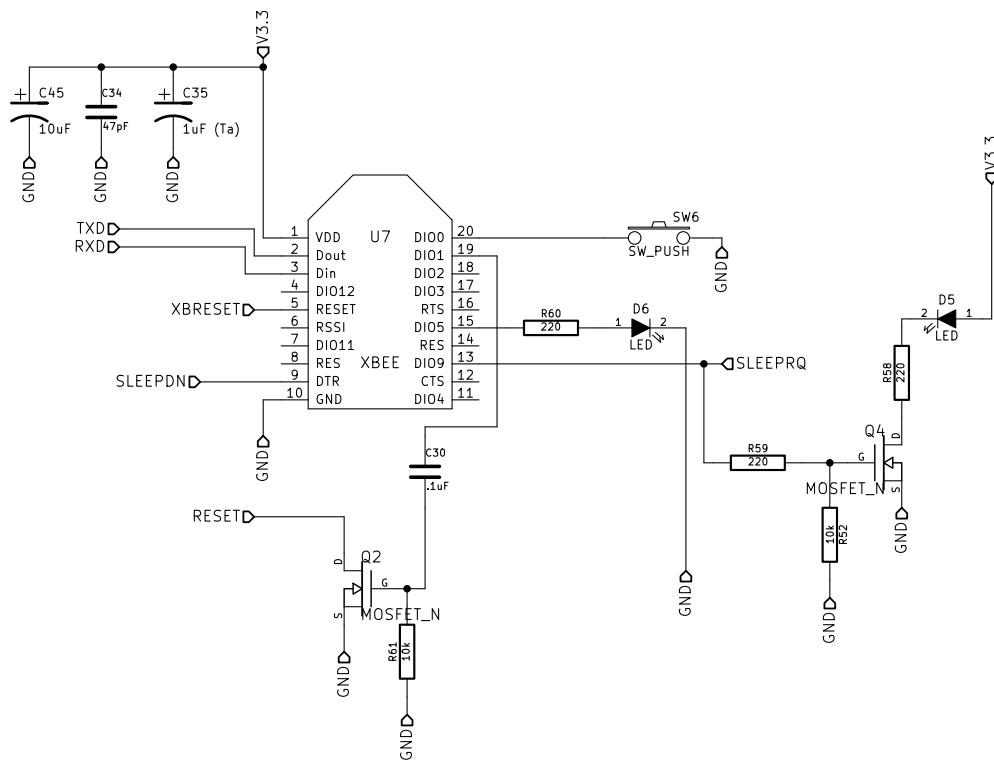


Figure 5.17: Schematic of XBee device as built into communication boards

from the control board by a 20 pin header connected by ribbon cable with power supply and ground cables. Power lines in this cable use two wires each to prevent wire failure. Several ground wires are used on the cable, positioned such that they alternate with the signal wires on the ribbon to prevent interference between lines. The K series carbon dioxide sensor is powered by a 5 V power line and communicates with the controller via I²C SDA/SDL port

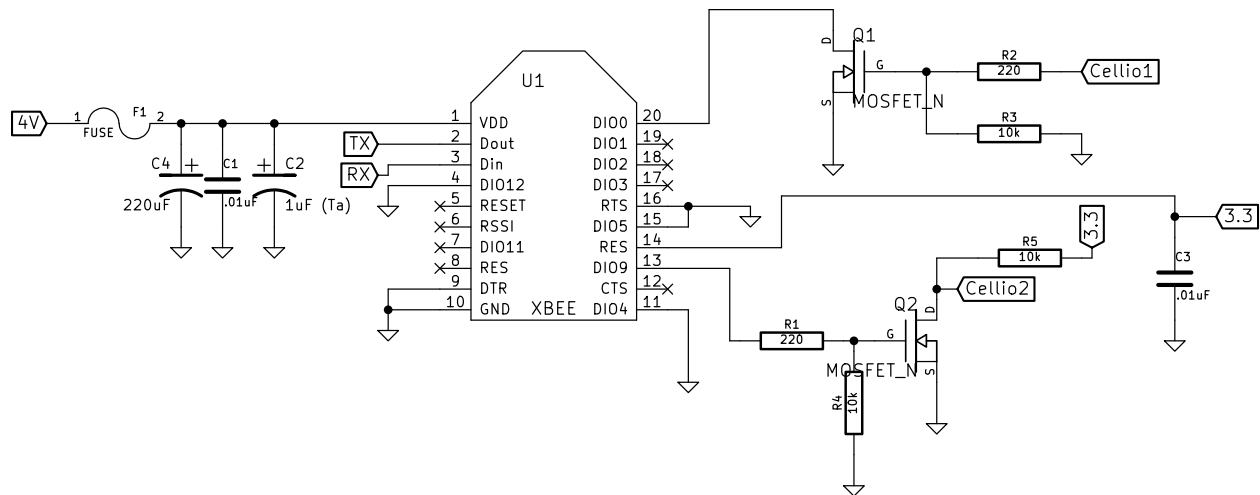


Figure 5.18: Cellular communication breakout board schematic.

(Figure 5.21). The I²C is translated through an NXP PCA9517A level translating repeater to shift the low voltage signals, which is limited by an internal resistor, up to the 5 V signal which matches the input voltage. This part was originally intended to shift the voltage from the 3.3 V I²C output from the K-series sensor. As the design progressed, the microcontroller requirement was discovered to be 3.3 V input. Due to the timeline of the project, the sensor boards were already printed with the level translator to convert the signal to 5 V. A separate level converter on the main board converts the signal back down to 3.3 V (Figure 5.22). This part of the circuit is vestigial. If one part of the device is changed in future versions, this grandfathered circuit may prove useful once again.

The MQ-4 methane sensor is mounted on the board by connecting it to a special MQ socket for the MQ series of gas sensors (Figure 5.25). The pin which connects to the heating coil of the MQ-4 sensor is powered by the 5 V power line. If 5 V power is being supplied to the sensors board, the heater will be powered on. The two other input pins on the MQ-4 sensor connect to 5 V power lines. These pins are connected after the sensor and pulled down by a 10 k Ω resistor before connecting to an op-amp. The op-amp is configured as a closed loop non-inverting amplifier to boost the analog signal output by the sensor. On the mainboard, the analog signal from the methane sensor is routed to a Maxim MCP3202 12 bit analog/digital converter with serial peripheral interface (Figure 5.26). The MCP3202 splits the analog signal into a digital component with comparison to a reference clock signal produced by the microcontroller, and it can be shutdown with a signal from the controller to

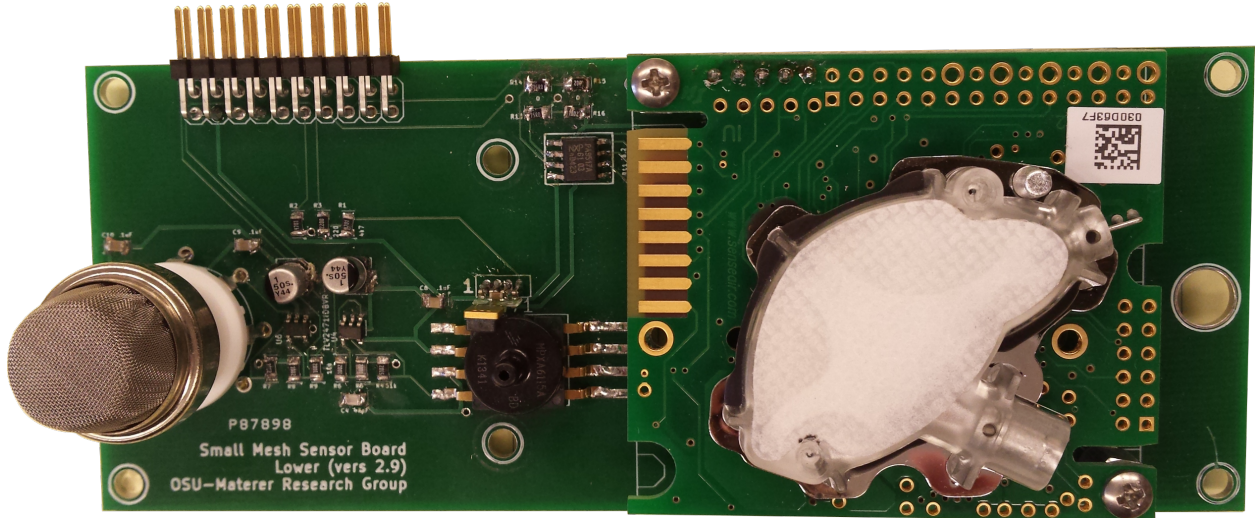


Figure 5.19: A picture of the sensor breakout board with encapsulating materials removed.

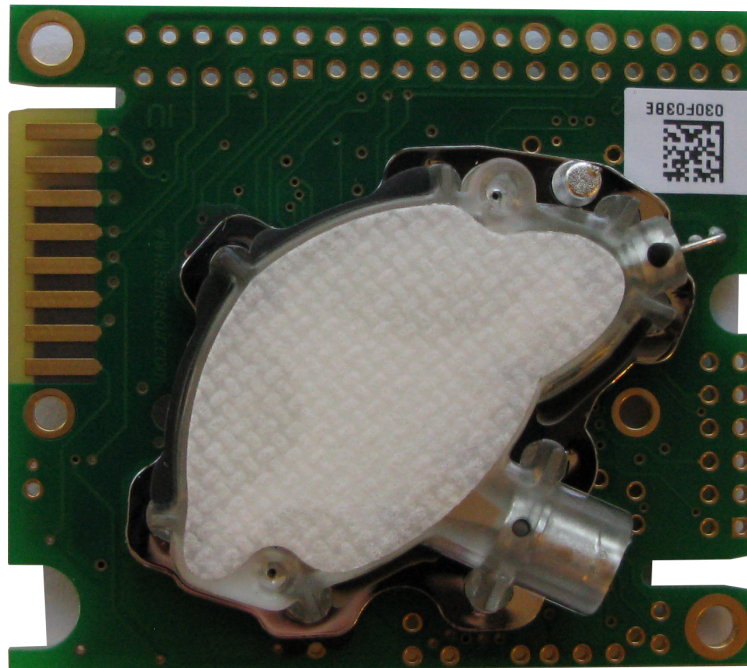


Figure 5.20: The K series CO₂ sensor is an optical sensor which detects gas passing through a membrane. This is mounted on a discrete board which is mounted with standoffs on the sensor breakout board.

reduce power consumption. Digital output from the A/D converter and digital input to it must pass through a Maxim MAX3390E low-voltage level translator. This converts the 5 V signal used by the sensors to the 3.3 V signal used by the ATmega 2560. The tri-state outputs of this level translator minimizes the current used by the chip in the translation, an

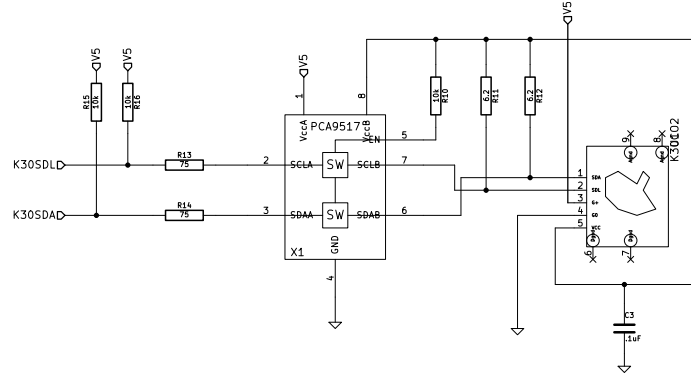


Figure 5.21: CO₂ sensor with level translator on sensor breakout board.

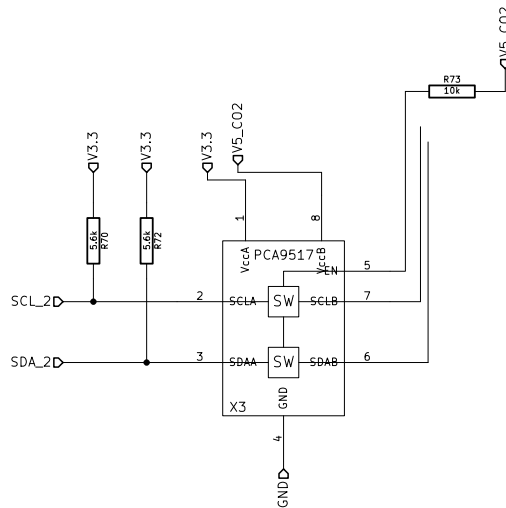




Figure 5.23: The MQ-4 CH₄ sensor is a pluggable unit. The wire mesh prevents damage to the delicate sensing parts, and, according to manufacturers, prevents explosions when applied to dangerous gas mixtures.



Figure 5.24: This image of the MQ-4 sensor with the metal mesh removed shows the actual sensor. A gas sensing layer on an Al₂O₃ substrate is connected with Au and Pt electrodes. A nichrome filament housed within the ceramic tube heats the area during detection to improve response.

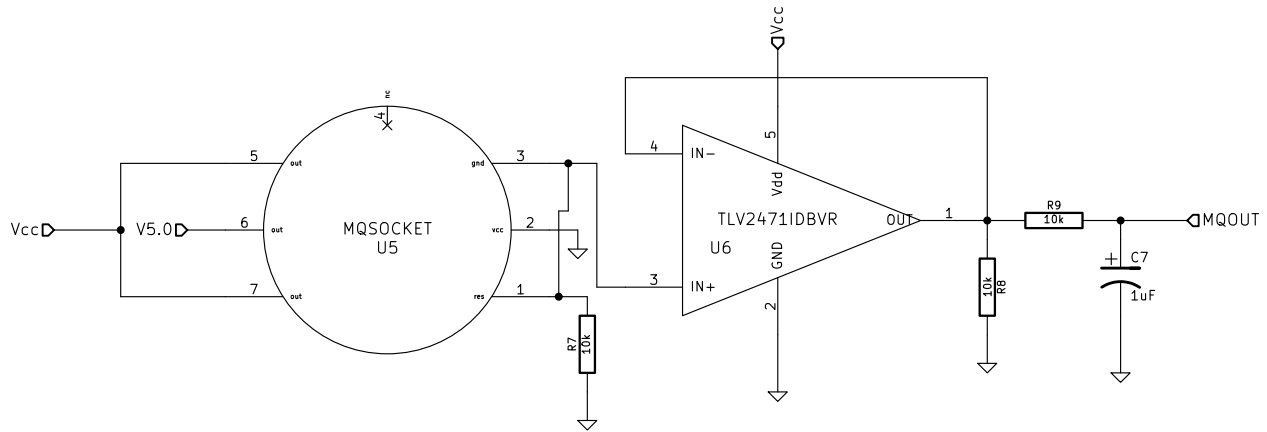


Figure 5.25: CH₄ sensor socket with amplifier.

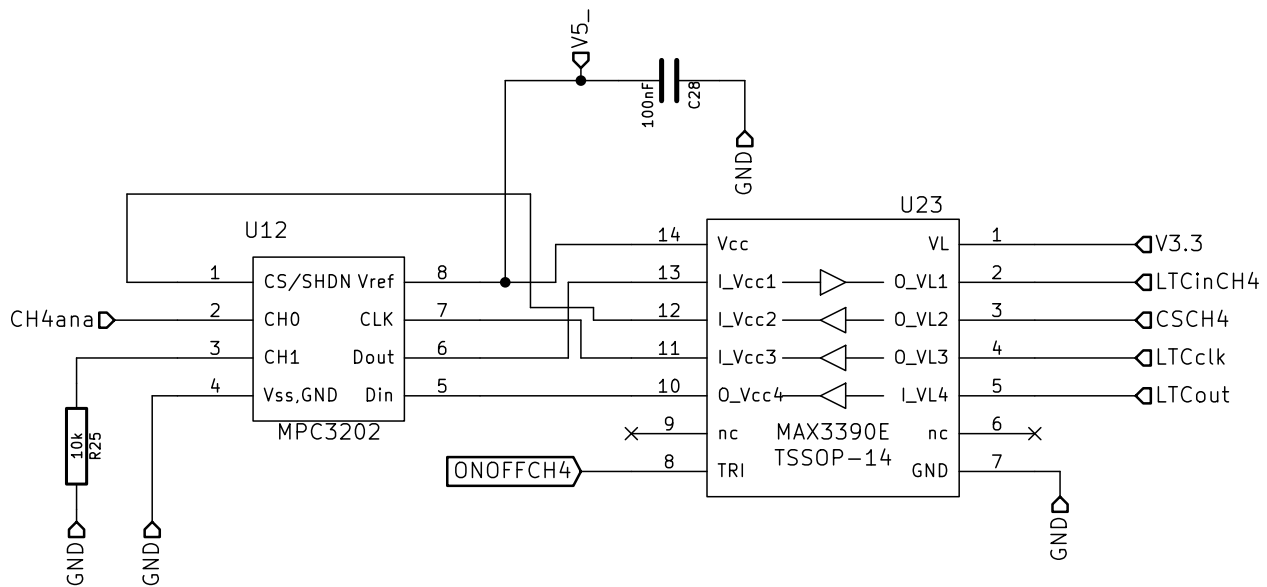


Figure 5.26: Serial peripheral interface and level translator connected to CH₄ sensor.

signal with an op-amp closed loop non-inverting amplifier circuit.

5.3.6 Gascard Implementation

The larger communication nodes have an additional sensor, the Edinburgh Gascard, for calibration purposes which has increased power requirements compared to the low power sensors. This sensor has several dedicated circuits for its operation. The Gascard operates under 12 V conditions, the same as is supplied by the battery, negating the need for a DC/DC converter. The power supplied by the battery passes through a VN5016AJ-E high

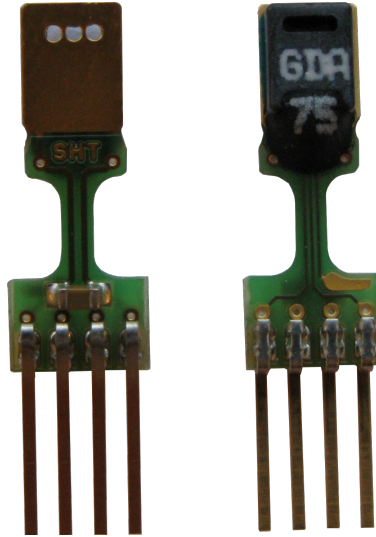


Figure 5.27: The Sensirion SHT75 temperature and humidity sensor consists of a small probe sticking which sticks out from the board. The end of this probe has a comparatively thick layer of metal monolith which acts as a heat sink to prevent erratic temperature changes which do not accurately reflect the true average temperature of the environment.

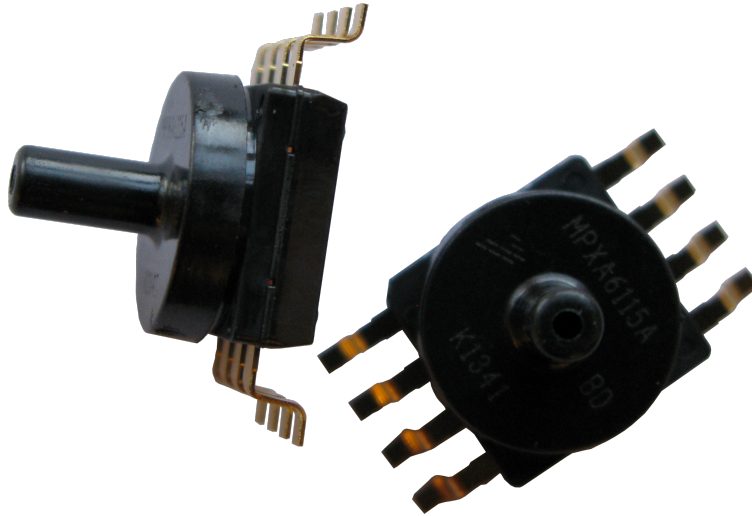


Figure 5.28: The Freescale MPXA6115 pressure sensor detects the external pressure with a membrane protected by a long stem tube. Though previous application of this sensor by the group have used tubing to connect the sensor on the board to the outside of the case, the design of each sensor units allows direct access.

side driver which is used to clamp the voltage and monitor the current output, amplified by a TLV2471IDBVR op-amp (Figure 5.33). The output of the high side driver is fused to protect the circuitry and connects to a terminal block header. A separate lead from the fuse, which is protected by resistors, is used to monitor the voltage output.

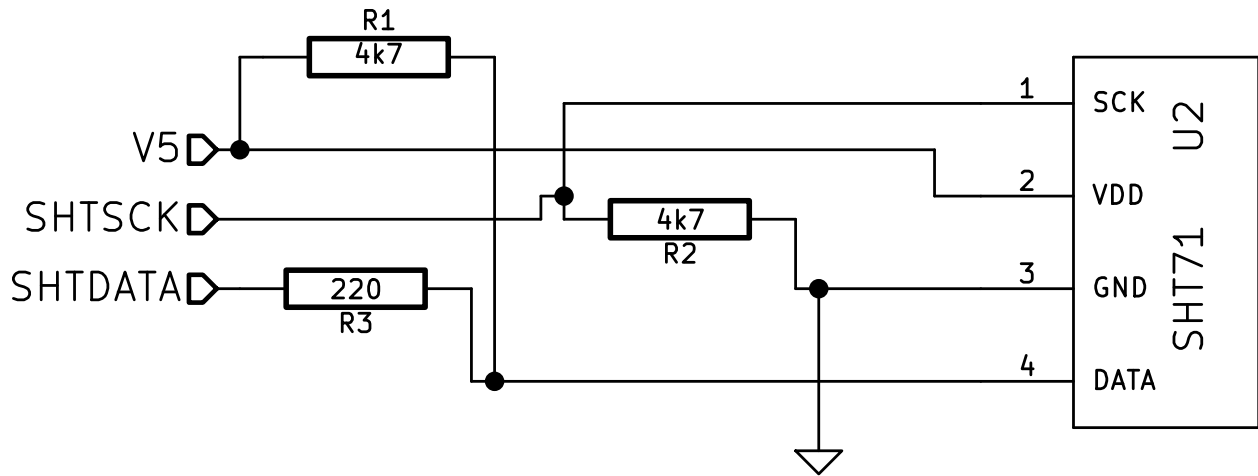


Figure 5.29: SHT75 schematic on sensor board.

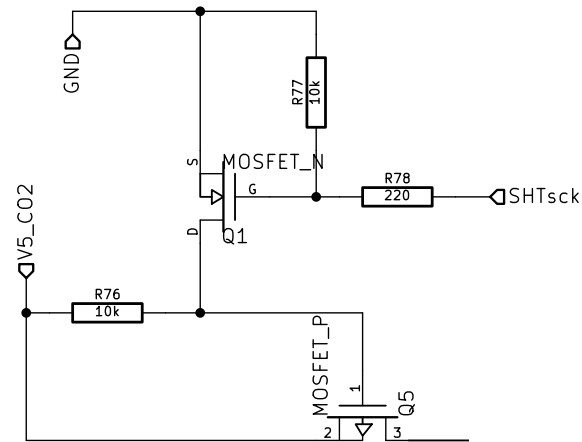


Figure 5.30: MOSFET switches used with the SHT75 clock line.

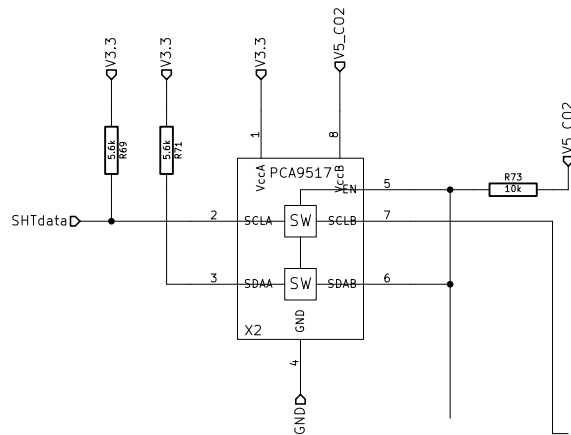


Figure 5.31: SHT75 data level translator on mainboard.

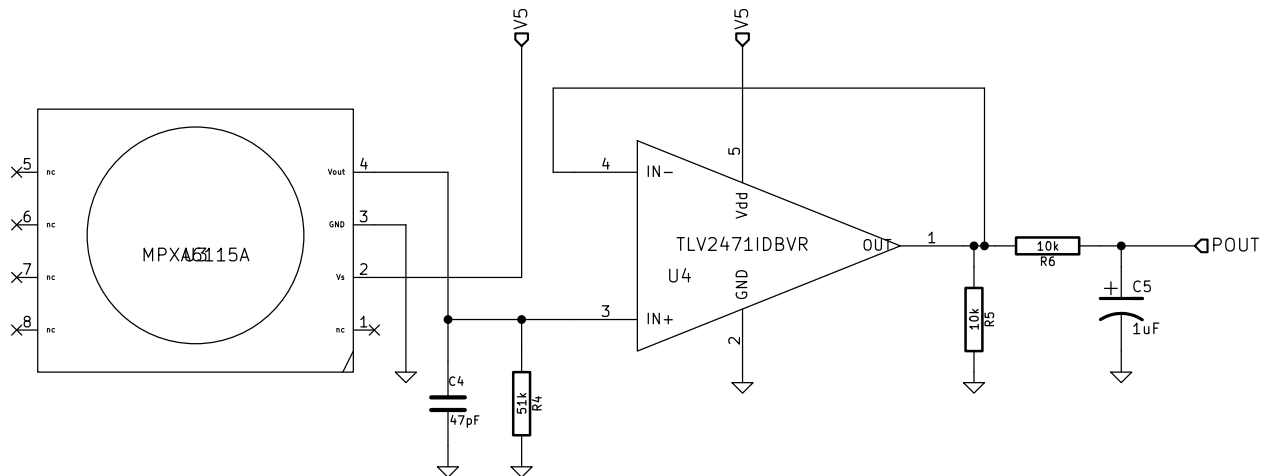


Figure 5.32: MPXA6115A pressure sensor and amplifier.

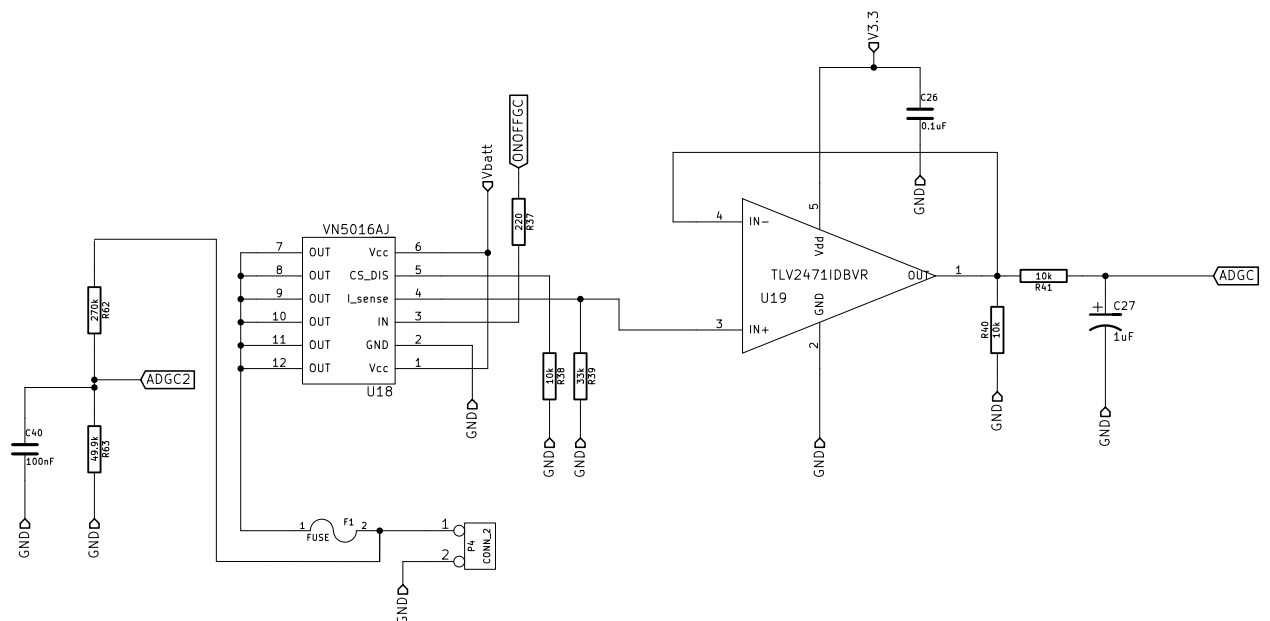


Figure 5.33: Gascard 4 V power supply circuitry

Unlike the membrane sensors used in the sensor nodes, the Gascard requires flow to operate. All sensors used in the communication nodes will therefore be operating through flow enclosures. This flow is produced by a Thomas 1410D/2.2/E/BLDC diaphragm pump. The pump is powered by the 12 V line and uses the same fused high side driver and op amp circuit as the Gascard (Figure 5.34). The pump is connected by a four pin header. Two of the pins are connected by a Bourns 3361P-1-103GLF potentiometer. This Cermet trimpot can be adjusted from 10 Ω to 10 k Ω , and it is used to adjust the speed of the pump.

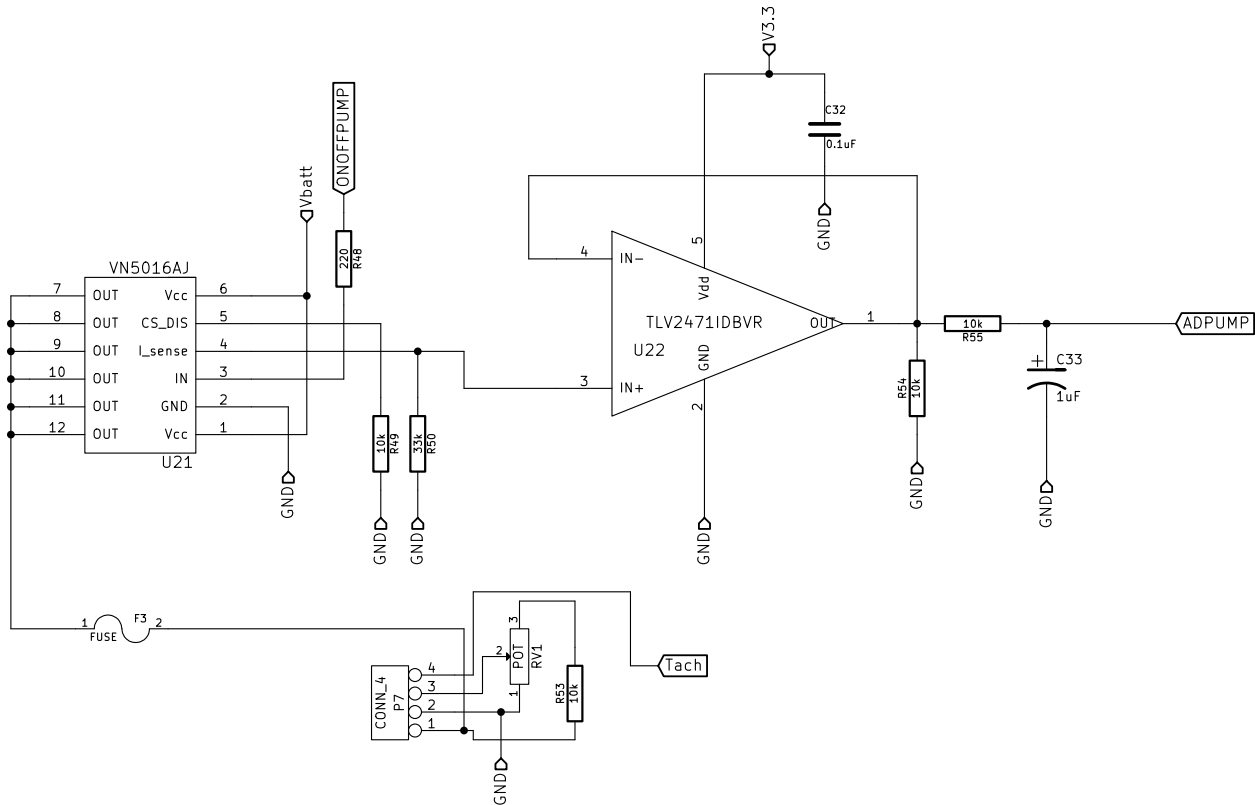


Figure 5.34: Pump power and adjustment for communication node main boards

Data communication to and from the Gascard occurs by means of a 10 pin header which connects the board to the sensor by ribbon cable. Communication with the microcontroller is translated through a Texas Instruments MAXRS3222 multichannel RS-232 line driver/receiver integrated circuit which translates the serial output of the Gascard to an asynchronous communication protocol (Figure 5.35). The IC is configured for operation at 3.3 V, using $0.47 \mu\text{F}$ capacitors on the charge pump capacitors. These capacitors are larger than the minimum required by the circuit, but the increased capacitance will reduce ripple current on the transmitter outputs, decrease power consumption, and prevent equivalent series resistance issues. The receive and transmit lines of the serial connection to the microcontroller are connected to the receiver output and driver input on the chip, respectively, and the serial receive and transmit coming from the gascard connect to the driver output and receive input on the chip. A digital input/output line from the microcontroller connects to a shutdown pin on the IC which is pulled down.

selected based on manufacturer recommendations for the associated components. Larger capacitors were chosen to eliminate sustained voltage drops, while the smaller capacitors were chosen to eliminate fast transient noise. A tantalum capacitor was used in applications that required a larger capacitor with low reactance. Multiple decoupling filters are used in series on lines where a wide range of signal noise may be encountered.

5.4 Air Sampling

Samples of the ambient air at the field site are collected by both the small sensor nodes and the large communication nodes. To minimize the power expenditure, the small nodes are set to passively sample the environmental conditions. The large nodes have greater power storage capabilities, so these units sample the conditions by active sampling.

5.4.1 Passive Sampling

The passive sampling method requires the sensor components to be directly exposed to the environment. This poses some potential problems since these components are soldered to the circuit board. Placing an exposed circuit board into the relatively harsh conditions of the field site invites potential issues from moisture causing corrosion, animal life interfering with the fragile components, and damage from collisions. To mediate this problem, it was determined that a plastic housing to isolate the sensor components from the circuit boards and power supply electronics should be constructed. With the solar panel enclosures already selected, the sensors would be placed in such a manner that they would have contact with the environment through holes pre-drilled on the enclosure. These holes are oriented towards the ground to prevent collection of rainwater and moisture. A preliminary plastic housing was designed by the team which would mount on the carbon dioxide sensor and stick out of one of these holes (see Figure 5.42). Expanding on this principle, a more complex plastic housing for individual sensor groups was proposed. To prevent the high tooling expense which would be required to construct over 100 of these relatively complex parts, a 3D printed part was utilized.

5.4.2 3D Printed Parts

Printing 3D parts is a process which “prints” individual layers of polymer on top of one another to produce a three dimensional object. The plastic housing was designed in a program called OpenSCAD, a free 3D computer aided design (CAD) program which renders a 3D object from a script file [95].

The part design is based on simple solids. Individual components of the design are commented within the code. The script used to generate the model can be viewed in the appendix under Listing D.1. A labeled image of the rendered model in Figure 5.36 illustrates these components. The use of simple solids such as a cube and a cylinder are manipulated with basic transformations like translation, rotation, and elongation to form the more detailed part. The bulk of the piece is an stretched cube. A thinner stretched cube is joined on the underside of the part to give enough clearance for the membrane on the CO₂ sensor. Two “stovepipes” are added on the top with a cylinder joined to the original cube and a narrower cylinder cut through these parts. The spacing of these two stovepipes corresponds to two of the pre-drilled holes in the sensor enclosure. Four screw holes are cut with cylinders at points which match the screw holes on the sensor circuit board. The holes have countersinks which keep a flush surface for mounting the part on the inside of the enclosure. A hole is cut on the edge with two cylinders to provide room for an antenna to project through a third pre-drilled hole in the enclosure and a room to allow the a covered vent on the enclosure to have exposure to the outside air, preventing rupture of the seal during pressure fluctuation. The pointed overlap of these two cylinders is cut with a cube to make this edge cleaner. A notch is cut with a cylinder to give room for a support brace nodule inside the enclosure. Areas referred to in the diagram and script as “digs” are cut out with several stretched cylinders and cubes to reduce the amount of material used for the part while still retaining structural integrity. A “lower portion cutoff” was cut from the edge which would be near an inside edge of the enclosure which was designed with a fillet. Since this cut area overlapped with a screw hole, some more complicated cutting was performed on the model near this screw to allow room for the fillet while still providing support for the screw. Finally, a part identified in the script as the “OptionalBox” was added on the underside of the part which is a thin hollow cube that acts as a containment for the parts inside by butting up against the circuit board.

The original plan was to print all of the parts on 3D printers owned and operated

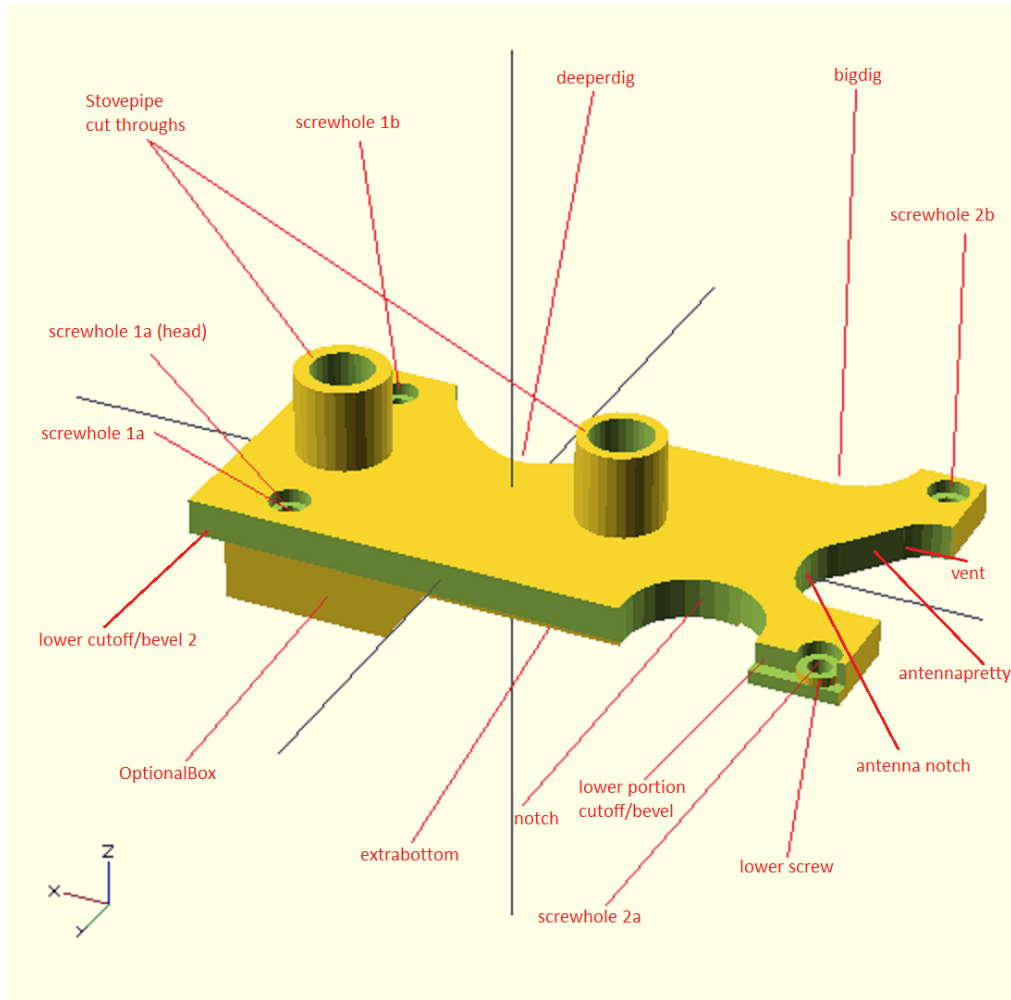


Figure 5.36: Rendering of plastic housing with component labels used in the OpenSCAD script. Naming convention carried over from shorthand used in code.

by Oklahoma State University. An early version of the model was printed on a MakerBot 2 using fused deposition modeling of softened polylactic acid (see Figure 5.37). The unit specifications list layer resolution of $100\ \mu\text{m}$ for the MakerBot 2.

Analysis of the printed object with a 10x magnification loupe show that the part which was printed by the university actually appears to have a $200\ \mu\text{m}$ layer resolution in the XY dimension (see Figure 5.38) and in the Z dimension (see Figure 5.39), with respect to orientation of the printed object on the build platform. A model was ordered from an outside source, i.materialise, to compare quality. The model from i.materialise was printed on an EOSINT P 700 by selective laser sintering of polyamide granules. The manufacturer

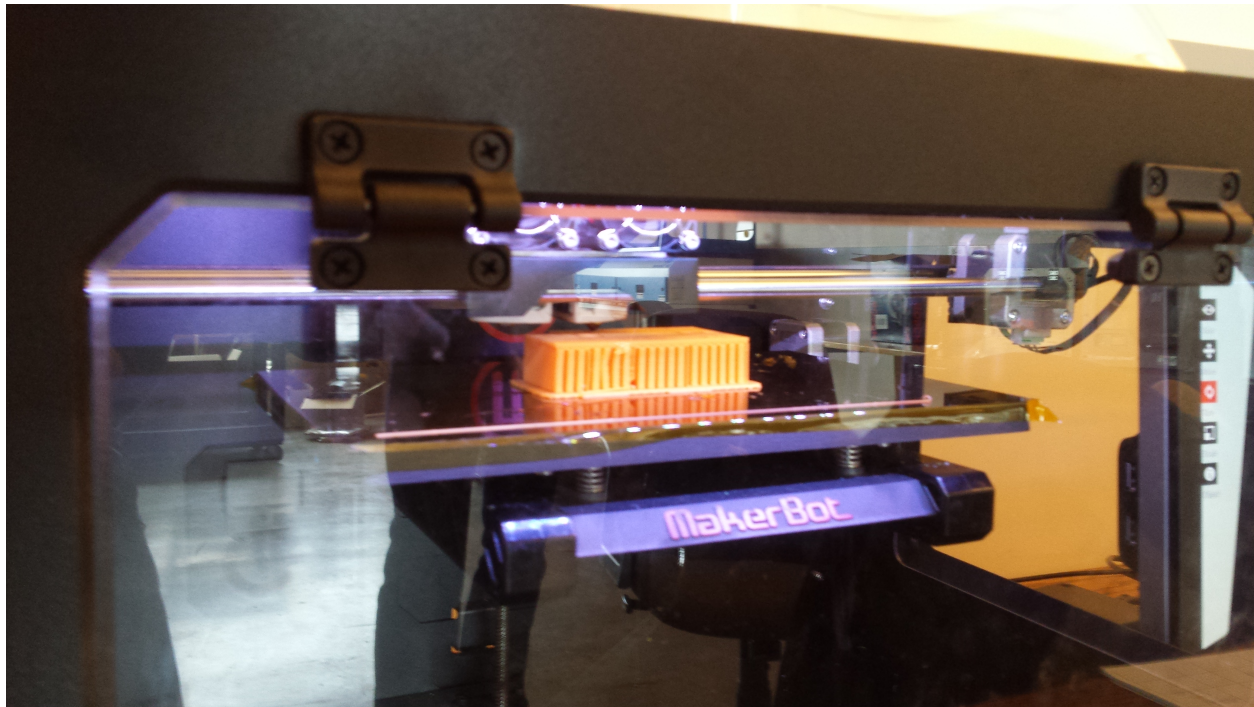


Figure 5.37: An early attempt at producing the 3D part on a Makerbot 2 3D printer.

specifications for this printer also claim a $100\ \mu\text{m}$ layer resolution, depending on the source material used. Analysis of the surface of the object under the same 10x loupe showed a much more amorphous surface. Photographs were taken comparing the surface in the same areas examined for the MakerBot 2 produced unit (see Figures 5.38 and 5.39). In these images, it is much more difficult to distinguish defined layers, and the surface has less intense surface deformation. The final order of the 3D printed parts was ordered from i.materialise due to the preferable ‘cleaner’ appearance.

The part is screwed into 3/4” standoffs which provide clearance from the board and sensors (see Figure 5.43). An isolating enclosure for the temperature and pressure sensors is mounted flush against the PCB and the void is filled with an epoxy potting compound. Enough of the potting compound is injected into this hole to cover the leads of the pressure and temperature sensors within without overfilling and preventing these sensors to operate. This effectively seals the sampling areas which are exposed to the environment, off from interior of the enclosure. No potting compound is necessary for the carbon dioxide sensor, as the extra bottom added to the cube compresses the outer edge of the membrane on that sensor and forms a satisfactory seal (see Figure 5.44). When the combined sensor circuit

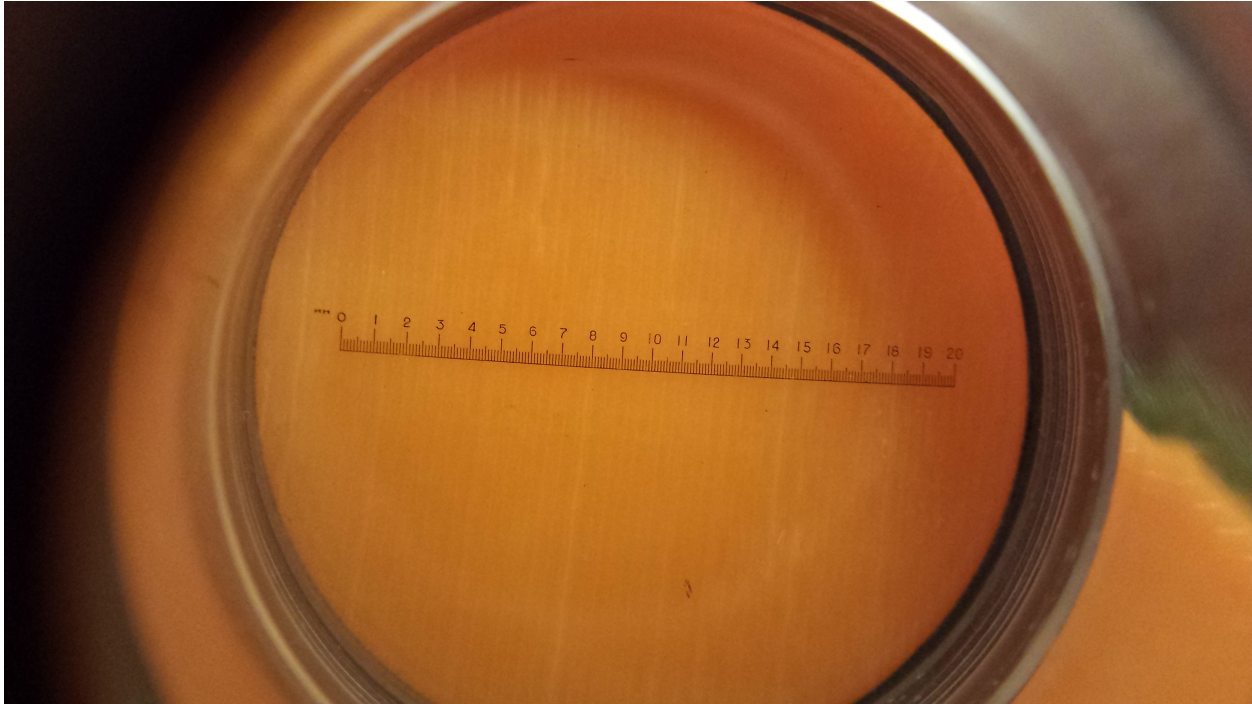


Figure 5.38: Flat mounting surface of part printed on MakerBot 2 on 3D printed part surfaces under 10x magnification loupe. Primary tick marks on ruler denote 1 mm increments, and the secondary tick marks denote 100 μm increments.

board and plastic part are attached to the enclosure, a small amount of silicone is applied to the flat surface of the plastic part, and the piece easily slips into the correct position on the enclosure (see Figure 5.45). Due to problems with small invertebrates making homes in the sensor holes during the prototyping phase, a 1 mm mesh screen is glued over the holes before the unit is deployed.

5.4.3 Active Sampling

The larger power reserves in the communication nodes allow active sampling of the environmental conditions. A Thomas 1410D/2.2/E/BLDC diaphragm pump pulls air from outside of the controller through a hole on the underside of the enclosure, through a 0.45 μm particle filter, to the pump diaphragm. Air is pushed out from the pump to a small plastic housing with the sensors that are used on the node sensors, then through the Gascard, and finally vented outside the enclosure. Since it was essential to use the same sensor board in the communication node as is used in the sensor nodes to enable direct comparison of results,

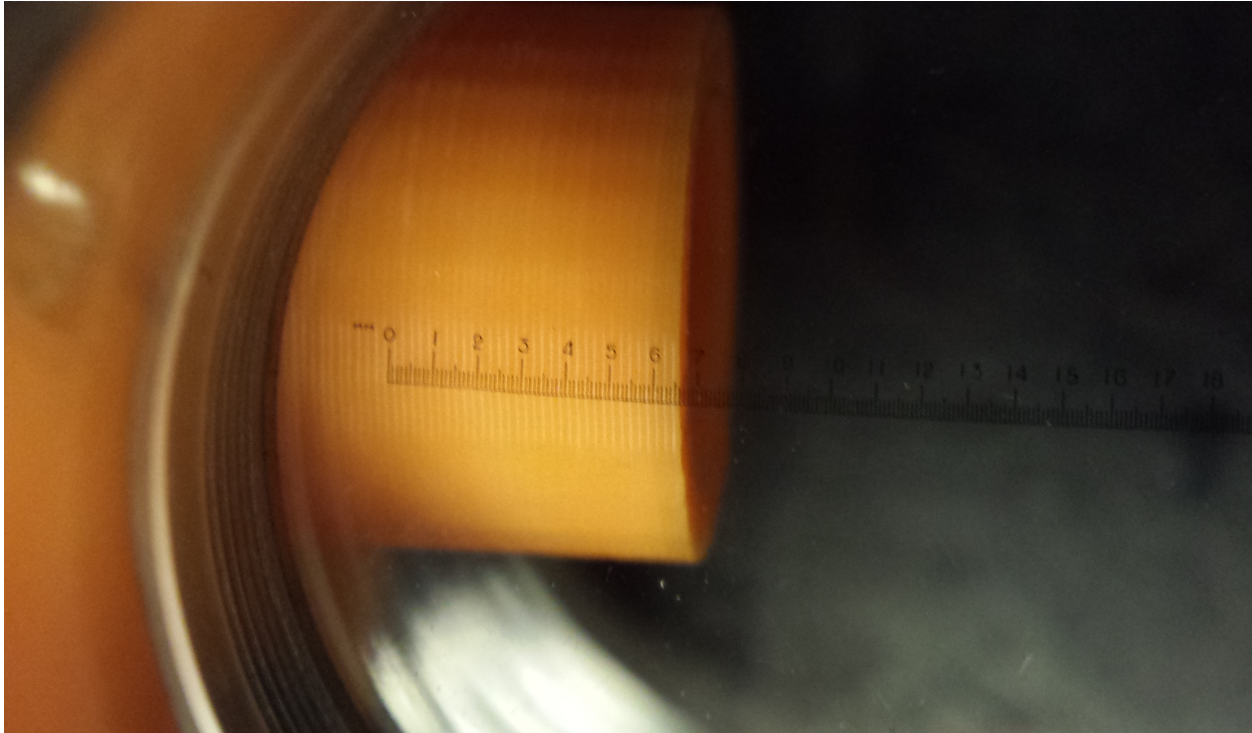


Figure 5.39: ‘Stovepipe’ surface of part printed on MakerBot 2 on 3D printed part surfaces under 10x magnification loupe. Primary tick marks on ruler denote 1 mm increments, and the secondary tick marks denote 100 μm increments.

special consideration was needed to adapt the passive sampling sensors for the flow mode in units with active sampling. To do this, a plastic housing was designed to hold the sensor board (see Figure 5.46).

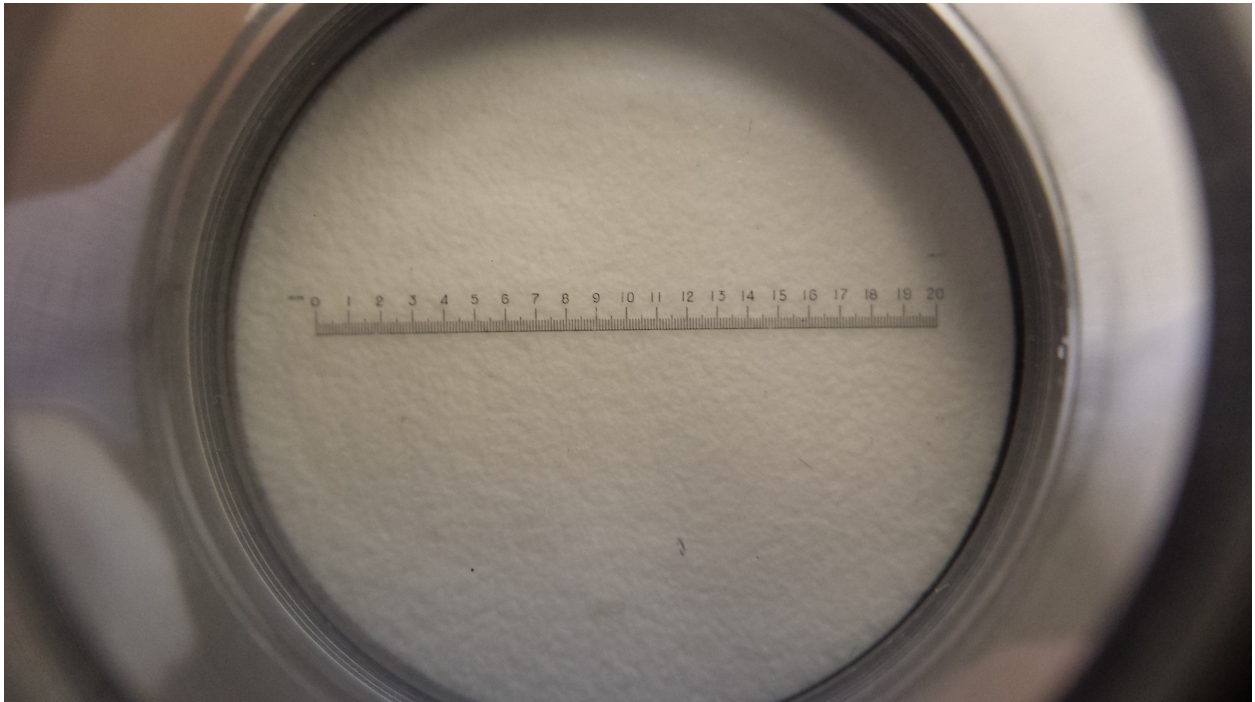


Figure 5.40: Flat mounting surface of part printed on EOSINT P 700 on 3D printed part surfaces under 10x magnification loupe. Primary tick marks on ruler denote 1 mm increments, and the secondary tick marks denote 100 μm increments.

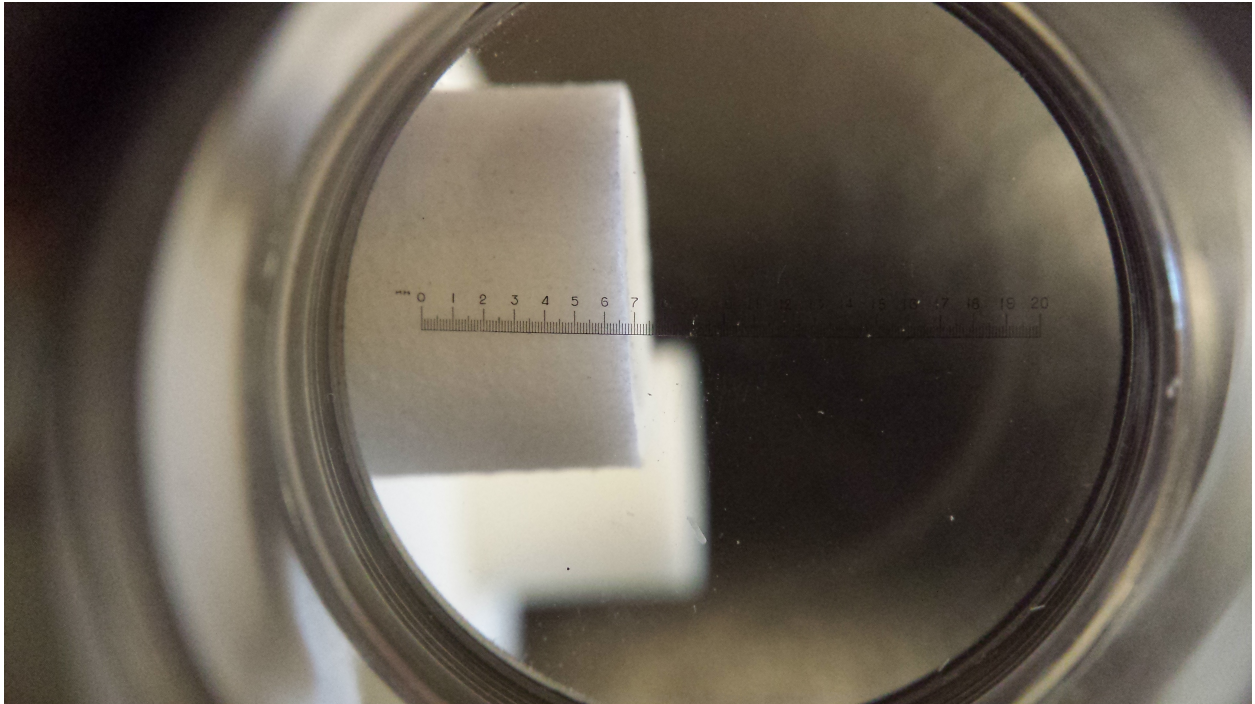


Figure 5.41: ‘Stovepipe’ surface of part printed on EOSINT P 700 on 3D printed part surfaces under 10x magnification loupe. Primary tick marks on ruler denote 1 mm increments, and the secondary tick marks denote 100 μm increments.

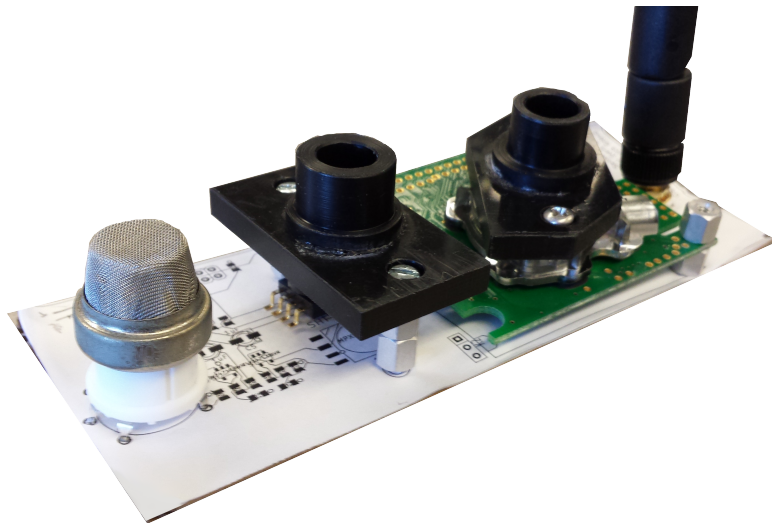


Figure 5.42: Early prototype of plastic parts to isolate and protect sensor components.

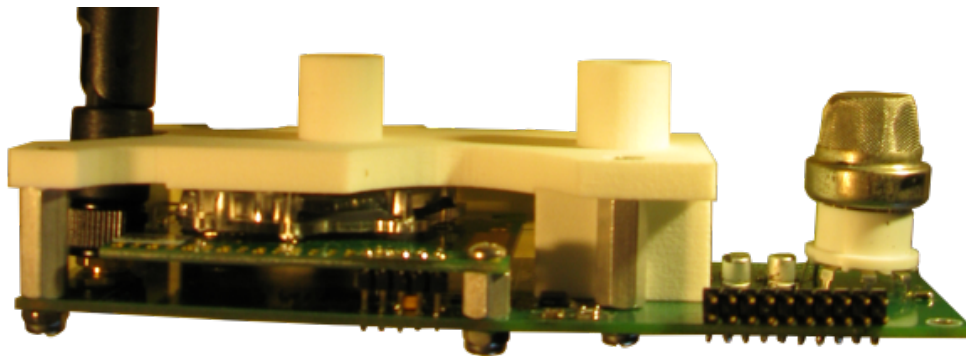


Figure 5.43: 3D printed part attached to the standoffs on the sensor board, showing the flush interface with the board and the carbon dioxide sensor.

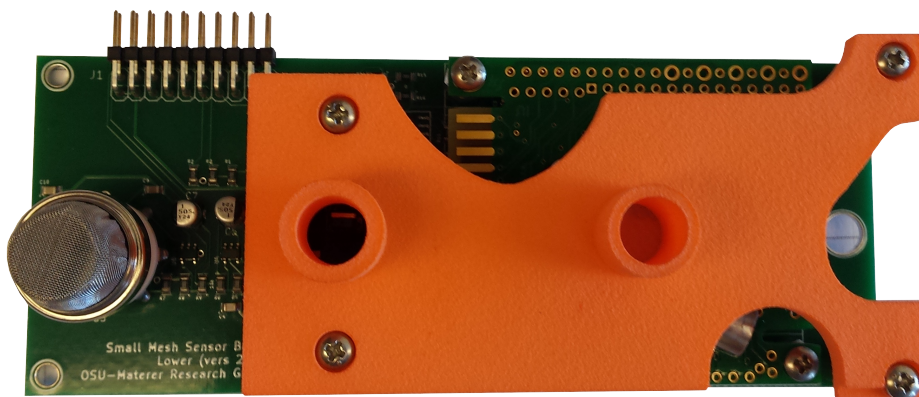


Figure 5.44: 3D printed part with silicone ready to be inserted into the enclosure.

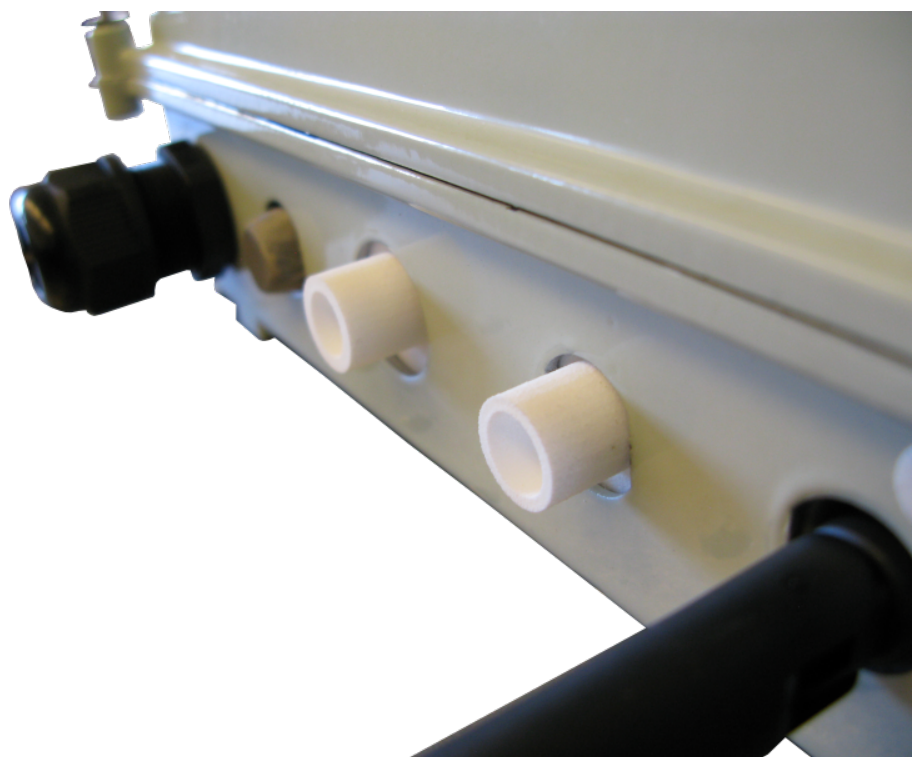


Figure 5.45: The custom part joins the sensor board and enclosure perfectly.



Figure 5.46: Lexan box housing sensor board for use in communication nodes. The box has been sealed from external flow by dichloromethane solvent at the joints.

5.5 Prototyping

Early iterations of the sensor board were based on the Arduino interface circuitry developed during sensor selection. This eliminated the need to develop a communications board before the sensor board as assembly plans were developed. The Arduino setup allowed for the sensor board to be tested for correct operation of each sensor during the development phase and provide quality control for each of the 150 completed sensor board units. To parallel the tests performed in laboratory setting, a series of tests were performed by constructing prototype models to conduct tests for field reliability. The prototypes utilized the completed sensor board, enclosure, solar power collector, and a simplified control board. The simplified control board consisted of an Arduino Mega with a commercially available Assembled Data Logging Shield purchased from Adafruit Industries, LLC. We chose to use Arduino Mega since it is based on the same microcontroller designated for use in the control board. The shield was chosen due to the ample breadboarding area, simple SD card logging, and real-time clock. The breadboarding area of the shield was fitted with a 20 pin interface for the sensor board and a rudimentary DC/DC power converter circuit. Power from the 12 V supply in the enclosure was converted to the 3.3 V required by the Arduino and sensors using one of the DC/DC power converters being investigated for use on the final model. The internal setup of the enclosure is pictured in Figure 5.47.

A second generation prototype was developed replacing the Arduino and shield with a hand-soldered prototype of the final control board. The updated internals of this board can be seen in Figure 5.48. This sensor unit was deployed in a residential section southwest of the Oklahoma State University main campus. These tests showed that the printed circuit board functioned identically to the early Arduino prototype model.

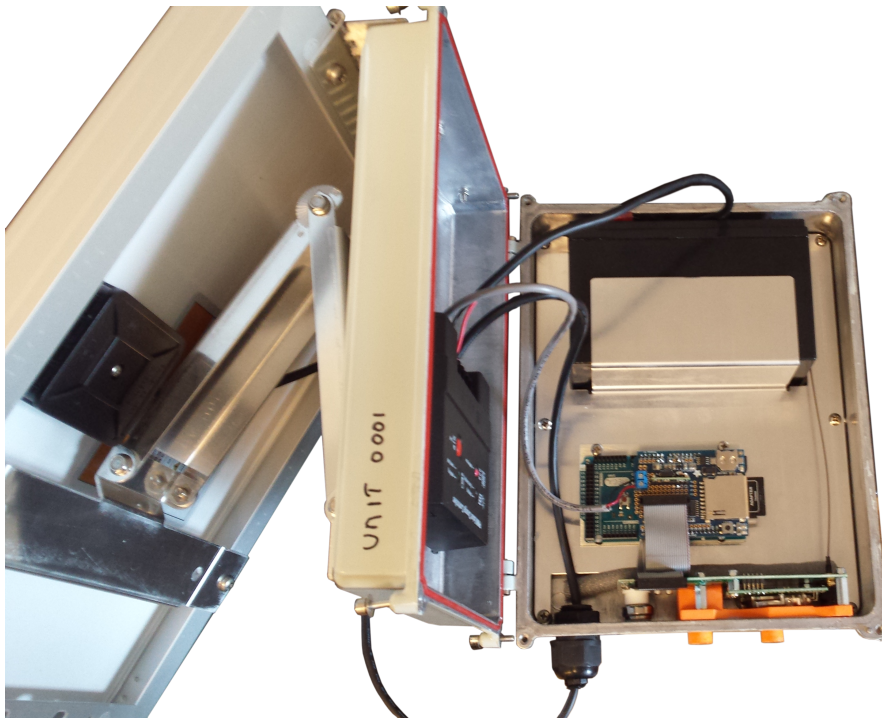


Figure 5.47: Arduino Mega development board with an real-time clock and SD card installed in an enclosure for testing.



Figure 5.48: The completed sensor node was made by replacing the prototyping Arduino Mega with the custom circuit board designed for this project. This shot of the internals shows the detail of the wiring between the components in the case.

5.6 Mass Production

The circuitry for the individual units was produced in stages. The sensor breakout board was printed and assembled early in the first quarter of 2015, the control board for both the communication and sensor nodes was printed and assembled in the 3rd quarter of 2015, and the cellular breakout board was printed early in the fourth quarter of 2015. All printed circuit boards and pick-and-place assembly was contracted through Advanced Circuits in Aurora, Colorado. The sensor boards, being designed first, were the first to be constructed. These completed sensor boards were used during the Arduino prototyping phase so device design would employ the actual sensors. This enabled development and honing of the serial communication with the sensors to and from the microcontroller. The control boards were produced after several developing several prototypes and printed in a single batch. Since the communication and sensor nodes utilize the same control board with different parts filled in, these boards were printed in a single batch. The pick-and-place assembly of parts was done as two separate orders. The cellular modem breakout board was only printed, due to the small number of parts required, and the simplicity of components. These boards were hand-soldered.

Construction of sensor nodes began in the beginning of the second quarter of 2015. One of the sensor nodes was assembled and documented. Using this documentation, a detailed instruction manual was produced. These instructions are included in Appendix E. The remaining nodes to be constructed, approximately 110 units, were assembled without the control boards by collaborators in the Oklahoma State University Civil Engineering department.

Due to small delays in the prototyping phase of the control board, the partially completed units were stored in the lab used for construction for over two months. Once the control boards were received, plans were made to finish the construction. It was discovered that during this time, all of the batteries had discharged. Multiple chargers were purchased to expedite the correction of this issue. However, the batteries had discharged beyond the chargeable threshold (discussed in detail in Chapter 3), and would require much more expensive charging equipment which neither the Chemistry nor the Civil Engineering department possessed. It was determined to be less costly to purchase all new batteries and recycle the



Figure 5.49: A delivery of control boards from the assemblers.

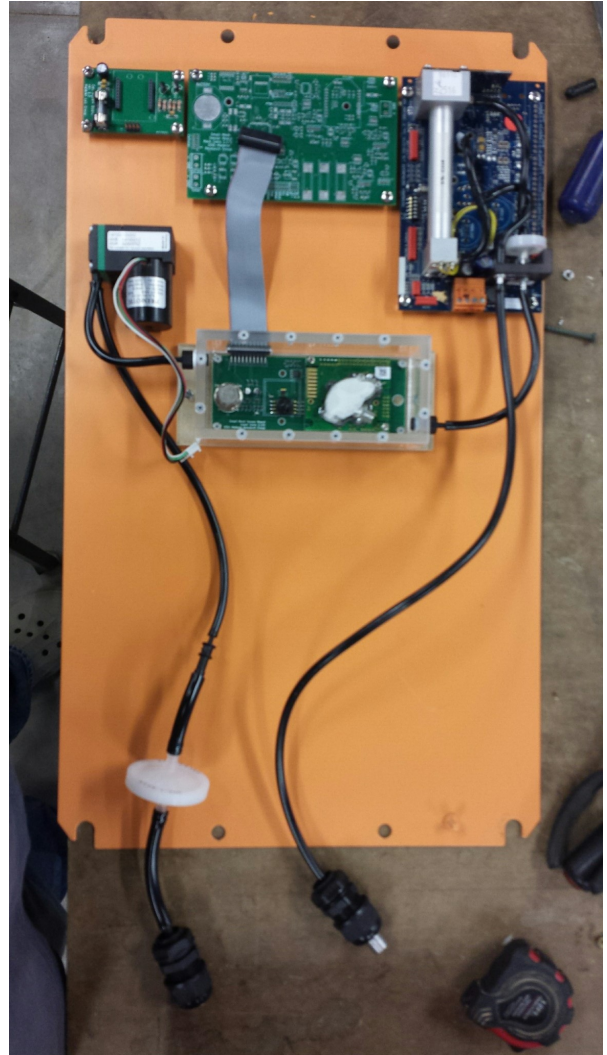
old. Installation of the batteries occurred simultaneously with the installation of the control boards. This final assembly phase was completed in waves of ten units at a time. After the engineers assembled the nodes, the devices were given a quality control inspection and programmed. The programmed sensor nodes were taken to the a proving ground north of campus and mounted on posts in sets of 10 sensor units. Each of these sensor cohorts were networked with one of the prototype communication nodes and allowed to collect data for several weeks. The data produced by the units were analyzed, and any devices producing unsatisfactory results was taken for repair. Analysis of these data are found in Chapter 6. The final cohort was deemed satisfactory in the 1st quarter of 2016.

Construction of the communication nodes began near the end of the 1st quarter in 2015. Clear Lexan boxes were ordered to built by the Civil Engineering mechanical shop to house the sensor breakout board for active sampling (see Section 5.4.3). Circuit boards were mounted to an orange back plate secured within the enclosure (Figure 5.50a). Only the top half of the plate was practical for mounting circuit boards, as the large batteries inside took up half of the volume of the enclosure. Vinyl tubing was used to plumb the unit. Input and output ports for gas were stuck through the bottom of the enclosure to pull gas from a

location with a similar orientation to the passive interfaces on the sensor nodes. The ports were placed on opposite ends of the bottom side of the enclosure to minimize recycling of gas which had already been analyzed. Only three of these large nodes were built at first as the primary goal at this point was construction and testing of the sensor nodes. Originally, the Lexan boxes were designed to easily disassemble in case modifications needed to be made on the sensor breakout board. However, flow testing gas through the box showed that 36.2% of the mass flow of gas through the entire system was being lost. All of the joining edges of the clear plastic on the box, including the edge meant to be disassembled with screws, was sealed using dichloromethane in addition to silicone seals around the ribbon cable connection. Construction on the rest of the communication nodes resumed in late 2015, finishing in the 1st quarter of 2016. Each communication node was tested in the field, much like the sensor nodes, for quality assurance of the units.



(a) The layout of components within the large communication nodes. The batteries take up most of the space inside the enclosure, so components were arranged to be bolted to the top of the back plate.



(b) Behind the batteries, tubing to direct the air for the active sampling is laid. Incoming air is passed through a filter and pumped through the clear box containing the sensor breakout board and the gas card sequentially before exiting the unit.

5.7 Conclusions

The circuits described in this chapter come together to produce an effective set of sensing units. The K-30 and MQ-4 gas sensors described in Chapter 2 have been applied to all units in the network. For added accuracy for methane detection, a Gascard sensor has been added to the Tier 1 Communication Nodes. This allows for the signals detected by the MQ-4

sensors on the network to be compared against a more reliable sensor to quantify potential concentration spikes. The units are powered by switched 12V to 5V DC/DC converters which draw power from the enclosure's solar charged batteries. The AVR processor issues commands to collect and store the data on the EEPROM memory and SD card backup. The processor also handles power management by shutting down power intensive tasks such as the MQ-4's heater during periods of low battery voltage. Communications between units are carried out by an XBee wireless radio with a limited range. Communication nodes also incorporate a cellular modem breakout board which allows for communication of data across 3G cellular networks to a local server. Individual sensors for gas concentration, pressure, temperature, and humidity measurements are incorporated onto a sensor breakout board which is mounted with access to the atmosphere. The atmospheric interface is a passive sampling regime using a 3D printed part to protect delicate electronics for the low level sensor nodes. The atmospheric sampling in communication nodes is an actively pumped regime to allow for the use of the 'flow-only' Gascard, and a special housing is used for the sensor breakout board to allow adaptation to this regime.

These individual parts working in concert allow for low-power operation, independent of human intervention for long periods of time. The sensing devices are separated by sampling regime and location in the units, while wired to the storage architecture to collect the data. The wireless networking capability of the units allows for the transfer and coordination of data as outlined in Chapter 4.

Devices have been produced in quantities of >100 units. The increased production scale allows for these units to be produced cheaply. The circuit boards and sensor infrastructure were assembled and programmed in batches during the 1st quarter of 2016. The testing of these units will be described in subsequent chapters.

CHAPTER 6

Results of Prototyping Tests and Long-term Tests of a Networked Sensor Array at a Proving Ground on the OSU Campus

6.1 Introduction

During the course of unit construction and further deployment, a single group of sensors was maintained at the proving ground on to the North of the Oklahoma State University campus. As the sensors progressed through the design phase and through several changes in programming, these devices collected data from the environment. These units monitored the area without any controlled gas test, and this data was used as a control set.

6.2 Preliminary Deployment and Unscheduled Mechanical Stress Testing

Originally, four of the prototype units were mounted on steel T-posts and deployed in a 4 yd. square North of the Oklahoma State University main campus, see Figure 6.1. The units have demonstrated resilience against extreme weather and wildlife in the area. Data from the unit were collected on SD cards at intervals to monitor the sensors for power failures and abnormal behavior of the sensors. The prototypes in question were simple sensor boards with Arduino Mega data collection equipment described in Chapter 5.

6.2.1 Detected Events

The relatively heavy power consumption of the prototype units forced the sensors during certain periods with heavy cloud cover as is apparent in Figure 6.2. After a sufficient



Figure 6.1: Field testing in a 4 yard square north of the OSU campus.

voltage was detected in the battery, the unit would power back on and resume collecting data. An interesting spike in the concentration of carbon dioxide can be observed on the night of June 3rd. During a routine check of the data by manually removing the SD cards due to lack of wireless capabilities in the prototype models on the morning of June 4th, a pile of deer droppings was noticed and logged in front of Sensor 0004. It is speculated that the concentration spike is due to the presence of grazing wildlife very near the units. This suggests that the devices are sensitive respiration of local wildlife.

In Figure 6.3, there is some overlap in detection periods by the two sensors. This illustrates one of the strengths of a distributed array. The methane sensors used in this test were uncalibrated, and values represent an arbitrary level of methane which is assumed to be constant in the air for sensors spaced so close to one another. While the methane results showed the large amount of error expected, the team was pleasantly surprised to see that the average of all detected values and the linear best fit line were so similar in each unit, indicating that the sensor will still be valuable for assessing methane concentration as averaged over a moderate amount of time.

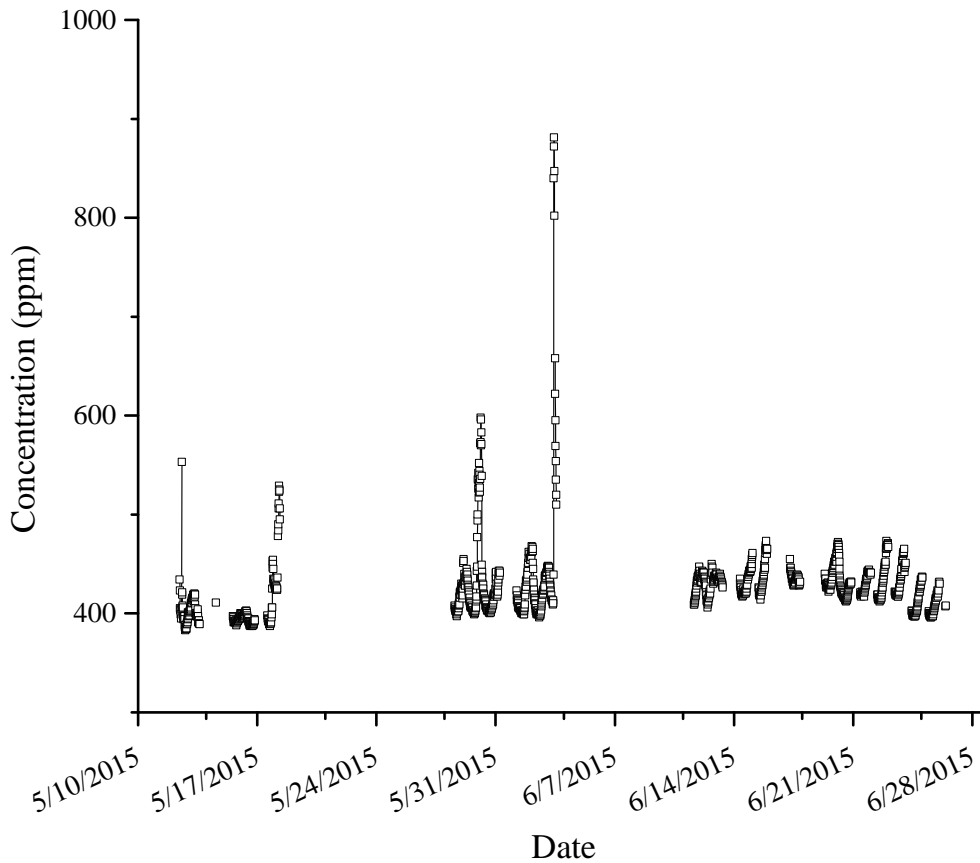


Figure 6.2: Carbon dioxide detection by a prototype unit in the field. Gaps represent power outages. The large concentration spike on June 3rd is likely the detection of local fauna grazing near the sensors.

6.2.2 Storm Damage

During a heavy storm in the early morning hours of September 11th, two prototype sensors incurred damage. The storm included heavy rains and wind gusts of up to 70 miles per hour [96]. At the field site, a large piece of metal debris (the roof of a nearby shed) struck two of the sensor units and caused heavy damage to the units (see Figure 6.4). Two units were unharmed, and the two other units were struck and rendered inoperable in the field. The damaged prototypes were returned to the lab for autopsy and analysis.

The first struck unit, designated UNIT 0003, suffered severe impact damage. The damage to this unit was incurred primarily on the solar panel mounting hardware. Figures 6.5 and 6.6 show detail of the damage. During the impact, the sensor was lifted up, pulling the

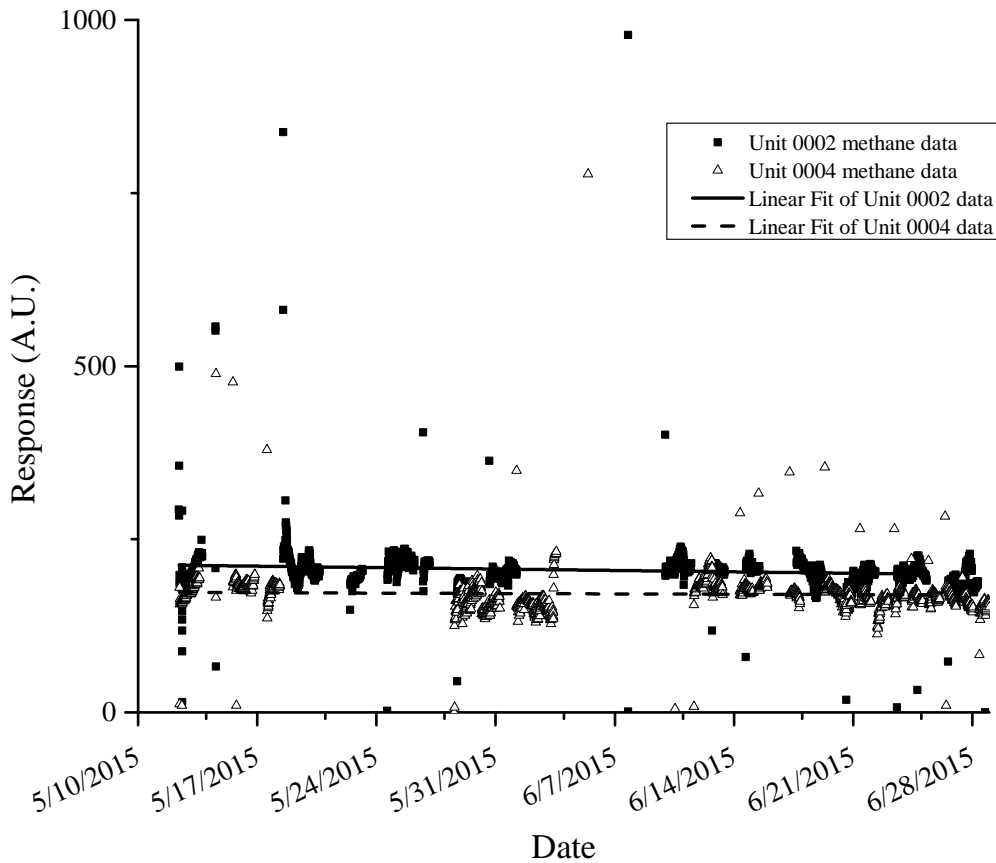


Figure 6.3: Methane detection by two prototype units. The linear fit shown indicates that the averaged methane value detected by the sensors was very stable.

topmost mounting hardware off of the T-post. Curved scratches on the backside of the sensor showed that it dangled for some time by a single mounting part until it was pulled off entirely either by the gusts of the storm or the lever force of the heavy unit being held by a single bracket. The solar panel was rendered inoperable by this damage, preventing recharge of the battery. While this damage appears catastrophic to the sensor, testing of the sensors and prototype board inside showed no damage.

The second struck unit, designated UNIT 0004, sustained less superficial damage. The mounting bracket was loosened by the impact, and the unit slipped down the T-post directly to the ground. This drop damaged antenna, as show in Figure 6.7, requiring it to be replaced. The sensor was not working when it was retrieved. Upon checking the internals, it became



Figure 6.4: Severe damage to prototype sensors at test site after debris strike (seen in background) during gusty weather.

clear that during the event, one of the power supply wires had become dislodged. When this was plugged in, the unit started up with no issues.

While damage incurred by the sensors during the storm caused device failure, it shows the resilience of the manufactured designs. It is not expected that sensors deployed to field sites will regularly undergo impacts by heavy metal objects. The sensors were more than capable of handling “normal” extreme weather events. The devices showed no water damage, and none of the important components were impaired. Furthermore, the unlikely impact showed that the devices were resistant to physical damage, as the enclosures properly protected the delicate internal circuitry.

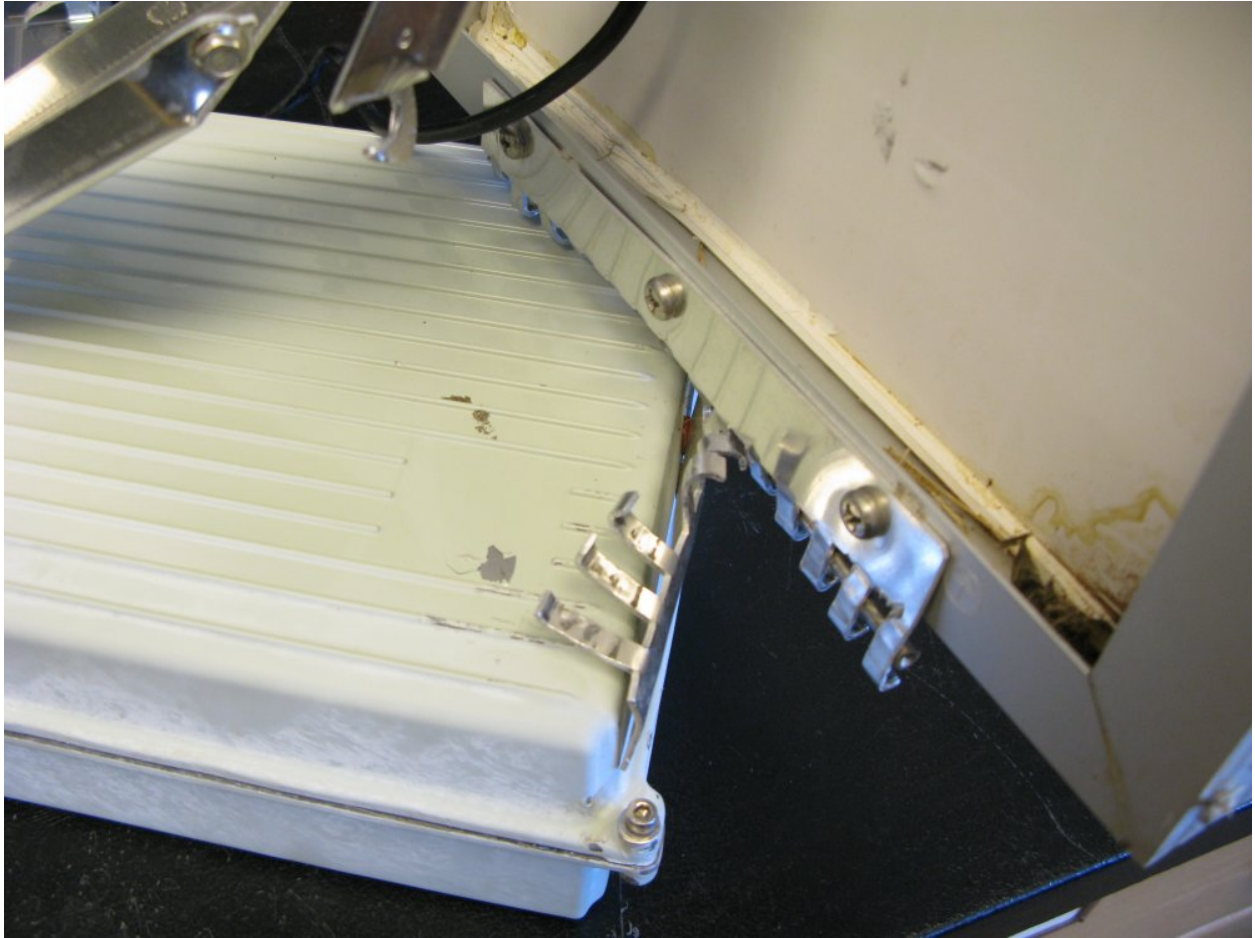


Figure 6.5: Damage to UNIT 0003: This image shows the steel hinge holding the solar panel on the Tycon enclosure has been sheared away by stress during the impact.



Figure 6.6: Damage to UNIT 0003: This image shows the bracket which supports the solar panel on the Tycon enclosure has been ripped by damage incurred during the impact.



Figure 6.7: Damage to UNIT 0004: This image shows the antenna which snapped after the impact. The mud flecks on the downward facing side of the sensor confirms that this sensor was dropped straight to the ground.

6.3 Comparing Collected Data from Long-Term Array against Accepted Weather Report Data

As the mass production of units was completed, a set of 10 sensors was deployed in the same proving ground area as the previous 4 prototype sensors. This new network was dubbed the Long-Term Study array. The units deployed at this site were the first to be completed. The goal of this network is to determine a baseline of the local concentration of carbon dioxide and methane. This site was chosen due to the low number of expected concentration change events due to the relative remoteness of the north campus site and the lack of methane leaking ground sites nearby. Collection of the data from this network is currently ongoing. The data were collected and analyzed during the project to report the efficacy of the network for quarterly reports to the funding agency. It is important to confirm that the devices designed during this project were capable of producing the data which was claimed by our group.

One method of analyzing the control data is comparison with known figures. Collected temperature, humidity, and pressure data were compared against data reported from a local weather station [97]. Data collected from an archive of reports from the KOKSTILL4 was collected and the values of the maximum, minimum, and average reported temperature, humidity, and pressure were extracted from the data set. These values were plotted as three lines over plots of the individual detected values of all of the sensors. The temperature and humidity data, shown in Figure 6.8 and Figure 6.9 respectively, are very similar to the weather station data. The sensors show a very regular cycling of these values, corresponding to the day-night cycle. The peaks and troughs of this cycle match closely with the minimum and maximum weather station data. The plot of pressure data (Figure 6.10) differs, in that the weather station data and the test data seem to be offset. The altitude of the KOKSTILL4 station (935 ft. above sea-level) does not differ enough from the test site (944 ft. above sea-level) to suggest that there would be a significant difference in pressure due to this. It is possible that there is some minor variation between the pressure in the two locations, approximately 2 miles apart. The sensor used by the weather station may also be inaccurate, there is no published calibration data for this station. It is also possible that the pressure sensors used by the sensor nodes are incorrect. Due to the large number of sensors involved,

this is improbable.

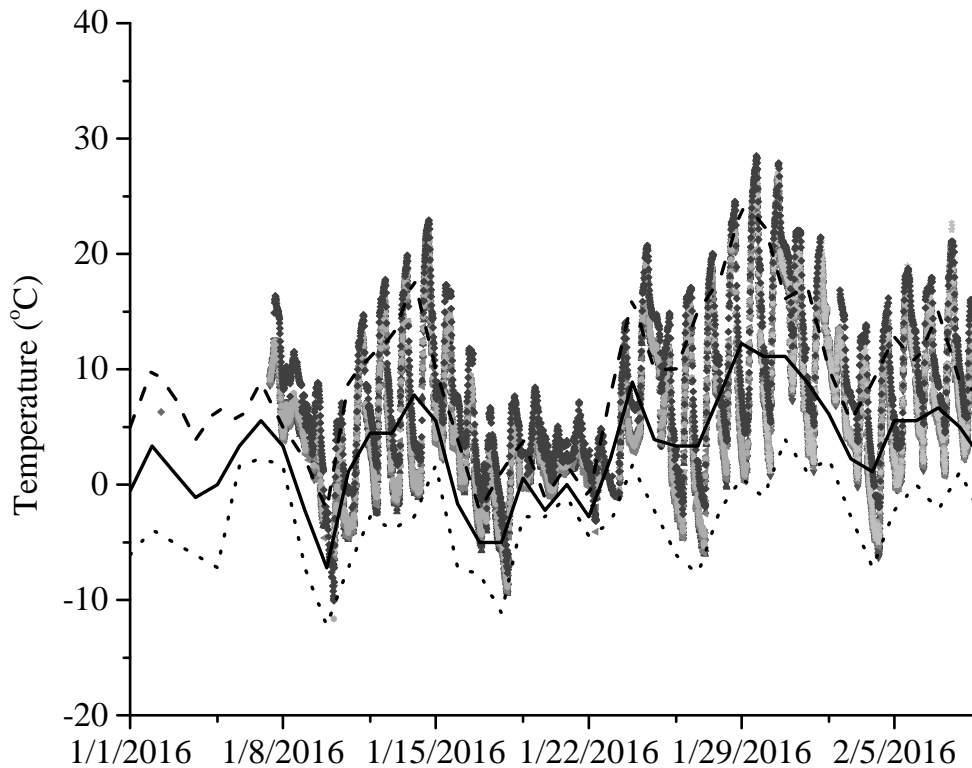


Figure 6.8: Temperature data collected from test sensors tracks with the reported weather data. Diurnal cycling is apparent. Weather data is from KOKSTILL4 weather station [97]. The dashed line and dotted line are the maximum and minimum value observed for each date, and the black line is the average value observed for that date.

As there is no local reporting agency for gas concentrations, validation of the values reported by the sensors is not as simple. Instead, the data were considered good if those reported by each sensor tracked well with the other sensors in the network. Data were collected from the sensors in the long-term study array and compared against the others in the same network. By visual analysis, shown in Figures 6.11 and 6.12 it can be seen that the reported values tracked well among the units. There is some variation between the units, as the sensors were uncalibrated. Yet, the diel cycle of concentrations track well between units. The average of the reported concentration of each gas is reasonable for the site location,

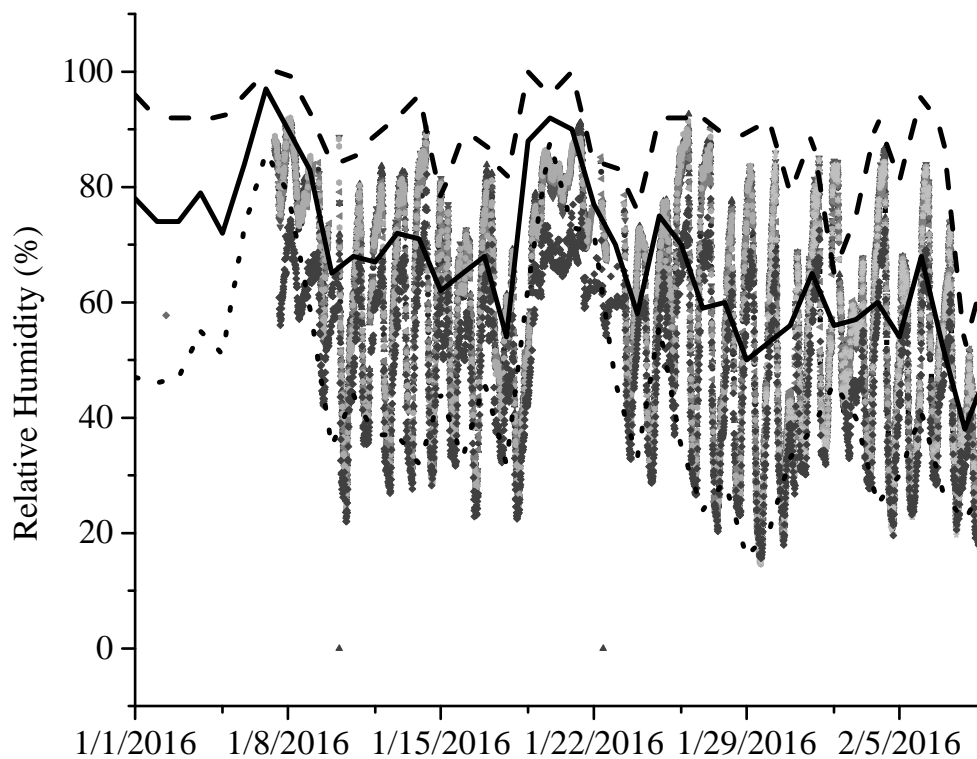


Figure 6.9: Humidity data collected from test sensors tracks with the reported weather data. Diurnal cycling is apparent. Weather data is from KOKSTILL4 weather station [97]. The dashed line and dotted line are the maximum and minimum value observed for each date, and the black line is the average value observed for that date.

based on reported background concentrations discussed in Chapter 1. The results from this study suggest that the use of a networked array of sensors can produce an acceptable single value for the local gas concentration by the law of averages.

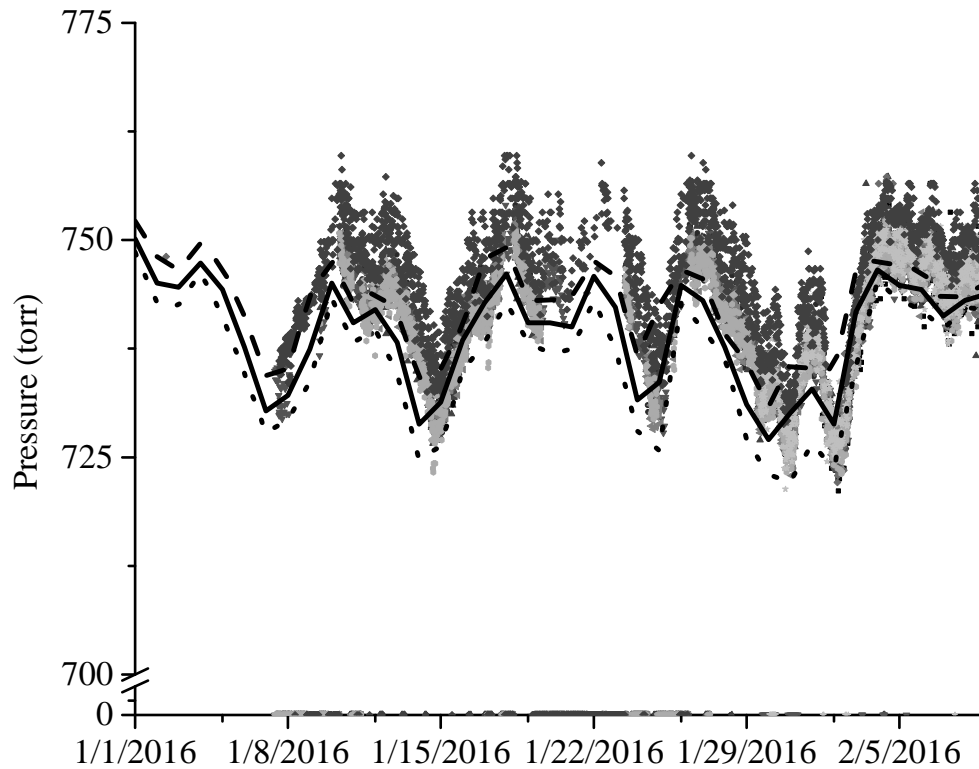


Figure 6.10: Pressure data collected from the test sensors is acceptably precise yet consistently lower than the reported weather data. This may indicate deviation of the sensors from the true value, local variation in pressure, or an inaccurate report from the weather station. Weather data is from KOKSTILL4 weather station [97]. The dashed line and dotted line are the maximum and minimum value observed for each date, and the black line is the average value observed for that date.

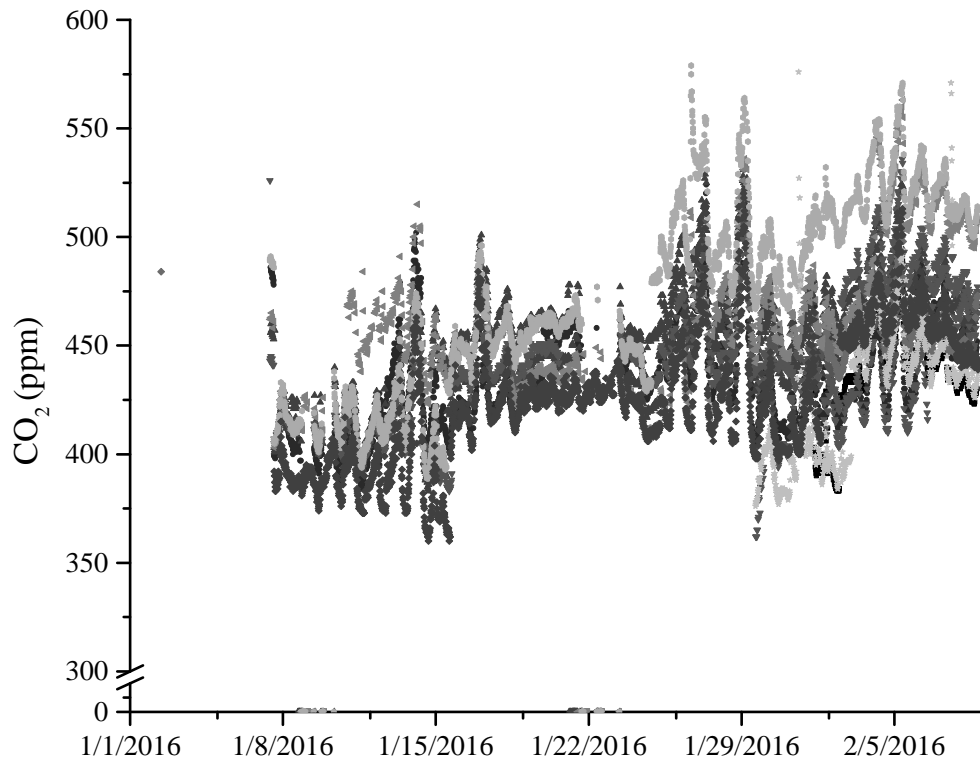


Figure 6.11: This plot shows carbon dioxide the data collected by the sensors in the long-term study network. The values reported by individual sensors vary somewhat (shown in gray), but they all follow similar patterns during the day-night cycle. The black trace shows the average value reported by all sensors in the network.

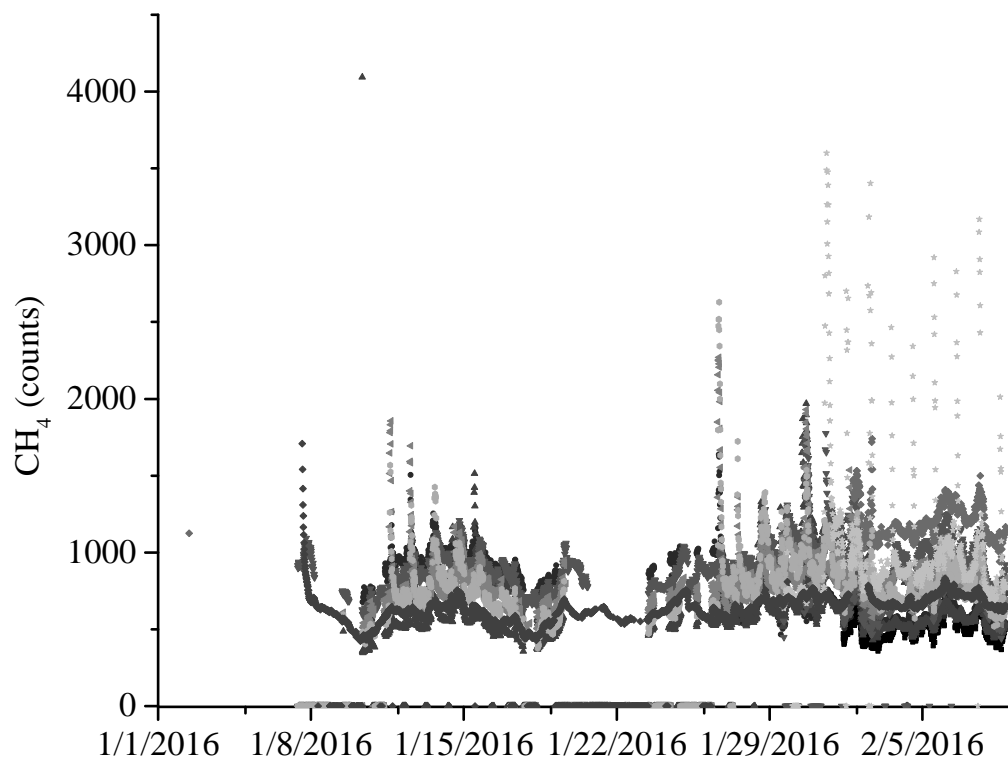


Figure 6.12: This plot shows methane the data collected by the sensors in the long-term study network. The values reported by individual sensors vary somewhat (shown in gray), but they all follow similar patterns during the day-night cycle. The black trace shows the average value reported by all sensors in the network.

6.4 Conclusions

The scale up of the proving ground site on the north side of the Oklahoma State University Stillwater campus from prototyping site to long-term study site shows valuable information about the capabilities of the sensor network. In one fortuitous observation, devices were shown to be able to detect small local concentration changes due to outside variables such as local wildlife. This suggests that the sensors are sensitive to small, local changes in gas concentration. Furthermore, it suggests that the time-scale on which the sensors are programmed to operate is sufficient to detect short term events. In another serendipitous experimental incident, the sensors were also shown to be capable of withstanding dangerous weather. Sensors struck by debris during extreme weather conditions were shown to have endured very little serious damage. Issues affected by this event were simple to repair. If similar incidents are encountered in the future, it is reasonable to assume that damage will be field-repairable. Finally, the long-term study can provide a reasonable baseline for the local area, and the data are shown to track well as a group. Application of accepted data from local weather stations allowed for facile verification of the device capabilities. All sensors deployed in this group were shown to produce data reasonably close to these accepted values. The results from this proving ground lend credence to the successful deployment of the sensors at other test sites.

CHAPTER 7

Results of Data Collected Tests from a Networked Sensor Array at the OSU Unmanned Airfield

7.1 Introduction

A second testing site was selected at the Oklahoma State University Mechanical and Aerospace Engineering's Unmanned Aircraft Systems (UAS) Airfield. This site, located approximately 16 miles east of the main Stillwater campus, is one of the few locations owned by a university which permits the testing of unmanned aerial vehicles. The 15 acre tract of land includes a garage, control facility, and polymer mat runway.

The UAS site was chosen for sensor deployment as a source of collaboration between the Chemistry and Engineering Departments on the gas sensing project. A network of sensors developed for this project would be deployed at the site in conjunction with flights of aerial sensors. One of these sensors can be seen in Figure 7.1. The goal of the collaborative project is to simultaneously collect data from the sensors at ground level while a UAV mounted sensor makes a controlled pass of the field from the air. In this way, concentration flux can be modeled in three dimensions, rather than the two dimensions provided by the current network setup. The site, which is managed by the University, is convenient for release testing of analyte gases. To properly conduct these tests, it is necessary to establish background readings for the site.



Figure 7.1: This image depicts one of the Unmanned Aerial Vehicles being researched at the UAS site. This unit includes a carbon dioxide and methane flow sensor mounted in the fuselage. Collaborative efforts are underway to compare the data detected by these aerial units to the units deployed in the sensor array.

7.2 Sensor Network

The sensor network was deployed along the fence line of the site. Metal T-posts were erected in regular intervals along this path. A map of the site and the locations of the sensors can be seen in Figure 7.2. Unlike the network discussed in Chapter 6 which consisted of a single network of sensors, this deployment includes multiple subnets. In Figure 7.2, the individual subnets are color coded. In this way, the network support for multiple subnets could be verified.

7.3 Data Analysis

Data were successfully collected by the sensors in the network, and the data were processed and pulled from the central home server on the OSU main campus. The data were collected over a period of approximately 9 months, and the site is still collecting data as of this publication. During this period, there were variations in pressure, temperature,



Figure 7.2: This Google Maps satellite image of the UAS airfield depicts the approximate locations of sensors at the site. The colored groups depict the individual subnets in the sensor network.

and humidity, as can be expected of an outdoor testing period of this time scale. One of the primary variations which can be quantified is the diel cycle. The data from each sensor were collected and sorted by time of day. A figure representing the range of values reported for these time points can be seen in Figure 7.3. The data from the carbon dioxide sensor shows that the concentration seems to be highest in the early morning hours, and decreases during the day. The opposite is the case for methane, with peak concentration occurring in the middle of the day. This cycle matches with reports on diel concentration flux by various authors and in various environments [98, 99, 100, 101]. The generally accepted cause of these variations is the flux between the ground and flora with the atmosphere. Carbon dioxide levels increase during the night as plants cease to photosynthesize. Methane levels increase during the day as heat from the sun generates flux of gas from that which is stored in the topsoil. Changes in relative humidity also play a role in this cycle by reducing the partial

pressure of carbon dioxide and methane components with respect to the partial pressure of the water vapor.

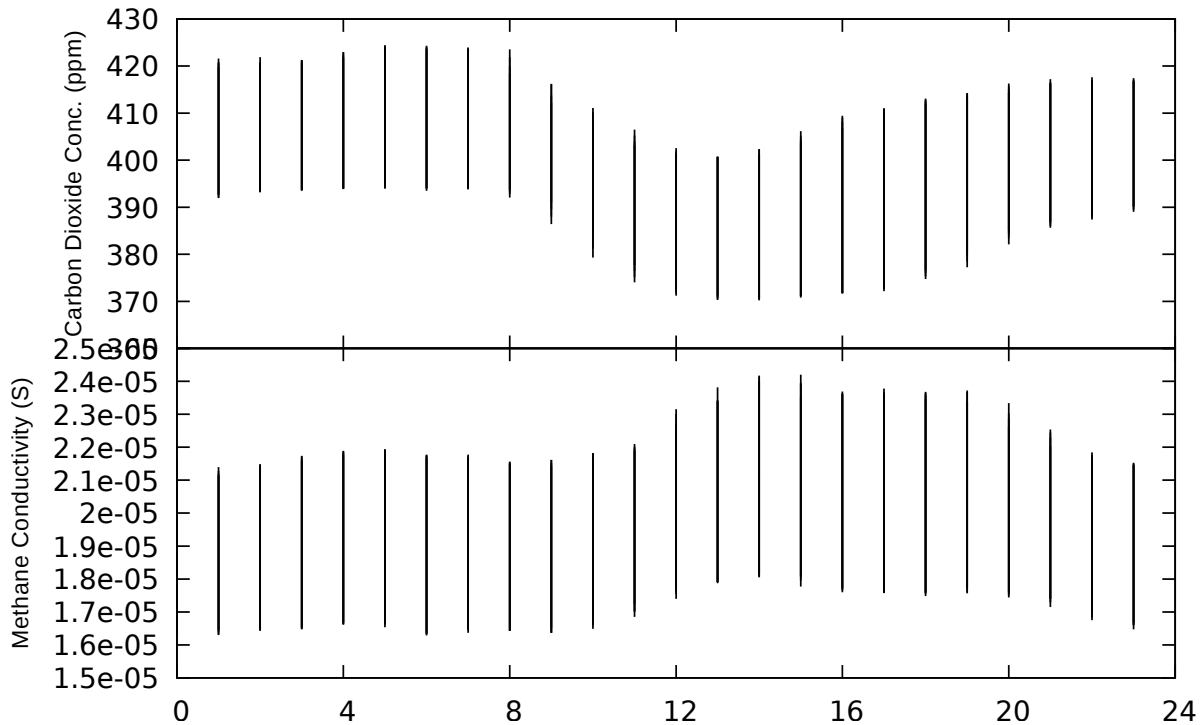


Figure 7.3: This plot shows the range of values recorded during each daily cycle at set time points. The plot shows the concentration changes in the typical day/night cycle at the site.

7.3.1 Carbon Dioxide

When the carbon dioxide concentration traces are stacked in a plot, as is depicted in Figure 7.4, the features of the plots line up nicely. This suggests that the sensors are all functioning correctly. For any large concentration change events, we would expect to see multiple sensors peaks. Peaks which appear in the reported data of a single unit are likely attributable to very localized environmental changes, such as the presence of an animal actively engaging in respiration. One trace has appears to show considerable deviation from the other traces. This unit is suspected to have a malfunctioning multiplier, which increases the intensity of the peaks and valleys of the detected concentrations.

When all of the data collected from the carbon dioxide sensors are averaged, the trace depicted in Figure 7.5 is generated. This plot shows all of the same characteristics as before

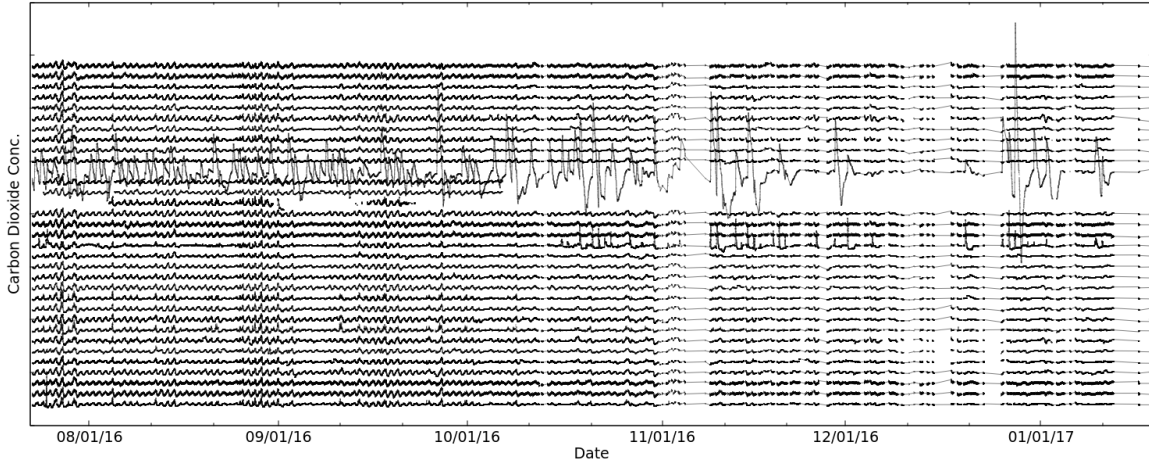


Figure 7.4: Data collected from the carbon dioxide sensors has been stacked in this graph to show the coincidence of peaks in the concentration.

including the diel cycles and any events detected by multiple sensors. From this averaged dataset, we can pull several pieces of information. By plotting all of the values detected by the sensors in single parts per million bins, we can plot a histogram of the values reported by the sensor, as depicted in Figure 7.6. A histogram was constructed of 100 bins with a size of 1.72 ppm. The data plotted on this histogram can be treated as a normal distribution. The peak average is 414 ppm. This is appreciably close to the mean global concentration of carbon dioxide at sea level. There is minimal skew with slight tailing to higher concentrations, possibly due to peak events. The kurtosis metric shows that the normal distribution is weighted more heavily toward the mean.

7.3.2 Methane

When the methane concentration traces are stacked in a plot, as is depicted in Figure 7.7, the features of the plots line up nicely. This suggests that the sensors are all functioning correctly. For any large concentration change events, we would expect to see multiple sensors peaks. Peaks which appear in the reported data of a single unit are likely attributable to very localized environmental changes, such as the presence of an animal actively engaging in respiration.

When all of the data collected from the methane sensors are averaged, the trace depicted in Figure 7.8 is generated. This plot shows all of the same characteristics as before

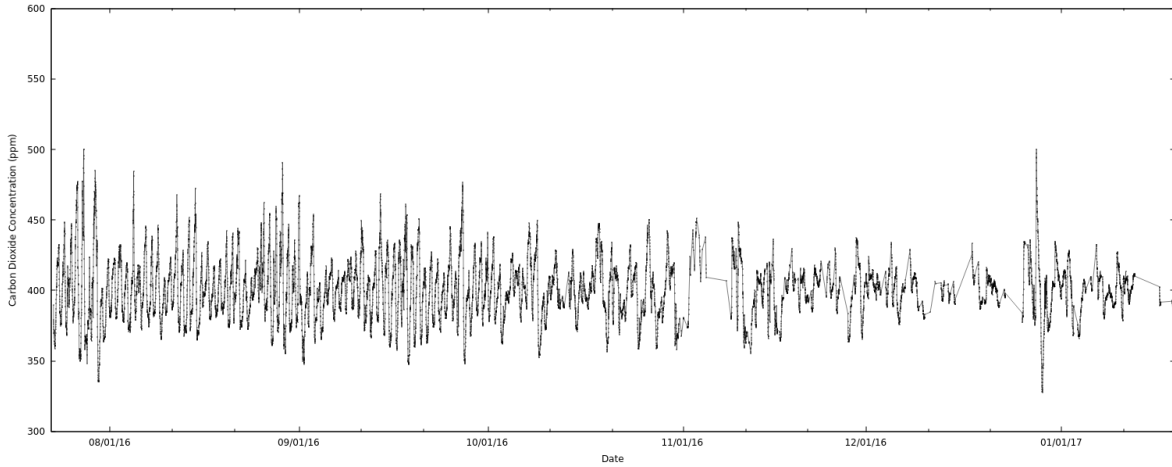


Figure 7.5: The traces from the UAS airfield have been averaged in this graph to show a single line which depicts the average concentration of carbon dioxide at the site.

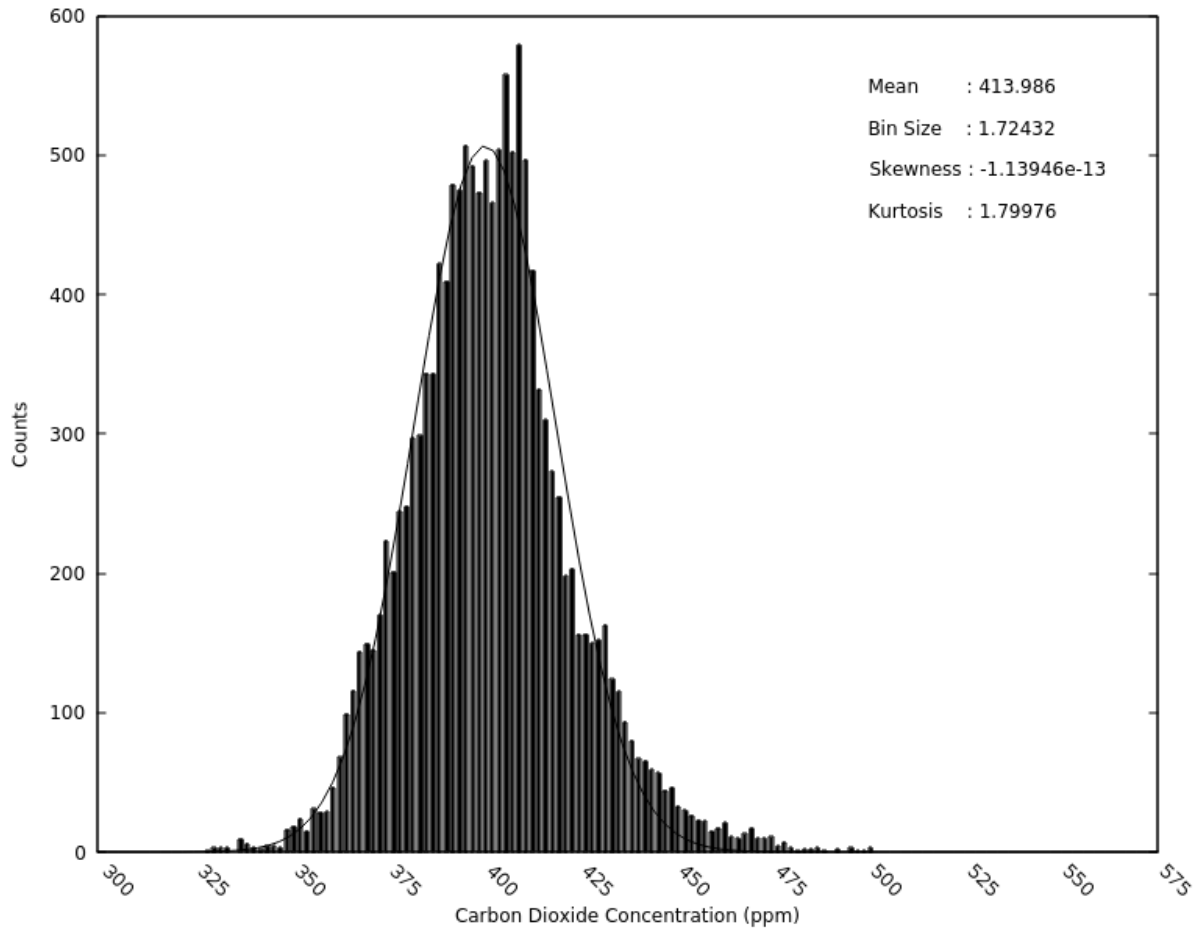


Figure 7.6: The data produced by the carbon dioxide sensors shows a Gaussian distribution.

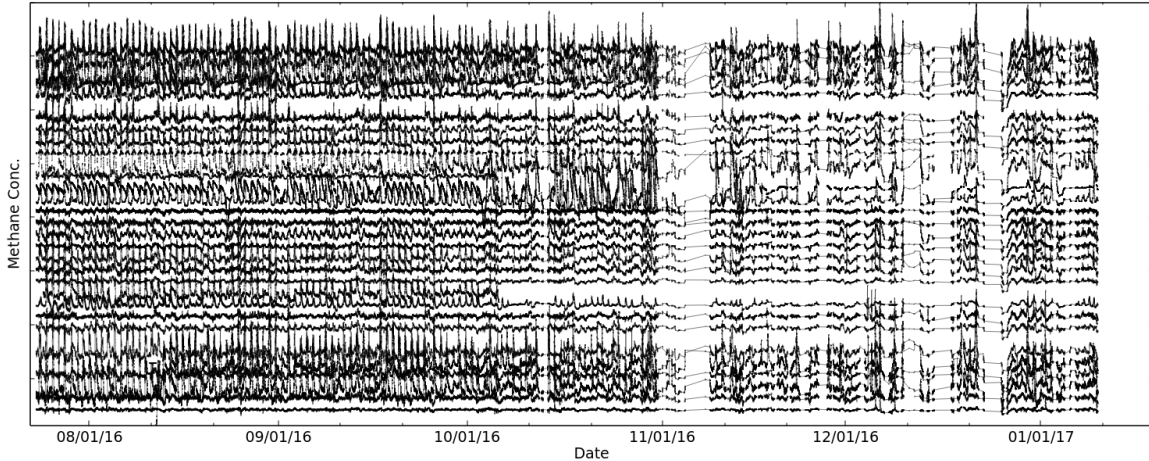


Figure 7.7: Data collected from the methane sensors has been stacked in this graph to show the coincidence of peaks in the concentration.

including the diel cycles and any events detected by multiple sensors. From this averaged dataset, we can pull several pieces of information. By plotting all of the values detected by the sensors in 10S bins, we can plot a histogram of the values reported by the sensor, as depicted in Figure 7.9. A histogram was constructed of 100 bins with a size of 4.38×10^{-7} S. The data plotted on this histogram can be treated as a normal distribution. The peak average is near 1.98×10^{-5} S. Since these sensors have not been accurately ascribed a calibration curve, we can only take note of the shape of the normal distribution. The peak is Gaussian with tailing to higher gas concentrations. This suggests that while most of the reported values from the sensors fall within a small window, there are several events which cause this skew. The kurtosis metric shows that the normal distribution is weighted more heavily toward the mean.

7.3.3 Peak Events

By applying some statistical analysis to the average of all sensors on the network for both carbon dioxide and methane, we can determine when peak concentrations were detected. These ‘Events’ were selected by determining if a value was greater than two standard deviations above the average. This selection method removes the natural variation in the diel cycle from generating a false positive. If we plot these events and their respective concentrations against time, we can look for patterns, this plot is shown in Figure 7.10. Some

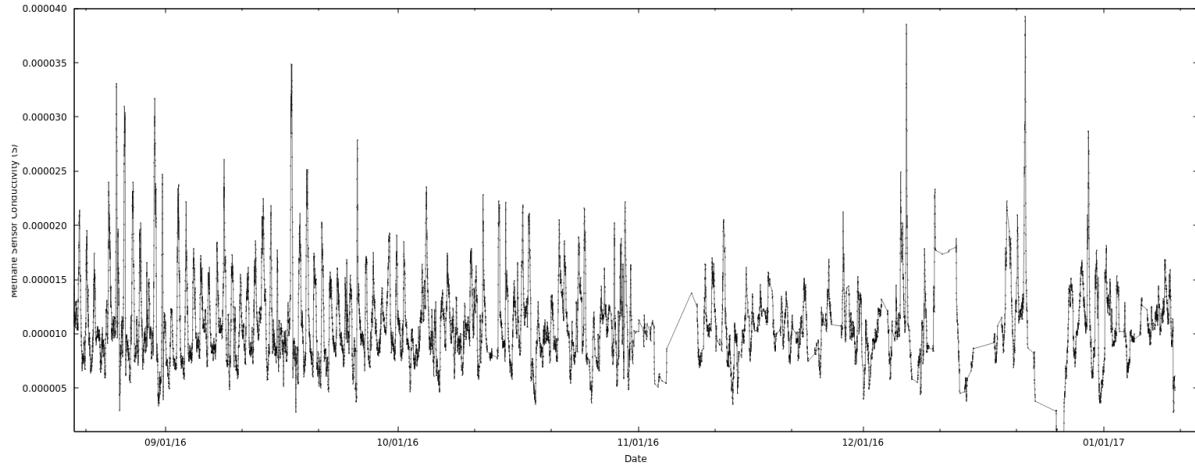


Figure 7.8: The traces from the UAS airfield have been averaged in this graph to show a single line which depicts the average concentration of methane at the site.

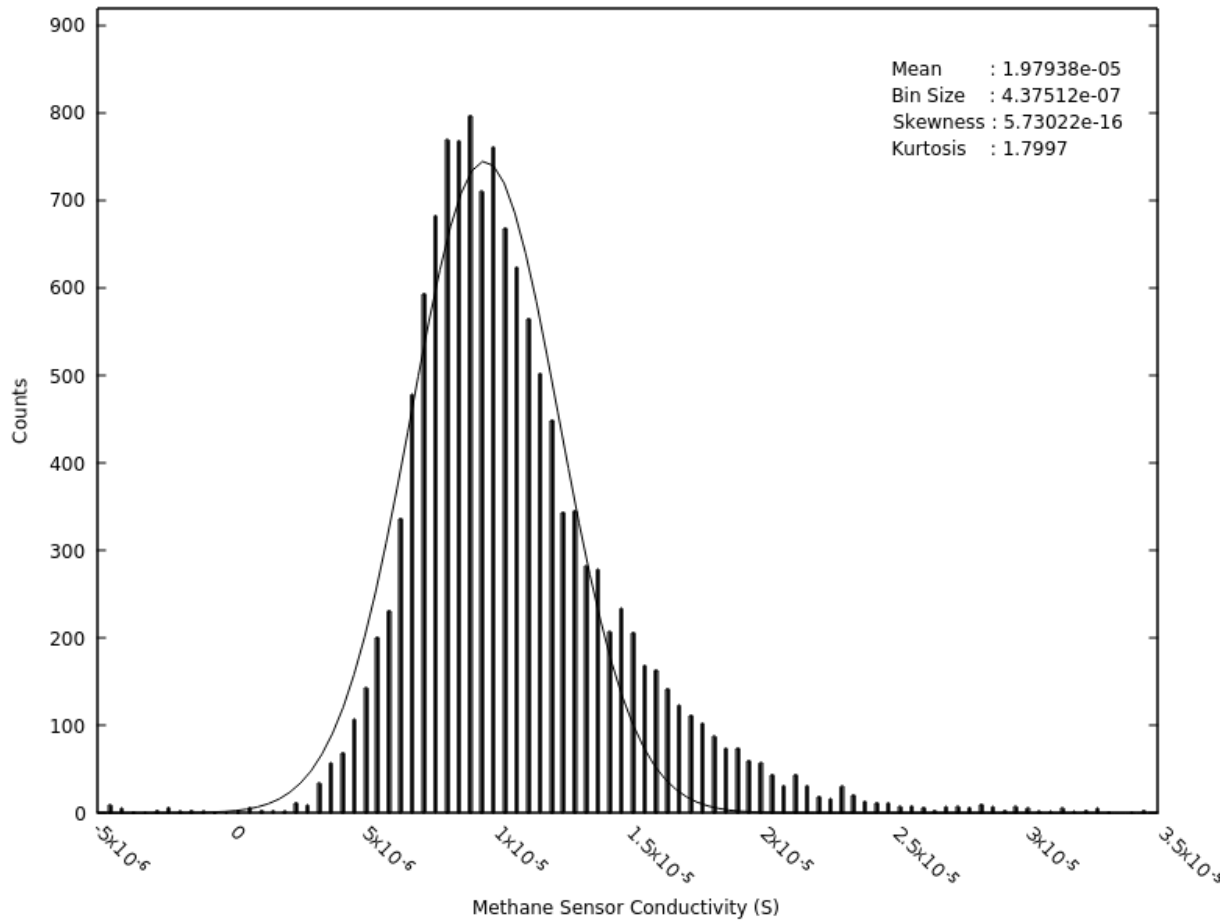


Figure 7.9: The data produced by the methane sensors shows a Gaussian distribution.

of these detected events, such as those early in the reported data, can be ruled out. Those peaks are likely due to human proximity to the sensors during transport and deployment. Few of the selected events occur at similar times. It would be a simple matter of analysis to say that these events are unrelated and occur during the peak times for each respective gas. No causal link to any source has been established for these events.

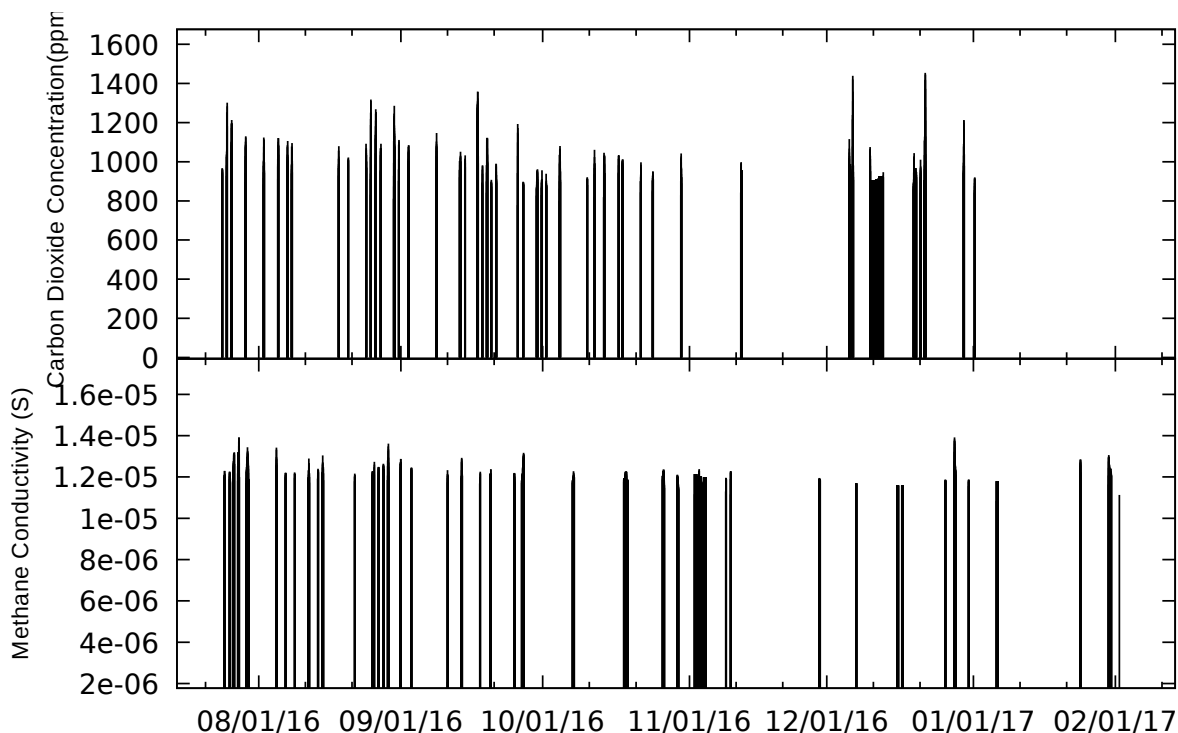


Figure 7.10: This plot shows the recorded events at the UAS site. Events were selected as points which were 2 standard deviations higher than the average at that time of day.

7.4 Conclusions

By setting up a field site near Stillwater, OK at the UAS airfield, the project members have greater access to the equipment to perform experiments. In establishing a baseline for these future experiments, we can see that the sensor networks report both carbon dioxide and methane concentration within expected diel cycling regimes. The carbon dioxide concentration at this site is higher than expected compared to the global average. By analyzing the average concentration detected by the sensors, we have been able to single out peak concentration

events which occurred during the data collection period. These events do not appear to be correlated the companion analyte gas.

CHAPTER 8

Results of Data Collected from a a Networked Sensor Array near a Gas Injection Well Field Site near Farnsworth, TX

8.1 Introduction

The ultimate test of the networked sensor array was to deploy it at a real injection well site. A location was selected in the panhandle of Texas near the town of Farnsworth. The site has been well characterized by geologists, and is managed by the Southwest REgional Partnership, a carbon dioxide sequestration consortium [102, 103]. A collaboration was formed between faculty who have had previous success in deploying new methods to characterize carbon sequestration seepage [104, 105] and faculty who have used similar technology for networked chemical sensor design [106, 107, 108] on this project, funded by the Department of Energy.

The site is above a pilot carbon dioxide injection well in the Morrow geological formation. The site has a large salt dome structure, and it has been noted as a possible storage site for carbon dioxide. The current goal of the pilot well is to use the compressed carbon dioxide supercritical fluid to elicit the remaining valuable hydrocarbons which previous wells have failed to completely extract. Above these mineral formations are large acreages of farmland. At the specific site the sensors were deployed, both cotton and corn were grown during the course of this experiment.

8.2 Sensor Network

In the original grant application which dictated the path of this project, the sensors were to be deployed in a grid on the site. A map of this site is shown in Figure 8.1. The red triangles depict the proposed location of sensors on the site, and the blue circles represent the location of wellheads at the site. The size of these circles represents the carbon dioxide flux from the soil in previous subsurface testing. The red line segments on the topographical map shows a truncated outline of the Farnsworth Oil Unit, which is the region that is expected to be effected by the injection wells.

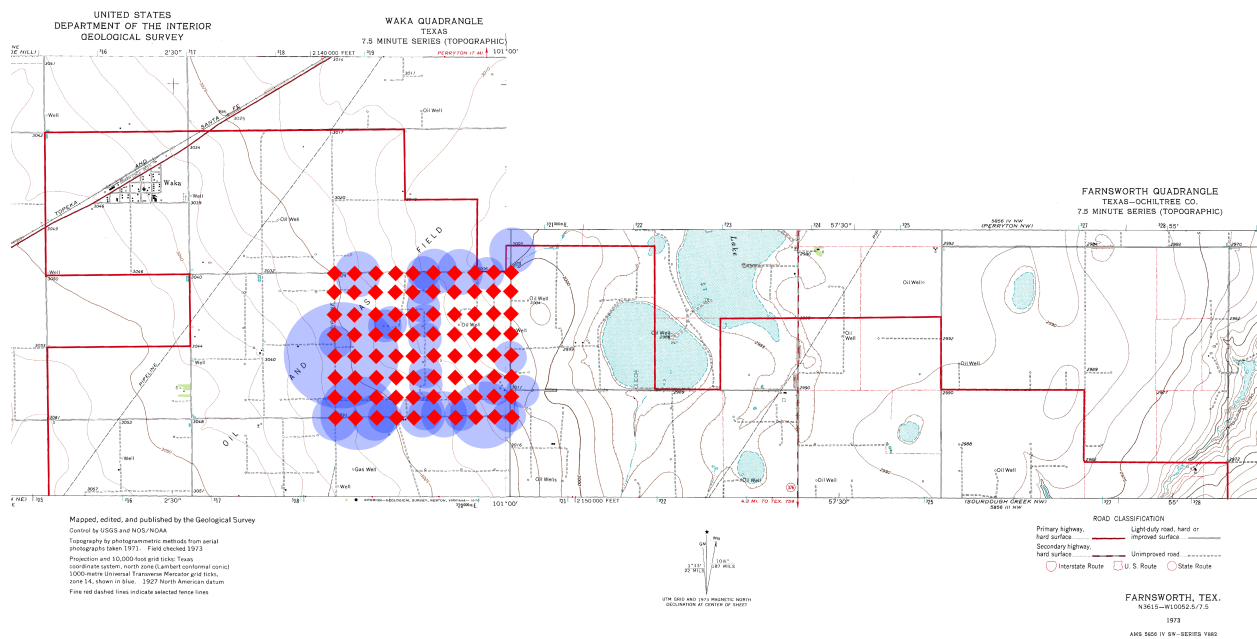


Figure 8.1: A map of a proposed grid of sensors on part of the Farnsworth Oil Unit. Red diamonds indicate proposed locations for the sensors in the array, and the blue circles indicate wellheads where the size of the circle is indicative of the CO₂ soil flux relative to the others. This map was produced using GIS topological maps of the area and an outline of the Farnsworth Oil Unit.

Upon investigation of the site, it became apparent that a full grid was not a reasonable layout. As the topsoil is actively used in center pivot irrigation farming. Deploying sensors within these circles would inhibit agricultural use, and create problems. Additionally, the logistics of transporting over 100 sensors to a site several hours from the Stillwater campus with limited manpower became an issue. Due to these restrictions, the sensors were mounted on existing wooden utility poles at the site. This limited the number and location of the

possible sites. Rather than the 100+ sensors planned for, a total of 33 units were deployed to the site in 3 subnets. The location of these sensors and networks is shown in Figure 8.2. The chosen poles are on access roads surrounding the primary injection well, as noted in the figure.

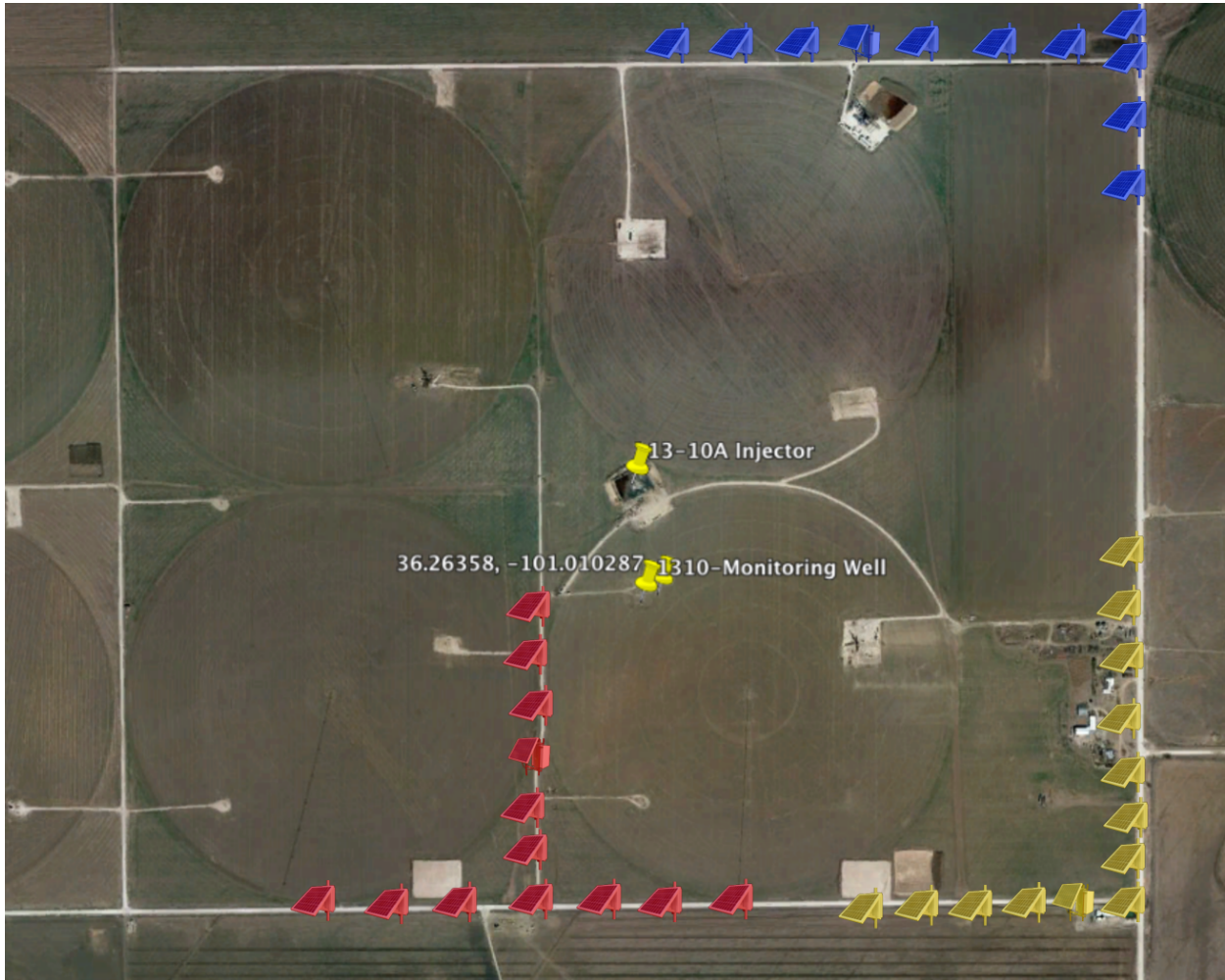


Figure 8.2: This Google Maps satellite image of the Farnsworth, TX site depicts the approximate locations of sensors at the site. The colored groups depict the individual subnets in the sensor network. Sensor locations were determined in part by the placement of existing power poles.

To facilitate installation on utility poles, a different mounting method from the existing T-post configuration needed to be designed. A piece of U-channel material (both aluminum and high density polyethylene were used) was fitted with holes to mount the sensor with bolts on the broad part of the channel and two slots on each arm of the channel. These slots allow pieces of stainless steel strapping to be fit around the pole and secure the sensor. Workers on

ladders could quickly mount these units with the strapping, as shown in Figure 8.3.



Figure 8.3: Workers installing the sensors on power poles at the Farnsworth, TX site. The nodes, equipped with special mounting brackets, were strapped to the poles with steel strapping. At the request of the site maintainers, great care was taken to not damage the poles.

The first network (blue in Figure 8.2) was deployed in April 2016, and the other two subnets were deployed in August of the same year. The units were allowed to collect data until February 2017, when the site was decommissioned.

8.3 Data Analysis

Data were successfully collected by the sensors in the network, and the data were processed and pulled from the central home server on the OSU main campus. Due to power communication errors in one of the networks (an antenna bent over), some data were not reported back to the home server. These periods of missing data have been recovered from

the sensors, as all of the data collected by a network is backed up in the SD card of the nodes. The data were collected over a period of approximately about a year before the sensors at the site were decommissioned. During this period, there were variations in pressure, temperature, and humidity, as can be expected of an outdoor testing period of this time scale. One of the primary variations which can be quantified is the diel cycle. The data from each sensor were collected and sorted by time of day. A figure representing the range of values reported for these time points can be seen in Figure 8.4. The data from the carbon dioxide sensor shows that the concentration seems to be highest in the early morning hours, and decreases during the day. The opposite is the case for methane, with peak concentration occurring in the middle of the day. This cycle matches with reports on diel concentration flux by various authors and in various environments [98, 99, 100, 101]. The generally accepted cause of these variations is the flux between the ground and flora with the atmosphere. Carbon dioxide levels increase during the night as plants cease to photosynthesize. Methane levels increase during the day as heat from the sun generates flux of gas from that which is stored in the topsoil. Changes in relative humidity also play a role in this cycle by reducing the partial pressure of carbon dioxide and methane components with respect to the partial pressure of the water vapor.

8.3.1 Carbon Dioxide

When the carbon dioxide concentration traces are stacked in a plot, as is depicted in Figure 8.5, the features of the plots line up nicely. This suggests that the sensors are all functioning correctly. For any large concentration change events, we would expect to see multiple sensors peaks. Peaks which appear in the reported data of a single unit are likely attributable to very localized environmental changes, such as the presence of an animal actively engaging in respiration.

When all of the data collected from the carbon dioxide sensors are averaged, the trace depicted in Figure 8.6 is generated. This plot shows all of the same characteristics as before including the diel cycles and any events detected by multiple sensors. From this averaged dataset, we can pull several pieces of information. By plotting all of the values detected by the sensors in single parts per million bins, we can plot a histogram of the values reported by the sensor, as depicted in Figure 8.7. A histogram was constructed of 100 bins with a size

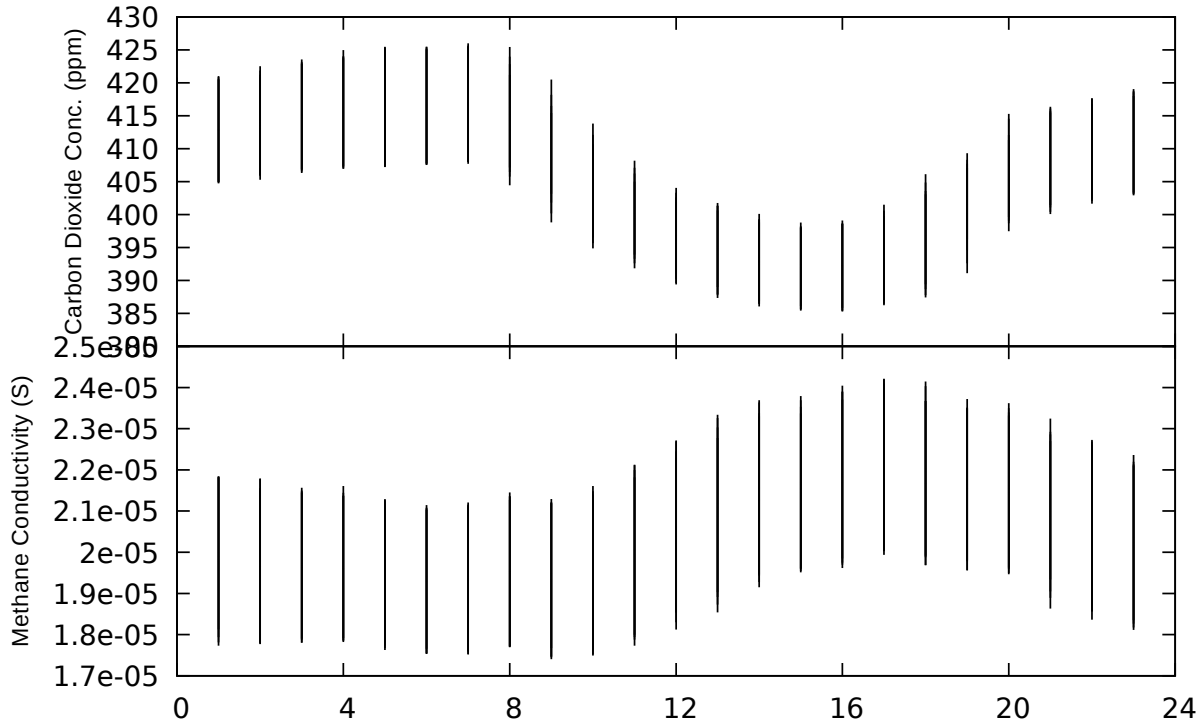


Figure 8.4: This plot shows the range of values recorded during each daily cycle at set time points. The plot shows the concentration changes in the typical day/night cycle at the site.

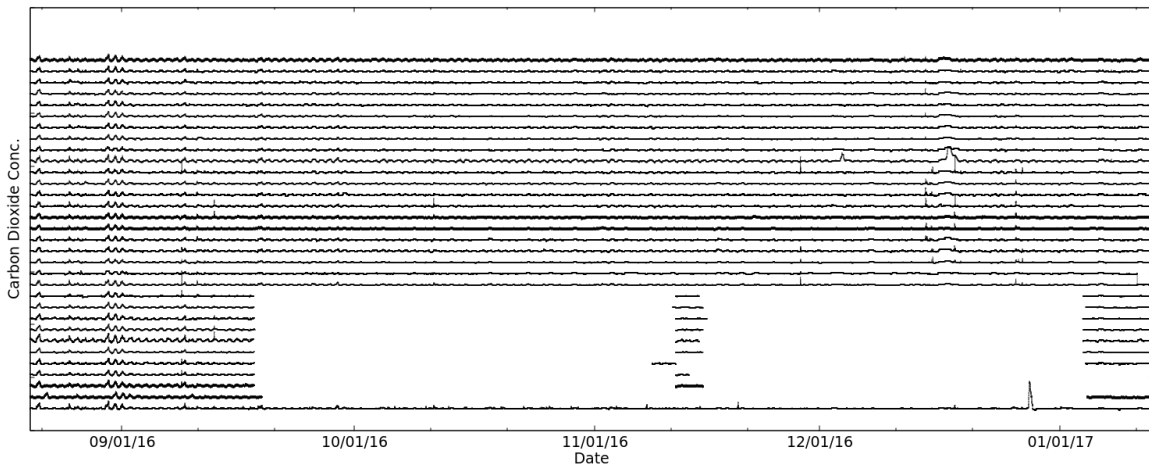


Figure 8.5: Data collected from the carbon dioxide sensors has been stacked in this graph to show the coincidence of peaks in the concentration. Gaps represent communication errors with a single sensor subnet.

of 2.02 ppm. The data plotted on this histogram can be treated as a normal distribution. The peak average is 478 ppm. This is appreciably close to the mean global concentration of carbon dioxide at sea level (as was discussed in Chapter 2). The kurtosis metric shows that

the normal distribution is weighted more heavily toward the mean. The Gaussian distribution shows long tail of values which were reported higher than the mean. These peak values will be discussed in more detail in Section 8.3.3.

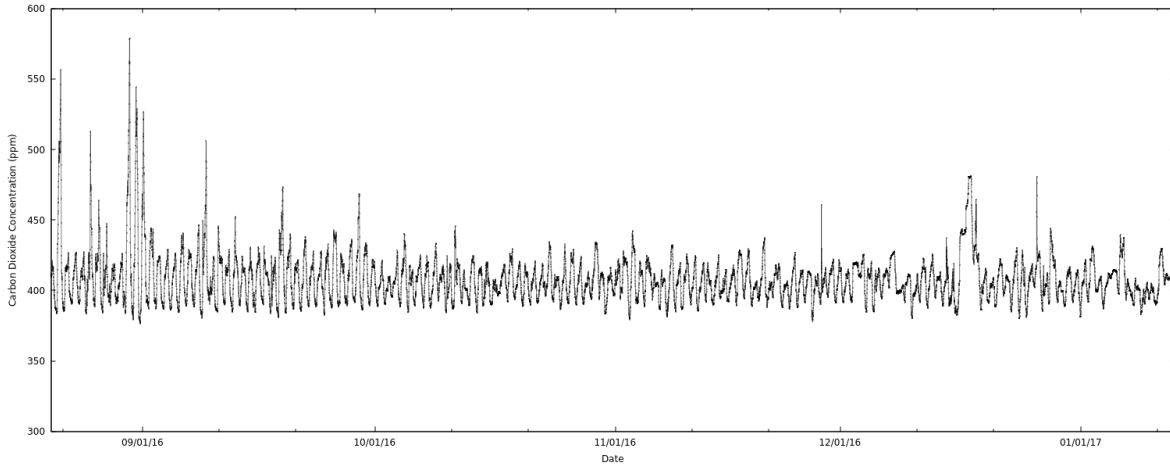


Figure 8.6: The traces from the Farnsworth, TX site have been averaged in this graph to show a single line which depicts the average concentration of carbon dioxide at the site.

8.3.2 Methane

When the methane concentration traces are stacked in a plot, as is depicted in Figure 8.8, the features of the plots line up nicely. This suggests that the sensors are all functioning correctly. For any large concentration change events, we would expect to see multiple sensors peaks. Peaks which appear in the reported data of a single unit are likely attributable to very localized environmental changes, such as the presence of an animal actively engaging in respiration.

When all of the data collected from the methane sensors are averaged, the trace depicted in Figure 8.9 is generated. This plot shows all of the same characteristics as before including the diel cycles and any events detected by multiple sensors. From this averaged dataset, we can pull several pieces of information. By plotting all of the values detected by the sensors in 10S bins, we can plot a histogram of the values reported by the sensor, as depicted in Figure 8.10. A histogram was constructed of 100 bins with a size of 5.28×10^{-7} S. The data plotted on this histogram can be treated as a normal distribution. The peak average is near 3.58×10^{-5} S. Since these sensors have not been accurately ascribed a calibration curve,

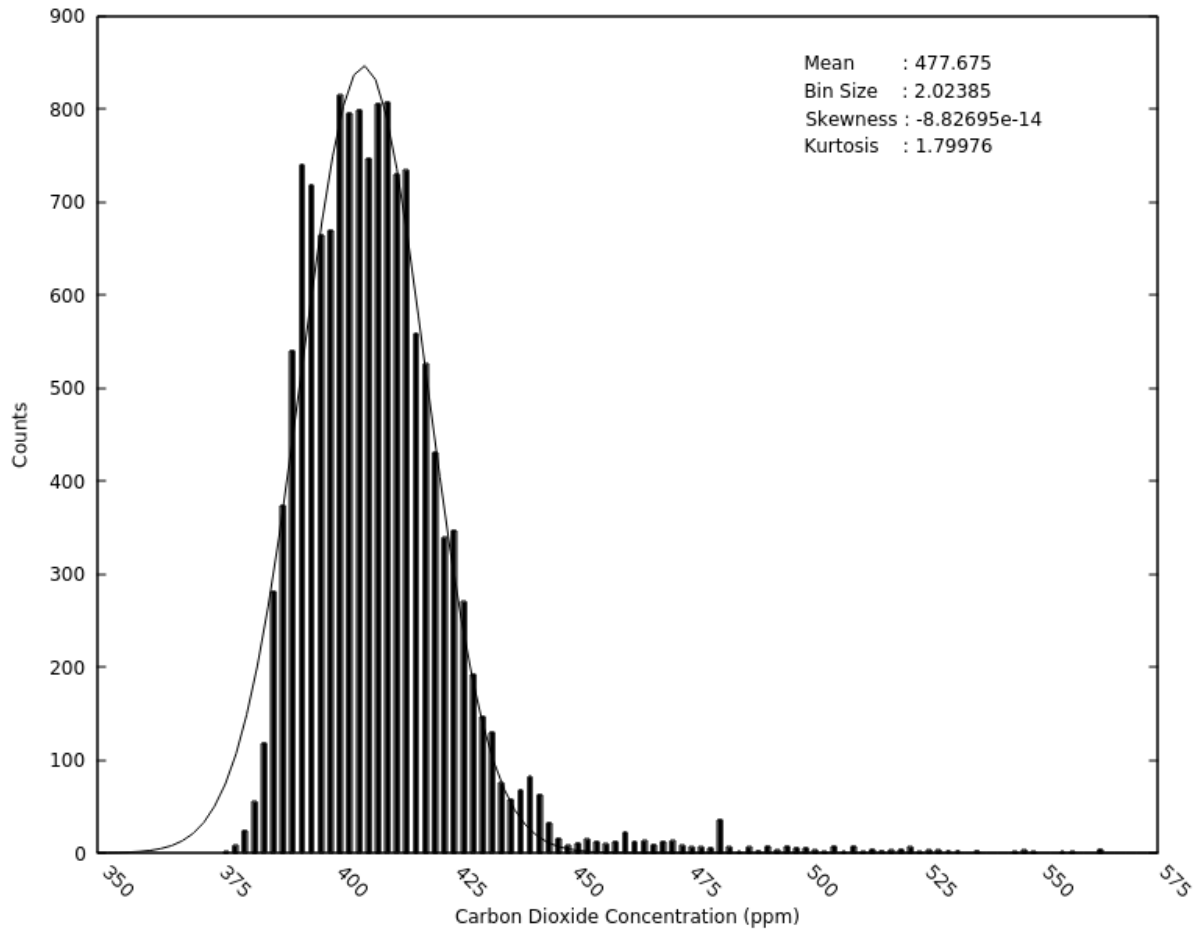


Figure 8.7: The data produced by the carbon dioxide sensors shows a Gaussian distribution.

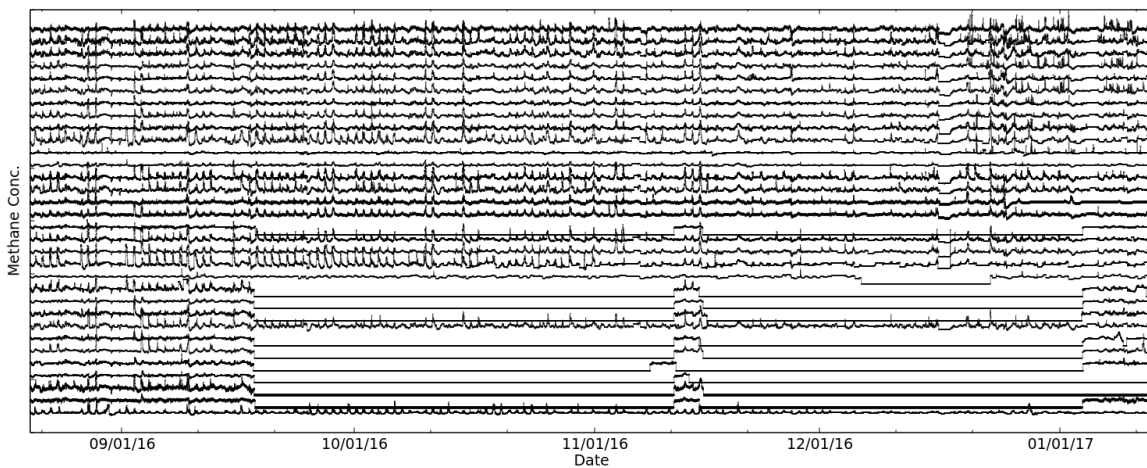


Figure 8.8: Data collected from the methane sensors has been stacked in this graph to show the coincidence of peaks in the concentration. Gaps represent communication errors with a single sensor subnet.

we can only take note of the shape of the normal distribution. The peak is Gaussian with tailing to higher gas concentrations. This suggests that while most of the reported values from the sensors fall within a small window, there are several events which cause this skew. The kurtosis metric shows that the normal distribution is weighted more heavily toward the mean.

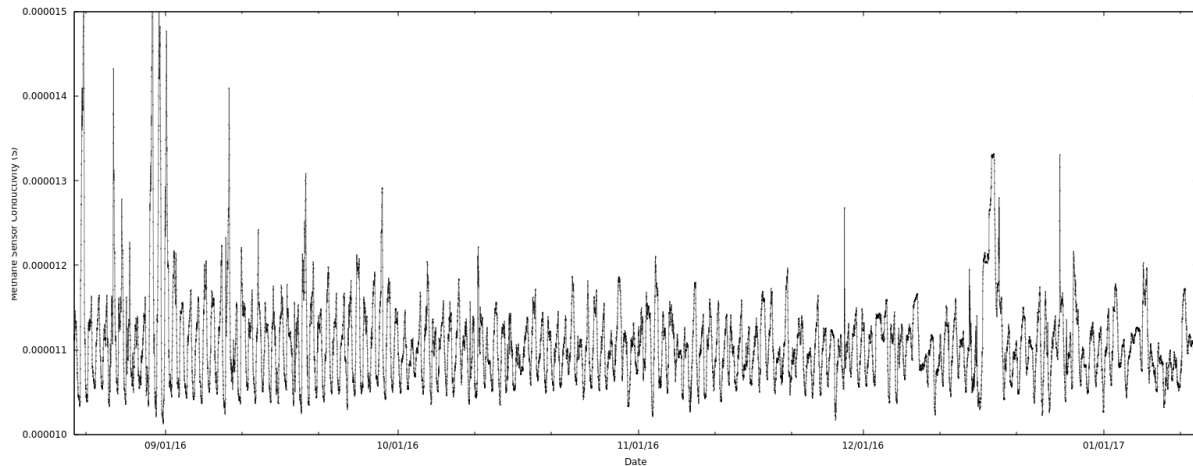


Figure 8.9: The traces from the Farnsworth, TX site have been averaged in this graph to show a single line which depicts the average concentration of methane at the site.

8.3.3 Peak Events

By applying some statistical analysis to the average of all sensors on the network for both carbon dioxide and methane, we can determine when peak concentrations were detected. These ‘Events’ were selected by determining if a value was greater than two standard deviations above the average. This selection method removes the natural variation in the diel cycle from generating a false positive. If we plot these events and their respective concentrations against time, we can look for patterns, this plot is shown in Figure 8.11. Looking at this plot, there are a few things which stand out as notable. First, there are broad events in the methane plot. These suggest that the methane concentration was raised to a high level and sustained for some time. Due to the multiple gas wells in the vicinity, it is possible that these events suggest sustained releases from the wells. However, it is also possible that this methane is due to anthropogenic gas production. The measurement period coincided with two harvest periods for the local farmers in the region. It is possible that

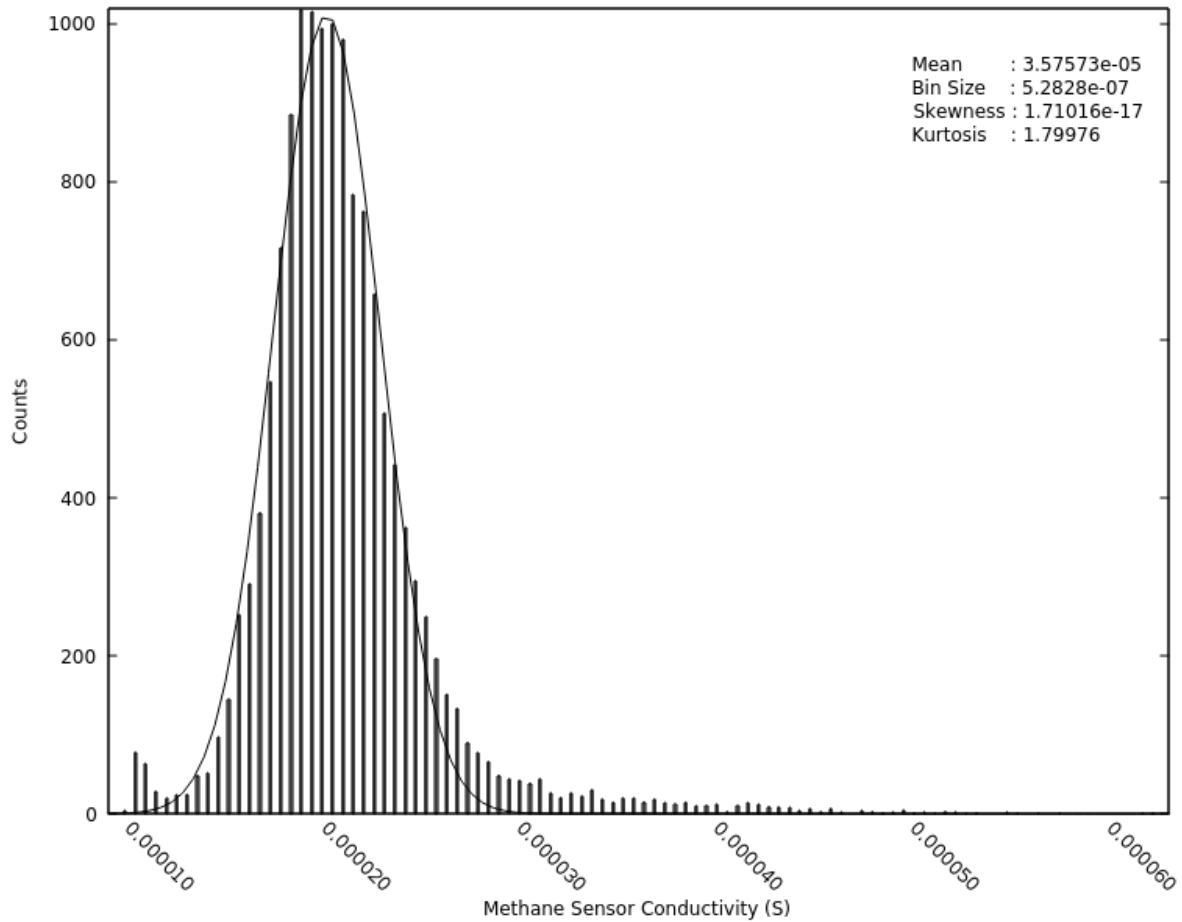


Figure 8.10: The data produced by the methane sensors shows a Gaussian distribution.

the increased methane levels are due to the operation of poorly filtered engines used in farm equipment. There are also a few events which line up directly between both gases. It is possible that these events are due to releases from the injection wells. We are currently communicating with the injection well company to determine if they have reported leaks or releases during the time periods of both the gas-matching events and the long timescale events.

8.4 Conclusions

The deployment of the sensor array networks near an injection well site have shown several successes. The network has proved resilient to long distance data transfer and antenna related downtime. The sensors have also reported two types of interesting events. The first is

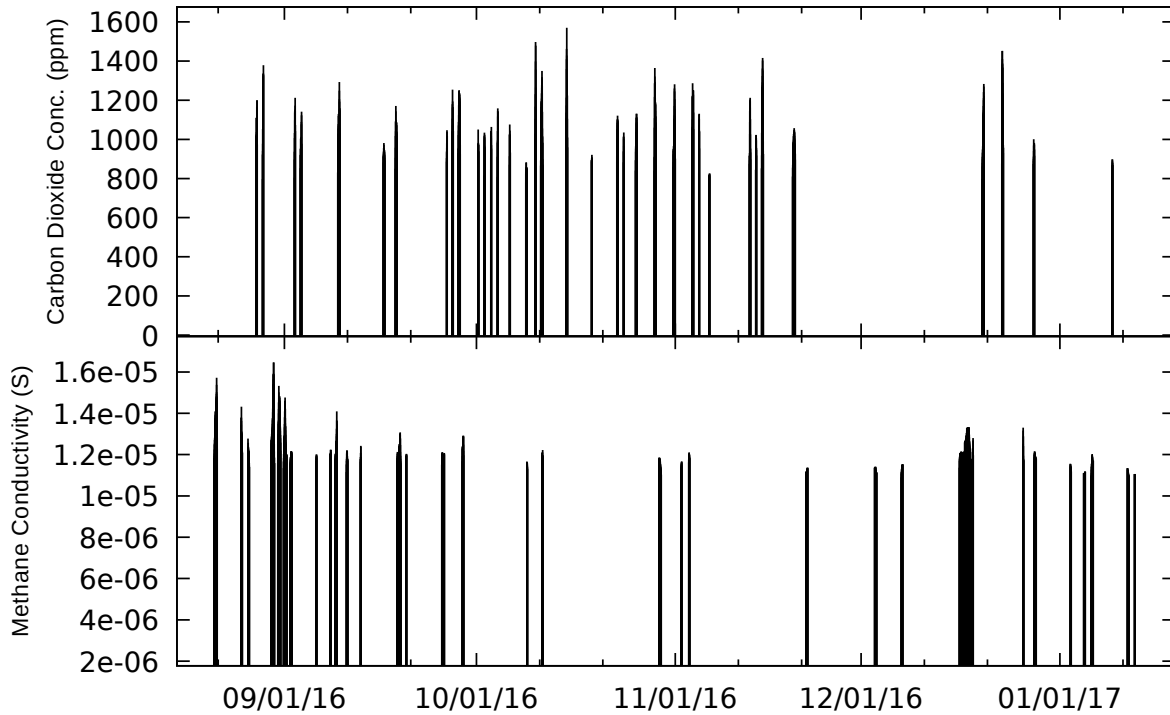


Figure 8.11: This plot shows the recorded events at the Farnsworth, TX site. Events were selected as points which were 2 standard deviations higher than the average at that time of day.

a long term increase in the baseline methane concentration. The second are concentration spikes that are detected by both carbon dioxide and methane sensors. It is possible that these events are due to the release of gas from nearby wells, and the correlation with reported release times is currently sought. This test demonstrates that the sensor network was successful in monitoring the type of site which is vulnerable to simultaneous carbon dioxide and methane bursts.

CHAPTER 9

Conclusion

9.1 Introduction

The goal of this project was to establish a wide-area sensing device using commercially available sensors and equipment for application to carbon dioxide injection wells. The device in question was a distributed system of networked units with appropriate sensors.

9.2 Summary of Work and Findings

Several commercially available sensors were compared for the determination of carbon dioxide and methane concentrations. Sensors were selected based on low cost, low power consumption, appreciable sensitivity near global concentration norms, and ready availability. The sensitivity of the sensors was determined by gas exposure tests compared against a high quality gas infrared instrument, the ZRE from California Analytical Instruments. In addition to the sensitivity measurements performed for sensor selection purposes, the baseline noise, limit of detection, and precision was determined for the available sensors. No single sensor for either gas was able to satisfy the previously determined requirements for the selection of a sensor in its entirety. Therefore, compromises were made based on the available technology. Most units were equipped with the K-30 carbon dioxide sensor from CO2Meter and the MQ-4 chemiresistive methane sensor from Hanwei electronics. Certain sensors in the array were equipped with a methane Gascard sensor from Edinburgh.

The particulars of certain elements of the sensor array were researched and documented

to facilitate design. With a solar power enclosure chosen, the characteristics of the batteries were monitored at several different currents to check the cutoff voltage, observed capacity, and cycling damage. Findings from these tests dictated certain measures be taken to ensure battery longevity by preventing the charging circuit from using the manufacturer determined cutoff point. The network was designed from available technology and theoretical work on optimal networking strategies by other researchers. With this information, it was determined that the most efficient model of moving the data from a field site to a home server was a hybrid mesh network of short range wireless radios coupled to a cellular modem. Data were moved through a ring buffer in the device code and synchronized with other units to add redundancy to the network.

With the sensors selected and with the battery and network characterized, the devices could be designed. Circuits were laid out which allowed for low power operation. The sensors were implemented using a daughter board which could interface with the surrounding environment in both passive sampling and flow regimes. For passive sampling, a 3D printed interfacing part was designed which would allow for the sensitive electrical components to be protected from unwanted environmental damage. Prototypes were built with these designs, and veracity was confirmed. The devices were manufactured at scale and prepared for field deployment.

Prototyping tests at the field site north of OSU campus provided for initial results and baseline confirmation. Long term data were collected with the units to compare with future work. The sensors were confirmed to be working by comparison with known weather data from verified sources, and reasonable measurements of gas concentrations were obtained.

Sensors were deployed at two sites and collected data were analyzed from both as a comparison. The first site was an unmanned aerial vehicle airport east of the OSU campus. Data from this site were analyzed and treated as a control for future experiments. Peak concentration events, determined by reported gas levels two standard deviations from the mean, were observed. An experimental field site was established in around a carbon dioxide injection well near Farnsworth, TX. This field site, when treated with the same statistical conditions, was shown to have broader timescale peak events as well as events in which high concentrations of both carbon dioxide and methane were observed coincident to each other. Comparing the peak events at the Farnsworth, TX site to the UAS site, we can see that there

are distinct differences in the event patterns. This suggests that we may be detecting the gas microseepage from the well head, the detection of which was the original goal of the project.

9.3 Beyond the Project Goals

With project goals met, it is possible to say that the implementation of a wide-area distributed networked sensor array is a reasonable method of determining gas concentration from areas below well heads. Further studies must be conducted to discover any possible correlation of detected microseepage at the Farnsworth, TX site to geological changes or geochemical processes occurring during the detection period. The current results suggest that this array is useful as an early warning type monitoring system. Additional work may determine that the capabilities of this array in conjunction with other technologies are suitable for a more comprehensive monitoring strategy for these types of sites.

Distributed sensors have a very wide range of use for any application requiring detection of properties over a large area or at multiple sites. Specifically, the technology developed for this project has direct application to other research as well. Carbon dioxide is known to leach from carbonaceous soils as a result of global warming in both temperate and permafrost regions [109, 110]. Additionally, tundra ice is known to release methane during thaw [111]. The sensor arrays could be deployed for measurement at these sites for long term monitoring. The under-reporting of methane emissions by gathering and processing facilities [112] may be partially remedied by deploying sensors at locations poorly monitored by the current standard, such as wellheads, drilling, and exploration sites. Landfills produce a large amount of methane leaking from the packed soil, currently measured by single FTIR sampling devices [113]. An always-on array of sensors could monitor the output from the soil in real time to detect and analyze fluctuations in this output. With small changes in hardware, the sensor array could be adapted to volcanology applications. During eruption events, efforts are undertaken to gather large quantities of data about the gaseous production of the volcano [114, 60]. During inactive periods however, only a few sensors are maintained to reduce cost and time spent on measurement. A sensor array could monitor a large area of land for development of new crevices and fissures producing gas without the need for an increase in labor.

The observations from this project are simple, yet they open doors to new possibilities for environmental monitoring devices. The completion of this project provides a fundamental

framework for the design of future devices. In addition to the obvious continuation of the project which promises more data and a continued stream of interesting observations, the core design of the networked sensor array gives rise to further possible work in areas outside of this project's scope.

Bibliography

- [1] Svante Arrhenius. XXXI. On the influence of carbonic acid in the air upon the temperature of the ground. *Philosophical Magazine Series 5*, 41(251):237–276, April 1896.
- [2] T. A. Boden, G. Marland, and R. J. Andres. Global, Regional, and National Fossil-Fuel CO₂ Emissions. Technical report, Carbon Dioxide Information Analysis Center, Oak Ridge National Laboratory, U.S. Department of Energy, Oak Ridge, Tenn., U.S.A., 2011.
- [3] Stefan Bachu. Sequestration of CO₂ in geological media: criteria and approach for site selection in response to climate change. *Energy Conversion and Management*, 41(9):953–970, June 2000.
- [4] Curt M. White, Brian R. Strazisar, Evan J. Granite, James S. Hoffman, and Henry W. Pennline. Separation and Capture of CO₂ from Large Stationary Sources and Sequestration in Geological Formations Coalbeds and Deep Saline Aquifers. *Journal of the Air & Waste Management Association*, 53(6):645–715, June 2003.
- [5] Hsien H. Khoo and Reginald B. H. Tan. Life Cycle Investigation of CO₂ Recovery and Sequestration. *Environmental Science & Technology*, 40(12):4016–4024, June 2006.
- [6] K. D. Romanak, P. C. Bennett, Changbing Yang, and Susan D. Hovorka. Process-based approach to CO₂ leakage detection by vadose zone gas monitoring at geologic CO₂ storage sites. *Geophysical Research Letters*, 39(15):n/a–n/a, August 2012.
- [7] R.A. Chadwick, D. Noy, R. Arts, and O. Eiken. Latest time-lapse seismic data from Sleipner yield new insights into CO₂ plume development. *Greenhouse Gas Control Technologies 9 Proceedings of the 9th International Conference on Greenhouse*

Gas Control Technologies (GHGT-9), 1620 November 2008, Washington DC, USA, 1(1):2103–2110, February 2009.

- [8] Curt M. White, Duane H. Smith, Kenneth L. Jones, Angela L. Goodman, Sinisha A. Jikich, Robert B. LaCount, Stephen B. DuBose, Ekrem Ozdemir, Badie I. Morsi, and Karl T. Schroeder. Sequestration of Carbon Dioxide in Coal with Enhanced Coalbed Methane Recovery A Review. *Energy & Fuels*, 19(3):659–724, May 2005.
- [9] Peter Cook, Rick Causebrook, John Gale, Karsten Michel, and Max Watson. What Have We Learned from Small-scale Injection Projects? *12th International Conference on Greenhouse Gas Control Technologies, GHGT-12*, 63:6129–6140, January 2014.
- [10] Vello A. Kuuskraa, Tyler Van Leeuwen, and Matt Wallace. Improving Domestic Energy Security and Lowering CO₂ Emissions with "Next Generation" CO₂-Enhanced Oil Recovery (CO₂-EOR). Technical Report DOE/NETL-2011/1504, National Energy Technology Laboratory, June 2011.
- [11] Vello A. Kuuskraa, Michael L. Godec, and Phil Dipietro. CO₂ Utilization from Next Generation CO₂ Enhanced Oil Recovery Technology. *GHGT-11*, 37:6854–6866, 2013.
- [12] Eduardo Jose Manrique, Viviana Eugenia Muci, and Mariano E. Gurfinkel. EOR Field Experiences in Carbonate Reservoirs in the United States. In *SPE-100063-MS*, SPE, January 2006. Society of Petroleum Engineers.
- [13] Yousif K. Kharaka, James J. Thordsen, Susan D. Hovorka, H. Seay Nance, David R. Cole, Tommy J. Phelps, and Kevin G. Knauss. Potential environmental issues of CO₂ storage in deep saline aquifers: Geochemical results from the Frio-I Brine Pilot test, Texas, USA. *IAGC Celebrates 40 Years Selected Papers from the 40th Anniversary Celebration of the International Association of GeoChemistry, Cologne, Germany, August 2007 and the Special Session at the 2007 Goldschmidt Conference in Memory of A. A. Levinson*, 24(6):1106–1112, June 2009.
- [14] George W. Kling, Michael A. Clark, Glen N. Wagner, Harry R. Compton, Alan M. Humphrey, Joseph D. Devine, William C. Evans, John P. Lockwood, Michelle L. Tuttle,

- and Edward J. Koenigsberg. The 1986 Lake Nyos Gas Disaster in Cameroon, West Africa. *Science*, 236(4798):169–175, April 1987.
- [15] H. Sigurdsson, J.D. Devine, F.M. Tchua, F.M. Presser, M.K.W. Pringle, and W.C. Evans. Origin of the lethal gas burst from Lake Monoun, Cameroun. *Journal of Volcanology and Geothermal Research*, 31(12):1–16, March 1987.
- [16] Ronald W. Klusman. Baseline studies of surface gas exchange and soil-gas composition in preparation for CO₂ sequestration research: Teapot Dome, Wyoming. *AAPG Bulletin*, 89(8):981–1003, August 2005.
- [17] Ronald W Klusman. Rate measurements and detection of gas microseepage to the atmosphere from an enhanced oil recovery/sequestration project, Rangely, Colorado, USA. *Applied Geochemistry*, 18(12):1825–1838, December 2003.
- [18] Susan Carroll, Yue Hao, and Roger Aines. Geochemical detection of carbon dioxide in dilute aquifers. *Geochemical Transactions*, 10(4), March 2009.
- [19] Vincent Vandeweyer, Bert van der Meer, Cor Hofstee, Frans Mulders, Daan DHoore, and Hilbrand Graven. Monitoring the CO₂ injection site: K12-B. *10th International Conference on Greenhouse Gas Control Technologies*, 4:5471–5478, January 2011.
- [20] C. M. Oldenburg, K. Pruess, and S. M. Benson. Process Modeling of CO₂ Injection into Natural Gas Reservoirs for Carbon Sequestration and Enhanced Gas Recovery. *Energy & Fuels*, 15(2):293–298, March 2001.
- [21] X. G. Zhang, P. G. Ranjith, M. S. A. Perera, A. S. Ranathunga, and A. Haque. Gas Transportation and Enhanced Coalbed Methane Recovery Processes in Deep Coal Seams: A Review. *Energy & Fuels*, 30(11):8832–8849, November 2016.
- [22] A. K. Singh, G. Baumann, J. Henniges, U.-J. Grke, and O. Kolditz. Numerical analysis of thermal effects during carbon dioxide injection with enhanced gas recovery: a theoretical case study for the Altmark gas field. *Environmental Earth Sciences*, 67(2):497–509, 2012.

- [23] Abdolvahab Honari, Branko Bijeljic, Michael L. Johns, and Eric F. May. Enhanced gas recovery with CO₂ sequestration: The effect of medium heterogeneity on the dispersion of supercritical CO₂CH₄. *International Journal of Greenhouse Gas Control*, 39:39–50, August 2015.
- [24] Milan J. Patel, Eric F. May, and Michael L. Johns. High-fidelity reservoir simulations of enhanced gas recovery with supercritical CO₂. *Energy*, 111:548–559, September 2016.
- [25] NETL. Best Practices for Monitoring, Verification, and Accounting of CO₂ Stored in Deep Geologic Formations - 2012 Update. Best Practices Report DOE/NETL-311/081508, U. S. Department of Energy, National Energy Technology Laboratory, 2012.
- [26] L. Bateson, M. Vellico, S.E. Beaubien, J.M. Pearce, A. Annunziatellis, G. Ciotoli, F. Coren, S. Lombardi, and S. Marsh. The application of remote-sensing techniques to monitor CO₂-storage sites for surface leakage: Method development and testing at LATERA (Italy) where naturally produced CO₂ is leaking to the atmosphere. *EGU General Assembly 2007: Advances in CO₂ Storage in Geological Systems EGU (2007)*, 2(3):388–400, July 2008.
- [27] E.J. Male, W.L. Pickles, E.A. Silver, G.D. Hoffmann, J. Lewicki, M. Apple, K. Repasky, and E.A. Burton. Using hyperspectral plant signatures for CO₂ leak detection during the 2008 ZERT CO₂ sequestration field experiment in Bozeman, Montana. *Environmental Earth Sciences*, November 2009.
- [28] Esther Salam, Cristina Barrado, and Enric Pastor. UAV Flight Experiments Applied to the Remote Sensing of Vegetated Areas. *Remote Sensing*, 6(11):11051–11081, November 2014.
- [29] D. R. Thompson, A. K. Thorpe, C. Frankenberg, R. O. Green, R. Duren, L. Guanter, A. Hollstein, E. Middleton, L. Ong, and S. Ungar. Space-based remote imaging spectroscopy of the Aliso Canyon CH₄ superemitter. *Geophysical Research Letters*, 43(12):6571–6578, 2016.

- [30] Jamie L. Barr, Seth D. Humphries, Amin R. Nehrir, Kevin S. Repasky, Laura M. Dobeck, John L. Carlsten, and Lee H. Spangler. Laser-based carbon dioxide monitoring instrument testing during a 30-day controlled underground carbon release field experiment. *International Journal of Greenhouse Gas Control*, 5(1):138–145, January 2011.
- [31] Seth D. Humphries, Amin R. Nehrir, Charlie J. Keith, Kevin S. Repasky, Laura M. Dobeck, John L. Carlsten, and Lee H. Spangler. Testing carbon sequestration site monitor instruments using a controlled carbon dioxide release facility. *Applied Optics*, 47(4):548–555, February 2008.
- [32] Jan M. Nordbotten, Dmitri Kavetski, Michael A. Celia, and Stefan Bachu. Model for CO₂ Leakage Including Multiple Geological Layers and Multiple Leaky Wells. *Environmental Science & Technology*, 43(3):743–749, February 2009.
- [33] Jan Martin Nordbotten, Michael A. Celia, Stefan Bachu, and Helge K. Dahle. Semianalytical Solution for CO₂ Leakage through an Abandoned Well. *Environmental Science & Technology*, 39(2):602–611, January 2005.
- [34] Ronald W. Klusman. Comparison of surface and near-surface geochemical methods for detection of gas microseepage from carbon dioxide sequestration. *International Journal of Greenhouse Gas Control*, 5(6):1369–1392, November 2011.
- [35] Arthur W. Wells, J. Rodney Diehl, Brian R. Strazisar, Thomas H. Wilson, and Dennis C. Stanko. Atmospheric and soil-gas monitoring for surface leakage at the San Juan Basin CO₂ pilot test site at Pump Canyon New Mexico, using perfluorocarbon tracers, CO₂ soil-gas flux and soil-gas hydrocarbons. *International Journal of Greenhouse Gas Control*, 14:227–238, May 2013.
- [36] Arthur W. Wells, J. Rodney Diehl, Grant Bromhal, Brian R. Strazisar, Thomas H. Wilson, and Curt M. White. The use of tracers to assess leakage from the sequestration of CO₂ in a depleted oil reservoir, New Mexico, USA. *Applied Geochemistry*, 22(5):996–1016, May 2007.

- [37] F.F. Craig, III. Field Use of Halogen Compounds To Trace Injected CO₂. In *SPE-14309-MS*, SPE, January 1985. Society of Petroleum Engineers.
- [38] G. Myhre, D. Shindell, F.-M. Bron, W. Collins, J. Fuglestvedt, J. Huang, D. Koch, J.-F. Lamarque, D. Lee, B. Mendoza, T. Nakajima, A. Robock, G. Stephens, T. Takemura, and H. Zhang. 2013: Anthropogenic and Natural Radiative Forcing Supplementary Material. In: *Climate Change 2013: The Physical Science Basis. Contribution of Working Group I to the Fifth Assessment Report of the Intergovernmental Panel on Climate Change*. Technical report, 2013.
- [39] J.A. Apps. A Review of Hazardous Chemical Species Associated with CO₂ Capture from Coal-Fired Power Plants and Their Potential Fate in CO₂ Geologic Storage. Technical report, United States, February 2006. DOI: 10.2172/888971.
- [40] Peter A. Raymond, Nina F. Caraco, and Jonathan J. Cole. Carbon dioxide concentration and atmospheric flux in the Hudson River. *Estuaries*, 20(2):381–390, 1997.
- [41] Michael L. Goulden, Scott D. Miller, Humberto R. da Rocha, Mary C. Menton, Helber C. de Freitas, Adelaine Michela e Silva Figueira, and Cleilim Albert Dias de Sousa. DIEL AND SEASONAL PATTERNS OF TROPICAL FOREST CO₂ EXCHANGE. *Ecological Applications*, 14(sp4):42–54, August 2004.
- [42] J. W. Raich, R. D. Bowden, and P. A. Steudler. Comparison of Two Static Chamber Techniques for Determining Carbon Dioxide Efflux from Forest Soils. *Soil Science Society of America Journal*, 54(6):1754–1757, 1990.
- [43] SEIKO OSOZAWA and SHUICHI HASEGAWA. DIEL AND SEASONAL CHANGES IN CARBON DIOXIDE CONCENTRATION AND FLUX IN AN ANDISOL. *Soil Science*, 160(2), 1995.
- [44] Ji-Qin Ni, Albert J. Heber, Claude A. Diehl, and Teng T. Lim. SE Structures and Environment. *Journal of Agricultural Engineering Research*, 77(1):53–66, September 2000.
- [45] S.C. MABERLY. Diel, episodic and seasonal changes in pH and concentrations of inorganic carbon in a productive lake. *Freshwater Biology*, 35(3):579–598, 1996.

- [46] Weixin Ding, Zucong Cai, and Haruo Tsuruta. Diel variation in methane emissions from the stands of *Carex lasiocarpa* and *Deyeuxia angustifolia* in a cool temperate freshwater marsh. *Atmospheric Environment*, 38(2):181–188, January 2004.
- [47] Tiina Kki, Anne Ojala, and Paula Kankaala. Diel variation in methane emissions from stands of *Phragmites australis* (Cav.) Trin. ex Steud. and *Typha latifolia* L. in a boreal lake. *Aquatic Botany*, 71(4):259–271, December 2001.
- [48] Yaohong Zhang and Weixin Ding. Diel methane emissions in stands of *Spartina alterniflora* and *Suaeda salsa* from a coastal salt marsh. *Aquatic Botany*, 95(4):262–267, November 2011.
- [49] B. Wang, H.U. Neue, and H.P. Samonte. The effect of controlled soil temperature on diel CH₄ emission variation. *Chemosphere*, 35(9):2083–2092, November 1997.
- [50] B. Wang, H.U. Neue, and H.P. Samonte. Factors controlling diel patterns of methane emission via rice. *Nutrient Cycling in Agroecosystems*, 53(3):229–235, 1999.
- [51] Frans-Faco W.A. Van Der Nat, Jack J. Middelburg*, Danille Van Meteren, and Annette Wielemakers. Diel methane emission patterns from *Scirpus lacustris* and *Phragmites australis*. *Biogeochemistry*, 41(1):1–22, 1998.
- [52] Antonio-Javier Garcia-Sanchez, Felipe Garcia-Sanchez, and Joan Garcia-Haro. Wireless sensor network deployment for integrating video-surveillance and data-monitoring in precision agriculture over distributed crops. *Computers and Electronics in Agriculture*, 75(2):288–303, February 2011.
- [53] Jude Allred, Ahmad Bilal Hasan, Saroch Panichsakul, William Pisano, Peter Gray, Jyh Huang, Richard Han, Dale Lawrence, and Kamran Mohseni. SensorFlock: An Airborne Wireless Sensor Network of Micro-air Vehicles. In *Proceedings of the 5th International Conference on Embedded Networked Sensor Systems*, SenSys '07, pages 117–129, New York, NY, USA, 2007. ACM.
- [54] Anna Korre, Claire E. Imrie, Franz May, Stan E. Beaubien, Vincent Vandermeijer, Sergio Persoglia, Lars Golmen, Hubert Fabriol, and Tim Dixon. Quantification techniques for

- potential CO₂ leakage from geological storage sites. *10th International Conference on Greenhouse Gas Control Technologies*, 4:3413–3420, 2011.
- [55] Zheng Yang, Nan Li, Burcin Becerik-Gerber, and Michael Orosz. A systematic approach to occupancy modeling in ambient sensor-rich buildings. *SIMULATION*, 90(8):960–977, August 2014. bibtex: yang_systematic_2014.
- [56] Wan-Young Chung and Seung-Chul Lee. A selective AQS system with artificial neural network in automobile. *Proceedings of the Eleventh International Meeting on Chemical Sensors IMCS-11IMCS 2006IMCS 11*, 130(1):258–263, March 2008. bibtex: chung_selective_2008.
- [57] Wangyun Won and Kwang Soon Lee. Nonlinear observer with adaptive grid allocation for a fixed-bed adsorption process. *Computers & Chemical Engineering*, 46:69–77, November 2012.
- [58] Pan Yi, L. Xiao, and Y. Zhang. Remote real-time monitoring system for oil and gas well based on wireless sensor networks. In *Mechanic Automation and Control Engineering (MACE), 2010 International Conference on*, pages 2427–2429, June 2010. bibtex: yi_remote_2010.
- [59] Andrey Somov, Alexander Baranov, Denis Spirjakin, Andrey Spirjakin, Vladimir Sleptsov, and Roberto Passerone. Deployment and evaluation of a wireless sensor network for methane leak detection. *Selected Papers from the 26th European Conference on Solid-State Transducers Krakw, Poland, 9-12 September 2012*, 202:217–225, November 2013. bibtex: somov_deployment_2013.
- [60] T.D. Pering, G. Tamburello, A.J.S. McGonigle, A. Aiuppa, A. Cannata, G. Giudice, and D. Patan. High time resolution fluctuations in volcanic carbon dioxide degassing from Mount Etna. *Journal of Volcanology and Geothermal Research*, 270:115–121, January 2014.
- [61] R.R. Black, C.P. (Mick) Meyer, A. Yates, L. Van Zweiten, and J.F. Mueller. Formation of artefacts while sampling emissions of PCDD/PCDF from open burning of biomass. *Chemosphere*, 88(3):352–357, July 2012.

- [62] Hui Guohua, Wang Lvye, Mo Yanhong, and Zhang Lingxia. Study of grass carp (*Ctenopharyngodon idellus*) quality predictive model based on electronic nose. *Sensors and Actuators B: Chemical*, 166167:301–308, May 2012.
- [63] S. Karunanithi, N. M. Din, H. Hakimie, C. K. Hua, R. C. Omar, and T. C. Yee. Performance of lab-scale solar powered wireless landfill monitoring system. In *Energy and Environment, 2009. ICEE 2009. 3rd International Conference on*, pages 443–448, December 2009. bibtex: karunanithi_performance_2009.
- [64] Derek G. Shendell, Jennifer H. Therkorn, Naomichi Yamamoto, Qingyu Meng, Sarah W. Kelly, and Christine A. Foster. Outdoor near-roadway, community and residential pollen, carbon dioxide and particulate matter measurements in the urban core of an agricultural region in central CA. *Atmospheric Environment*, 50:103–111, April 2012.
- [65] Shih-Wen Chiu and Kea-Tiong Tang. Towards a Chemiresistive Sensor-Integrated Electronic Nose: A Review. *Sensors*, 13(10):14214–14247, October 2013.
- [66] Clifford K. Ho, Michael T. Itamura, Michael Kelley, and Robert C. Hughes. Review of Chemical Sensors for Real-Time In-Situ Sensing. Technical Report SAND2001-0643, Sandia National Laboratories, 2001.
- [67] T Blasing. Recent Greenhouse Gas Concentrations. Technical report, U. S. Department of Energy, CDIAC, 2016.
- [68] Ed Dlugokencky and Pieter Tans. Trends in Atmospheric Carbon Dioxide. Technical report, NOAA/ESRL, 2016.
- [69] A. J. Turner, D. J. Jacob, J. Benmergui, S. C. Wofsy, J. D. Maasackers, A. Butz, O. Hasekamp, and S. C. Biraud. A large increase in U.S. methane emissions over the past decade inferred from satellite data and surface observations. *Geophysical Research Letters*, 43(5):2218–2224, March 2016.
- [70] I. Bamberger, J. Stieger, N. Buchmann, and W. Eugster. Spatial variability of methane: Attributing atmospheric concentrations to emissions. *Environmental Pollution*, 190:65–74, July 2014.

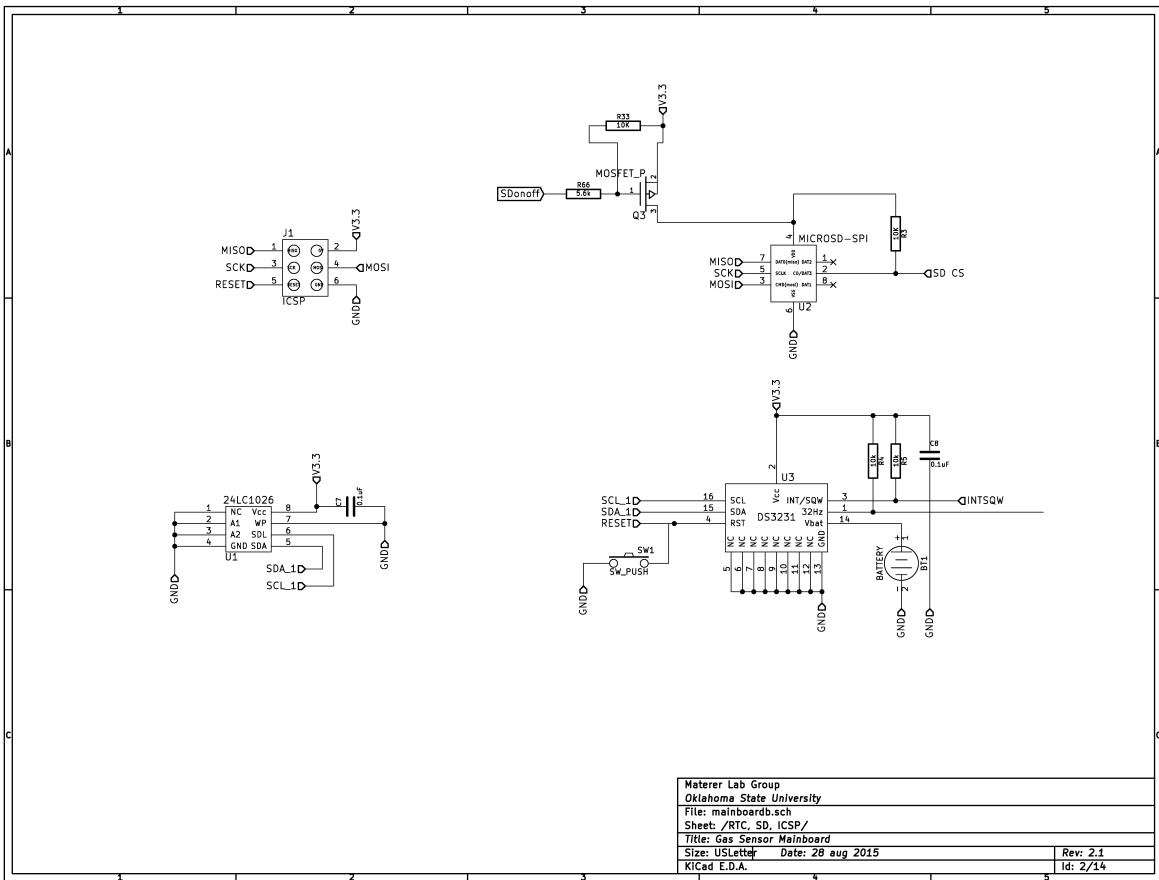
- [71] Ed Dlugokencky. Trends in Atmospheric Methane. Technical report, NOAA/ESRL, 2016.
- [72] Giovanni Neri. First Fifty Years of Chemoresistive Gas Sensors. *Chemosensors*, 3(1):1–20, January 2015.
- [73] R. Frodl and T. Tille. A High-Precision NDIR Gas Sensor for Automotive Applications. *IEEE Sensors Journal*, 6(6):1697–1705, December 2006.
- [74] Zipeng Zhu, Yuhui Xu, and Binqing Jiang. A One ppm NDIR Methane Gas Sensor with Single Frequency Filter Denoising Algorithm. *Sensors (Basel, Switzerland)*, 12(9):12729–12740, 2012.
- [75] Zoltn Bacsik, Jnos Mink, and Gbor Keresztury. FTIR Spectroscopy of the Atmosphere. I. Principles and Methods. *Applied Spectroscopy Reviews*, 39(3):295–363, December 2004.
- [76] Coblenz Society, Inc. Evaluated Infrared Reference Spectra. In P. J. Lindstrom and W. G. Mallard, editors, *NIST Chemistry WebBook*, number 69 in NIST Standard Reference Database. National Institute of Standards and Technology, Gaithersburg MD, 20899.
- [77] Keith J. Albert, Nathan S. Lewis, Caroline L. Schauer, Gregory A. Sotzing, Shannon E. Stitzel, Thomas P. Vaid, and David R. Walt. Cross-Reactive Chemical Sensor Arrays. *Chemical Reviews*, 100(7):2595–2626, July 2000.
- [78] Chengxiang Wang, Longwei Yin, Luyuan Zhang, Dong Xiang, and Rui Gao. Metal oxide gas sensors: sensitivity and influencing factors. *Sensors*, 10(3):2088–2106, 2010.
- [79] Maria Prudenziati and Bruno Morten. Thick-film sensors: an overview. *Sensors and Actuators*, 10(1):65–82, September 1986.
- [80] Corrado Di Natale, Fabrizio Davide, Guido Faglia, and Paolo Nelli. Study of the effect of the sensor operating temperature on SnO₂-based sensor-array performance. *The workshop on new developments in semiconducting gas sensors*, 23(2):187–191, February 1995.

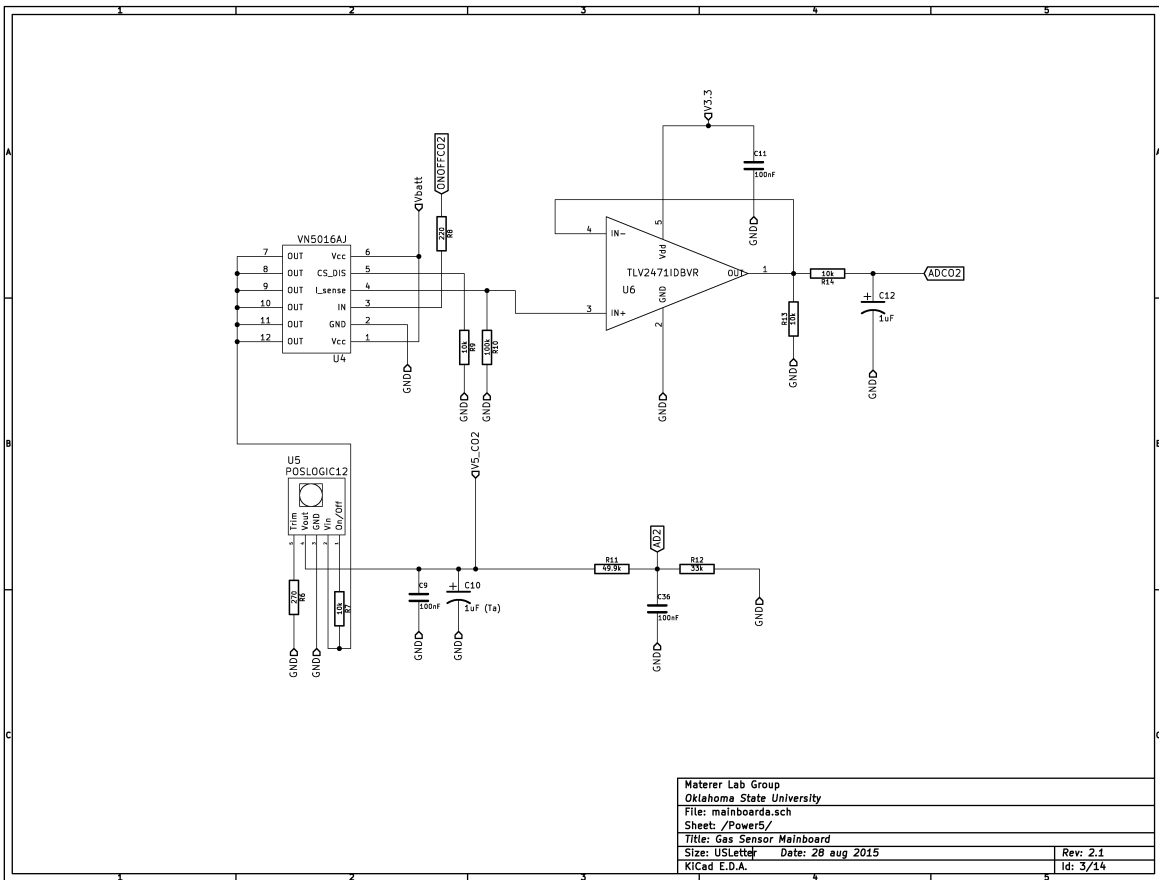
- [81] Ling Wang and R.V. Kumar. Thick film CO₂ sensors based on Nasicon solid electrolyte. *Solid State Ionics*, 158(34):309–315, March 2003.
- [82] W. Eugster and G. W. Kling. Performance of a low-cost methane sensor for ambient concentration measurements in preliminary studies. *Atmospheric Measurement Techniques*, 5(Copyright (C) 2015 American Chemical Society (ACS). All Rights Reserved.):1925–1934, 2012.
- [83] Lawrence H. Keith, Warren Crummett, John Deegan, Robert A. Libby, John K. Taylor, and George Wentler. Principles of environmental analysis. *Analytical Chemistry*, 55(14):2210–2218, 1983.
- [84] Mocak J., Bond A. M., Mitchell S., and Scollary G. A statistical overview of standard (IUPAC and ACS) and new procedures for determining the limits of detection and quantification: Application to voltammetric and stripping techniques (Technical Report). *Pure and Applied Chemistry*, 69(2):297, 2009.
- [85] T. Williams and C. Kelley. gnuplot 5.0: An Interactive Plotting Program, January 2016.
- [86] Tycon Power Systems. RemotePro Data Sheet, November 2014.
- [87] Ramin Hekmat. *Ad-hoc Networks: Fundamental Properties and Network Topologies*. Springer Netherlands, 2006.
- [88] Victor O. K. Li, Y. F. Lam, T. C. Hou, and Joesph H. Yuen. Topology Design and Performance Analysis of an Integrated Communication Network. JPL Publication JPL Pub. 85-97, California Institute of Technology, Jet Propulsion Laboratory, September 1985.
- [89] FCC ID: MCQ-XB900hp. FCC License MCQ-XB900HP, Federal Communications Commission, 2012.
- [90] IEEE Standard for Local and metropolitan area networks Part 15.4: Low-Rate Wireless Personal Area Networks (LR-WPANs). Technical Report IEEE 802.15.7, The Institute of Electrical and Electronics Engineers, Inc., 2011.

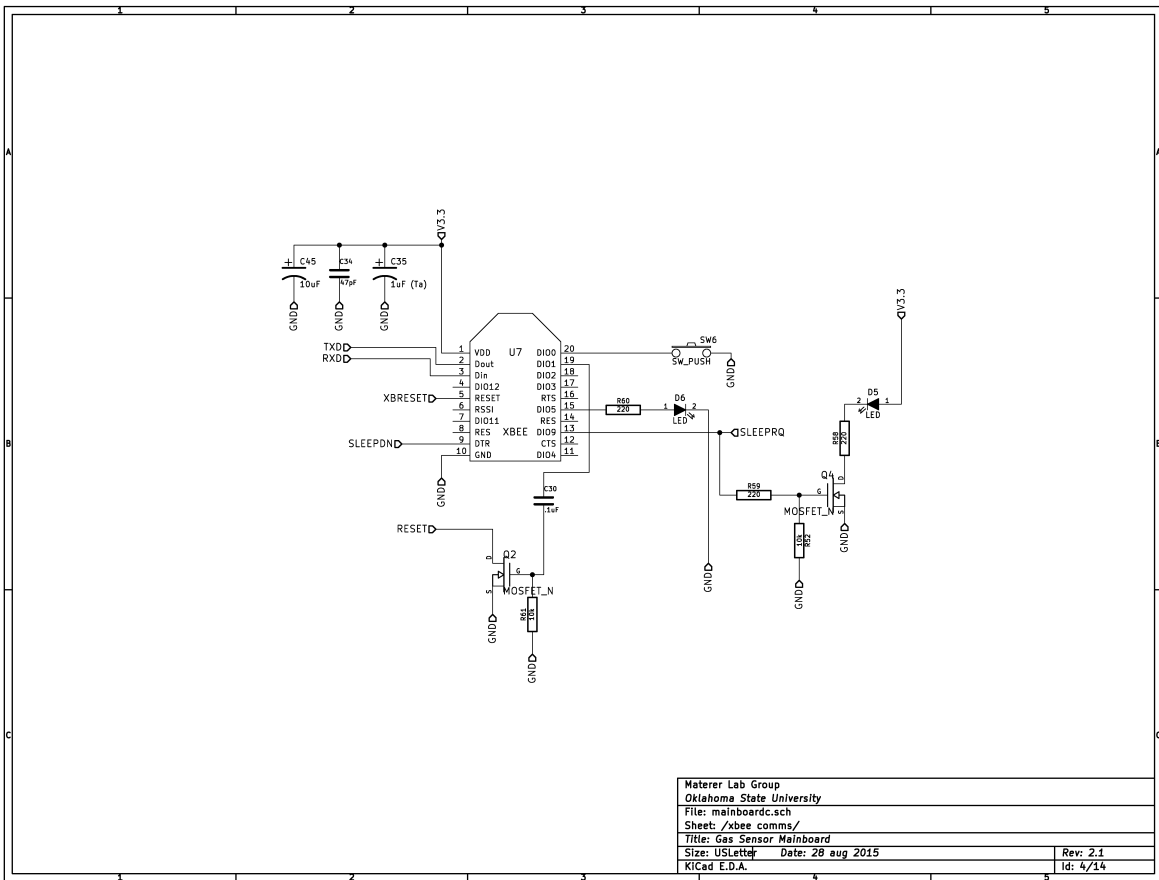
- [91] Wireless Mesh Networking ZigBee vs. DigiMesh. Technical report, 2008.
- [92] Robert Faludi. *Building wireless sensor networks: with ZigBee, XBee, arduino, and processing.* ” O’Reilly Media, Inc.”, 2010.
- [93] Qualcomm Incorporated. EV-DO Rev. A and B: Wireless Broadband for the Masses. Technical report, December 2007.
- [94] KSWO. Weather History for KSWO from July 1, 2014 to July 31, 2015 [Dataset], 2015.
- [95] M Kintel and C Clifford Wolf. OpenSCAD, The Programmers Solid 3d CAD Modeller. 2011.
- [96] KSWO. Weather History for KSWO from September 11, 2015 [Dataset], 2015.
- [97] KSWO. Weather History for KSWO from January 1, 2016 [Dataset], 2016.
- [98] M. G. Tarnawski, T. G. A. Green, B. Buedel, A. Meyer, H. Zellner, and O. L. Lange. Diel changes of atmospheric CO₂ concentration within, and above, cryptogam stands in a New Zealand temperate rainforest. *New Zealand Journal of Botany*, 32(3):329–336, July 1994.
- [99] Seok-In Yun, Woo-Jung Choi, Jae-Eul Choi, and Han-Yong Kim. High-Time Resolution Analysis of Diel Variation in Methane Emission from Flooded Rice Fields. *Communications in Soil Science and Plant Analysis*, 44(10):1620–1628, May 2013.
- [100] D. Y. F. Lai, N. T. Roulet, E. R. Humphreys, T. R. Moore, and M. Dalva. The effect of atmospheric turbulence and chamber deployment period on autochamber CO₂ and CH₄ flux measurements in an ombrotrophic peatland. *Biogeosciences*, 9(8):3305–3322, 2012.
- [101] S. M. McGinn, K. A. Beauchemin, T. Coates, and E. J. McGeough. Cattle Methane Emission and Pasture Carbon Dioxide Balance of a Grazed Grassland. *Journal of Environmental Quality*, 43(3):820–828, 2014.
- [102] Mahlon M. Ball, Mitchell E. Henry, and Sherwood E. Frezon. Petroleum Geology of the Anadarko Basin Region, Province (115), Kansas, Oklahoma, and Texas. USGS Survey 88-450W, USGS, 1991.

- [103] M.D. White, B.J. McPherson, R.B. Grigg, W. Ampomah, and M.S. Appold. Numerical Simulation of Carbon Dioxide Injection in the Western Section of the Farnsworth Unit. *12th International Conference on Greenhouse Gas Control Technologies, GHGT-12*, 63:7891–7912, 2014.
- [104] NETL. New Approach for Long Term Monitoring of Potential CO₂ Leaks from Geologic Sequestration. Project Fact Sheet FWPAACH139, U. S. Department of Energy, National Energy Technology Laboratory, 2010.
- [105] NETL. Site Characterization for CO₂ Storage from Coal-fired Power Facilities in the Black Warrior Basin of Alabama. Project Fact Sheet FE0001910, U. S. Department of Energy, National Energy Technology Laboratory, 2012.
- [106] N. Materer, A. Apblett, and D. Scott. Chlorine dioxide sensor, August 2010.
- [107] N. Materer, P. Field, N. Ley, A. Soufiani, D. Scott, T. Ley, and A. Apblett. Passive Wireless Detection of Corrosive Salts in Concrete Using Wire-Based Triggers. *Journal of Materials in Civil Engineering*, 26(5):918–922, June 2013.
- [108] M. Pour-Ghaz, T. Barrett, T. Ley, N. Materer, A. Apblett, and J. Weiss. Wireless Crack Detection in Concrete Elements Using Conductive Surface Sensors and Radio Frequency Identification Technology. *Journal of Materials in Civil Engineering*, 26(5):923–929, July 2013.
- [109] D. S. Jenkinson, D. E. Adams, and A. Wild. Model estimates of CO₂ emissions from soil in response to global warming. *Nature*, 351(6324):304–306, May 1991.
- [110] Edward A. G. Schuur, Jason G. Vogel, Kathryn G. Crummer, Hanna Lee, James O. Sickman, and T. E. Osterkamp. The effect of permafrost thaw on old carbon release and net carbon exchange from tundra. *Nature*, 459(7246):556–559, May 2009.
- [111] Stephen C. Whalen and William S. Reeburgh. A methane flux time series for tundra environments. *Global Biogeochemical Cycles*, 2(4):399–409, December 1988.
- [112] Anthony J. Marchese, Timothy L. Vaughn, Daniel J. Zimmerle, David M. Martinez, Laurie L. Williams, Allen L. Robinson, Austin L. Mitchell, R. Subramanian, Daniel S.

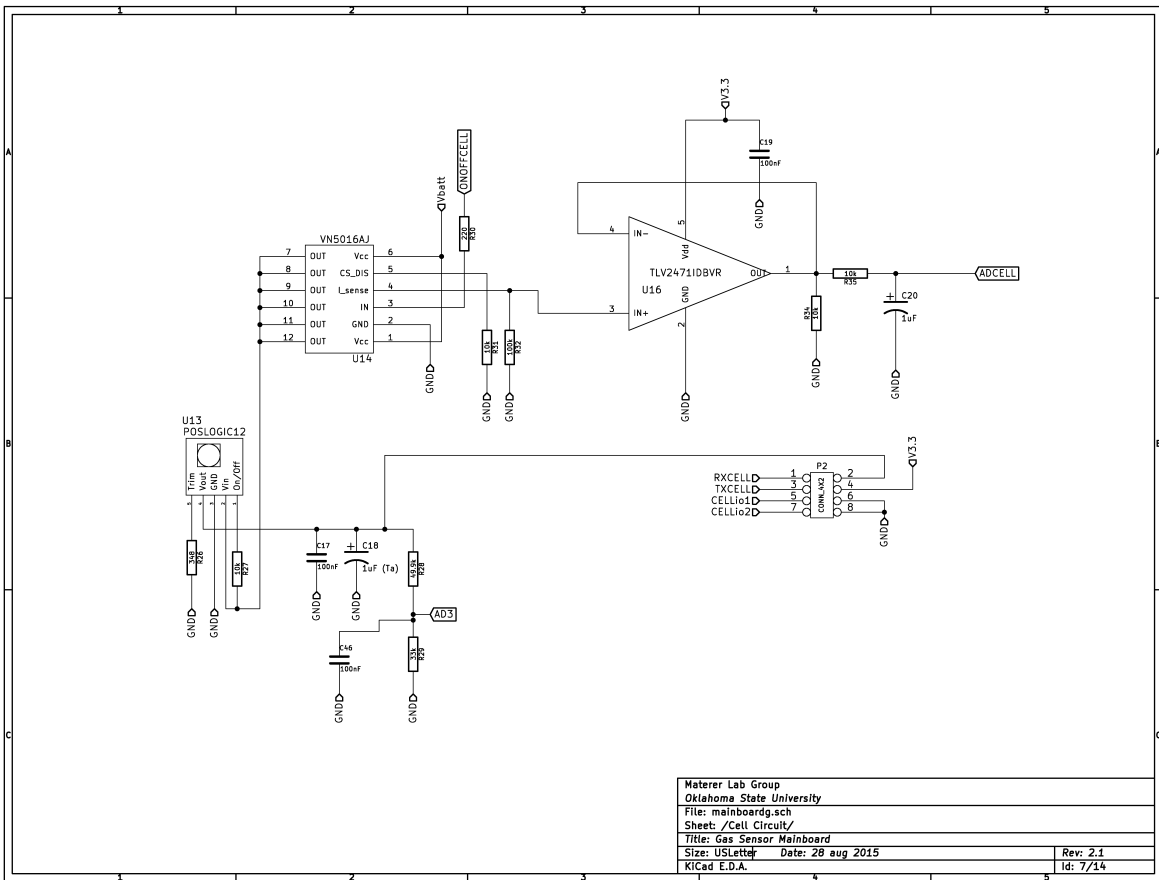
- Tkacik, Joseph R. Roscioli, and Scott C. Herndon. Methane Emissions from United States Natural Gas Gathering and Processing. *Environmental Science & Technology*, 49(17):10718–10727, September 2015.
- [113] Bo Galle, Jerker Samuelsson, Bo H. Svensson, and Gunnar Brjesson. Measurements of Methane Emissions from Landfills Using a Time Correlation Tracer Method Based on FTIR Absorption Spectroscopy. *Environmental Science & Technology*, 35(1):21–25, January 2001.
- [114] Hayley J Duffell, Clive Oppenheimer, David M Pyle, Bo Galle, Andrew J.S McGonigle, and Mike R Burton. Changes in gas composition prior to a minor explosive eruption at Masaya volcano, Nicaragua. *Journal of Volcanology and Geothermal Research*, 126(34):327–339, August 2003.

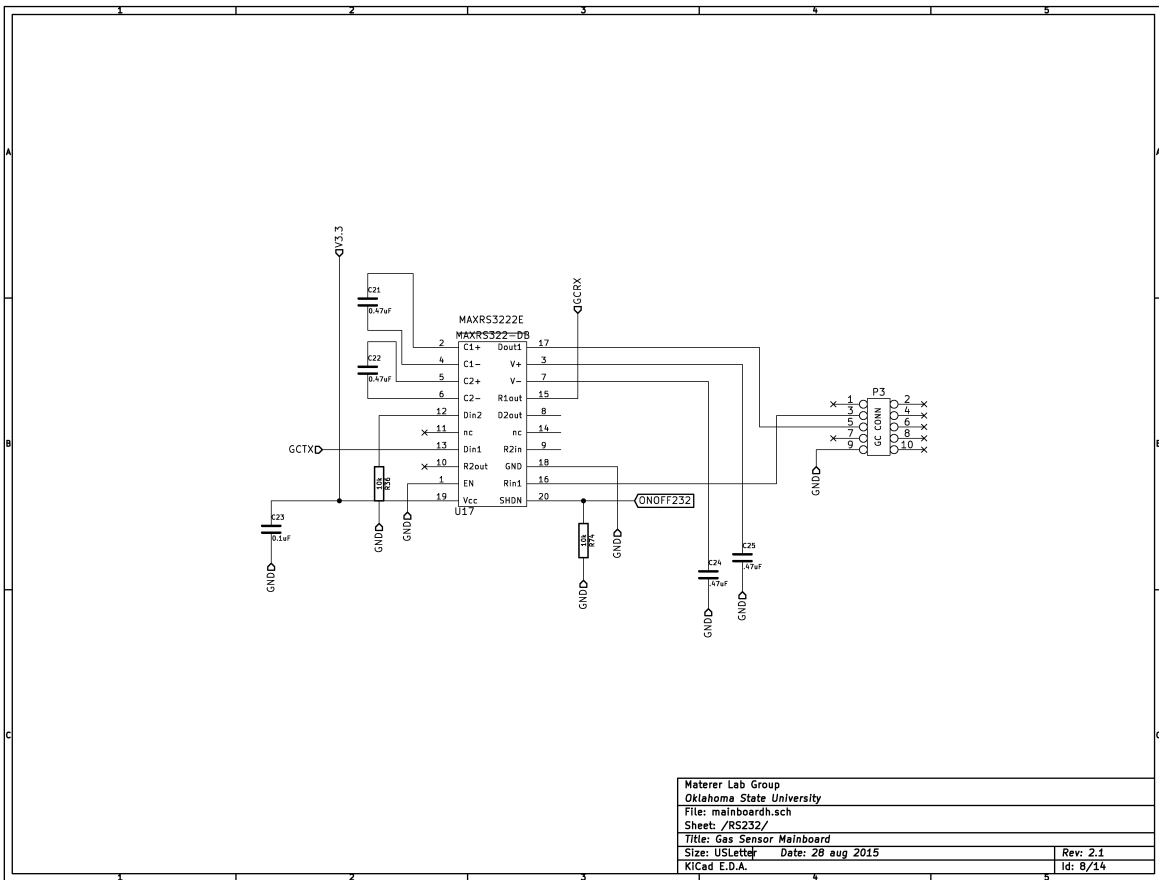




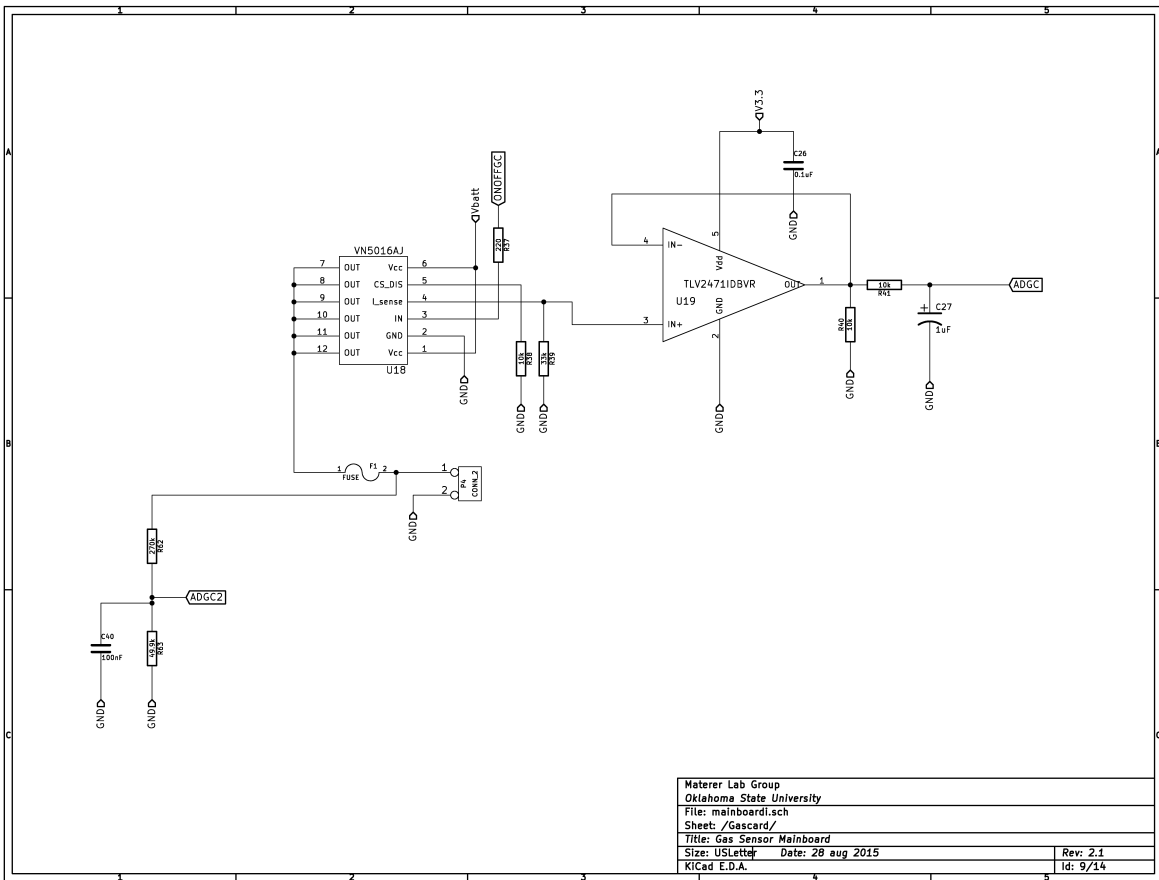


Materer Lab Group	
Oklahoma State University	
File: mainboardc.sch	
Sheet: /xbee comms/	
Title: Gas Sensor Mainboard	
Size: USLetter	Date: 28 aug 2015
KiCad E.D.A.	Rev: 2.1 Id: 4/14

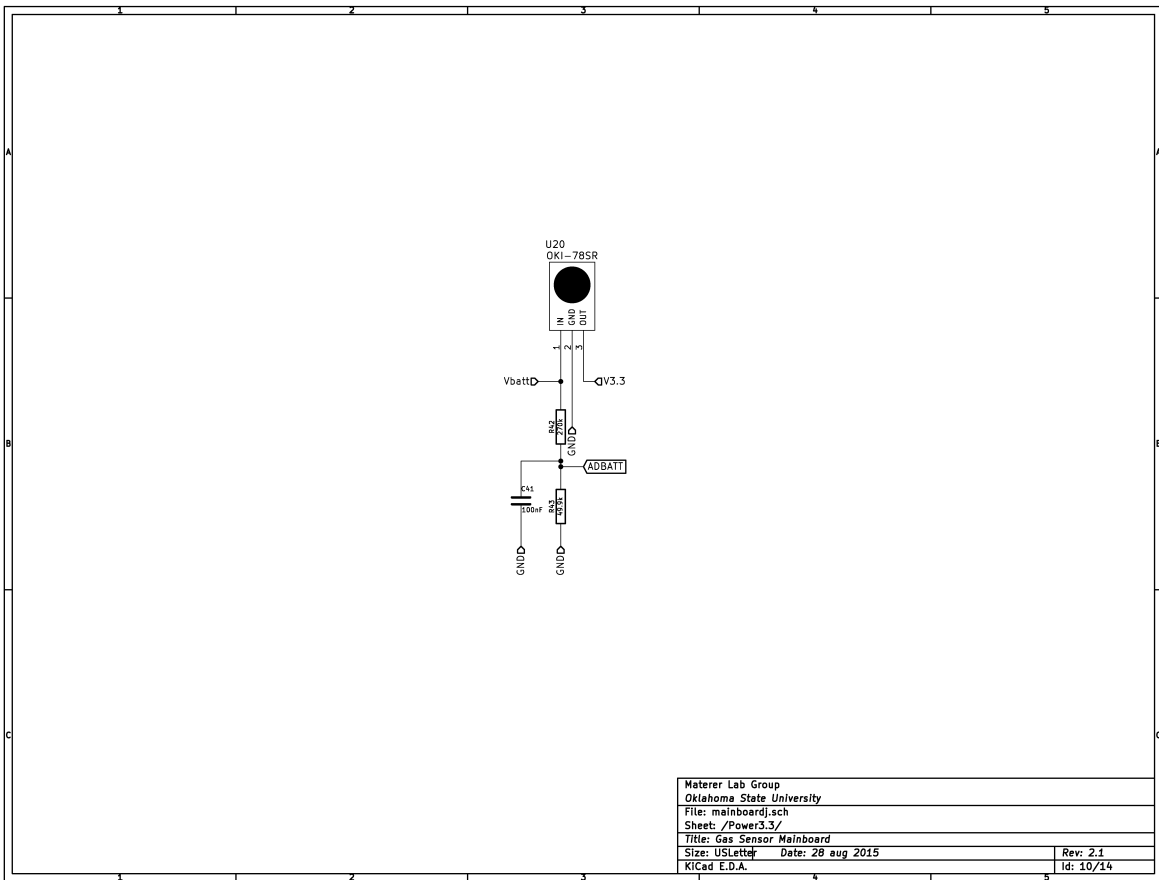


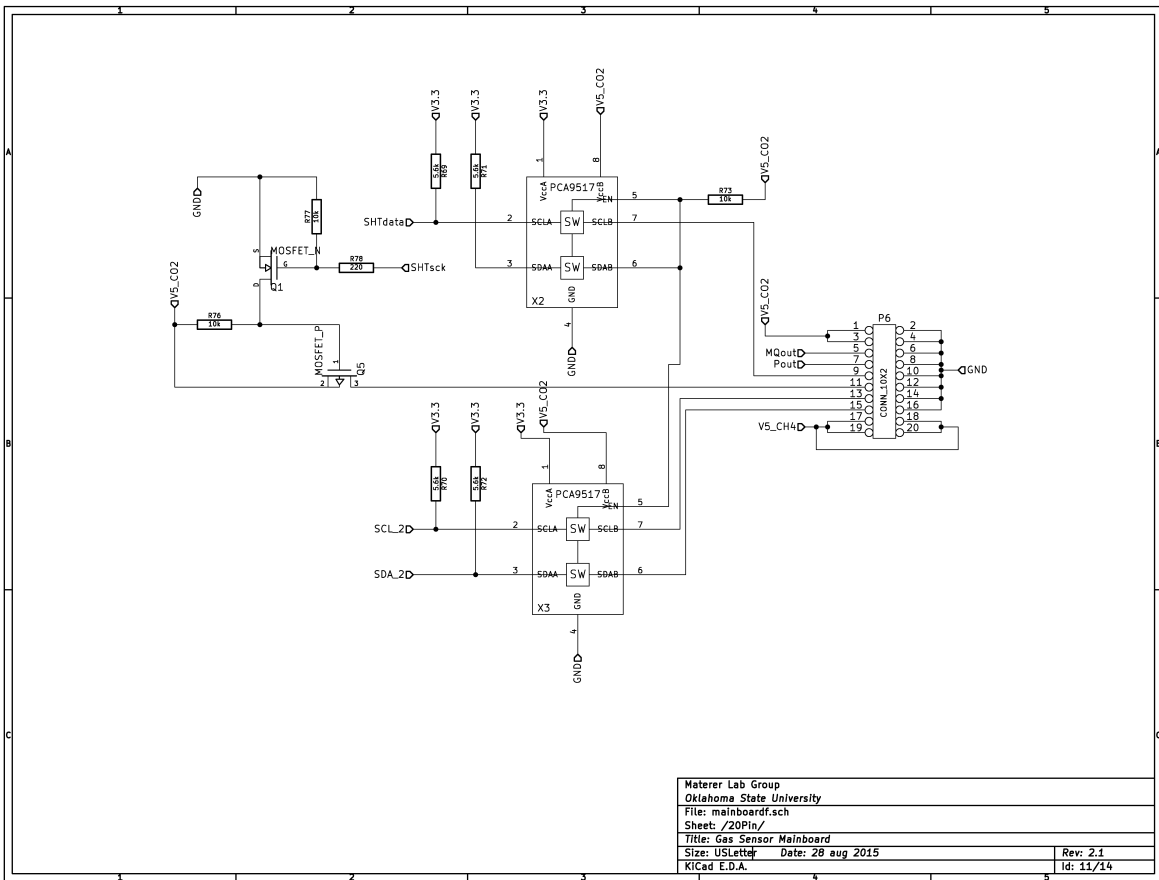


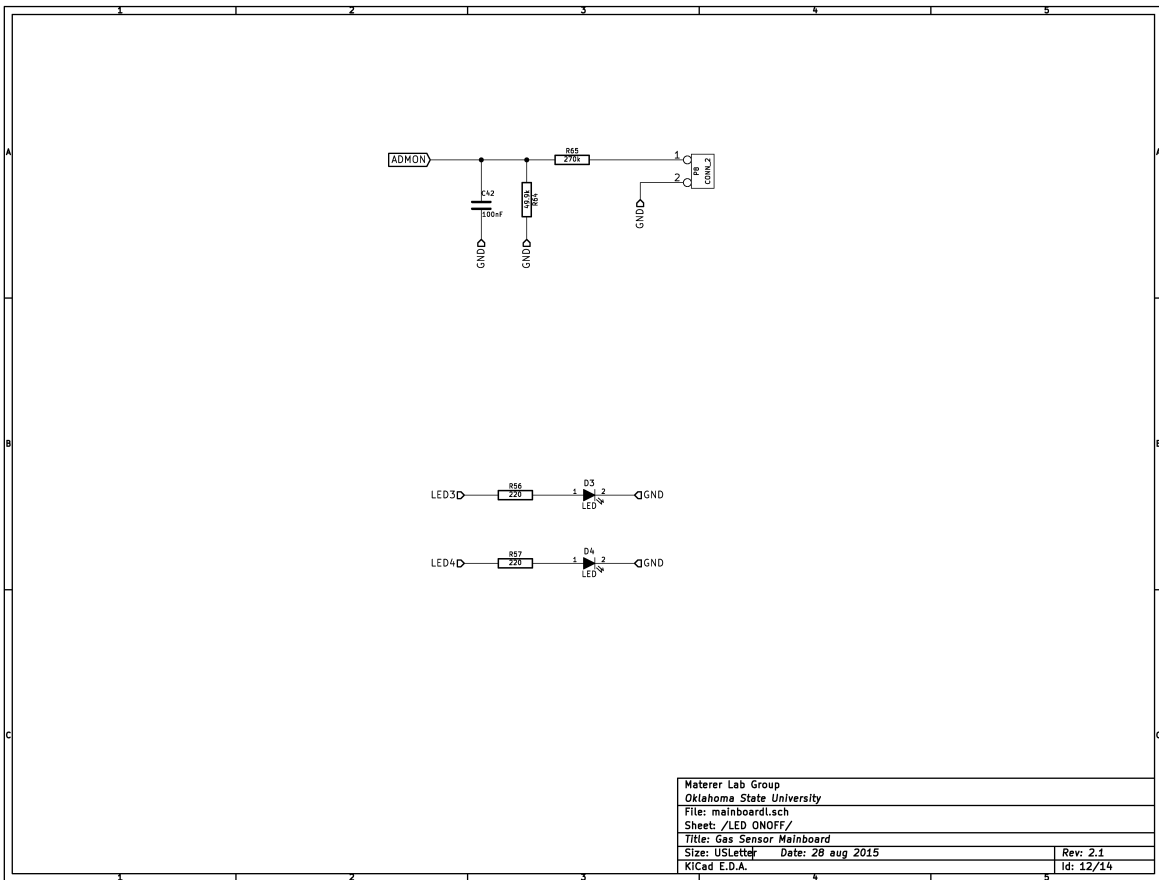
Materer Lab Group	
Oklahoma State University	
File: mainboardr.sch	
Sheet: /RS232/	
Title: Gas Sensor Mainboard	
Size: USLetter	Date: 28 aug 2015
KiCad E.D.A.	Rev: 2.1 Id: 8/14

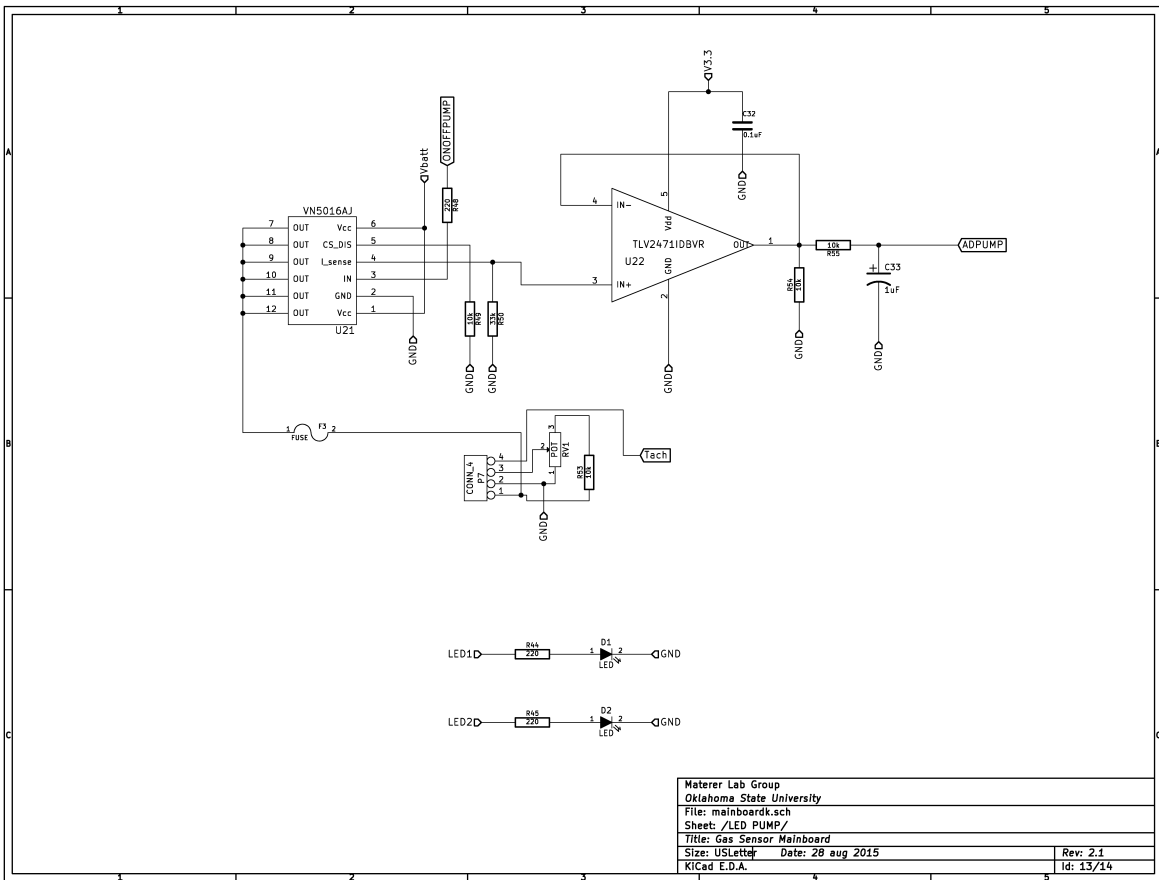


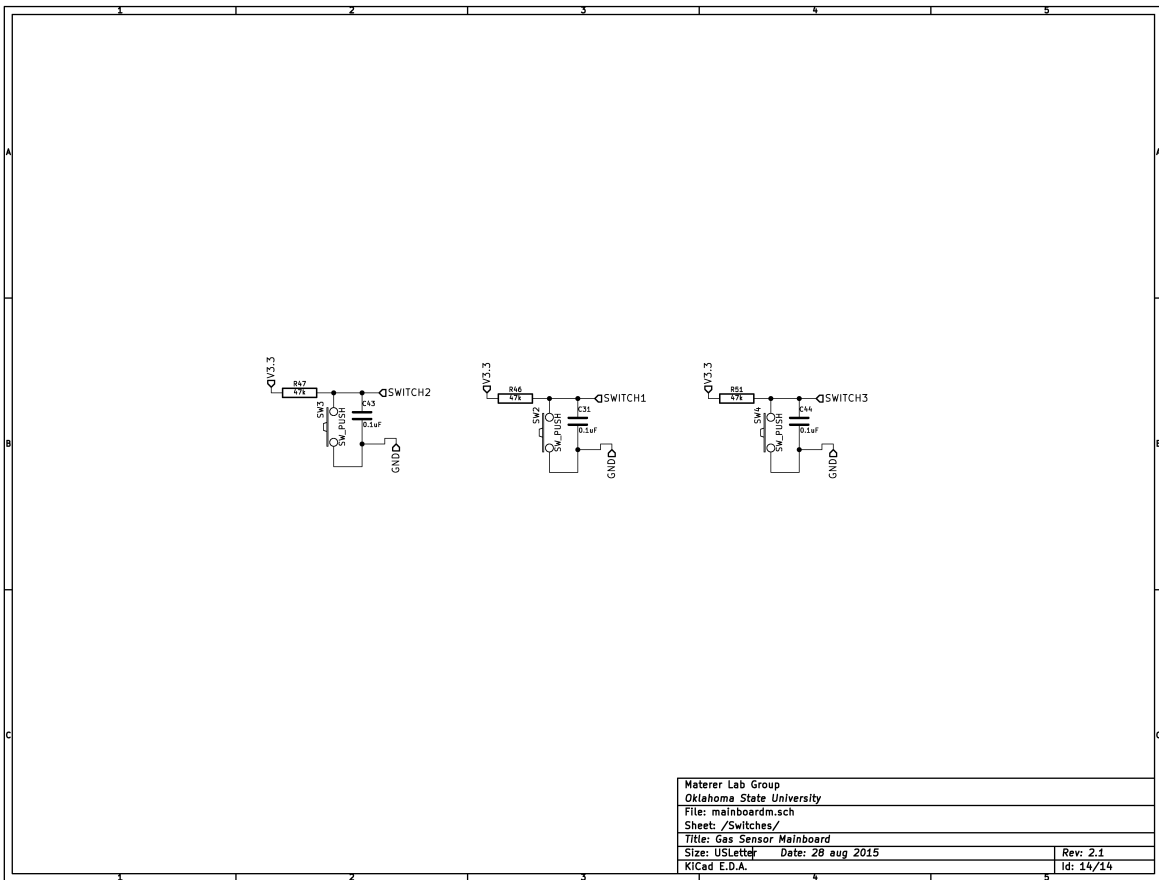
Materer Lab Group	
Oklahoma State University	
File: mainboard1.sch	
Sheet: /Gascard/	
Title: Gas Sensor Mainboard	
Size: USLetter	Date: 28 aug 2015
KiCad E.D.A.	Rev: 2.1 Id: 9/14







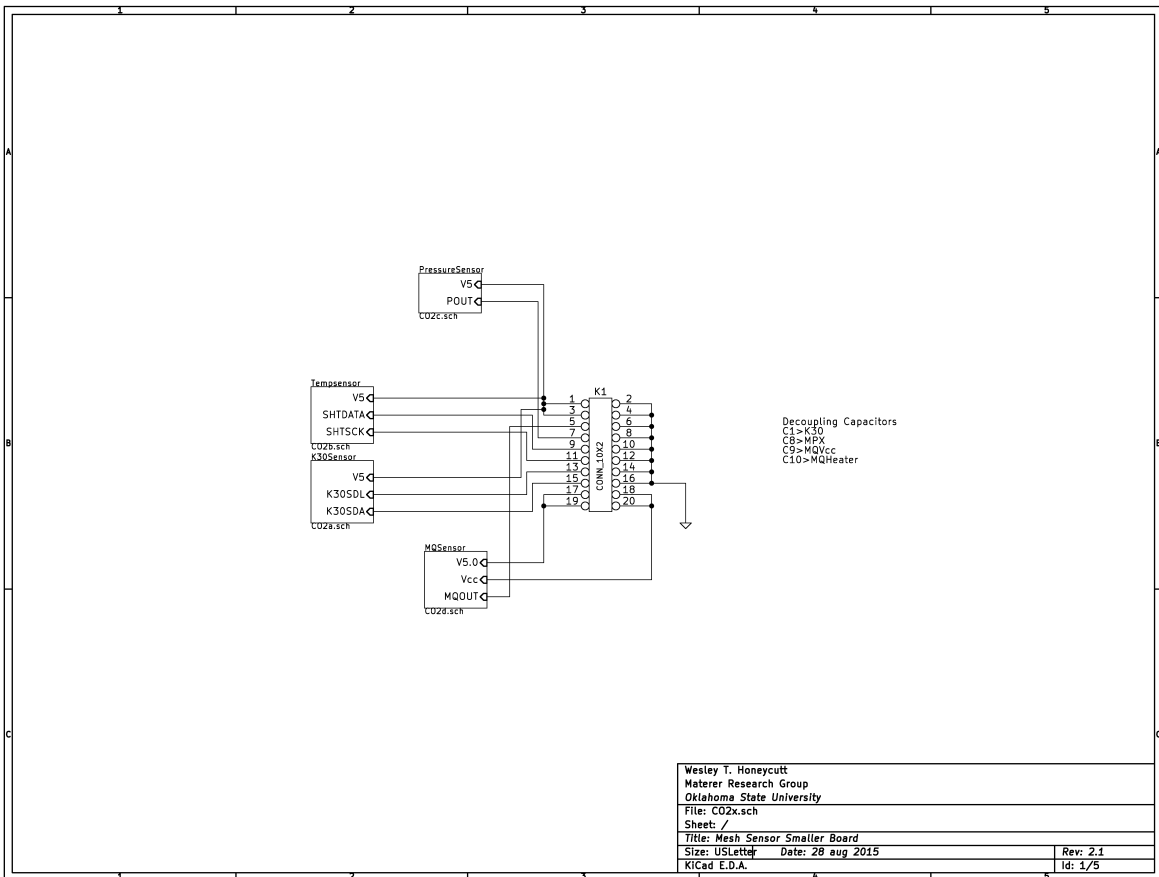


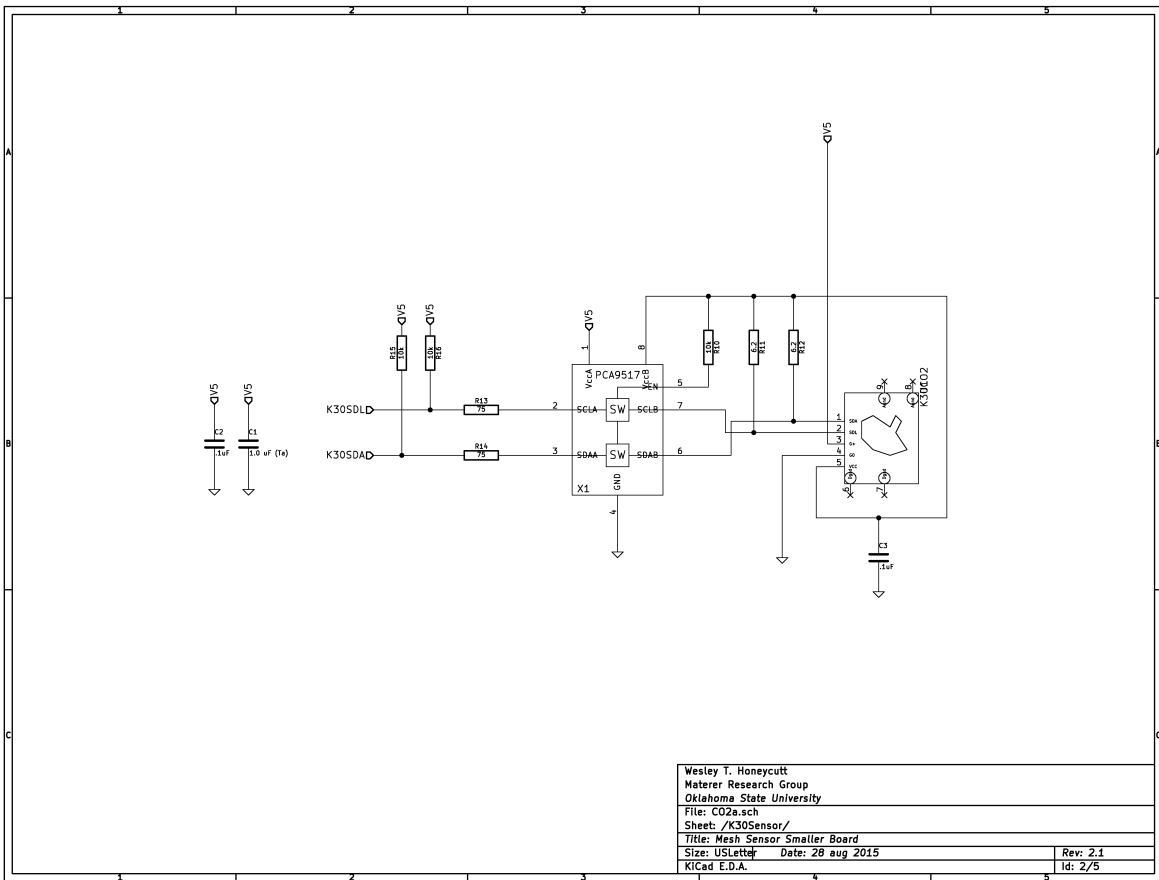


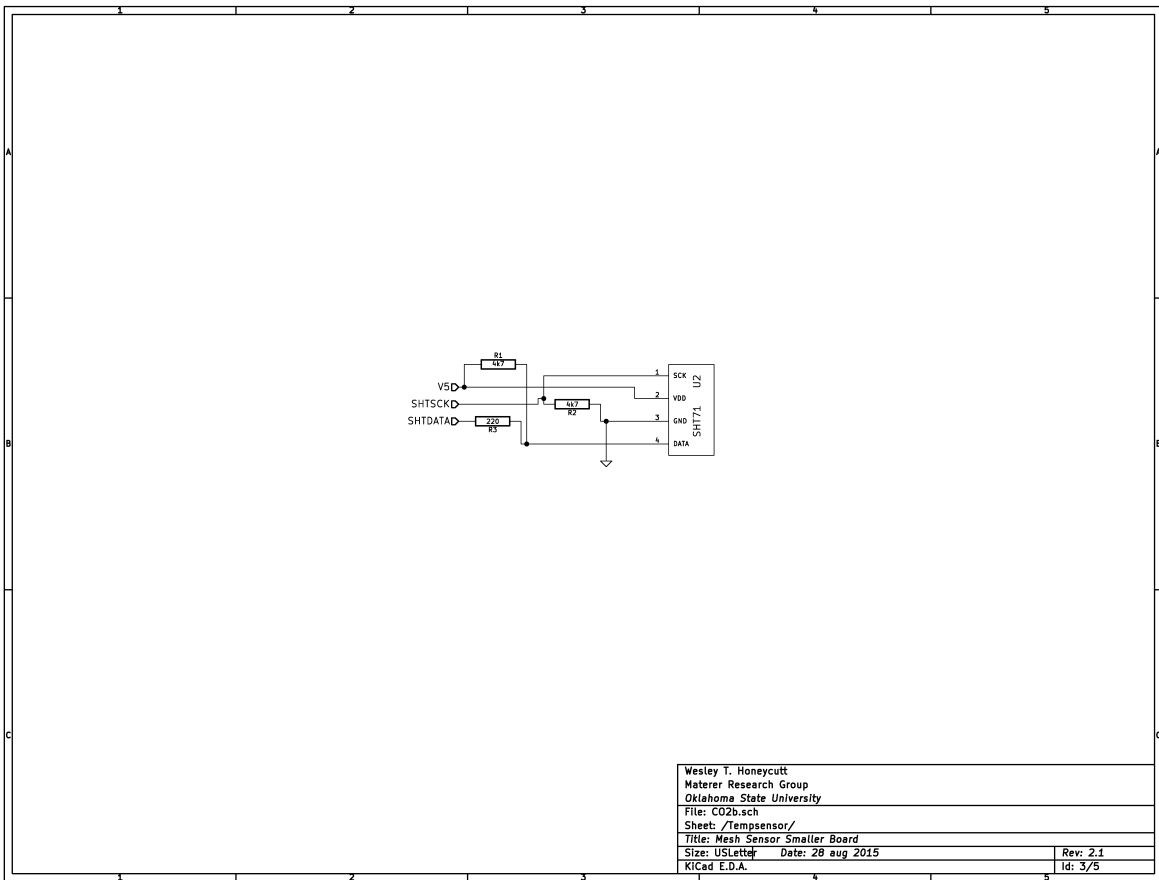
Materer Lab Group	
Oklahoma State University	
File: mainboardm.sch	
Sheet: /Switches/	
Title: Gas Sensor Mainboard	
Size: USLetter	Date: 28 aug 2015
KiCad E.D.A.	Rev: 2.1
	Id: 14/14

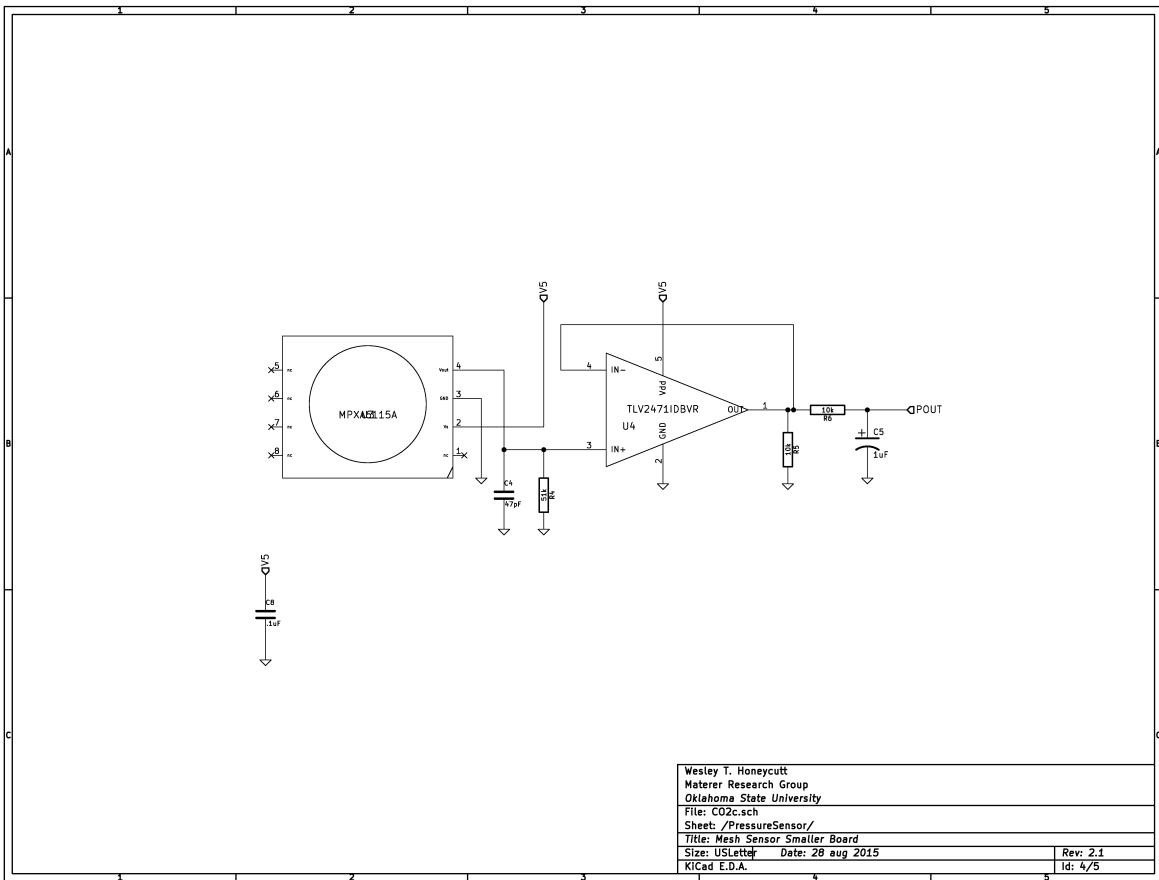
APPENDIX B

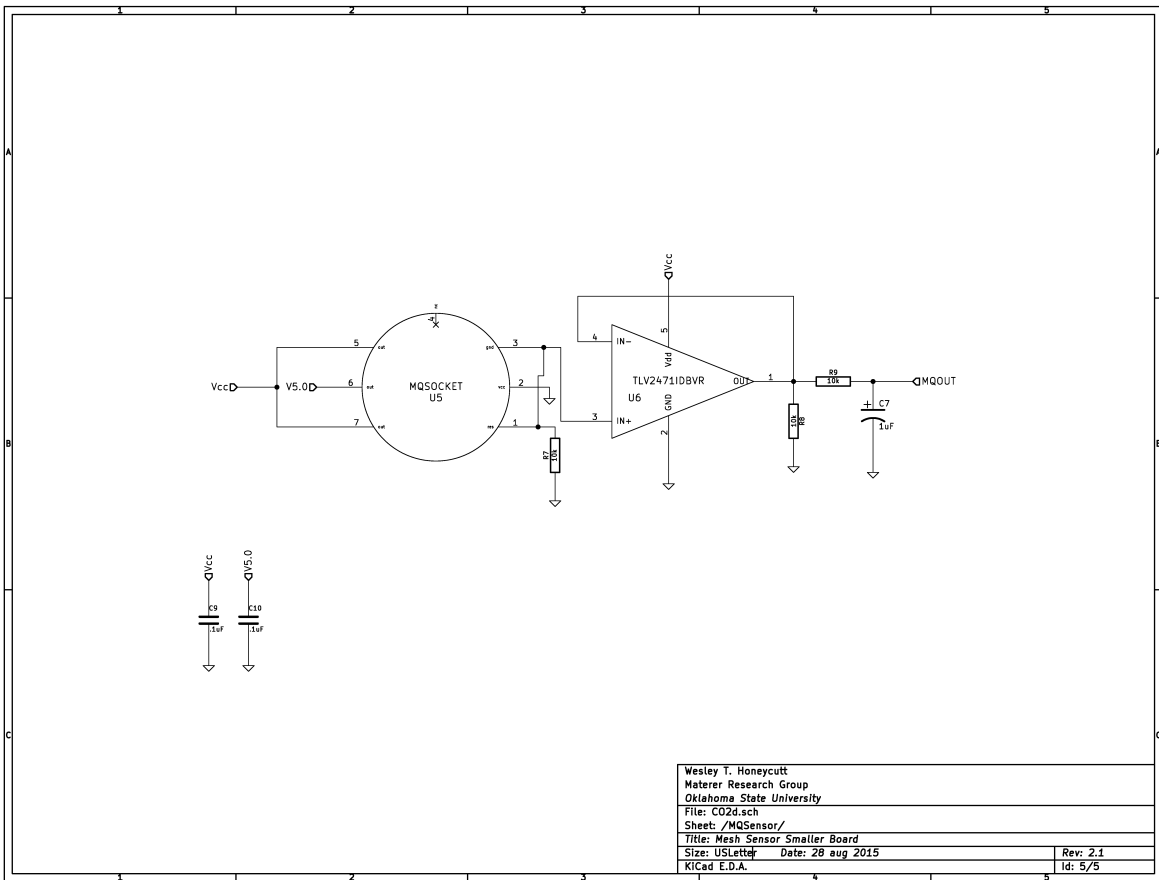
Sensor Board - Sensors Breakout Circuit





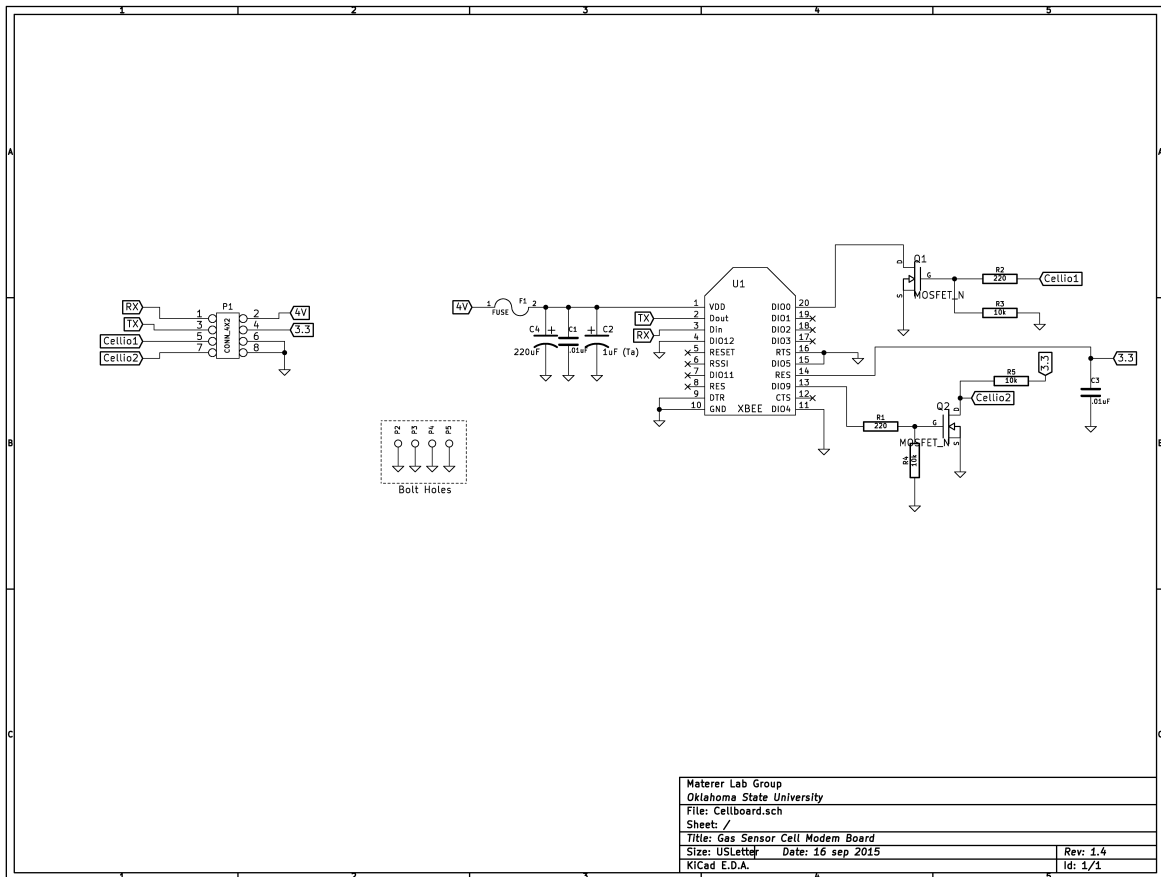






APPENDIX C

Sensor Board - Cellular Modem Breakout Circuit



APPENDIX D

OpenSCAD Code Used for 3D Printed Part

Listing D.1: OpenSCAD script which generates plastic housing 3D model

```
module RequiredBit ()
{
$fs = 0.01;
difference ()
{
union ()
{

//main box
translate ([-.4, -.0878, 0])
cube ([3.875, 2.15, .208], center = true);
translate ([1.0365, 0, .351])
cylinder (h = .494, r = .275, center = true);
translate ([-.6565, 0, .351])
cylinder (h = .494, r = .2525, center = true);
//extrabottom
translate ([-.500, 0, -.106])
cube ([2.075, 1.752, .054], center = true);
```

```

}
//stovepipe cut throughs
translate([1.0365, 0, .351])
cylinder(h = 1.000, r = .185, center = true);
translate([- .6565, 0, .351])
cylinder(h = 1.200, r = .185, center = true);
//screwwhole 1 a (boxend, notch)
translate([1.0365, .650, -.039])
cylinder(h = .130, r = .0675, center = true);
translate([1.0365, .650, .065])
cylinder(h = .078, r = .12, center = true);
//screwwhole 1 b (boxend, top)
translate([1.0365, -.670, -.039])
cylinder(h = .230, r = .0675, center = true);
translate([1.0365, -.670, .065])
cylinder(h = .078, r = .12, center = true);
//screwwhole 2 a (freeend, notch)
translate([-2.1761, .8354, -.039])
cylinder(h = .230, r = .0675, center = true);
translate([-2.1761, .8354, .065])
cylinder(h = .078, r = .12, center = true);
//screwwhole 2 b (freeend, top)
translate([-2.1761, -.9968, -.039])
cylinder(h = .230, r = .0675, center = true);
translate([-2.1761, -.9968, .065])
cylinder(h = .078, r = .12, center = true);
//antenna notch
translate([-2.0525, 0, 0])
cylinder(h = 1, r = .3125, center = true);
translate([-2.0525, 0.08, 0])
cylinder(h = 1, r = .3125, center = true);

```

```

translate([-2.05, 0.04, 0])
cylinder(h = 1, r = .3125, center = true);
//antennapretty - cleans up antenna hole
translate([-2.365, 0, 0])
cube([.625, .625, 1], center = true);
translate([-2.365, 0.08, 0])
cube([.625, .625, 1], center = true);
//vent - adds notch for vent hole on enclosure
translate([-2.3, -0.4, 0])
cylinder(h = 1, r = .25, center = true);
translate([-2.1, -0.23, 0])
rotate(51.5)
cube([.5, .396, 1], center = true);
//notch - to accommodate enclosure shape
translate([-1.4375, .8, 0])
cylinder(h = 1, r = .3875, center = true);
translate([-1.4375, 1.2, 0])
cube([.775, .775, 1], center = true);
//bigdig - reduces material used in part
translate([-1.585, -1.2, 0])
cube([2, .8, 1], center = true);
translate([-1.55, -1.2, 0])
cylinder(h = 1, r = .4, center = true);
translate([.785, -1.2, 0])
cube([2, .6, 1], center = true);
//deeperdig - reduces material used in part
rotate(42)
translate([-1.25, -.8, 0])
scale (v=[1, 2, 1])
cylinder(h = 1, r = .3, center = true);
rotate(138)

```

```

translate([-4, .59, 0])
scale (v=[1, 1.7, 1])
cylinder(h = 1, r = .3, center = true);
//lower portion cutoff/bevel - accommodates fillet in enclosure
translate([0, 1.01, 0])
cube([3.3, .25, 1], center = true);
//lower screw- strengthens screw hole near cutoff/bevel
difference ()
{
translate([-2.1761, 1, .04])
cube([1, .25, .13], center = true);
translate([-2.1761, .8354, 0])
cylinder(h = .078, r = .12, center = true);
}
//lower cutoff/bevel2 - accommodates fillet in enclosure
translate([-2.1761, 1.08, -.065])
cube([1, .25, .081], center = true);
}
}

module OptionalBox()
{
translate([1.0365, 0, -.4165])
difference ()
{
cube([1.000, 1.000, .625], center = true);
cube([.910, .910, .625], center = true);
}
}

//OptionalBox adds isolating box around pressure and temperature sensors.

```

OptionalBox ();
RequiredBit ();

APPENDIX E

Assembly Instructions For Sensor Nodes

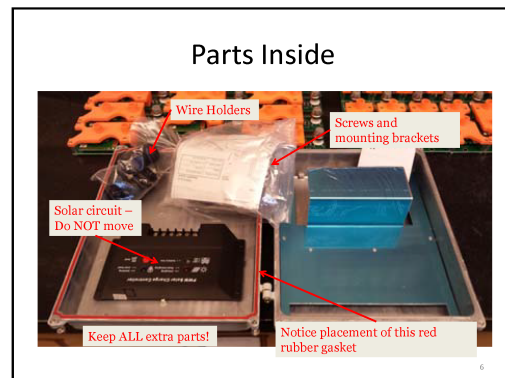
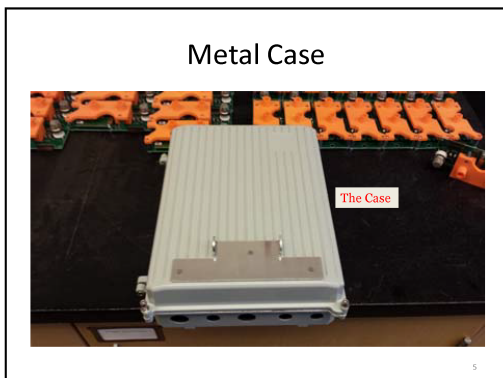
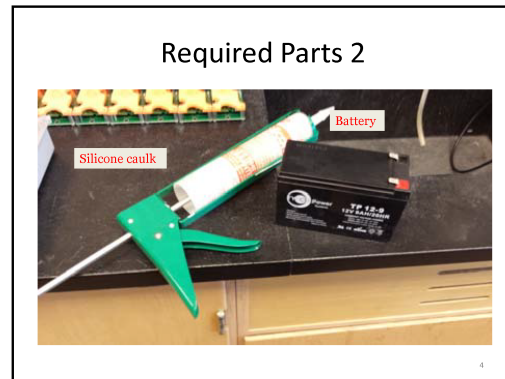
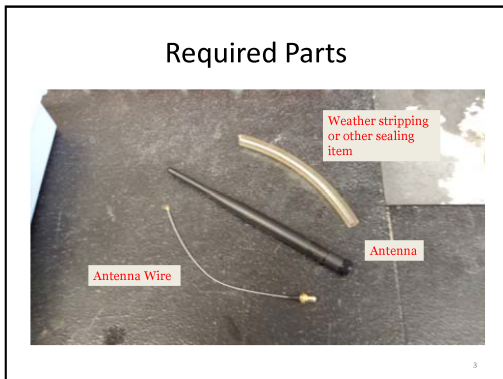
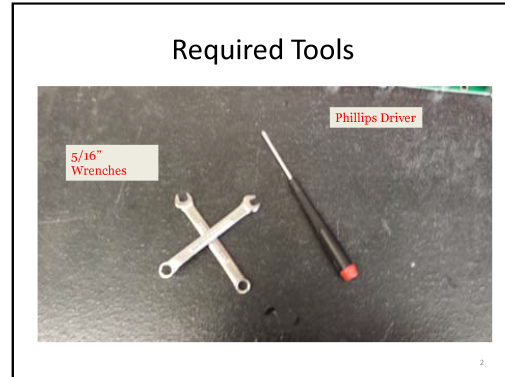


Figure E.1: Instructions for sensor node assembly, slides 1-6.

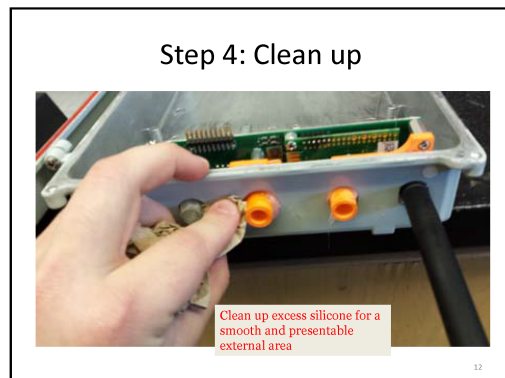
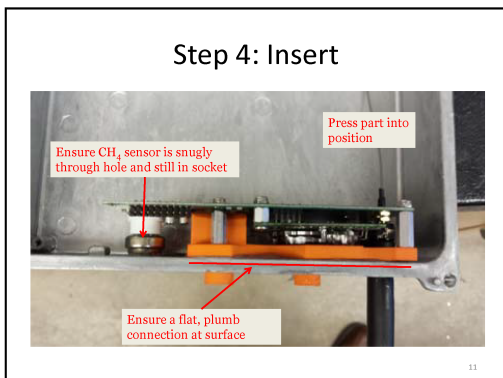
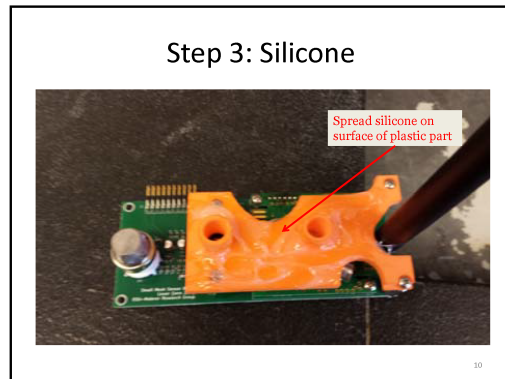
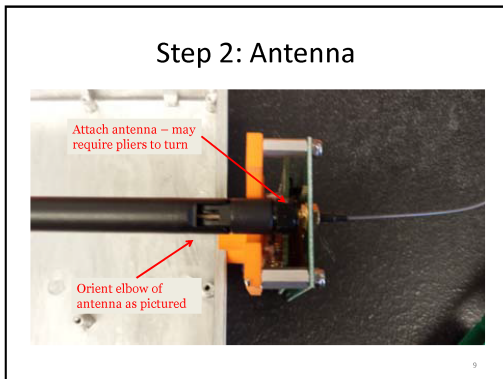
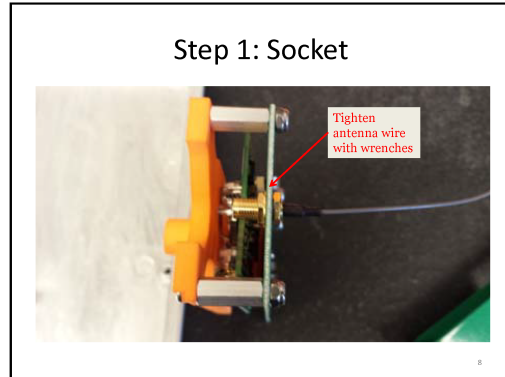


Figure E.2: Instructions for sensor node assembly, slides 7-12.

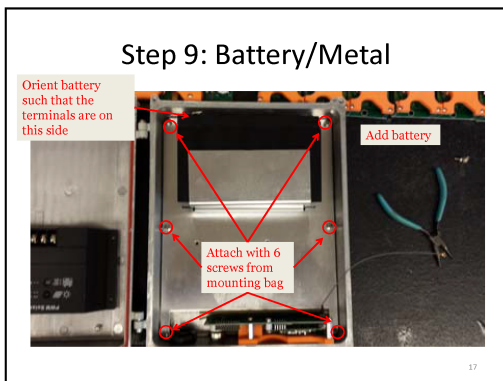
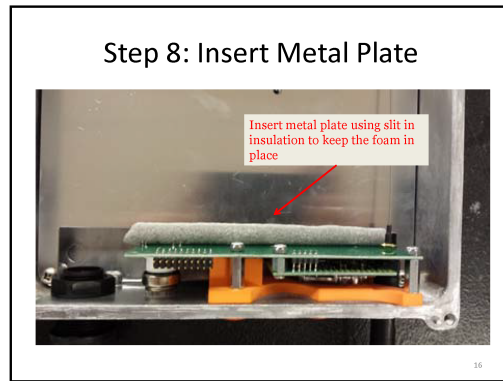
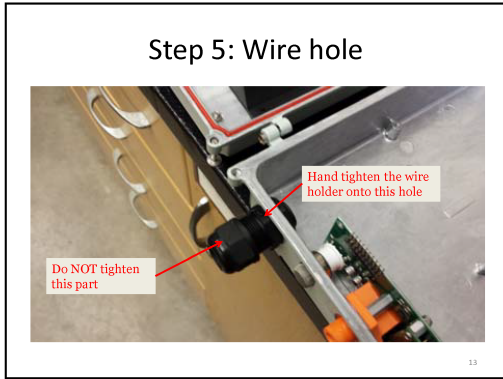
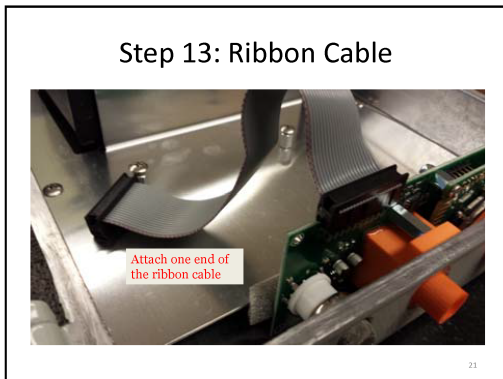
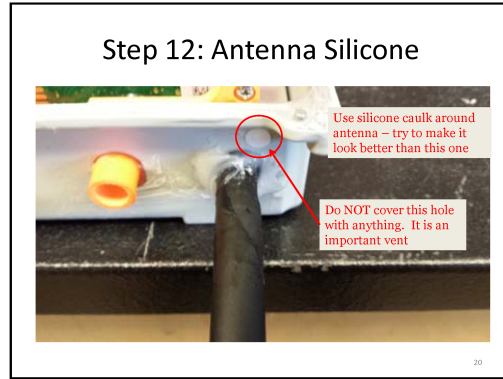


Figure E.3: Instructions for sensor node assembly, slides 13-18.



UPDATE TO ASSEMBLY (5/29/15)

23

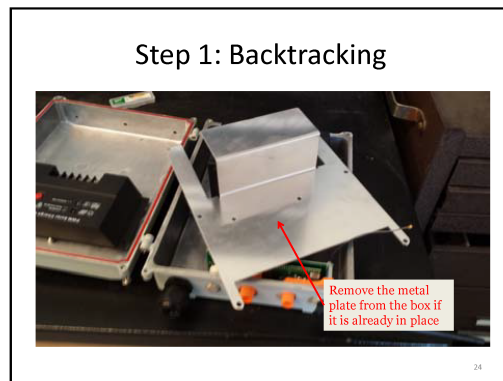


Figure E.4: Instructions for sensor node assembly, slides 19-24.

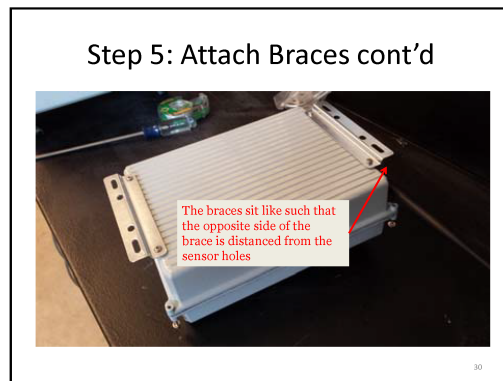
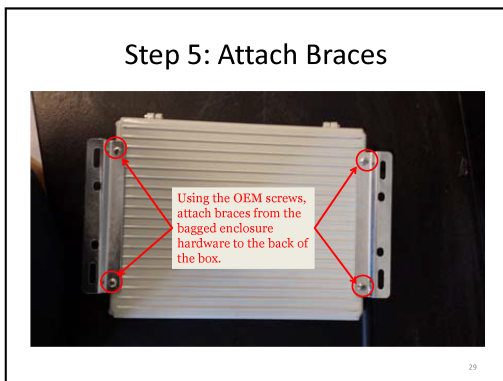
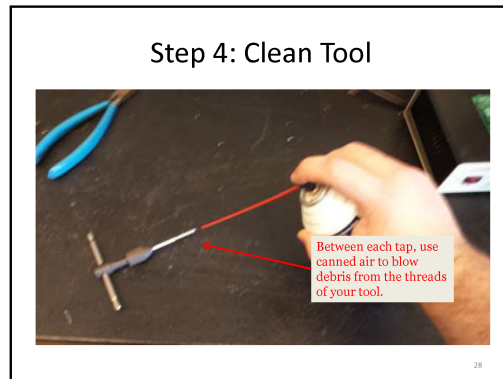
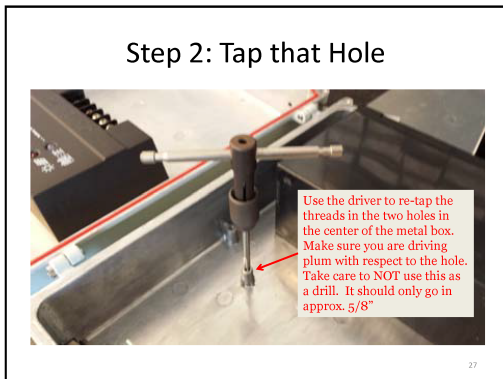
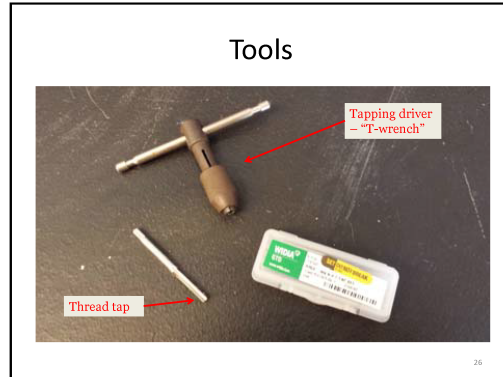
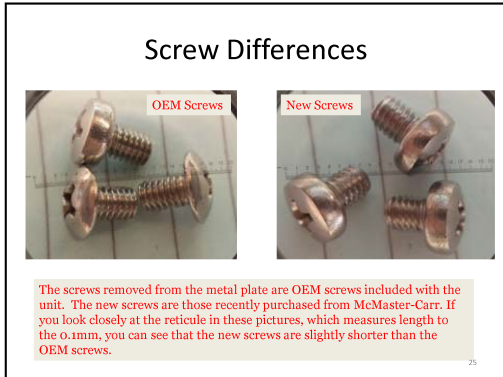


Figure E.5: Instructions for sensor node assembly, slides 25-30.

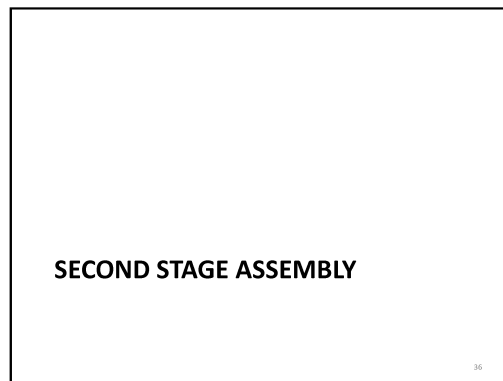
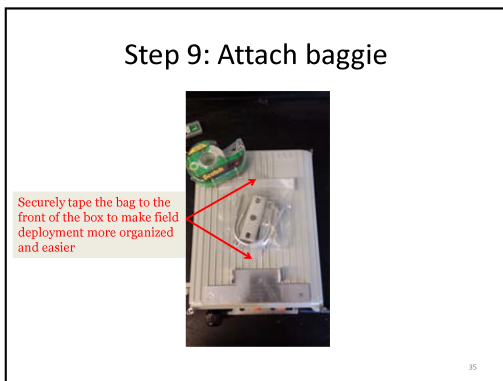
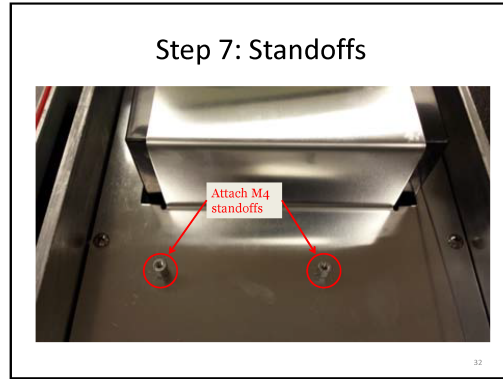
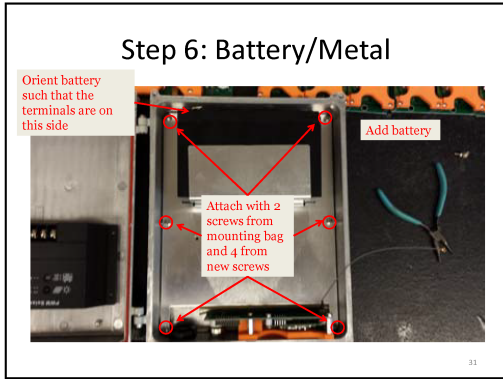


Figure E.6: Instructions for sensor node assembly, slides 31-36.

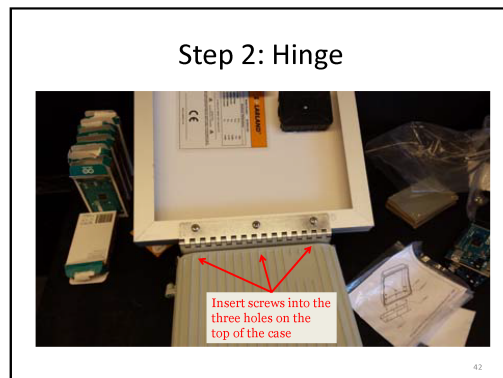
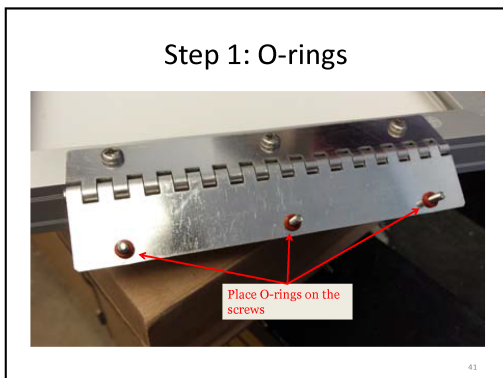
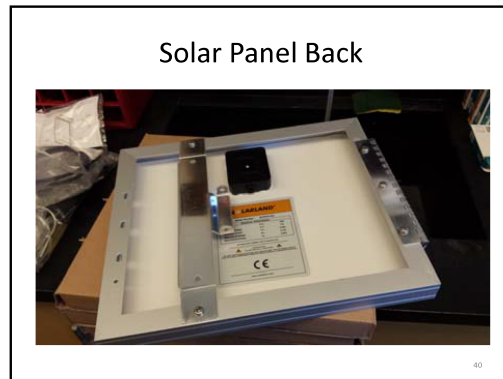
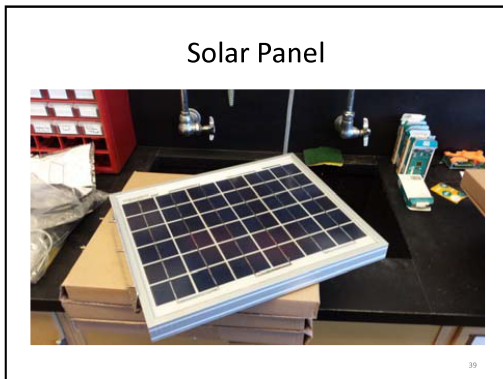
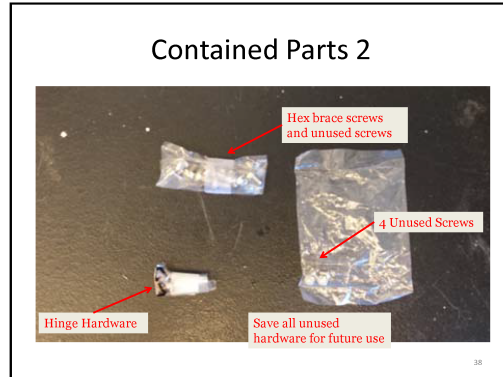
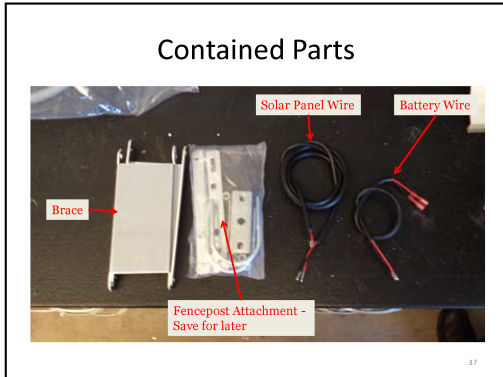


Figure E.7: Instructions for sensor node assembly, slides 37-42.

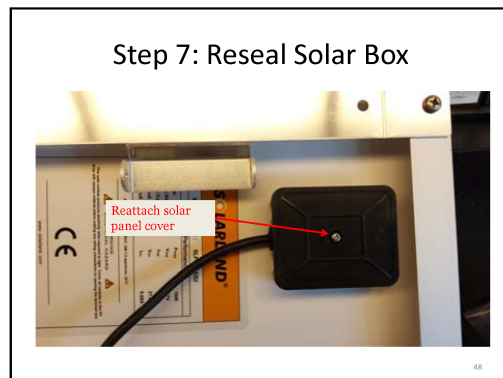
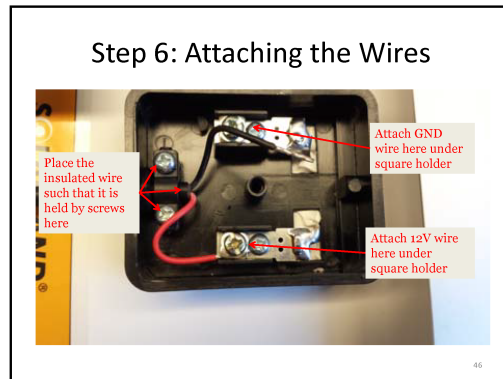
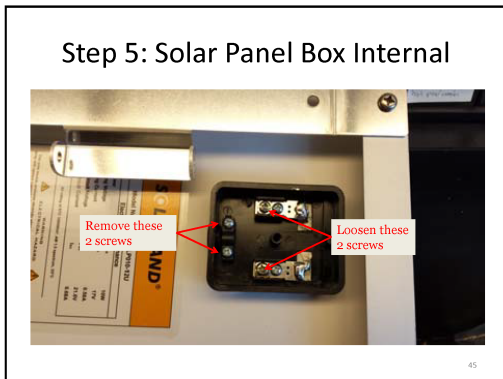
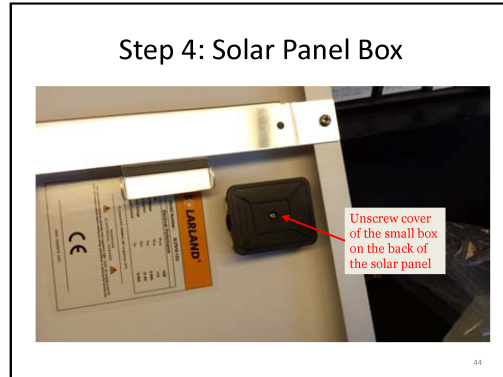


Figure E.8: Instructions for sensor node assembly, slides 43-48.

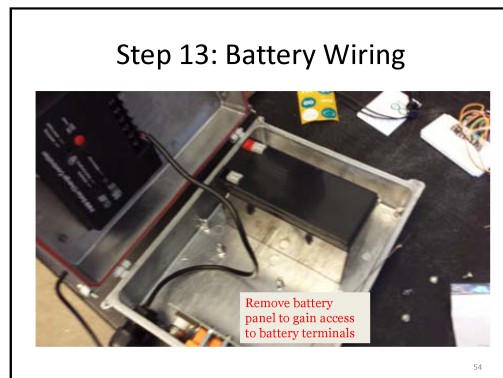
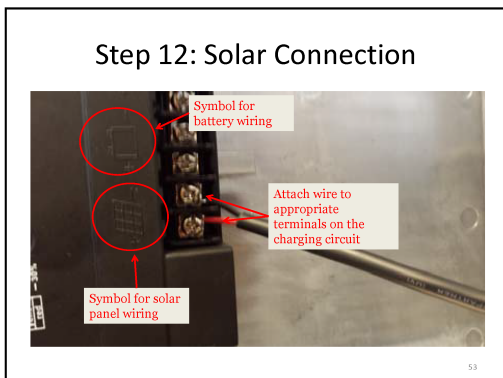
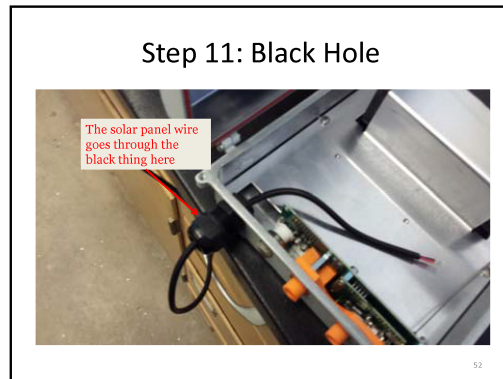
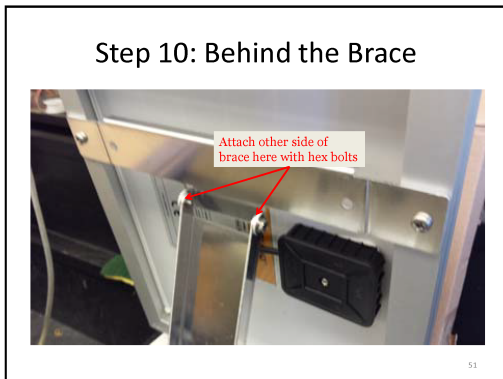
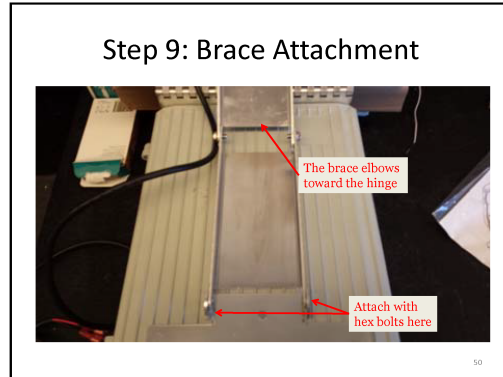
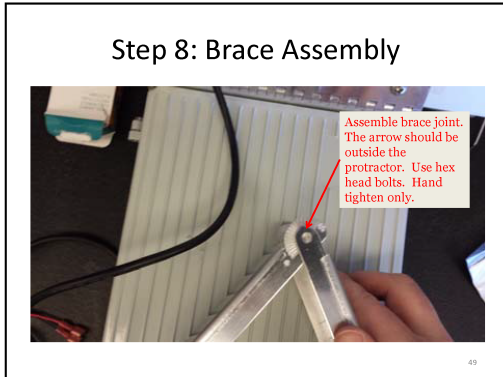


Figure E.9: Instructions for sensor node assembly, slides 49-54.

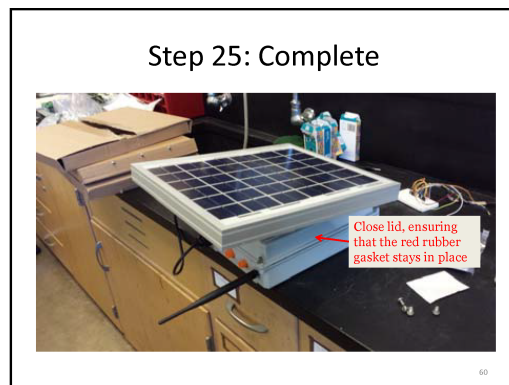
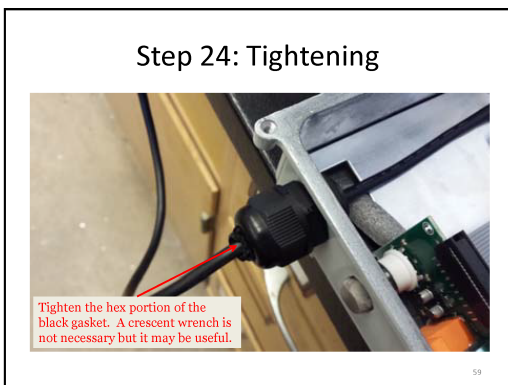
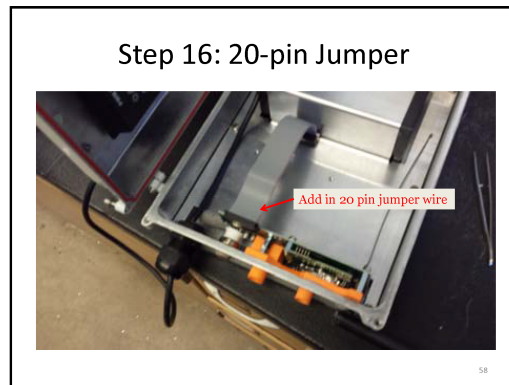
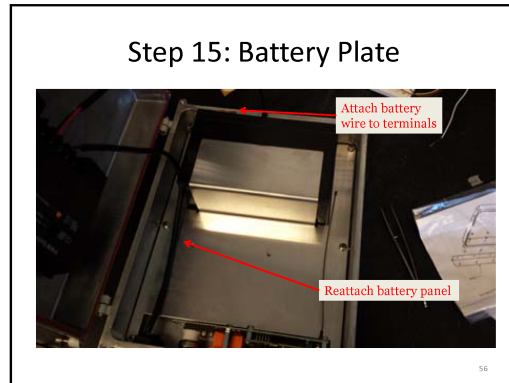
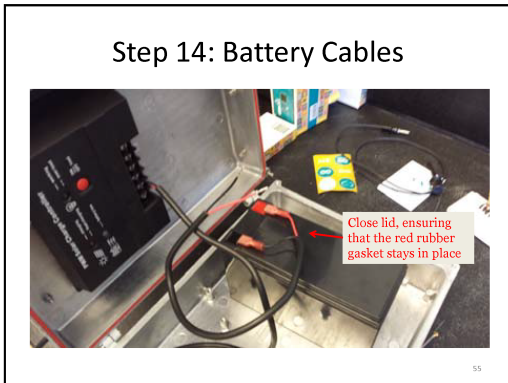


Figure E.10: Instructions for sensor node assembly, slides 55-60.

VITA

Wesley T. Honeycutt

Candidate for the Degree of:

Doctor of Philosophy

Thesis: DEVELOPMENT AND APPLICATIONS OF CHEMICAL SENSORS FOR THE DETECTION OF ATMOSPHERIC CARBON DIOXIDE AND METHANE

Major Field: Chemistry

Biographical:

Education:

Completed the requirements for Doctor of Philosophy in Chemistry at Oklahoma State University, Stillwater Oklahoma in May, 2017.

Completed the requirements for Bachelor of Science in Chemistry at University of Oklahoma, Norman Oklahoma in 2011.

Experience:

Employed by Oklahoma State University in the position of Research/Teaching Assistant in Stillwater, Oklahoma from August 2012 to date.

Employed by ChevronPhillips Chemical Company in the position of Polymer Technician in Bartlesville, Oklahoma from July 2011 to March 2012.

Professional Memberships:

President of OSU Phi Lambda Upsilon as of August, 2016.